Variational Sensitivity Analysis and Data Assimilation Studies of the Coupled Land Surface-Atmospheric Boundary Layer System

by

Steven A. Margulis

Submitted to the Department of Civil and Environmental Engineering
in partial fulfillment of the requirements for the degree of

Doctor of Philosophy

at the

MASSACHUSETTS INSTITUTE OF TECHNOLOGY

June 2002

Author .....
Department of Civil and Environmental Engineering
March 12, 2002

Certified by .....
Dara Entekhabi
Professor
Thesis Supervisor

Accepted by .....
Oral Buyukozturk
Chairman, Departmental Committee on Graduate Students

Variational Sensitivity Analysis and Data Assimilation Studies of the Coupled Land Surface-Atmospheric Boundary Layer System

by

Steven A. Margulis

Submitted to the Department of Civil and Environmental Engineering
on March 12, 2002, in partial fulfillment of the
requirements for the degree of
Doctor of Philosophy

Abstract

One of the fundamental components of Earth system science is understanding coupled land-atmosphere processes. The land plays an especially important role in the climate system principally via the regulation of surface fluxes of moisture and energy into the atmosphere. Due to the mutual dependence of these fluxes on surface and atmospheric states, the land and boundary layer comprise a coupled system with complicated interactions and feedbacks which are significant factors in modulating the variability of the weather and climate. In this thesis we develop a framework for exploratory sensitivity analysis and data assimilation in the coupled land-atmosphere system using a variational (or adjoint) approach.

The framework is applied to three distinct case studies of interest. First, the variational framework is used to quantify land-atmosphere coupling and feedbacks. The model and its adjoint are used to investigate the differences in the daytime sensitivities of land surface fluxes to model states and parameters when used in coupled and uncoupled modes. Results show that the sensitivities between the two cases are significantly different because of boundary layer feedbacks. Depending on the particular case, sensitivities can be either amplified or dampened due to the presence of an interactive boundary layer. Next, we used the variational data assimilation framework to investigate the potential of estimating land and ABL states and fluxes from readily-available micrometeorological observations and radiometric surface temperature. Results from an application to a field experiment site showed that using both surface temperature and micrometeorology allows for the accurate estimation of land surface fluxes even during non-ideal conditions. Furthermore the assimilation scheme shows promise in diagnosing model errors that may be present due to missing process representation and/or biased parameterizations. Finally, a combined variational-ensemble framework is used to estimate boundary layer growth and entrainment fluxes. The results from our application to the field site indicate a much larger ratio of entrainment to surface fluxes compared to early literature values. The fact that the entrainment parameter is larger than first hypothesized serves to further bolster the importance of land-atmosphere coupling.

Thesis Supervisor: Dara Entekhabi
Title: Professor

Acknowledgments

I wish to thank NASA for their financial support of this thesis through the NASA Earth System Science Fellowship Program.

I am greatly indebted to my advisor Dara Entekhabi for his support and encouragement throughout my graduate career at MIT. I have benefited enormously from his direction and insight and feel fortunate to have had the opportunity to work with him.

I extend many thanks to my thesis committee members: Dennis McLaughlin, John Galantowicz, and Jean-Francois Louis who have provided helpful comments and insight throughout the process.

I would also like to thank all of the members of the Entekhabi research group during my tenure in the Parsons Lab. In particular, Karen Plaut Berger, Susan Dunne, and Enrique Vivoni have been great colleagues and friends.

I also wish to thank Jeremy Pal, Freddi-Jo Eisenberg, Julie Kiang, Rolf Reichle, Nicole Gasparini, Dave Senn, Jenny Jay, and Pat Yeh who have all provided support and friendship on various levels. Getting to know them over the last few years has been a pleasure. I wish them all nothing but the best. I also extend thanks to everyone else in the Parsons Lab who has helped make this thesis possible. Special thanks go to Sheila Frankel, Jim Long, and Vicki Murphy who make all of our lives in the Parsons Lab much easier. They are the oil that keeps the machine running smoothly.

Finally, I wish to thank my parents and brother Josh, my long-time friends Renzo Misitano and Steve Singer, and Rachel Adams who have provided more support and encouragement than anyone could rightfully ask for. I will always be indebted to them.

Contents

List of Figures

List of Tables

Chapter 1

Introduction

1.1 Land-Atmosphere Interaction

The Earth system, collectively made up of the land, biosphere, atmosphere, and ocean sub-systems, consists of an extremely complex set of processes that exhibit a wide range of characteristic space and time scales. Earth system science research generally involves an effort to obtain an understanding of the system at various scales by "describing how its component parts and their interactions have evolved, how they function, and how they may be expected to continue to evolve on all time scales" (Asrar 1998). One of the fundamental components of the ongoing research effort in Earth system science is the continued development of our understanding of land-atmosphere interaction. The land plays an especially important role in the climate system principally via the regulation of fluxes of moisture and energy into the atmosphere. A large fraction of incoming solar radiation passes through the atmosphere and is dissipated at the surface through partitioning into turbulent and radiative fluxes back into the atmosphere. Precipitation incident on the land surface is similarly partitioned into infiltration and runoff where stored water can eventually make its way back to the atmosphere via evaporation (latent heat). The biosphere plays a large role in the system as vegetation is responsible for mediating a significant fraction of the hydrologic exchanges between the soil and atmosphere. Conversely, moisture availability plays a key role in determining vegetation types and distributions (Entekhabi et al. 1999).

Historically hydrologists have defined their primary control volume from the land surface downward: including the unsaturated and/or saturated soil zones, where energy (net radiation) and/or moisture (infiltration, recharge) fluxes are the primary forcing of land surface response. Conversely, meteorologists generally have considered the atmosphere as their control volume, where the primary forcing comes from the surface via turbulent fluxes of energy (sensible and latent heat) and momentum. The "outputs" from one community were used as "inputs" for the other. However, in general these fluxes are mutually dependent on both surface and atmospheric states. Thus the land surface and lower atmosphere comprise a coupled system with complicated interactions and feedbacks which are significant factors in modulating the variability of the weather and climate. The predictability and analysis of fluctuations in the climate system require the accurate representation of these feedback mechanisms and two-way land-atmosphere coupling. It is becoming recognized that emphasis on the coupled system should be a focus of hydrologic research (Entekhabi et al. 1999).

In this study we aim to develop a framework for exploratory sensitivity analysis and

data assimilation studies of the coupled land-atmosphere system. Representation of the coupled nature of the system has important implications in simulation and sensitivity analysis, where neglecting feedbacks in the system can lead to erroneous or misleading results. For data assimilation systems, incorporating an atmospheric component can both reduce the necessary forcing requirements and add potentially useful data streams (i.e. micrometerology, radiosonde data, etc.), which might otherwise go unused or be used as forcing for offline land surface models. Specific science questions we wish to address in this thesis include:

- What is the strength of coupling between the land surface and atmosphere? How does it vary with time?
- To which parameters are land-atmosphere interactions most sensitive?
- Do these sensitivities vary in time, and if so, how?
- Can we estimate land surface and ABL states and fluxes from readily-available system observations?
- Can structural model errors be diagnosed using the assimilation framework?
- What role does ABL growth and entrainment play over land?
- Can the entrainment fluxes be estimated using a data assimilation approach?

These research pursuits are linked in this study via the variational approach used to solve sensitivity and data assimilation problems.

1.1.1 The Land Surface

In this study the focus is on the diurnal interactions and vertical exchanges of energy and moisture between the land surface and overlying atmosphere. As mentioned above, the land surface plays an important role in the climate system. Unfortunately, the fluxes between the land surface and atmosphere are extremely difficult, if not impossible, to directly measure. Thus we often are forced to use models of the system. The primary goal of modeling the land surface is to represent the influence of vegetation and soil type on the regulation of fluxes between the atmosphere and surface. In recent years, models in this field have evolved from oversimplified "bucket" models to highly complex parameterizations which try to model interactions between the atmosphere, biosphere, and subsurface. Work has been done to better represent the surface through the development of so-called soil-vegetation-atmosphere-transfer (SVAT) schemes (e.g. Dickinson et al. (1986), Sellers et al. (1986)). These complex models attempt to better represent the biophysical influence of vegetation and soil on: the fractional absorption of solar radiation and emission of thermal radiation at the surface, the transfers of momentum, sensible heat, and moisture (latent heat) between the surface and atmosphere, and the resulting evolution of temperature and soil moisture profiles in the subsurface. These states (especially soil moisture) add memory to the system which can then feedback on the atmospheric states. The development, testing, and application of these types of models have become widespread in hydrology. However, much of the focus has been on studying land surface response to prescribed atmospheric boundary conditions. Because of the strongly coupled nature of the system, treating the system in this way can lead to misleading or erroneous results. While these models aim

to more realistically represent the physical processes at the atmosphere-surface interface, their complexity dictates a more thorough examination of their components in order to understand the behavior of the system and how to best represent it.

1.1.2 The Atmospheric Boundary Layer (ABL)

While meteorologists generally consider the entire troposphere (up to roughly 11 km), the influence of the land surface is only felt within the boundary layer (lowest 1–3km). In fact a definition of the boundary layer is: "that part of the troposphere that is directly influenced by the presence of the earth's surface, and responds to surface forcings with a timescale of about an hour or less" (Stull 1988). Thus it is a natural step for hydrologists to extend the control volume of interest to include the atmospheric boundary layer (ABL) along with the land surface. In comparison to the ABL, the "free atmosphere" which is that part of the troposphere above the boundary layer, evolves on a much longer timescale than the land surface-ABL system. This is illustrated in Figure 1-1 where the temperature within the ABL ($\sim$ 100 m) exhibits a strong diurnal cycle, while above the ABL ($\sim$ 1100 m), there is no discernible diurnal variability.

As a direct result of interactions with the land surface, the atmospheric boundary layer has a well defined vertical structure that evolves over the diurnal cycle. The three primary components of this structure are the surface layer, the mixed-layer, and the entrainment zone, which together span the vertical distance from the land surface to the overlying free atmosphere. The surface layer is the region at the bottom of the boundary layer (generally the lowest 10%) and is marked by significant gradients in temperature (unstable thermal stratification during daytime), moisture, and wind speed due to the presence of the land surface boundary. Convection causes turbulence which tends to mix heat, moisture, and momentum uniformly in the vertical in the mixed-layer (neutrally stratified during daytime). The altitude over which this turbulent mixing occurs corresponds to the height of the mixed-layer. A stable layer at the top of the mixed-layer acts as a lid to the rising thermals from the surface. Figure 1-2a shows typical profiles of specific humidity, potential temperature, and wind speed in the boundary layer. Note the nearly uniform profiles of each variable within the mixed-layer. The ABL model, which is described in the next chapter, is based on idealized representations of these profiles (Tennekes (1973), Smeda (1979), Driedonks (1982), and McNaughton and Spriggs (1986), Brubaker and Entekhabi (1995), Kim and Entekhabi (1998)). The model consists of a slab-type representation of the boundary layer with uniform potential temperature and specific humidity profiles throughout the mixed-layer, which is overlain with inversions in the potential temperature and specific humidity (see Figure 1-2b). As turbulent mixing becomes more vigorous during the day, eddies entrain warm and dry air from above the ABL causing the mixed-layer to grow in depth. This conceptualization of the ABL leads directly to the development of relatively simple conservation and dynamic equations which in conjunction with a land surface model, explicitly account for the land-atmosphere interactions we are interested in.

1.2 Variational Approach to Diagnosis and Estimation of Land-ABL System

The overall objective of this research is to develop a new diagnostic tool for coupled land-atmosphere models and design frameworks for the statistically optimal assimilation of ob-

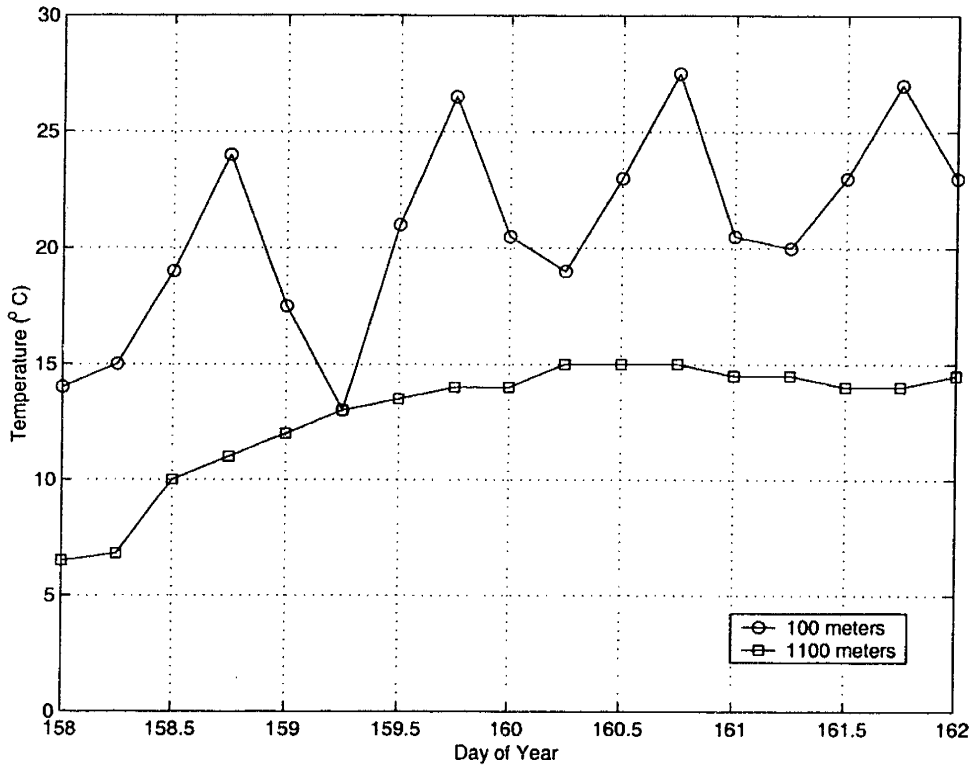

Figure 1-1: Illustrative example of temperature evolution measured near the ground (100 meters) and at a height of 1100 meters above the ground from radiosonde launches from Ft. Still OK. (Taken from Stull, 1988)).

servations. We aim to accomplish this goal by using the variational (or adjoint) technique. The adjoint model is derived from a forward model of the coupled land-atmosphere system. The adjoint method was chosen primarily for two reasons: 1) Results from the adjoint model can not only be used to obtain parameter sensitivities with greater efficiency than those obtained with traditional simulation techniques, but they also provide physical insight into how these sensitivities arise, which leads to diagnostic insight into the behavior of the system; 2) The adjoint model can be used in a variational data assimilation framework to yield dynamically consistent estimates of land surface states and fluxes which optimally combine observations with the model of the physical system.

In meteorology and oceanography there is a well-established history of using variational techniques for both sensitivity studies (e.g. Hall et al. (1982), Hall (1986), Errico and Vukicevic (1992), Rabier et al. (1992), Zivković et al. (1995), and Li and Navon (1998)) and data assimilation (e.g. LeDimet and Talagrand (1986), Talagrand and Courtier (1987), Thacker and Long (1988), Li et al. (1993), and Lu and Hsieh (1997)). This is due in large part to the nature of many research problems in these fields. For example, in meteorology, trying to diagnose how much a particular aspect of some synoptic feature will change if perturbations are made to antecedent synoptic conditions is of great importance. In another example, numerical weather prediction is posed as an initial value problem, where the goal is to use meteorological measurements and a physical model (along with their known error

characteristics) over the last forecast cycle to obtain optimal estimates of initial conditions, which can then be used for the next forecast. In these and other examples, large state, parameter, and forcing fields and/or extensive datasets of meteorological measurements require an efficient technique to evaluate sensitivities. Adjoint models can be ideal tools in such circumstances due to their relative computational efficiency in comparison to other more traditional simulation techniques.

While variational techniques have some history in solving inverse problems in groundwater hydrology (e.g. Sun and Yeh (1990), Yeh and Sun (1990), and McLaughlin and Townley (1996)), it is only much more recently that adjoint models have begun to be used in surface hydrology applications (e.g. Callies et al. (1998), Rhodin et al. (1999), Bouyssel et al. (1999), Reichle et al. (2001a), and Reichle et al. (2001b)). Over the same time span that models have increased in complexity, hydrology has gone from a somewhat "data poor" to a "data rich" environment as hydrologic data have become much more prevalent with the increase in remote sensing capabilities. With the advent of large datasets and complex models, many of the issues that led meteorologists and oceanographers to use adjoint techniques are now at the forefront in hydrology.

1.3 Organization of Thesis

In Chapter 2 a coupled land surface-boundary layer model and its adjoint are developed. The model and its adjoint are thoroughly tested with an application to a particular field experiment site. Simple sensitivity and data assimilation examples are then presented to illustrate use of the model and its adjoint as a general tool for sensitivity and data assimilation studies. The framework is then applied to three distinct case studies of interest. In Chapter 3 the model and its adjoint is used to investigate the differences in the daytime sensitivities of land surface fluxes to model states and parameters when used in coupled and uncoupled modes. The adjoint model allows for the diagnosis of important sensitivity pathways in the system. In Chapter 4 the variational data assimilation framework is used to investigate the potential of estimating land and ABL states and fluxes from readily-available micrometeorological observations and radiometric surface temperature. We also use the framework as a test bed to investigate the estimation of structural model errors from these data streams. In Chapter 5 the focus is on the estimation of boundary layer growth and entrainment. The problem is posed as a parameter estimation problem where the assimilated observations are radiosonde and micrometeorology data. We also investigate the potential to estimate entrainment from only the micrometeorological data for cases where radiosondes may be unavailable. Finally, in Chapter 6 the key findings are summarized along with potential directions of future research.

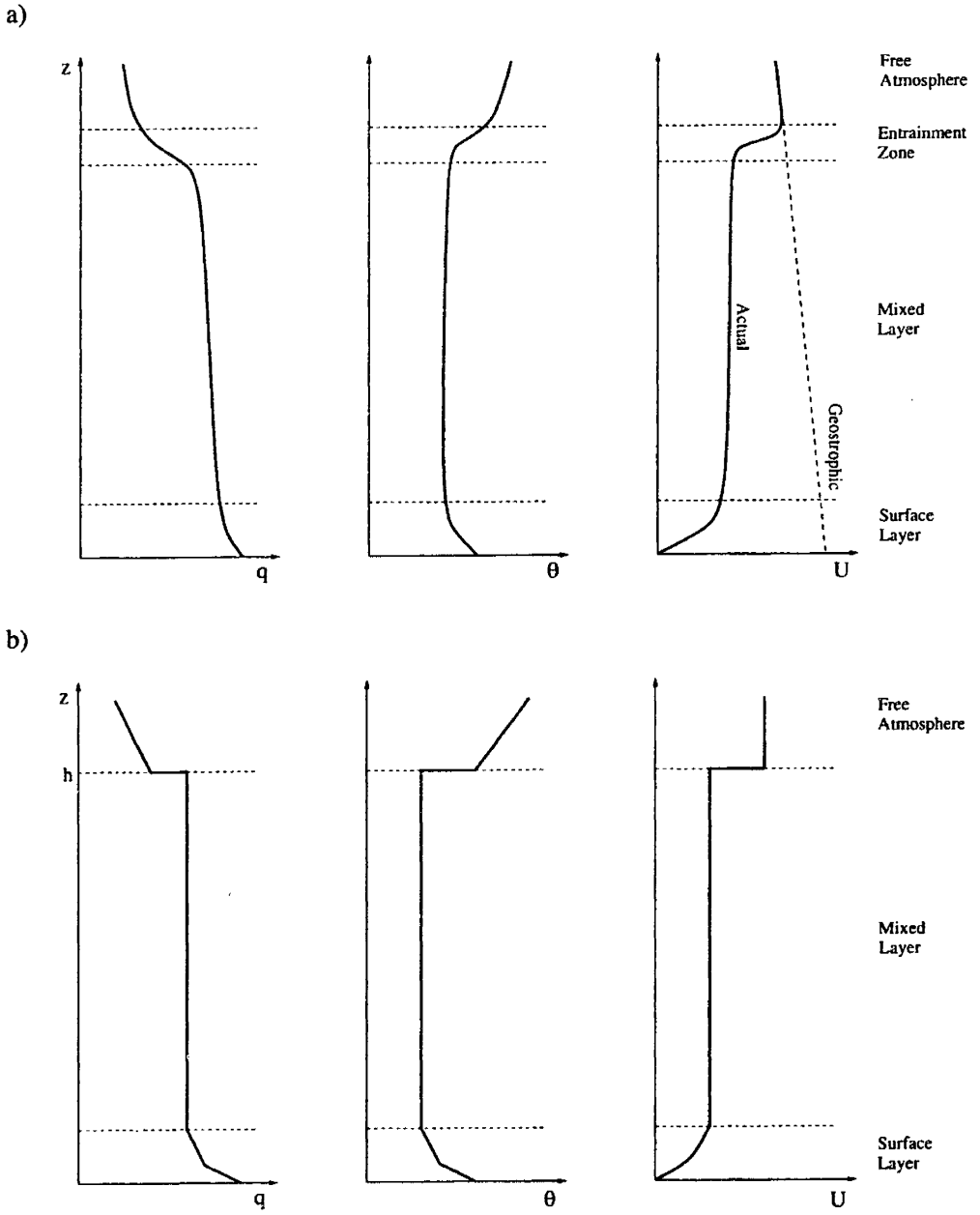

Figure 1-2: a) Typical daytime profiles of mean specific humidity (q), potential temperature (θ), and wind speed (U). b) Idealized profiles of q, θ, and U to be used in boundary layer model.

Chapter 2

A Coupled Land Surface-Boundary Layer Model and Its Adjoint

In this chapter we introduce a simple coupled land surface-boundary layer model and its adjoint are introduced. The primary goal is to demonstrate the capabilities of the adjoint model as a flexible tool for sensitivity analysis and data assimilation. Simple illustrative examples of each type of application are used to give a glimpse of the type of problems that can be addressed using the model and its adjoint. Subsequent chapters will present more results from specific case studies. In Sections 2.1 and 2.2 the coupled model and present results from model testing at a field experiment site are introduced. Sections 2.3 and 2.4 discuss the development and validation of the adjoint model. Finally, in Sections 2.5 and 2.6 simple examples of applications of the adjoint model to a sensitivity experiment and data assimilation problem are presented.

2.1 Model Development

One of the underlying objectives of this study is to redefine the boundaries of the system which should be used in land-atmosphere sensitivity studies and data assimilation schemes. While the boundary traditionally used has been the land-atmosphere interface, a more physically appropriate one is the top of the atmospheric boundary layer (ABL). By extending the system to include the ABL, the artificial constraint imposed on the land surface component of the system by forcing it with prescribed micrometeorological data is removed. Further, a physically realistic coupling between the land surface and atmosphere is allowed without the burden of including a full numerical model of the atmosphere. Based on these arguments, we have developed a coupled model of the land surface-boundary layer system that serves as a simple exploratory tool for land-atmosphere interaction studies.

A comprehensive description of the model is given in Appendices A and B. Only the key components of the model are presented here. A list of the symbols used throughout the text is given in Appendix C.

2.1.1 Surface Energy and Moisture Budget

The core of the model involves solving the coupled energy and water budget equations between the land surface and overlying atmospheric boundary layer (ABL). We first present (Sections 2.1.1-2.1.3) the model in dynamical form (i.e. as a set of prognostic equations)

since it is with respect to this framework that the adjoint model will be developed. In the subsequent Sections (2.1.4-2.1.7) the fluxes (energy and moisture) which determine the evolution of the state variables are discussed.

The land surface component of the model consists of prognostic equations for three temperature states (canopy temperature (T_c), surface ground temperature (T_g), and deep ground temperature (T_d)) and three soil moisture states (W_1, W_2, and W_3) representing the soil profile throughout the root-zone. The surface energy budget is given by the following equations:

$$C_c \frac{dT_c}{dt} = R_{nc} - H_c - L_v E_c \tag{2.1}$$

$$C_g \frac{dT_g}{dt} = (R_{ng} - H_g - L_v E_g) - \frac{2\pi C_d}{\tau_d}(T_g - T_d) \tag{2.2}$$

$$C_d \frac{dT_d}{dt} = \frac{1}{2(\pi \tau_a)^{1/2}}(R_{ng} - H_g - L_v E_g) \tag{2.3}$$

In Equation (2.1), the vegetation canopy is heated by incoming net radiation and cooled by sensible and latent heat flux to the ABL. The soil energy balance, given by Equations (2.2 and (2.3), uses a force-restore formulation (e.g. Bhumralkar (1975), Deardorff (1978), Lin (1980), and Hu and Islam (1995)) where T_g is forced by the incoming ground heat flux (the residual of the ground surface energy balance) while simultaneously being restored to a deep temperature (T_d) which varies slowly over the annual cycle.

For the moisture budget the soil column is discretized into three layers: a surface layer, root-zone layer, and recharge zone which make up the top 1–2 m of soil. The prognostic equations for the surface moisture budget are given by:

$$\frac{dW_1}{dt} = \frac{1}{\theta_s d_1}[P_{W1} - Q_{1,2} - \frac{1}{\rho_w} E_g - \frac{1}{\rho_w} E_{c1}] \tag{2.4}$$

$$\frac{dW_2}{dt} = \frac{1}{\theta_s d_2}[Q_{1,2} - Q_{2,3} - \frac{1}{\rho_w} E_{c2}] \tag{2.5}$$

$$\frac{dW_3}{dt} = \frac{1}{\theta_s d_3}[Q_{2,3} - Q_3] \tag{2.6}$$

In Equation (2.4), moisture is supplied to the soil via infiltration from above (P_{W1}). Soil moisture loss comes via evapotranspiration and vertical exchange of moisture between layers. Transpiration taps soil moisture from the top two soil layers (E_{c1} and E_{c2}), while there is also bare-soil evaporation from the uppermost layer (E_g). Vertical moisture fluxes between layers (Q_{12} and Q_{23}) and drainage from the bottom layer (Q_3) are functions of the matric head in adjacent layers.

2.1.2 ABL Energy and Moisture Budget

For the atmospheric boundary layer component we use a mixed-layer model (see Figure 2-1). This formulation is an idealization of profiles seen in convectively driven atmospheric boundary layers. In our model the boundary layer is convectively mixed, producing constant (with height) profiles of potential temperature (θ) and specific humidity (q). The shallow layer of air between the mixed-layer and the ground is called the surface layer which is convectively unstable during the growth phase of the boundary layer. This type of slab model, which also idealizes the entrainment zone as an instantaneous "jump" in the potential temperature and humidity states, has been used often to describe the convective boundary layer (e.g. Tennekes (1973), Smeda (1979), Driedonks (1982), and McNaughton and Spriggs (1986)).

The corresponding energy and moisture budget equations for the mixed-layer are:

$$\rho c_p h \frac{d\theta}{dt} = [R_{ad} + R_{cu} + R_{gu}]\epsilon_a - R_{Ad} - R_{Au} + H_c + H_g + H_{top} \tag{2.7}$$

$$\rho h \frac{dq}{dt} = E_c + E_g + E_{top} \tag{2.8}$$

In Equation (2.7) radiative fluxes enter the ABL from the free atmosphere above (R_{ad}) and the surface below (R_{cu} and R_{gu}). The fraction which is absorbed by the mixed-layer depends on the column emissivity of the ABL (ϵ_a) which is a function of the specific humidity. The ABL is also warmed by sensible heat flux from the surface (H_c and H_g) and the entrainment flux at the top of the mixed-layer (H_{top}), which is generally positive due to the relatively warm free atmosphere air overlying the ABL (Stull 1988). Radiative cooling of the ABL occurs through the radiative fluxes emitted upward and downward from within the mixed-layer (R_{Au} and R_{Ad} respectively). Condensation is assumed to occur above the mixed-layer and therefore there is no latent heating within the ABL. In Equation (2.8), the ABL is moistened from below by evaporation from the surface. There is also an entrainment flux from above the mixed-layer (E_{top}) which is generally negative since the air above the ABL is usually drier than that within the mixed-layer (Stull 1988).

2.1.3 Mixed-Layer Height Evolution

As mentioned above, the height of the mixed-layer is a dynamic quantity which evolves throughout the day. Turbulent eddies caused by both free and forced convection entrain air from the overlying free atmosphere causing the ABL to grow. The virtual heat flux at the surface (H_v), which causes free convection mixing, is primarily responsible for ABL growth during the day. When the virtual heat flux vanishes at the end of the day, the turbulence dissipates quickly, and the ABL collapses to a residual level which is maintained through forced convection. The diurnal range of the ABL generally varies between ~100–300 m in the early morning to ~ 1–3 km by late afternoon.

Smeda (1979) derived a model for the diurnal evolution of the ABL height by considering the balance between turbulent kinetic energy (TKE) due to thermal convection, TKE generated by windshear, and the dissipation of TKE within the boundary layer. Following his derivation we have an expression for the daytime growth of the ABL height in terms of

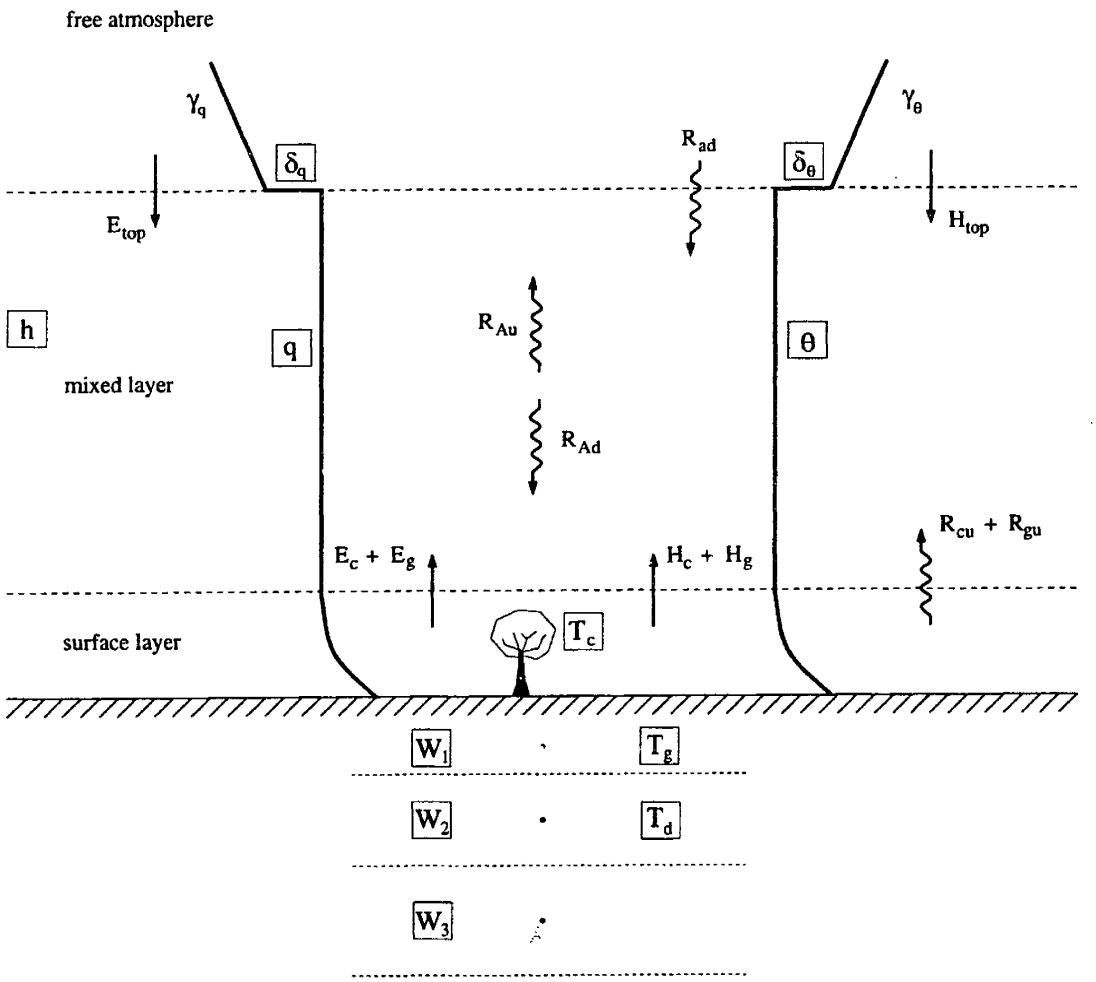

Figure 2-1: Schematic diagram of coupled land surface-atmospheric boundary layer model showing idealized profiles of ABL states and corresponding fluxes between the mixed-layer and land surface and the mixed-layer and overlying atmosphere. Surface turbulent fluxes occur across the surface layer (of thickness $\sim 0.1h$) and entrainment fluxes occur across the interface between the free atmosphere and mixed-layer (at height h). The system state variables are bounded by boxes. All symbols are defined in Appendix C.

the net TKE generation:

$$\frac{dh}{dt} = \frac{2\theta G_* e^{-\xi h}}{gh\delta_\theta} + (1 - 2 \times 0.4)\frac{H_v}{\rho c_p \delta_\theta} \tag{2.9}$$

The first term on the right hand side represents the net generation of TKE due to forced convection and the second term the net generation of TKE due to free convection. During the daytime the term representing generation of turbulent energy due to thermal convection dominates. When the surface virtual heat flux switches sign near sunset, there is a transition from unstable to stable conditions which causes the collapse of the ABL as the turbulence dissipates. The model includes a parameterization of this collapse, but for brevity (and because the rest of the chapter focuses on daytime ABL growth only) it is not presented here. The formulation of the collapse of the ABL is discussed in Appendix A.

As seen in Figure 2-1, the ABL slab model contains instantaneous jumps in temperature and humidity at the top of the boundary layer. The strengths of these inversions (δ_θ and δ_q) evolve in conjunction with the rest of the system. For the potential temperature inversion there are two factors which cause it to change. As the boundary layer warms, the inversion strength decreases. Also, as the boundary layer grows the inversion strength will increase. The prognostic equation for potential temperature inversion strength can therefore be written as:

$$\frac{d\delta_\theta}{dt} = \gamma_\theta \frac{dh}{dt} - \frac{d\theta}{dt} \tag{2.10}$$

Along similar lines, the specific humidity inversion strength will increase (become more negative) as the boundary layer becomes more moist, and will also increase as the boundary layer grows. The result is the following prognostic equation for the specific humidity inversion:

$$\frac{d\delta_q}{dt} = \gamma_q \frac{dh}{dt} - \frac{dq}{dt} \tag{2.11}$$

The parameters γ_θ and γ_q are the lapse rates in potential temperature and specific humidity above the mixed-layer and serve as forcing parameters.

2.1.4 Entrainment Fluxes

The mixed-layer is generally capped by inversions in potential temperature and specific humidity (see Figure 2-1). Due to the boundary layer growth, warm dry air from above will be entrained into the mixed-layer. Through consideration of the conservation of heat and moisture across the interface as the mixed-layer grows, expressions for the entrainment fluxes can be derived. The entrainment fluxes are given by:

$$H_{top} = \rho c_p \delta_\theta \frac{dh}{dt} \qquad\qquad E_{top} = \rho \delta_q \frac{dh}{dt} \tag{2.12}$$

2.1.5 Radiative Fluxes

The incoming shortwave radiation at the land surface is a function of location, time of day and year, and atmospheric conditions. Since we focus on clear-sky conditions, if observations are unavailable, a simple formulation such as that given by Hartmann (1994) yields a good

estimate of the diurnal cycle in incoming solar radiation at a given location and time of year.

The absorption and emission of longwave radiation in the model are derived using a broadband emissivity approach taken from Brutsaert (1975) and extended by Brubaker and Entekhabi (1995). The expressions for the longwave fluxes are presented below, while those of the corresponding emissivity expressions are summarized in Appendix A.

The longwave radiation from the free atmosphere overlying the ABL (R_{ad}) depends on the pressure, temperature, and humidity profiles above the ABL. For clear skies, using the profiles of a standard atmosphere, Brutsaert (1975) derived the expression:

$$R_{ad} = \sigma \epsilon_{ad} T_{h+}^4 \tag{2.13}$$

where T_{h+} is the air temperature just above the mixed-layer height h. The expressions for the upward and downward longwave radiative fluxes emanating from within the mixed-layer were derived by Brubaker and Entekhabi (1995) and are given by:

$$R_{Ad} = \sigma \epsilon_d \theta^4 \qquad\qquad R_{Au} = \sigma \epsilon_u \theta^4 \tag{2.14}$$

which are functions of the mixed-layer potential temperature and effective emissivities which depend on the mixed-layer specific humidity (see Appendix A).

The vegetation radiative transfer model is derived from the two-stream approximation used by Sellers (1985) which describes the interception, reflection, transmission, and absorption of short- and longwave radiation by the vegetation and underlying soil. From this formulation the net radiation absorbed by the canopy and ground can be written as a sum of radiative components across wavelength bands Λ (visible, near-infrared, and thermal) and direction of radiation μ (beam or diffuse):

$$R_{nc} = \sum_{\Lambda} \sum_{\mu} F_{\Lambda,\mu(c)} \qquad\qquad R_{ng} = \sum_{\Lambda} \sum_{\mu} F_{\Lambda,\mu(g)} \tag{2.15}$$

The reader is referred to Appendix A for the detailed expressions for each component of solar and thermal radiation absorbed by the canopy and ground.

Finally, the radiative fluxes emitted upward from the canopy and ground into the mixed-layer are given by:

$$R_{cu} = \sigma T_c^4 V_c \delta_T \qquad\qquad R_{gu} = \sigma \epsilon_g T_c^4 (1 - V_c \delta_T) \tag{2.16}$$

where δ_T is the fraction of incident thermal radiation absorbed by the canopy.

2.1.6 Surface Turbulent Fluxes

The turbulent fluxes in the model consist of the sensible and latent heat fluxes from the canopy and ground. A resistance network identical to the one used in SiB2 (Sellers et al. 1996) is used to describe the fluxes of heat and water from the surface. The aerodynamic resistance depends on the wind profile in the unstable surface layer, which is determined by the surface-layer parameterization given by Louis et al. (1982). The fluxes from the canopy into the canopy air are given by:

$$H_c = \frac{\rho c_p (T_c - T_a)}{r_b} \qquad\qquad L_v E_c = \frac{\rho c_p}{\gamma} \frac{(e_*(T_c) - e_a)}{\overline{r_c} + 2r_b} \tag{2.17}$$

Similarly, the ground sensible and latent heat fluxes into the canopy air are given by:

$$H_g = \frac{\rho c_p (T_g - T_a)}{r_d} \qquad L_v E_g = \frac{\rho c_p}{\gamma} \frac{(h_{soil} e_*(T_g) - e_a)}{r_{soil} + r_d} \tag{2.18}$$

The expressions for the aerodynamic resistances r_b and r_d are taken from the LSX model (Bonan et al. 1993) and the expression for soil resistance is taken directly from SiB2. Finally, the bulk canopy resistance ($\bar{r}_c$) is modeled using the formulation given by Sellers (1985) and subsequently modified by Koster and Suarez (1996). The reader is referred to Appendix A for the appropriate expressions.

2.1.7 Moisture Transport Within the Soil

The parameterization used to describe the isothermal vertical exchange of moisture between soil layers is identical to that used in SiB (Sellers et al. 1986) which uses the soil water retention parameterization of Clapp and Hornberger (1978) and assumes gravitational drainage from the bottom soil layer. The bulk redistribution scheme is an approximation to Richards equation. For a detailed description of the parameterization, see Appendix A.

2.2 Model Testing

The primary benefit of the above model is that it is entirely forced by only incoming solar radiation, large-scale wind speed, and the lapse rates γ_θ and γ_q above the mixed-layer. It thus avoids the vast amount of micrometeorological data (e.g. air temperature, humidity, and downward longwave radiation at a reference level) needed to force many offline land surface models by simultaneously taking into account the coupled nature of the land surface-ABL system. In fact, model predictions of these variables can be used to test the model by comparing them to observed micrometeorology.

We have chosen to test the model using observations taken during the First ISLSCP Field Experiment (For an overview of FIFE see Sellers et al. (1992)). This is done primarily because of the extensive observations taken during the experiment and the subsequent modeling studies of the site which have led to parameter sets that have been thoroughly tested. Our goal in developing this model was not to perfectly simulate land-atmosphere interactions over a particular site, but as a general tool which along with its adjoint model could be used to perform sensitivity studies and data assimilation for different scenarios. The comparison with FIFE data was performed in order to give us confidence that the model satisfactorily captures the behavior of the system for a realistic set of parameters.

The model was extensively tested using observations from the three so-called "golden days" as well as a relatively cloud-free five day drydown event during summer in 1987. The primary sources of data for the testing are the spatially-averaged surface measurements compiled by Betts and Ball (1998) and the ABL observations of W. Brutsaert (see Strebel et al. (1994)). The spatially averaged surface measurements consist of surfaces fluxes (incoming solar, reflected solar, net radiation, sensible and latent heat, and incoming and outgoing longwave radiation) as well as surface (skin) temperature. The ABL measurements consist of radiosonde profiles of potential temperature and specific humidity over the field site. While the surface measurements give an almost continuous (30 minute interval) and relatively accurate characterization of the land surface over the diurnal cycle, the radiosonde data is more intermittent, consisting of 0–8 launches between sunrise and sunset

on any particular day. Also, due to the nature of radiosonde sampling, it is not always clear that the measurements are representative of a spatial average over the site, thus making comparison between model and observations more complicated. For the required model parameters we took values from Colello et al. (1998) who modeled the FIFE site using SiB2 and from Koster and Suarez (1996) who provided the required canopy resistance parameters. There was no tuning of the model parameters; the only parameters not taken from the above sources were the initial conditions of the state variables, which in most cases could be inferred from the FIFE observations.

The results for the three golden days were qualitatively the same, therefore for brevity we provide examples of the comparison results for a single golden day (15 August 1987) as well as the five day drydown at the end of July. In all cases the measured solar radiation and wind speed were used as forcing along with lapse rates estimated from the radiosondes. The comparison results for the 15 August 1987 golden day are shown in Figure 2-2. Figure 2-2a shows the comparison between the observed and modeled incoming and outgoing radiative fluxes. The absorbed solar radiation at the surface is very close to the measured value throughout the day indicating that the effective surface albedo is captured well by the model. The upward longwave flux ($LW^{\uparrow} = R_{cu} + R_{gu}$) is modeled quite well, while there is a positive bias in the downward longwave ($LW^{\downarrow} = R_{ad}(1 - \epsilon_a) + R_{Ad}$) which contributes to an overestimation of the net radiation at the surface (Figure 2-2b). The latent heat flux (Figure 2-2b) is predicted very well throughout the day while there is an overestimation of the sensible heat flux throughout the day due to the overestimation of net radiation. Figure 2-2c shows the comparison of surface temperatures. The FIFE surface temperature data is the radiometric skin temperature while T_s from the model is an effective surface temperature which is a combination of T_c and T_g weighted by the canopy fractional cover ($T_s = T_c V_c + T_g(1 - V_c)$). While these two quantities are not strictly the same (since T_g is a depth-averaged ground temperature), under these conditions there is a general agreement between the two variables. Figure 2-2d shows the mixed-layer potential temperature from the model and that inferred from the radiosondes. The error bars on the FIFE measurements represent the error in defining the (depth-averaged) mixed-layer values from radiosondes. Another source of error, which cannot be as easily quantified is whether the radiosonde point measurements are a representative spatial average for the FIFE site. For the 15 August 1987 radiosonde data, the modeled potential temperature is underestimated throughout the day by 1–2°K. Similar underestimation was seen for the other golden days indicating that the model most likely has a bias. Further analysis suggested that the overestimation of downward longwave radiation (Figure 2-2a) causes too much cooling of the ABL, thus explaining most of this bias. Finally, the evolution of specific humidity (Figure 2-2e) and ABL height (Figure 2-2f) are reasonably close to the measurements.

For the drydown period (19-24 July 1987) no radiosondes were launched over the FIFE site, so only a comparison of surface states and fluxes was performed. The incoming and outgoing radiative fluxes (Figure 2-3a) show similar levels of agreement between model and observations as for the golden days. The absorbed solar and upward longwave radiation are again modeled quite well with an overestimation in the downward longwave. This bias causes a slight overestimation of the net radiation at the surface (Figure 2-3b). The modeled latent heat flux captures the drydown quite well which causes the excess net radiation to lead to an overestimation of the sensible heat flux (Figure 2-3b). The comparison of FIFE skin temperature to surface temperature is shown in Figure 2-3c. Unlike in the golden day case, the difference between skin temperature and the weighted surface temperature of the model is more clearly seen. As one would expect, the measured skin temperature slightly

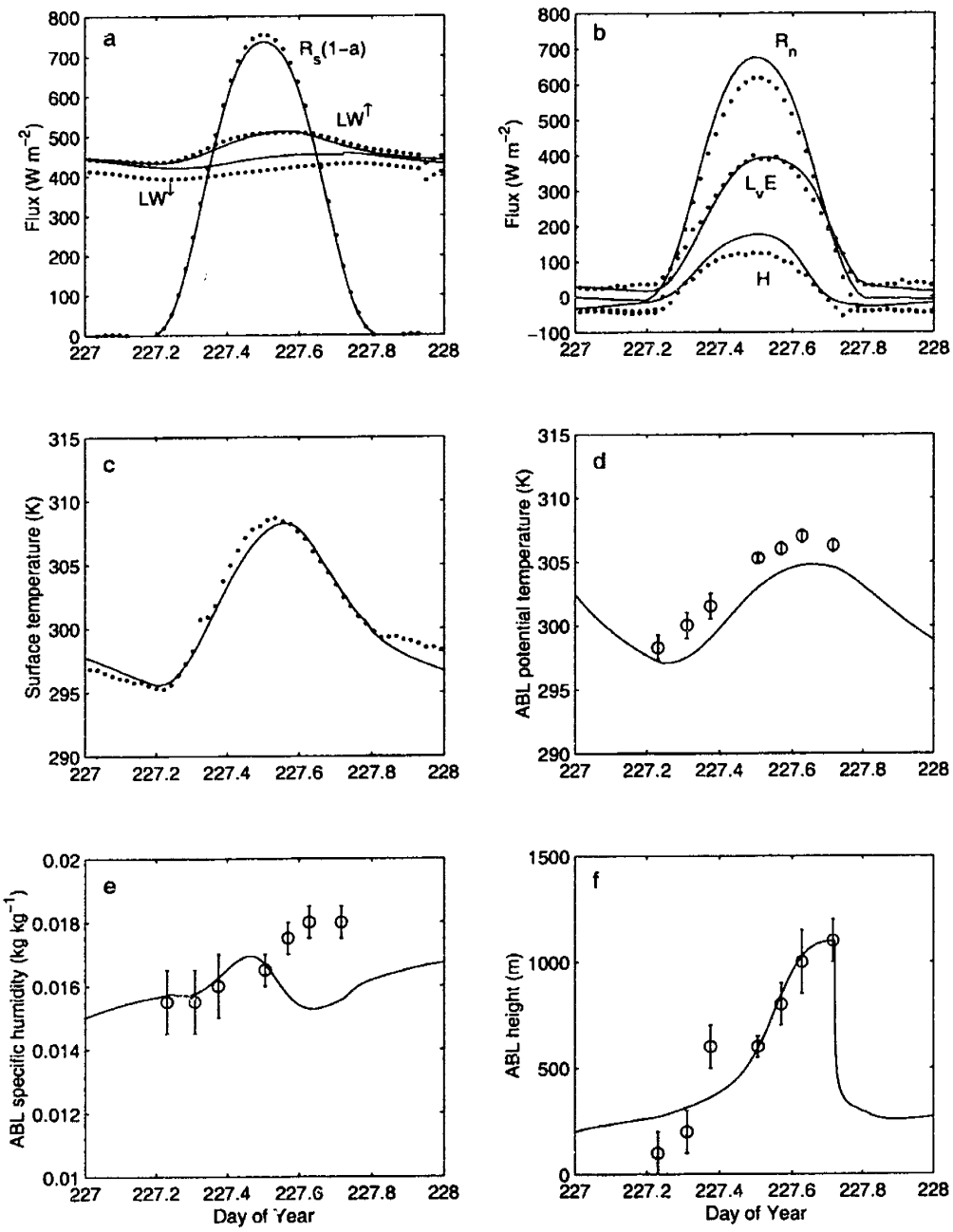

Figure 2-2: Results from a golden day simulation during FIFE for 15 August 1987. The solid lines indicate model results, the '•' symbols mark the average surface measurements, and the 'o' symbols mark the ABL radiosonde observations.

leads (in phase) and is greater in amplitude that the modeled surface temperature (which includes the depth-averaged T_g).

Overall, the correspondence between the model and observations for the golden days and the drydown event is satisfactory, especially since the effects of lateral advection are neglected and no calibration of the model was performed.

2.3 Adjoint Model Formulation

While sensitivity studies and data assimilation may at first seem like rather disparate pursuits, using a variational approach we can develop the adjoint model for use in both under the same general framework (Errico 1997). In order to do so we use a very general formulation for which adjoint sensitivity and variational data assimilation are special cases. Consider that the physical model is represented in vector form by the following system of coupled nonlinear differential equations:

$$\frac{\partial \mathbf{y}}{\partial t} = \mathbf{F}(\mathbf{y}, \boldsymbol{\alpha}) \tag{2.19}$$

where $\mathbf{y}(t)$ is an $N_s \times 1$ state vector (where N_s is the number of state variables augmented to include all spatial locations for a distributed physical system), and $\mathbf{F}$ is an $N_s \times 1$ nonlinear vector operator which is a function of the states themselves and the $N_p \times 1$ vector of time-invariant spatially distributed model parameters $\boldsymbol{\alpha}$ (where N_p is the number of parameters). For example, our model is easily expressed in this dynamical form in Equations (2.1)-(2.11). We next define a scalar "model response functional" generally as:

$$J = \int_t \phi(\mathbf{y}, \boldsymbol{\alpha}) dt \tag{2.20}$$

where ϕ is a nonlinear function of the state variables and model parameters. For example, in a sensitivity study it may represent an important quantity of interest (e.g. diurnally-averaged evaporation) or for data assimilation this would represent the objective function which is generally a least-squares performance index that measures the difference between model predictions and measurements. In either case we are generally interested in obtaining sensitivity derivatives. For sensitivity studies, these derivatives give the sensitivity of the model response to various model parameters. This gives insight into the relative sensitivities of different parameters as well as which physical processes are most important in the system. In data assimilation we generally need the derivatives of the least-squares objective function with respect to the parameters we are interested in estimating as input to an optimization scheme. With this general pursuit in mind, we first adjoin the model to the model response functional using a vector of Lagrange multipliers:

$$J = \int_t \phi(\mathbf{y}, \boldsymbol{\alpha})\, dt + \int_t \boldsymbol{\lambda}^T(t) \left[\frac{\partial \mathbf{y}}{\partial t} - \mathbf{F}(\mathbf{y}, \boldsymbol{\alpha}) \right] dt \tag{2.21}$$

where T represents the vector transpose operator. This is simply a formal mathematical step which does not change the model response in any way since in general we wish for the model to be satisfied, thus making the second term equal to zero. Next, we rewrite the

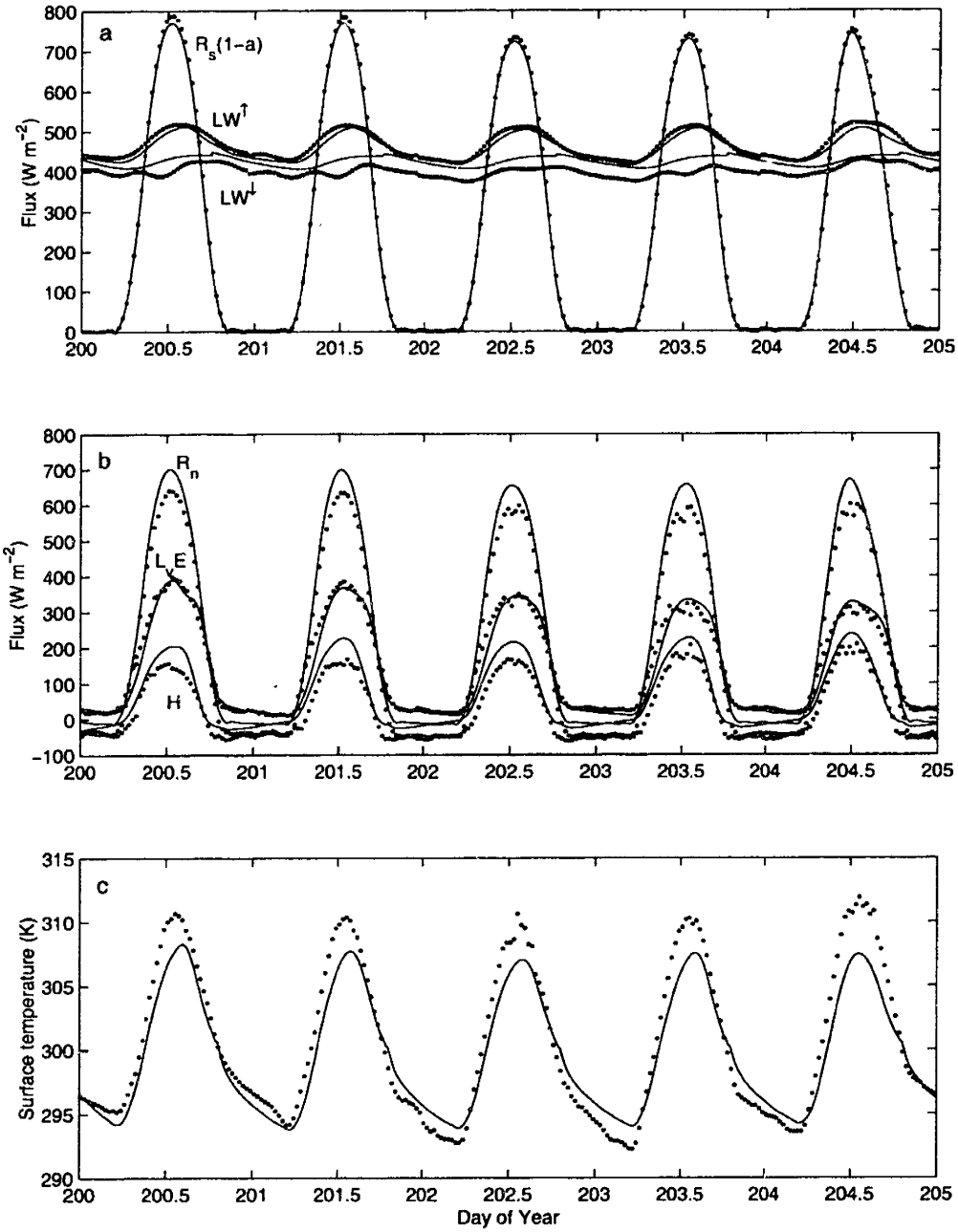

Figure 2-3: Results from a five day drydown simulation during FIFE for 19-24 July 1987. The solid lines indicate model results and the '•' symbols mark the average surface measurements.

above expression by integrating the term $\boldsymbol{\lambda}\frac{\partial \mathbf{y}}{\partial t}$ by parts:

$$J = \int_t \phi(\mathbf{y}, \boldsymbol{\alpha})\, dt + \boldsymbol{\lambda}^T \mathbf{y}\Big|_{t_0}^{t_f} - \int_t \frac{\partial \boldsymbol{\lambda}^T}{\partial t}\mathbf{y}\, dt - \int_t \boldsymbol{\lambda}^T \mathbf{F}(\mathbf{y}, \boldsymbol{\alpha})\, dt \tag{2.22}$$

Now we can express the first variation in J as:

$$\delta J = \frac{\partial J}{\partial \mathbf{y}}\delta\mathbf{y} + \frac{\partial J}{\partial \boldsymbol{\alpha}}\delta\boldsymbol{\alpha} + \frac{\partial J}{\partial \mathbf{y}_0}\delta\mathbf{y}_0 + \frac{\partial J}{\partial \mathbf{y}_f}\delta\mathbf{y}_f \tag{2.23}$$

where $\delta\mathbf{y}_0$ and $\delta\mathbf{y}_f$ are the variations in the state variables at the initial and final times respectively. The above expression can then be written out term-by-term as:

$$\delta J = \left(\int_t \left[\frac{\partial \phi}{\partial \mathbf{y}}^T - \frac{\partial \boldsymbol{\lambda}}{\partial t} - \frac{\partial \mathbf{F}}{\partial \mathbf{y}}^T \boldsymbol{\lambda}\right]^T dt\right)\delta\mathbf{y} + \left(\int_t \left[\frac{\partial \phi}{\partial \boldsymbol{\alpha}}^T - \frac{\partial \mathbf{F}}{\partial \boldsymbol{\alpha}}^T \boldsymbol{\lambda}\right]^T dt\right)\delta\boldsymbol{\alpha} +$$

$$\left(\boldsymbol{\lambda}_f^T\right)\delta\mathbf{y}_f - \left(\boldsymbol{\lambda}_0^T\right)\delta\mathbf{y}_0 \tag{2.24}$$

where $\boldsymbol{\lambda}_0$ and $\boldsymbol{\lambda}_f$ are the Lagrange multiplier vectors at the initial and final times respectively. Since the Lagrange multipliers are arbitrary we choose $\boldsymbol{\lambda}$ such that $\partial J/\partial \mathbf{y} = 0$ is satisfied in the above equation (i.e. the first term on the right-hand-side is set to zero). This is done primarily because $\delta\mathbf{y}$ is a complicated function of time as well as the model parameters and would be very tedious to compute. Similarly, $\delta\mathbf{y}_f$ is difficult to compute so we choose $\boldsymbol{\lambda}_f = 0$. By choosing $\boldsymbol{\lambda}$ as stated, the first term in Equation (2.24) yields:

$$\frac{\partial \boldsymbol{\lambda}}{\partial t} = -\left(\frac{\partial \mathbf{F}}{\partial \mathbf{y}}\right)^T \boldsymbol{\lambda} + \frac{\partial \phi}{\partial \mathbf{y}}^T \tag{2.25}$$

again, with the terminal condition $\boldsymbol{\lambda}(t_f) = 0$. The Lagrange multipliers ($\boldsymbol{\lambda}$) are called the adjoint state variables, and hence Equation (2.25) is called the adjoint model which has to be integrated backward in time as a terminal value problem. The adjoint variables themselves have some physical meaning which will be discussed below. Note that the homogeneous part of this linear differential equation (first two terms) is only dependent on the Jacobian of the forward model ($\partial\mathbf{F}/\partial\mathbf{y}$), while the forcing (third term) is dependent on the gradient of the model response ($\partial\phi/\partial\mathbf{y}$). Therefore the homogeneous adjoint model can be constructed separately and then used in conjunction with the different model response functionals. Based on the choices for $\boldsymbol{\lambda}$ above, Equation (2.23) simplifies to:

$$\delta J = \frac{\partial J}{\partial \boldsymbol{\alpha}}\delta\boldsymbol{\alpha} + \frac{\partial J}{\partial \mathbf{y}_0}\delta\mathbf{y}_0 \tag{2.26}$$

where

$$\frac{\partial J}{\partial \boldsymbol{\alpha}} = \int_t \left[\left(\frac{\partial \phi}{\partial \boldsymbol{\alpha}}^T - \frac{\partial \mathbf{F}}{\partial \boldsymbol{\alpha}}^T \boldsymbol{\lambda}\right)\right]^T dt \tag{2.27}$$

and

$$\frac{\partial J}{\partial \mathbf{y}_0} = -\boldsymbol{\lambda}_0^T \tag{2.28}$$

Equations (2.27) and (2.28) are the derivatives we are ultimately interested in for either sensitivity or data assimilation studies and can be computed once $\boldsymbol{\lambda}$ is known (by integrating the adjoint model). Herein lies one of the primary benefits of the adjoint method in that once the adjoint model is developed, all of the derivatives can be obtained very efficiently through a single forward model run and a single adjoint model run. This is possible due to the fact that the adjoint model is developed analytically from the forward model and propagates the sensitivity information backward in time over the model integration. For comparison, obtaining these derivatives via a finite-difference approach would take $(N_p + N_s + 1)$ model simulations. Examples of coupled surface-ABL sensitivity studies using the simulation approach are: Ek and Cuenca (1994), Sun and Bosilovich (1996), Cuenca et al. (1996), and Alapaty et al. (1997).

2.4 Adjoint Model Development and Verification

Based on the general formulation shown above we were able to develop the adjoint of our coupled land-atmosphere model. It should be noted that the strict application of the "classical" adjoint methodology discussed above requires the system to be differentiable with respect to the states and parameters. The issue of differentiability can be a limitation to the general application of the classical adjoint technique. Often, before developing an adjoint model, the existing forward model is heavily modified to make it differentiable. This cost can be especially high when the forward and adjoint models are developed independently of each other. However by developing our forward model with its adjoint in mind we were able to limit the non-differentiable functions to those in the canopy resistance stress functions. These functions can easily be replaced by "smooth" versions (see Appendix B). In our study the focus is on the growth of the ABL in response to heating and buoyancy generation at the surface. While the classical adjoint technique requires that the model be differentiable, there are some studies on ways to derive adjoints even in the presence of thresholds and switches (e.g. Bao and Warner (1993), Xu (1996a), Xu (1996b), Zou (1997)). As a result, the nocturnal ABL collapse can in general be accommodated via the piece-wise integration of the adjoint variable in time and the matching of boundary conditions at the switch points (Appendix B).

In the mode we wish to perform the analysis (using different model responses) it is convenient to view the adjoint model, (2.25), in two components, the homogeneous model:

$$\frac{\partial \boldsymbol{\lambda}}{\partial t} = -\left(\frac{\partial \mathbf{F}(\mathbf{y}, \boldsymbol{\alpha})}{\partial \mathbf{y}}\right)^T \boldsymbol{\lambda} \tag{2.29}$$

which only depends on the forward model operator ($\mathbf{F}$), and the adjoint model forcing term:

$$\frac{\partial \phi(\mathbf{y}, \boldsymbol{\alpha})^T}{\partial \mathbf{y}} \tag{2.30}$$

which depends on the particular model response functional. By separating the adjoint model in this way, we can develop and validate the homogeneous model using a simple forcing function. Once it is validated, we can specify different forcing functions depending on what type of analysis we wish to perform. This is helpful because in our applications deriving the homogeneous adjoint model is much more difficult (i.e. prone to errors) than deriving the forcing function. It also illustrates how we wish to use the adjoint model, i.e.

as a general tool for different sensitivity experiments and data assimilation problems where the homogeneous adjoint model is developed and validated once and then different model responses are substituted for different applications.

The development of the adjoint model is straightforward and simply involves differentiating analytically the forward model nonlinear vector operator ($\mathbf{F}$) with respect to the model states to get the $N_s \times N_s$ Jacobian matrix $\partial\mathbf{F}/\partial\mathbf{y}$. While straightforward, this process involves multiple applications of the chain rule which is both tedious and error prone. It is therefore very important to validate the adjoint model before applying it to a given problem. The best way to test the validity of the adjoint model is by comparing the sensitivity derivatives obtained by the adjoint model to those obtained from the nonlinear forward model using a finite-difference approach. For any model response functional we can expand it around $\boldsymbol{\alpha}$ using a Taylor series (where $\boldsymbol{\alpha}$ can represent a vector including the model initial conditions as well as parameters):

$$\Delta J = J(\boldsymbol{\alpha} + \Delta\boldsymbol{\alpha}) - J(\boldsymbol{\alpha}) = \frac{\partial J}{\partial \boldsymbol{\alpha}}\Delta\boldsymbol{\alpha} + \frac{1}{2}\frac{\partial^2 J}{\partial \boldsymbol{\alpha}^2}(\Delta\boldsymbol{\alpha})^2 + \cdots \tag{2.31}$$

As $\Delta\boldsymbol{\alpha}$ approaches zero, the finite-difference sensitivity derivatives ($\frac{\Delta J}{\Delta \boldsymbol{\alpha}}$) should match the sensitivity derivatives from the adjoint model ($\frac{\partial J}{\partial \boldsymbol{\alpha}}$). The easiest way to validate the homogeneous adjoint model is by using a very simple model response functional and then comparing these derivatives. To do so, we used the diurnally averaged ground temperature:

$$J = \frac{1}{\tau}\int_t T_g dt \tag{2.32}$$

or using the notation above $\phi(\mathbf{y}, \boldsymbol{\alpha}) = T_g/\tau$. We chose this simple, but physically meaningful, model response because in addition to validating the adjoint model we will use it to illustrate adjoint sensitivity analysis in the next section. Because of the simplicity of the corresponding adjoint model forcing function, once we have validated the adjoint sensitivities we can infer that the homogeneous adjoint model has been developed correctly. Thus results from future applications of the adjoint model can be accepted as valid as long as the forcing function for each application has been shown to be accurate.

For the validation of the adjoint model itself we simply need focus on the sensitivity derivatives with respect to the the initial conditions ($\frac{\partial J}{\partial \mathbf{y}_0}$). Recall from Equation (2.28) that these derivatives are given by the corresponding adjoint variables at the initial time t_0 (multiplied by -1). These sensitivity derivatives should approach those obtained from a finite-differencing of results from forward model runs as the perturbations in the initial conditions approach zero. For our model the state vector is defined as:

$$\mathbf{y} = (T_c, T_g, \theta, q, \delta_\theta, \delta_q, h, W_1, W_2, W_3, T_d)^T \tag{2.33}$$

where for the validation we defined a nominal perturbation to the initial conditions $\Delta\mathbf{y}_0$ which is defined in Table 2.1. We then performed the comparison between finite-difference sensitivities and those obtained from the adjoint model for four cases of consecutively smaller perturbations by multiplying this nominal perturbation vector by 3, 1, 10^{-1}, and 10^{-3} (see Table 2.1). Note that, as we would expect, there are some significant differences for large perturbations (a clear sign of the nonlinearity of the model), but as the perturbations approach zero, the relative error also approaches zero such that for a perturbation of $\Delta\mathbf{y}_0 \times 10^{-3}$ the relative error for each variable is much less than 1%. These results give us a high

degree of confidence that the adjoint model is formulated properly. In the next two sections we give illustrative examples of how the adjoint model can be used as a tool for sensitivity experiments and data assimilation.

Table 2.1: Relative error (%) between finite-difference and adjoint sensitivity derivatives of average daily ground temperature with respect to initial conditions for different size perturbations (Multiplicative factor is applied to the nominal perturbation $\Delta\mathbf{y}_0 = (1, 1, 1, 1 \times 10^{-3}, 0.5, 0.5 \times 10^{-3}, 50, 0.02, 0.02, 0.02, 1)^T$). Appendix C lists the units for the vector $\mathbf{y}_0$ components.

Multiplicative factor =		3	1	10^{-1}	10^{-3}
	$\mathbf{y}_0$				
	T_c	1.37704	0.53586	0.11378	0.06552
	T_g	1.08671	0.49553	0.22976	0.20052
	θ	0.38336	0.00749	0.04561	0.04633
	q	1.93478	0.73187	0.14745	0.08113
	δ_θ	5.20865	1.80001	0.24374	0.07134
	δ_q	0.46335	0.25561	0.13480	0.12034
	h	5.62582	1.74892	0.20082	0.04115
	W_1	6.90354	2.52037	0.25025	0.01083
	W_2	69.19165	19.49968	1.73404	0.00936
	W_3	1.23360	0.37766	0.08819	0.05932
	T_d	0.17092	0.09665	0.06132	0.05735

2.5 A Simple Sensitivity Experiment Using the Adjoint Model

As mentioned above, the adjoint technique provides a means of more efficiently evaluating model sensitivities in comparison to a traditional finite-difference forward sensitivity approach. While this is certainly an advantage of the technique, perhaps more important for sensitivity experiments is the added insight into how these sensitivities arise which make the

adjoint model such a useful tool. We can obtain diagnostic insight into relative sensitivities and estimate influence functions for different parameters. We can also determine the sensitivity pathways through the decomposition of the adjoint sensitivities. Before presenting a simple example, the types of results which can be obtained through the application of the adjoint method are described below.

2.5.1 Physical Interpretation of Adjoint Functions

Physical insight into the behavior of the system comes once we have integrated the adjoint model backward in time yielding $\boldsymbol{\lambda}(t)$, which have physical meaning in their own right. Up to this point they simply entered the problem formally when we added the forward model as a constraint to the model response J. In fact they entered the problem such that their values were arbitrary, which ultimately led to the definition of the adjoint model. Hall and Cacuci (1983) formally derived the physical meaning of the adjoint variables. Recall that each adjoint variable is uniquely related to a particular state variable and that we showed above in Equation (2.28) that the adjoint variable at $t = 0$ is directly related to the sensitivity of the model response to the initial condition of the corresponding state variable. The derivation by Hall and Cacuci (1983) is not repeated here, but the primary result is that, analogously, the adjoint variable at *any* time ($t = t_s$) is directly related to the sensitivity of J to a perturbation in its corresponding state variable at that particular time:

$$\boldsymbol{\lambda}_s^T = \boldsymbol{\lambda}^T(t = t_s) = -\frac{\partial J}{\partial \mathbf{y}}(t = t_s) \tag{2.34}$$

Since there is an adjoint function corresponding to each state variable we can cross compare between states to see which states are most important at different times during the model integration. Thus the adjoint variables contain information about state sensitivity pathways.

2.5.2 Decomposition of Adjoint Sensitivities

Once we have the adjoint variables, we can compute other sensitivity information. In doing so we first decompose Equation (2.26) as follows :

$$\delta J = \int_t \left[\left(\frac{\partial \phi}{\partial \alpha_1} - \frac{\partial \mathbf{F}}{\partial \alpha_1}^T \boldsymbol{\lambda} \right) \delta\alpha_1 + \cdots + \left(\frac{\partial \phi}{\partial \alpha_{N_p}} - \frac{\partial \mathbf{F}}{\partial \alpha_{N_p}}^T \boldsymbol{\lambda} \right) \delta\alpha_{N_p} \right] dt +$$

$$(-\lambda_{0_1})\delta y_{0_1} + \cdots + (-\lambda_{0_{N_s}})\delta y_{0_{N_s}} \tag{2.35}$$

$$= \delta J_1 + \cdots + \delta J_{N_p} + \delta J_{N_p+1} + \cdots + \delta J_{N_p+N_s} \tag{2.36}$$

where each term δJ_k represents the individual contribution of a perturbation of a particular parameter to the total model response δJ (where the initial conditions can be thought of as model parameters). Note that once the adjoint variables are determined, each of the above terms can be computed since $\partial\phi/\partial\alpha_k$ and $\partial\mathbf{F}/\partial\alpha_k$ are only functions of the nominal forward model solution and model parameters. Embedded in this equation is information about the relative sensitivity of model response to each parameter, as well as the temporal distribution of variation in model response to a given parameter.

2.5.3 Relative parameter sensitivities

The relative sensitivities are a measure of the percent change in model response due to a percent change in a given parameter. The relative sensitivity, r_k, to parameter α_k is expressed as:

$$r_k = \frac{\delta J_k}{J}\frac{\alpha_k}{\delta \alpha_k} = \frac{\partial J}{\partial \alpha_k}\ \frac{\alpha_k}{J} \tag{2.37}$$

where $\partial J/\partial \alpha_k$ is computed once the adjoint variables are determined. This gives a non-dimensional measure of the relative importance of each parameter in determining the model response we are interested in. This part of the analysis gives initial insight into which parameters are most important in affecting model response, thus giving hints into the important response pathways in the model, as well as information about those parameters that may be inconsequential in affecting model response.

2.5.4 Temporal Influence Functions and Sensitivity Pathways

Next we focus on the temporal influence of perturbations in a given parameter on model response. For this we concentrate on the individual contribution of each parameter to the overall variation in model response, which can be expressed as:

$$\delta J_k = \int_t \left(\frac{\partial \phi}{\partial \alpha_k} - \frac{\partial \mathbf{F}}{\partial \alpha_k}^T \boldsymbol{\lambda} \right) dt\, \delta \alpha_k \tag{2.38}$$

Note that depending on whether or not the given model response ϕ is an explicit function of parameter α_k, the first term may be equal to zero. For example, if our model response is average ground temperature, then ϕ is not explicitly related to any model parameters. In either case, for a given term (δJ_k), we can obtain the temporal influence function of that particular parameter on model response from the integrand of the above equation:

$$\delta J_k(t) = \left(\frac{\partial \phi(t)}{\partial \alpha_k} - \frac{\partial \mathbf{F}(t)}{\partial \alpha_k}^T \boldsymbol{\lambda}(t) \right) \delta \alpha_k \tag{2.39}$$

which is a time dependent function of the variation (per unit time) in model response due to a perturbation of parameter α_k.

Finally, for those parameters which are not explicitly related to a given model response, we can also obtain information about how the perturbation in a parameter propagates through each state variable. Again, note that each model state is related uniquely to a specific adjoint variable. By separating out the $\boldsymbol{\lambda}$ vector in the above equation while integrating over time we have:

$$\delta J_k = \int_t \left(-\frac{\partial F_1}{\partial \alpha_k}^T \lambda_1 \right) dt\, \delta \alpha_k + \cdots + \int_t \left(-\frac{\partial F_{N_s}}{\partial \alpha_k}^T \lambda_{N_s} \right) dt\, \delta \alpha_k = \delta J_k(1) + \cdots + \delta J_k(N_s) \tag{2.40}$$

where, for example, $\delta J_k(1)$ is the contribution to δJ_k through the first state variable (T_c). The easiest way to visualize this is to see that $\frac{\partial F_1}{\partial \alpha_k}$ represents the effect of α_k on the evolution of T_c, and that λ_1 represents the effect of changes in T_c on J. Therefore $\delta J_k(1)$ represents the integrated effect α_k has on J through the evolution of T_c. This gives a measure of the

strength of different sensitivity pathways in the system for a particular model response and parameter. Further, just as in Equation (2.39) the temporal influence through each state variable can be examined by looking at the integrand of each term in Equation (2.40).

2.5.5 Sensitivity Experiment

In this section we present a simple adjoint sensitivity experiment, the results of which are intended to be mostly illustrative. For the model response we again choose average ground temperature:

$$J = \overline{T}_g = \frac{1}{\tau} \int_{t_0}^{t_f} T_g dt \tag{2.41}$$

for the 15 August 1987 FIFE simulation, where for simplicity we only integrate the model during the daytime growth phase of the ABL (for this model integration $\overline{T}_g = 304.8$ K). Also, while the model is a function of many parameters, for brevity we chose a small subset to be used in the adjoint analysis, namely $\boldsymbol{\alpha} = (\gamma_\theta \; \gamma_q \; z_0 \; V_c \; B_s \; \psi_s \; L_T)^T$. The procedure involves first integrating the forward model, then integrating the adjoint model backward in time, and finally evaluating and decomposing the sensitivities as described above. The first results from the adjoint model are the adjoint variables themselves, which give insight into how perturbations in each state variable affect the average daily ground temperature. Just as the state variables are of disparate scales (e.g. $h \sim \mathcal{O}(10^3)$ and $q \sim \mathcal{O}(10^{-3})$) so too are the corresponding adjoint variables which have dimensions of $[J]/[y_i]$. To cross-compare between states and gain insight into their relative influence, we define the non-dimensional adjoint variables as:

$$\Lambda_i(t) = -\lambda_i(t) \frac{y_i(t)}{J} \tag{2.42}$$

which gives the percent change in J due to a percent change in y_i at a given time. For the 15 August simulation, the non-dimensional adjoint variables are shown in Figure 2-4. They are plotted in Figure 2-4a-d from most influential variables (top panel) to least influential (bottom panel). Note that all of the adjoint variables are equal to zero at t_f. Mathematically, this is a direct result of the terminal condition placed on the adjoint model which was discussed above. Physically, this represents the causal nature of the system, in that perturbations in the state variables beyond the integration window (i.e. $t > t_f$) can have no influence on the model response, which is defined as the average ground temperature within the integration window ($t_0 < t < t_f$). As t proceeds backward in time toward the initial condition, each variable will influence the model response in different ways depending on the model dynamics. The adjoint model integrates this information backward in time, marking the influence of each state on the average ground temperature over the integration window.

The three most important states in determining average daily surface ground temperature are the surface ground temperature itself, the deep ground temperature, and the ABL potential temperature (see Figure 2-4a). All three non-dimensional adjoint variables are positive throughout the model integration. Therefore a positive perturbation in T_g, T_d, or θ at any time during the day will cause a positive perturbation in $\overline{T}_g$. Note however that T_g is most influential only over time scales of ~ 1.5 hours, with T_d and θ more influential over the time scale of the entire day. This can be seen by starting at t_f and working backward

in time for longer and longer model simulations. If the model had been integrated only over the last 1–2 hours of the day, the initial condition of T_g would be most influential in determining $\overline{T}_g$ (via a direct effect) followed in importance by θ and T_d. However as the length of model integration increases, it is the indirect effects, which propagate perturbations through the model dynamics, that become more important, such that the initial conditions of θ and T_d are much more influential than that of T_g in determining $\overline{T}_g$. This result can be explained physically by considering the size of each temperature reservoir. The surface ground temperature only represents the average temperature over the top 5 cm of soil. So any perturbation in T_g will be relatively quickly dissipated through the increase in radiative, sensible, and latent heat fluxes which cool the surface. Conversely, the other two temperature states represent much larger reservoirs of heat which can ultimately affect the average daily ground temperature (through radiative and conductive effects) over longer time scales. At the other extreme for example, the contribution of T_c (Figure 2-4d) is minimal compared to even T_g due to the even smaller heat capacity of the vegetation canopy.

The next most important state variables are the specific humidity of the ABL and the surface soil moisture (Figure 2-4b). The adjoint variable corresponding to q is positive indicating that a positive perturbation will serve to increase $\overline{T}_g$. This is a direct consequence of both the increased greenhouse insulation (due to more water vapor in the ABL) as well as the decreased surface evaporation (due to a decreased moisture gradient). The sensitivity of $\overline{T}_g$ to W_1 is negative throughout the integration. This is indicative of the cooling effect of soil moisture. For a positive perturbation in surface soil moisture, more of the net radiation will be partitioned into evaporation instead of sensible heat flux, thus making the surface cooler than it would otherwise be.

While the remaining model states (Figure 2-4c,d) are not as important in determining $\overline{T}_g$ as those discussed above, we can still learn some interesting things from examining the adjoint functions. For example, in Figure 2-4c we see that those variables closely associated with ABL growth (h, δ_θ, and δ_q) behave similarly in that their contribution is negligible during the afternoon when the ABL is not growing very rapidly. Only perturbations in the morning, before and during ABL growth, have a discernible effect on the average ground temperature. We see in Figure 2-4d that the sensitivity of $\overline{T}_g$ to canopy temperature actually switches sign for a couple hours at midday. Thus, while a positive perturbation in T_c will positively impact average ground temperature for most of the day, around solar noon the impact is negative. The only explanation for this is that at midday the increase in transpiration from the surface due to a perturbation in T_c outweighs the effects which would otherwise warm the ground surface. Finally, as with W_1, perturbations in W_2 and W_3 contribute negatively to $\overline{T}_g$ throughout the day. For a multi-day drydown event we would expect the relative importance of the soil moisture variables to be more important as they contain a larger degree of memory than temperature states.

In addition to the insight from the adjoint variables themselves, we can determine the relative contribution of model parameters in determining $\overline{T}_g$. In Table 2.2 we show the absolute and relative sensitivities of $\overline{T}_g$ to all model initial conditions and each parameter in the vector $\boldsymbol{\alpha}$ shown above. The sensitivities related to initial conditions come directly from the adjoint variables at t_0, which were discussed above. The absolute and relative sensitivity of $\overline{T}_g$ to each model parameter is obtained using Equations (2.27) and (2.37) respectively. Table 2.2 shows that the highest relative sensitivity is for the fractional vegetation cover, V_c (which is of similar magnitude to that of the initial condition of W_1), followed by leaf area index (L_T or LAI), roughness length (z_0), lapse rates in potential temperature and

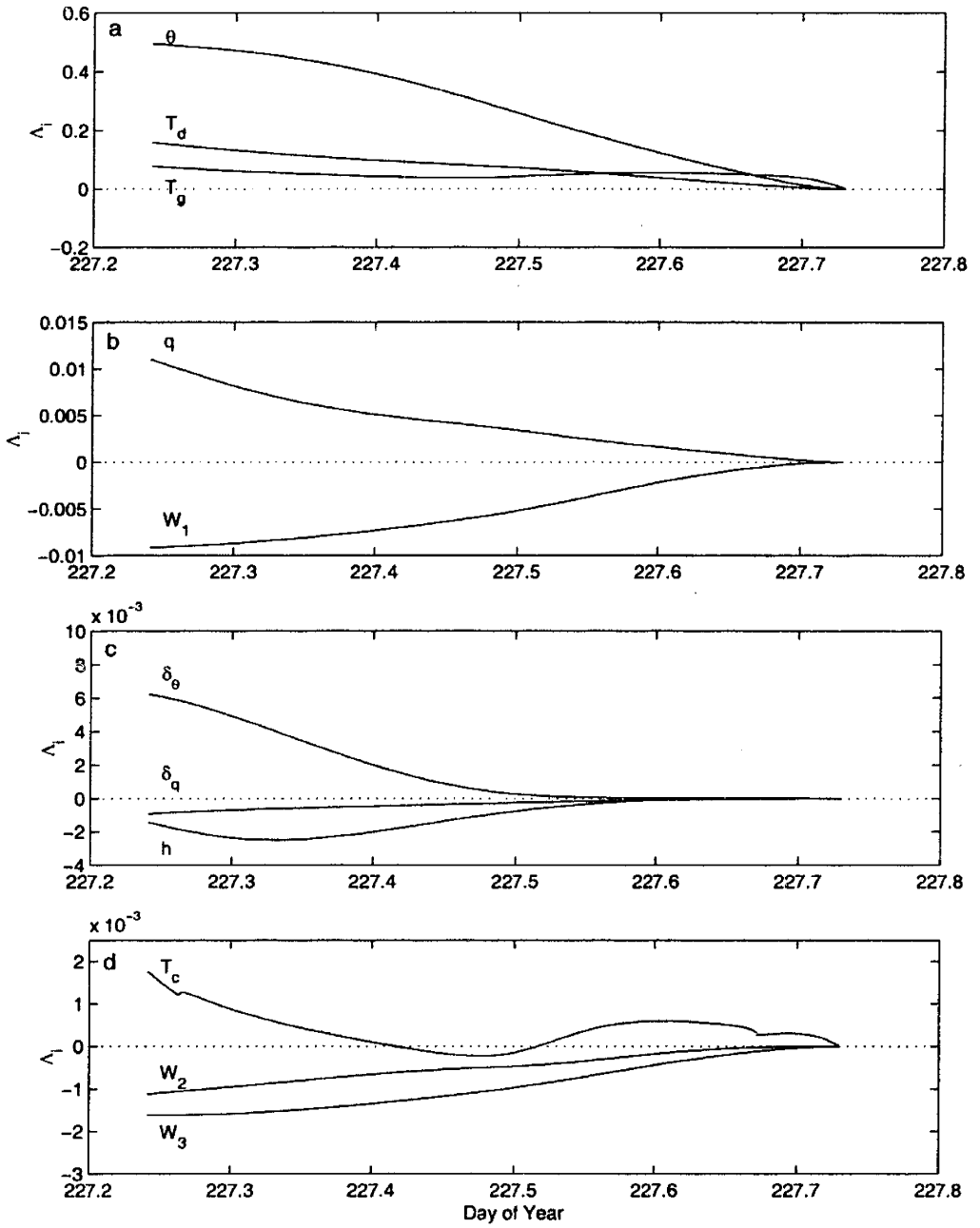

Figure 2-4: Nondimensional adjoint functions obtained from adjoint model for 15 August FIFE simulation (Each adjoint function is marked by its corresponding state variable).

humidity (γ_θ and γ_q), and soil water retention parameters (B_s and ψ_s). In general, the sensitivities to many of the initial conditions are greater in magnitude than those for model parameters. However it must be noted again that this example simulation is relatively short and therefore initial conditions play a dominant role.

Table 2.2: Absolute and relative sensitivities of average daytime ground temperature to model initial conditions and parameters. The units of J are degrees Kelvin and the units of $\mathbf{y}_0$ and $\boldsymbol{\alpha}$ components are listed in Appendix C.

Initial Conditions				Model Parameters			
$\mathbf{y}_0$	$\frac{\partial J}{\partial \mathbf{y}_0}$	r_k	Rank	$\boldsymbol{\alpha}$	$\frac{\partial J}{\partial \boldsymbol{\alpha}}$	r_k	Rank
T_c	1.82e-03	1.77e-03	8	γ_θ	8.39e+01	1.04e-03	4
T_g	7.98e-02	7.74e-02	3	γ_q	1.46e+04	-1.83e-04	5
θ	5.08e-01	4.95e-01	1	z_0	8.04e+00	1.85e-03	3
q	2.13e+02	1.10e-02	4	V_c	-7.01e+00	-1.84e-02	1
δ_θ	3.29e-01	6.23e-03	6	B_s	8.43e-03	1.49e-04	6
δ_q	7.48e+01	-9.22e-04	11	ψ_s	-4.52e-03	7.42e-06	7
h	-1.60e-03	-1.42e-03	9	L_T	-7.80e-01	-8.70e-03	2
W_1	-5.64e+00	-9.13e-03	5				
W_2	-6.94e-01	-1.14e-03	10				
W_3	-1.00e+00	-1.90e-03	7				
T_d	1.63e-01	1.59e-01	2				

It is important to recognize that these relative sensitivities do not tell the whole story. They represent the integrated importance of the parameter over the entire simulation. However it is of interest to know how these sensitivities arise so that insight gained from this sensitivity experiment may be extended to other situations. To do this, we use Equation (2.39) to decompose the sensitivities into their respective temporal contributions. For illustration, we do so for three of the parameters: V_c and L_T, which have the highest relative sensitivities, and ψ_s, which has the lowest. The results are plotted in Figures 5a-c as the

fraction of total sensitivity distributed in time. Thus the fraction shown at any given time multiplied by the sensitivity shown in Table 2.2 yields the sensitivity of $\overline{T}_g$ (per unit time) to that parameter at that moment in time. Also plotted are the fractional contributions to the overall sensitivity through each state equation, obtained using Equation (2.40), which gives a measure of the important sensitivity pathways in the model. It is this additional information, along with the relative sensitivities which gives a more complete picture of the system behavior.

From Figure 2-5a we see that the temporal contribution of V_c to $\overline{T}_g$ is concentrated in the middle ~ 7 hours of the day, with maxima in mid-morning and afternoon. Almost all of the effect of V_c is through direct effects on the ground temperature state equation. The sensitivity roughly follows the diurnal cycle of solar radiation as it is the decrease in R_{ng} due to a positive perturbation in V_c which is most influential. The distribution of sensitivity for L_T is similar with a more concentrated peak near midday. It also mostly affects average daily ground temperature directly through the ground temperature state equation. This is again due to the large influence of leaf area index on the radiative transfer within the canopy, which ultimately directly affects the net radiation absorbed by the ground. While these results are ones we might have expected, many effects in the dynamic model due to perturbations of a given parameter are not as straightforward.

The results for ψ_s, which are given in Figure 2-5c, provide insight that we would not have obtained had we only looked at relative sensitivities. First of all, from the the temporal distribution of sensitivity we see that there is almost no contribution early in the morning, a large contribution ($\sim -250\%$) in the late morning, and a large opposing contribution ($\sim +250\%$) during the early afternoon. For example, this indicates that had our simulation been from sunrise to noon only, the sensitivity would not only have been much larger, but opposite in sign. It is only when integrated over the entire day that the positive and negative contributions cancel out, yielding a small sensitivity. Thus depending on the time of day, parameters which have a smaller overall relative sensitivity may be of comparable importance to those with higher relative sensitivities. The decomposition of the sensitivity into sensitivity pathways also yield interesting results. Whereas for V_c and L_T, the vast majority of sensitivity was through direct effects on T_g, for ψ_s the largest contribution is through T_c, with similarly important (but opposite) contributions through q and W_1. We can further try to explain the overall temporal sensitivity evolution by looking at the temporal evolution of sensitivity through each of these three states (Figure 2-6). Figure 2-6 shows that the contributions from q and W_1 are opposite (in sign) to the integrated sensitivity (shown in Table 2.2) throughout the day. Thus a positive perturbation in ψ_s causes a warming of the ground through the evolution of q (a resulting increase in evaporation into the ABL leads to greenhouse warming) and W_1 (a resulting decrease in soil moisture via increased moisture transport decreases ground evaporation). The temporal contribution through T_c is more complicated. In the morning and in the afternoon the contribution is in the same direction as the integrated sensitivity, while at midday it is opposite in sign. The only effect of ψ_s on the evolution of T_c is through transpiration. Thus in the morning and afternoon, the sensitivity of canopy transpiration to ψ_s is positive. This means that the primary effect of a positive perturbation in ψ_s is to reduce the canopy resistance which leads to an increase in transpiration that cools the surface. At midday, this decrease in resistance is not enough to offset the decrease in vapor pressure gradient $(e_*(T_c) - e_a)$ which drives transpiration and thus the effect is a decrease in transpiration which warms the surface. We see that the combined effects of all three variables leads to the overall temporal pattern shown in Figure 2-5c.

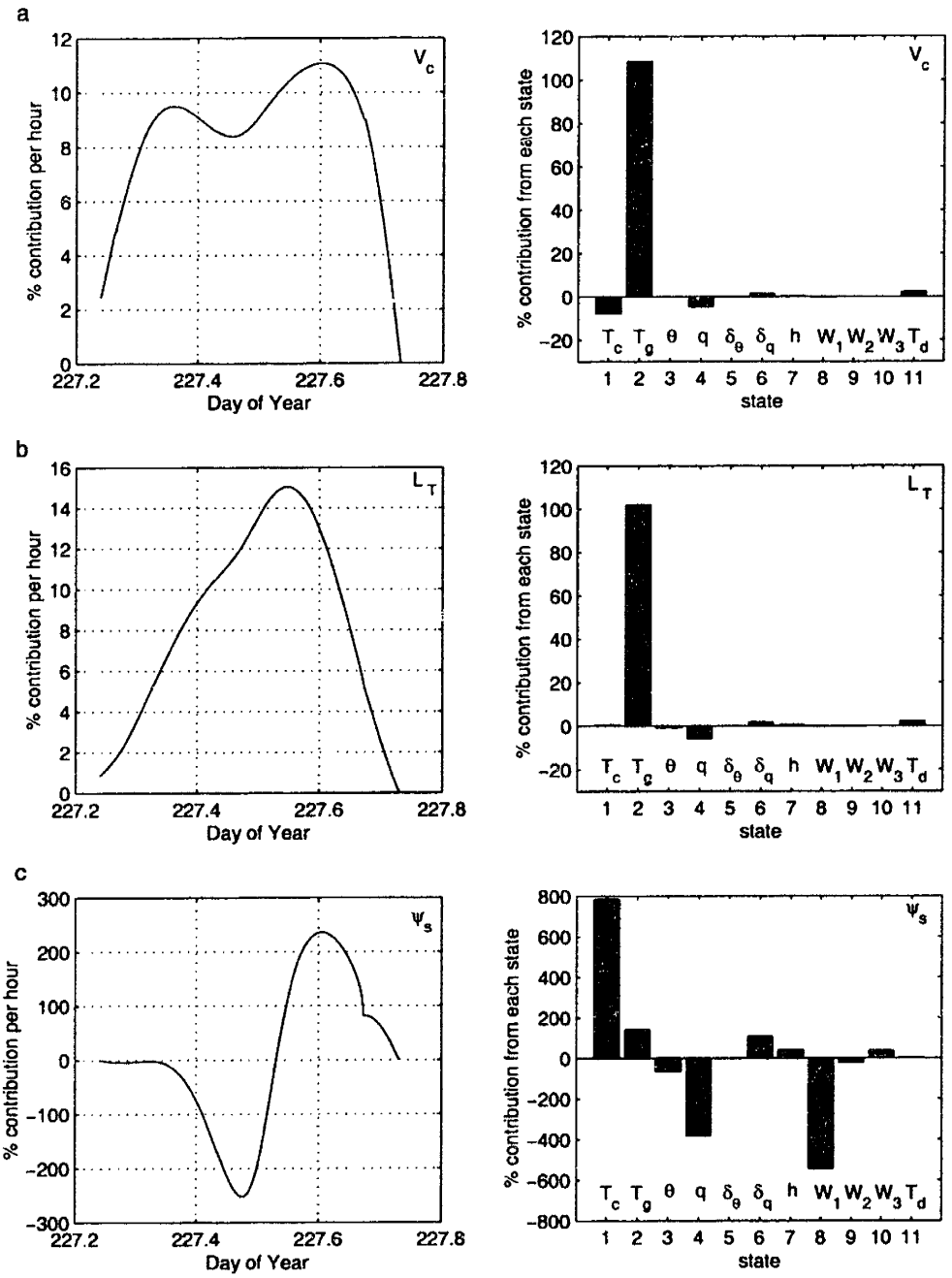

Figure 2-5: Temporal distribution of sensitivity and sensitivity pathways for $\overline{T_g}$ with respect to three model parameters: V_c, L_T, and ψ_s.

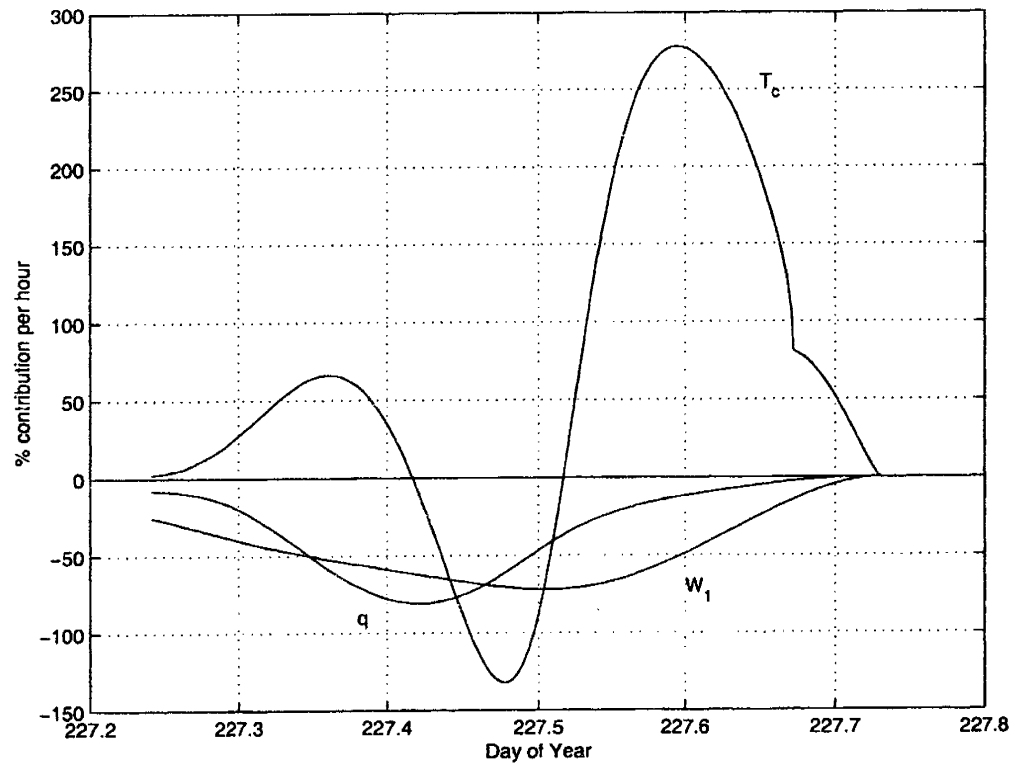

Figure 2-6: Temporal sensitivity contributions of perturbation in ψ_s to $\overline{T_g}$ through T_c, q, and W_1.

The above sensitivity analysis gives a glimpse into the type of insight that can be gained through application of the adjoint method. Even for this simple illustrative example, with the adjoint model we were able to obtain results that would be more difficult or impossible to obtain using a more traditional simulation approach. For more complicated problems (e.g. a multi-day drydown event, different biomes, seasons, etc.), where we are interested in examining other model response functionals $\phi(\mathbf{y}, \boldsymbol{\alpha})$ (e.g. turbulent fluxes between the land surface and atmosphere) with a more complete model parameter set, the advantages of the adjoint method become even more exaggerated. Thus the adjoint method is ideally suited for use as a general and comprehensive sensitivity tool that can diagnose the important processes and parameters involved in land-atmosphere interaction.

2.6 A Simple Data Assimilation Problem Using the Adjoint Model

In addition to sensitivity analysis the adjoint model can be used as an estimation tool. State estimation posed as a variational data assimilation problem fits quite naturally within the general framework shown in Section 4. The basic idea is that given some measurements of the system, which may be nonlinearly related to model states and parameters, we wish to obtain optimal estimates for a set of control parameters which minimize a weighted least-squares objective function. In general the control parameter vector may include: initial conditions, model parameters, and even model error. McLaughlin (1995) outlines a general framework that includes all of these factors. For simplicity and ease of illustration we focus on a synthetic initialization problem in which our objective is to estimate the initial conditions which minimize the model-measurement misfit, where we assume no model error and perfect model parameters.

For the synthetic problem, the imperfect measurements used are of ground temperature, which are represented by:

$$T_g^{obs} = T_g + \nu \tag{2.43}$$

where ν is unbiased measurement error with covariance C_ν. For simplicity we assume the measurement errors are uncorrelated. (The more general case of correlated noise is examined by Boni et al. (2001) in the context of a soil heat equation example.) We then wish to minimize the following objective function:

$$J = \int_t (T_g^{obs} - T_g)^T \, \mathsf{C}_\nu{}^{-1} \, (T_g^{obs} - T_g) \, dt + (\mathbf{y}_0 - \overline{\mathbf{y}_0})^T \, \mathsf{C}_{\mathbf{y}_0}{}^{-1} \, (\mathbf{y}_0 - \overline{\mathbf{y}_0}) \tag{2.44}$$

where $\overline{\mathbf{y}_0}$ is the prior estimate of the initial condition vector, and $\mathsf{C}_{\mathbf{y}_0}$ is the prior error covariance. The two error covariances (C_ν and $\mathsf{C}_{\mathbf{y}_0}$) weight the model-measurement misfit and prior estimate misfit respectively based on the uncertainty involved in each component. For example, if the measurement error was very small and the prior knowledge of the initial conditions was poor, then we would expect the estimation procedure to greatly change the initial conditions in an effort to fit the model output to the measurements. Conversely, if our confidence in the prior conditions was high, while the measurement error was also high, then we would not expect the initial conditions to change much during the estimation procedure. In practice, the situation is generally in between these extremes so that there is a competing influence between the measurements and our prior information.

By adjoining the forward model and taking the first variation as before, we obtain the same homogeneous adjoint model which is now forced by the model-measurement misfit:

$$\frac{\partial \boldsymbol{\lambda}}{\partial t} = -\frac{\partial \mathbf{F}}{\partial \mathbf{y}}^T \boldsymbol{\lambda} - 2\frac{\partial T_g}{\partial \mathbf{y}} \mathsf{C}_\nu^{-1} \left(T_g^{obs} - T_g\right) \tag{2.45}$$

Once the adjoint model is integrated backward in time, the gradient of the objective function with respect to the initial conditions can be computed:

$$\frac{\partial J}{\partial \mathbf{y_0}} = 2\mathsf{C}_{\mathbf{y_0}}^{-1} \left(\mathbf{y_0} - \overline{\mathbf{y_0}}\right) - \boldsymbol{\lambda}_0 \tag{2.46}$$

Note the additional term (in comparison to Equation (2.28)) results from the prior term in the objective function which is a function of the initial conditions.

Using this framework, the estimation procedure is as follows: Based on the prior guesses of the initial conditions ($\overline{\mathbf{y_0}}$), the forward model is integrated yielding $\mathbf{y}(t)$. This state estimate is used in the adjoint model (2.45), along with the model-measurement misfit as forcing, and is integrated backward in time yielding the vector $\boldsymbol{\lambda}_0$. The gradient of the objective function to each initial condition is then computed based on Equation (2.46) and input into a gradient-based search algorithm to obtain a new estimate for $\mathbf{y_0}$. This procedure is repeated iteratively until convergence is reached. Having obtained optimal estimates of the initial conditions, dynamically consistent optimal estimates of the model states and fluxes are obtained via a forward model integration.

For our illustrative example we used synthetic measurements of ground temperature at 30 minute intervals with appropriate noise added (0.2 K standard error). We chose to estimate initial conditions of the following states: T_g, T_d, θ, q, W_1, and W_2 from the synthetic measurements of ground temperature. The other initial conditions were not estimated because ground temperature was not sufficiently sensitive to them for such a short model run (daytime ABL growth only). This illustrates an important point in that for a data assimilation problem to be successful, those measurements being used must be sensitive to the parameters trying to be estimated, otherwise the algorithm will often diverge. Adjoint sensitivity analysis could be a useful preliminary step in diagnosing which parameters can potentially be estimated. For example, in the previous section we saw that average daily ground temperature was not very sensitive to T_c, δ_θ, δ_q, h, and W_3. Further analysis showed that a ground temperature "measurement" (i.e. at a given time) was similarly insensitive to initial conditions in these states for a daytime model integration.

We integrated the forward model with a given set of initial conditions to obtain a synthetic set of model states and fluxes. For the estimation problem the initial conditions were perturbed based on the prior error variance of each parameter. We then implemented the estimation algorithm to see if the actual initial conditions (and hence all subsequent model states and fluxes) could be recovered. The estimation algorithm was applied for 15 iterations and the results are shown in Figure 2-7. In all cases the initial conditions were recovered quite well within about 10 iterations. It is encouraging to note that the parameters were recovered in a relatively small number of iterations using a crude "steepest descent" gradient search (Gill et al. (1981)). To estimate a much larger parameter set, a more sophisticated gradient-based search algorithm (e.g. conjugate gradient) is usually needed. Nevertheless, this simplified case, illustrates how well the variational technique can work in data assimilation problems. In addition to the case shown in Figure 2-7, other scenarios were tested, but are not shown here for brevity. In general, the estimated values

were robust for reasonable perturbations in the prior values. If perturbations are too large however, there can exist other estimates which reproduce the measured ground temperature, but are different from the actual state of the system. In real problems other measurements may be needed (e.g. remotely sensed brightness temperature, micrometeorological humidity and temperature, etc.) to uniquely define the true model state.

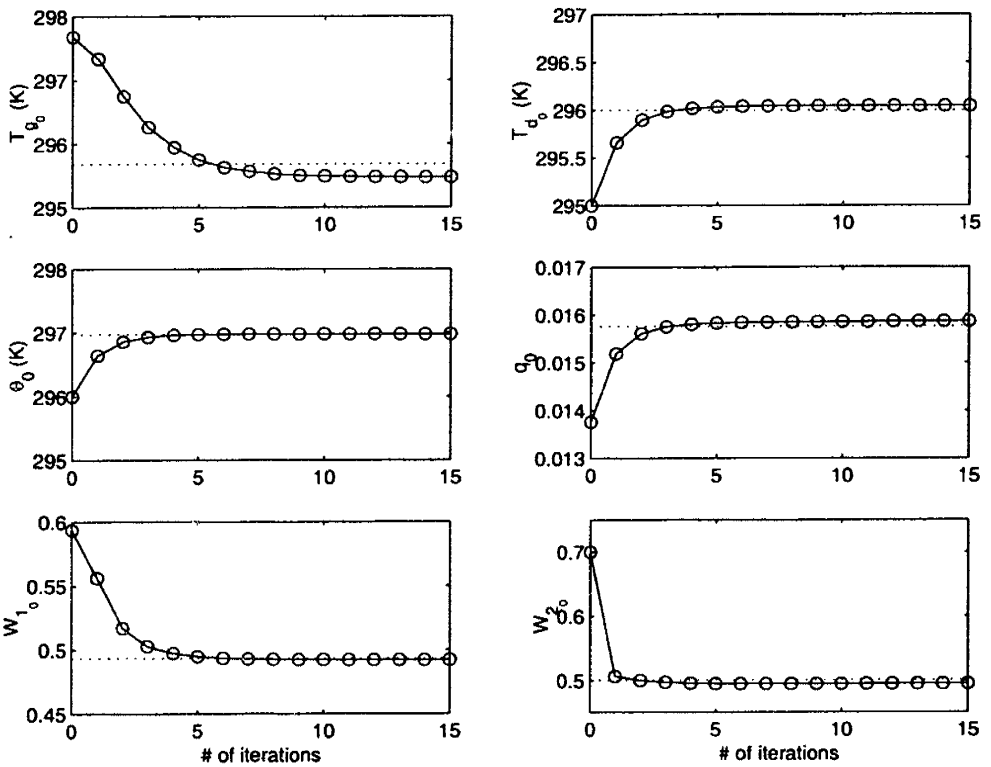

Figure 2-7: Convergence of estimated parameters (marked by 'o' symbols) to actual values (marked by dotted line).

As mentioned above, once the initial conditions are estimated we can also obtain state estimates by integrating the forward model with the estimated initial states. Figure 2-8 illustrates how much improvement is gained in representing the states by assimilating the ground temperature observations. Figure 2-8a shows how the algorithm fits the temperature state to the measurements quite well once convergence has been reached. Additionally, through the model dynamics, other states (for which there are no assimilated measurements) are also updated, removing strong biases ($\sim 1-5$ K in the temperature states; $\sim 1-2$ g kg^{-1} in specific humidity; and $\sim 10-20\%$ in soil moisture) that were present based on the prior parameter values. Also, we are often most interested in estimating the fluxes between the land surface and atmosphere which constitute the surface energy balance. Figure 2-9 shows an example of how fluxes can be estimated under this framework. The actual sensible and latent heat fluxes from the ground are plotted in comparison to those from the model simulation using the prior parameter values and from the simulation using the estimated parameters. The estimates based on the prior values underestimated peak sensible heat flux by ~ 20 Wm^{-2} and overestimated peak latent heat flux by ~ 40 Wm^{-2}, while also having

a large bias throughout the day. In contrast, the sensible and latent heat flux values from the estimated parameters almost exactly reproduce the actual values throughout the day (Figure 2-9).

2.7 Summary

In this chapter the coupled land surface-boundary layer model and its corresponding adjoint model are presented. Together they comprise a general tool which can be used to investigate important science questions related to land-atmosphere interaction. Two simple examples are used to illustrate how the framework allows diagnostic sensitivity analyses, which lead to a better understanding of the behavior of the system, and hydrologic data assimilation, which yields dynamically consistent estimates of model parameters, states, and fluxes. In the sensitivity experiment we show how the sensitivity of average daily ground temperature to all model states and parameters can be efficiently computed once the adjoint model is developed. These sensitivities give information about the relative contribution of each model state and parameter, but more importantly the decomposition of the sensitivities gave further insight into how these sensitivities arise, based on their temporal influence and pathways of propagation. In the synthetic data assimilation example, the adjoint model is used as an estimation tool to initialize the coupled model properly through assimilation of ground temperature observations. As a result, great improvement in prediction of model states and fluxes are obtained. While the examples presented in this chapter were primarily geared toward demonstration of the application of an adjoint model in a hydrological context, in more complex problems the benefits of using the adjoint technique become even more apparent.

In the following chapters the framework developed here is used to thoroughly examine topics including: the consequences of using uncoupled versus coupled models of the land and ABL on system sensitivities (importance of feedback), estimation of model states and fluxes using remotely sensed and micrometeorological observations, and estimation of ABL growth and entrainment via assimilation of radiosonde and micrometeorology observations.

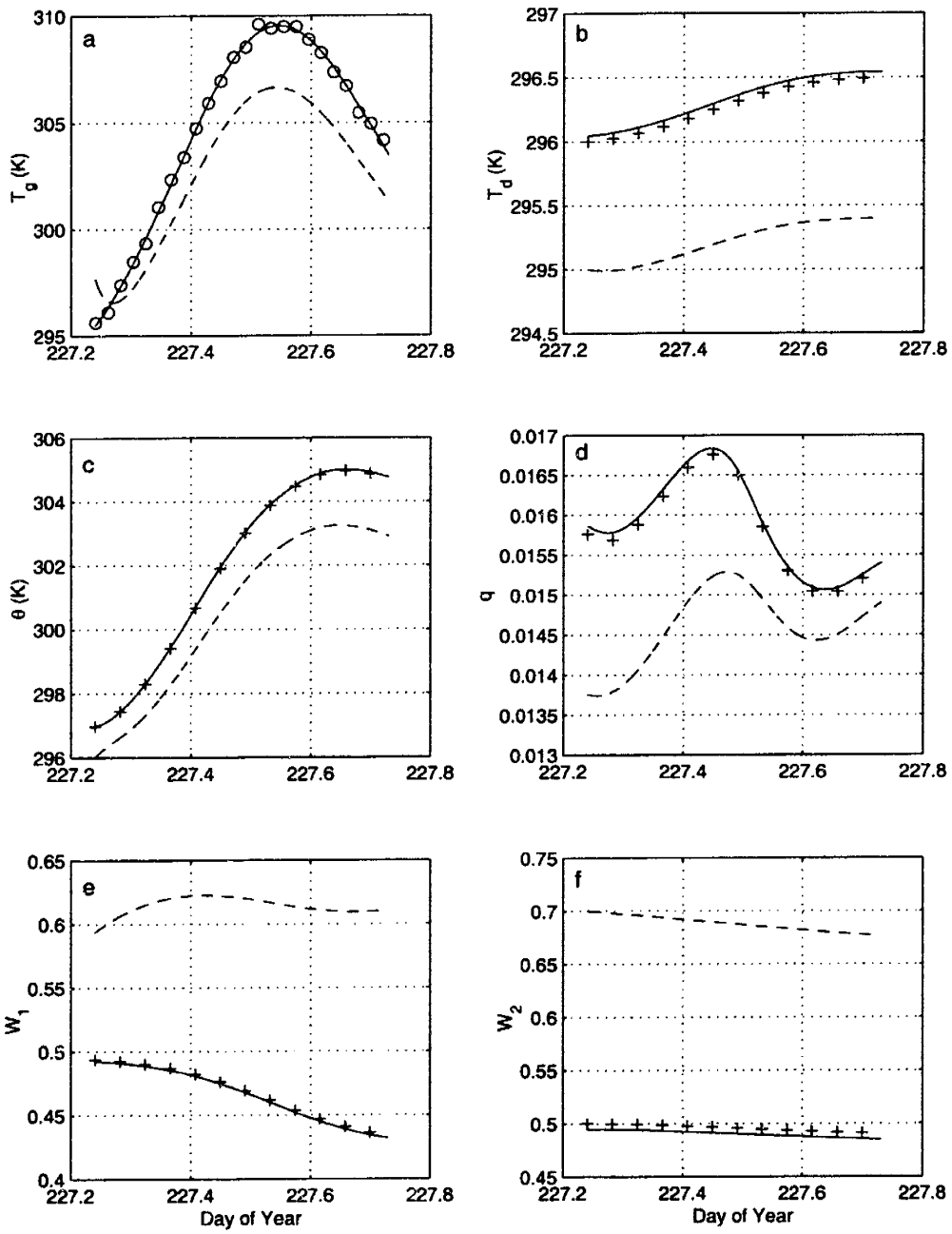

Figure 2-8: Comparison of actual state variables ('+' symbols) to those using prior (dashed line) and estimated parameter values (solid line). The ground temperature measurements assimilated into the model are marked by 'o' symbols.

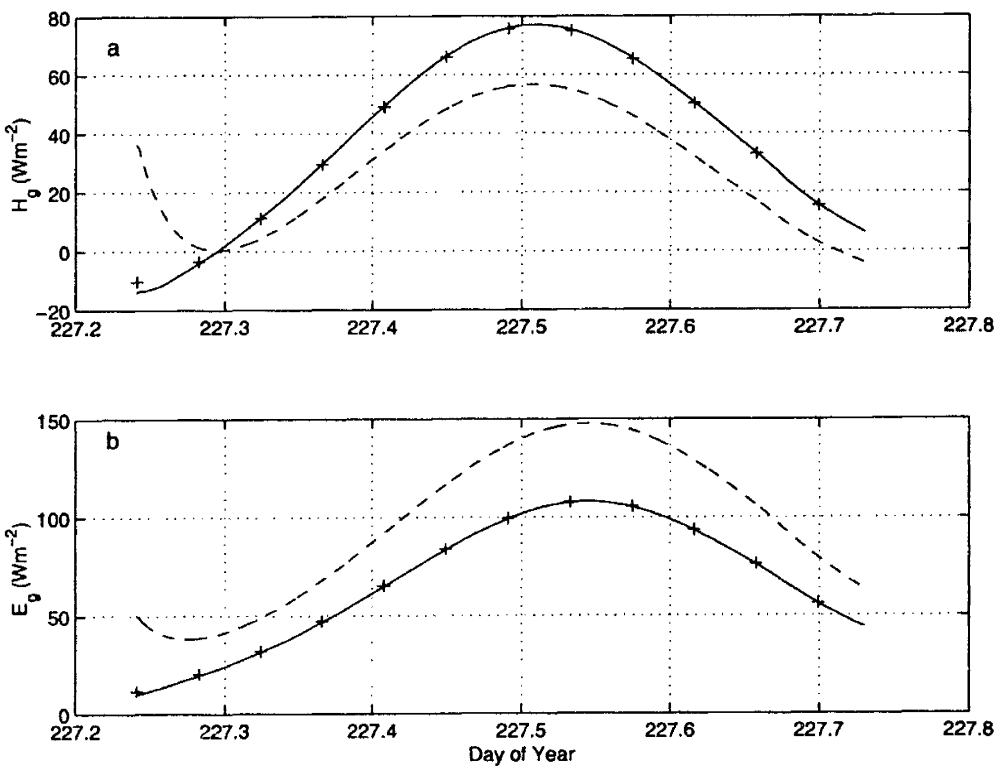

Figure 2-9: Comparison of actual turbulent sensible and latent heat fluxes from the ground ('+' symbols) to those using prior (dashed line) and estimated parameter values (solid line).

Chapter 3

Feedback Between the Land Surface and Atmospheric Boundary Layer

3.1 Background

The water and energy fluxes between the land and atmosphere are a vital link between two major components of the Earth system. They are in general dependent on the state (temperature and moisture) of the both surface and the lower atmosphere. As a result of these fluxes and their mutual dependence on surface and atmospheric states, the land surface and atmospheric boundary layer (ABL) comprise a tightly coupled system with complicated interactions and feedbacks which are significant factors in modulating the variability of weather and climate (Entekhabi 1995).

Many early modeling studies showed the climate system to be sensitive to the representation of the land surface (e.g. Manabe (1969), Walker and Rowntree (1977), Shukla and Mintz (1982), and Mintz (1984)). Based on the results from these studies, which used simple land surface representations, there has been a large effort to develop highly complex parameterizations (often with dozens of parameters) which try to explicitly model interactions between the atmosphere, biosphere, and subsurface (e.g. Dickinson et al. (1986), Sellers et al. (1986), and Sellers et al. (1996)). While these models aim to more realistically represent the physical processes at the atmosphere-surface interface, their complexity dictates a more thorough examination of their components in order to understand the behavior of the system and how to best represent it.

In recent years a considerable amount of effort has been devoted to trying to better understand how the land-atmosphere system behaves through not only model development and simulation, but through sensitivity analyses of the models themselves. There are several sensitivity analysis methods which have been applied in hydrology including: the traditional perturbation (one-factor-at-a-time) technique (e.g. Wilson et al. (1987) Mihailovic et al. (1992), Bonan et al. (1993), Pitman (1994),Ek and Cuenca (1994)), sensitivity equations method (e.g. Yeh (1986)), variational (adjoint) methods (e.g. Skaggs and Barry (1996), factorial methods (e.g. Henderson-Sellers (1993), Alapaty et al. (1997)), Fourier amplitude sensitivity tests (e.g. Collins and Avissar (1994)), and multi-criteria methods (e.g. Bastidas et al. (1996)). Each of these techniques have benefits and drawbacks. For a thorough discussion of the pros and cons of the various methods see Skaggs and Barry (1996) or Gao

et al. (1996).

Many of the studies mentioned above have performed land-atmosphere interaction sensitivity studies in "off-line" mode where the land surface model has been driven by specified atmospheric forcing to avoid the heavy computational burden of using a full atmospheric model (e.g. Henderson-Sellers et al. (1993)). While off-line testing may be appropriate during model development, results from off-line sensitivity tests must be viewed with caution. By imposing micrometeorological forcing inputs on the land surface model, a strong constraint is placed on the land surface, which does not allow it to evolve as it would if coupled to the atmosphere. In fact, using models of varying complexity, studies by Jacobs and DeBruin (1992), Pitman (1994), Hu and Islam (1996), and Kim and Entekhabi (1998) have concluded that the lack of atmospheric feedback can lead to misleading or even erroneous results in model behavior and resulting sensitivities.

An intermediate modeling approach which includes the most important processes in the coupled system, but avoids the computational overhead of a full atmospheric model, is a coupled land surface-atmospheric boundary layer model. Several recent sensitivity studies (e.g. Ek and Cuenca (1994); Quinn et al. (1995); Sun and Bosilovich (1996); Cuenca et al. (1996); Alapaty et al. (1997), Niyogi et al. (1999)) have taken this approach to gain insight into how system responses such as the land surface state, surface turbulent fluxes, ABL development, etc. respond to variations in model parameters within the context of a coupled model. The aim of this paper is to compare coupled and uncoupled sensitivities using the adjoint framework. As will be explained below, this proposed methodology allows for the efficient (relative to the methods described above) computation of sensitivities and, more importantly, yields diagnostic insights into the behavior of the system in ways that are not readily provided in other approaches (e.g. sensitivity pathways, time-variations in sensitivity, etc.).

In Section 3.2 a brief description of the coupled land surface-ABL model used in this study is presented. Section 3.3 provides a description of the adjoint framework and how it is used in the context of this study. In Section 3.4 results from some sensitivity experiments are presented. Finally in Section 3.5 the results are summarized and conclusions which can be drawn from this study are discussed.

3.2 Coupled Land Surface-Boundary Layer Model

The forward model used in this application is described fully in Chapter 2 and Appendix A. The model is used in its dynamical form in the adjoint sensitivity framework below. Special focus is given to the surface turbulent fluxes (latent and sensible heat) which are mutually dependent on surface and boundary layer states.

3.3 Adjoint Sensitivity Analysis

In this study land-atmosphere interactions and feedbacks are analyzed using an adjoint sensitivity approach. Specifically we wish to focus on the comparison of sensitivities from the coupled and uncoupled land-atmosphere system. Previous studies have compared sensitivities using a forward approach with two forward models (one coupled and one uncoupled) each of which is integrated in a control run and then in perturbation runs to compute the sensitivities of a particular model response to individual parameters. A subtle but important point is that, in a forward approach, the nominal model trajectories (from the control

integrations) are not always identical for the coupled and uncoupled cases. Depending on the specified atmospheric forcing, the uncoupled model may yield a different nominal trajectory (i.e. climate) compared to the coupled model. Thus differences in model response to a particular parameter are not only due to the additional feedback pathways in the coupled model, but can also be due to the differing nominal trajectories themselves. To truly diagnose those effects due solely to the additional interaction pathways in the coupled model, it is desirable that the nominal trajectories for the coupled and uncoupled models (about which sensitivities are obtained) be identical. Because this is implicitly satisfied in the adjoint framework (discussed below), the adjoint sensitivity approach is well suited to this problem. Also, and most importantly, the adjoint framework provides valuable insight into the sensitivity pathways in the model, which explain how and why the differences in sensitivities appear. Moreover, the task of obtaining the sensitivities are generally less computationally expensive in the adjoint approach.

At the heart of this analysis is the assertion that the uncoupled model is a special case of the coupled one, where the atmospheric pathways which allow propagation of perturbations in the coupled model are "closed" in the uncoupled case. In other words, the nominal trajectory for each model is the same, but the responses of each model to perturbations are different due to the additional feedbacks in the coupled case. The derivation of the adjoint model corresponding to the coupled model described above was presented in Chapter 2. Other examples of the use of adjoint models for sensitivity analysis can be found most notably in the meteorology and oceanography literature (e.g. Hall et al. (1982), Rabier et al. (1992), Errico and Vukicevic (1992)). The coupled model can be defined generally in dynamical form:

$$\frac{d\mathbf{y}}{dt} = \mathbf{F}(\mathbf{y};\boldsymbol{\alpha}) \tag{3.1}$$

where $\mathbf{y}(t)$ is the state vector, and $\mathbf{F}$ is a nonlinear vector operator which is a function of the states themselves and the vector of time-invariant structural model parameters $\boldsymbol{\alpha}$. The model is presented in this format in Appendix A. For the purposes of sensitivity analysis, we define a model response functional as:

$$J = \int_{t_0}^{t_f} \phi(\mathbf{y};\boldsymbol{\alpha})dt \tag{3.2}$$

where ϕ is a nonlinear function of the state variables and model parameters, which can represent any number of responses that are generally used in sensitivity studies (e.g. average surface states or fluxes, Bowen ratio, etc.).

The state vector for the coupled model can be decomposed into surface and ABL states as $\mathbf{y} = [\mathbf{y}_s, \mathbf{y}_a]^T$, where T is the vector transpose operator. For our model the surface states ($\mathbf{y}_s$) include canopy temperature (T_c), surface ground temperature (T_g), deep ground temperature (T_d), and the soil moisture in each soil layer (W_1, W_2, and W_3), while the ABL states ($\mathbf{y}_a$) include potential temperature (θ), specific humidity (q), inversions in potential temperature and specific humidity (δ_θ and δ_q respectively), and mixed-layer height (h). Following this new notation, we can write the uncoupled and coupled models respectively

as:

$$\frac{d\mathbf{y}_s}{dt} = \mathbf{F}_s(\mathbf{y}_s; \mathbf{y}_a, \boldsymbol{\alpha}) \tag{3.3}$$

$$\frac{d}{dt}\begin{bmatrix} \mathbf{y}_s \\ \mathbf{y}_a \end{bmatrix} = \begin{bmatrix} \mathbf{F}_s(\mathbf{y}_s, \mathbf{y}_a; \boldsymbol{\alpha}) \\ \mathbf{F}_a(\mathbf{y}_s, \mathbf{y}_a; \boldsymbol{\alpha}) \end{bmatrix} \tag{3.4}$$

The function $\mathbf{F}_s$ includes only the surface water and energy balance equations and $\mathbf{F}_a$ includes the ABL balance and dynamics equations. Written in this way, it is evident that the uncoupled model (3.3) is a special case of the coupled model (3.4), where the surface states are governed by the same prognostic equations as in the coupled model ($\mathbf{F}_s$), but the ABL states are specified as forcing (i.e. not allowed to vary as a result of variations in $\mathbf{y}_s$ or $\boldsymbol{\alpha}$). In contrast, for the coupled model the evolution of both the surface and ABL states depend on each other as well as on the time-invariant model parameters $\boldsymbol{\alpha}$. Under this framework, we do not need to separately integrate an "uncoupled model" to get its nominal trajectory, since it is given via the integration of the coupled model under the implicit condition that the ABL states (obtained from the coupled model) act as forcing. It is only under perturbations to the nominal trajectory that the effects of the specified forcing of the uncoupled model (i.e. lack of atmospheric feedbacks), would show up as differences in response. It is with the adjoint model that we can readily diagnose these differences.

Following the derivation used in Chapter 2, the adjoint models corresponding to the coupled and uncoupled forward models (3.3) and (3.4) can be written as:

$$\frac{d\boldsymbol{\lambda}_s^u}{dt} = -\left(\frac{\partial \mathbf{F}_s}{\partial \mathbf{y}_s}\right)^T \boldsymbol{\lambda}_s^u + \frac{\partial \phi}{\partial \mathbf{y}_s} \tag{3.5}$$

$$\frac{d}{dt}\begin{bmatrix} \boldsymbol{\lambda}_s^c \\ \boldsymbol{\lambda}_a^c \end{bmatrix} = \begin{bmatrix} -\left(\frac{\partial \mathbf{F}_s}{\partial \mathbf{y}_s}\right)^T \boldsymbol{\lambda}_s^c - \left(\frac{\partial \mathbf{F}_a}{\partial \mathbf{y}_s}\right)^T \boldsymbol{\lambda}_a^c + \frac{\partial \phi}{\partial \mathbf{y}_s} \\ -\left(\frac{\partial \mathbf{F}_s}{\partial \mathbf{y}_a}\right)^T \boldsymbol{\lambda}_s^c - \left(\frac{\partial \mathbf{F}_a}{\partial \mathbf{y}_a}\right)^T \boldsymbol{\lambda}_a^c + \frac{\partial \phi}{\partial \mathbf{y}_a} \end{bmatrix} \tag{3.6}$$

where the adjoint model is developed analytically from the forward model and propagates sensitivity information backward in time over the model integration ("u" and "c" denote uncoupled and coupled variables respectively). Each adjoint variable (λ_i) is uniquely related to a corresponding model state and represents the sensitivity (multiplied by a negative sign) of the model response J to a perturbation in the corresponding state at that time:

$$\left(\frac{\partial J}{\partial y_i(t)}\right)_p = -\lambda_i^p \qquad p = u, c \tag{3.7}$$

where "p" denotes either uncoupled or coupled sensitivities and "i" represents a particular state variable. For example, if J was specified to be the average evaporation over the model integration, then the adjoint variable corresponding to canopy temperature at a particular time would represent the sensitivity of average evaporation to canopy temperature at that moment in time. Similarly there is an adjoint variable corresponding to every other state variable, such that the dimensions of the adjoint state vectors $\boldsymbol{\lambda}_s$ and $\boldsymbol{\lambda}_a$ are the same as that of the state vectors $\mathbf{y}_s$ and $\mathbf{y}_a$ respectively. By construction, the terminal condition of the adjoint variables is known ($\boldsymbol{\lambda}(t_f) = 0$). We can thus directly obtain the

uncoupled and coupled state sensitivities by integrating the coupled and uncoupled adjoint models backward in time. This state sensitivity information is the key to obtaining insight into sensitivity pathways, temporal sensitivity contributions, and parameter sensitivities that will be discussed below. Note that to get the same state sensitivity information in a perturbation approach would require an additional perturbation run at each time step for each state variable and thus would be prohibitively expensive.

By comparing the adjoint models given by (3.5) and (3.6) we see that, as with the forward models, the uncoupled adjoint model is a special case of the coupled adjoint model, where the Jacobian matrices $\frac{\partial \mathbf{F}_a}{\partial \mathbf{y}_s}$, $\frac{\partial \mathbf{F}_s}{\partial \mathbf{y}_a}$, $\frac{\partial \mathbf{F}_a}{\partial \mathbf{y}_a}$, and vector $\frac{\partial \phi}{\partial \mathbf{y}_a}$ are all zero. This is simply a mathematical statement of the implicit assumptions in the uncoupled model where the atmospheric states ($\mathbf{y}_a$) are specified (non-interactive). Based on the definition of the adjoint variables, it is evident that each term in the adjoint model represents a pathway through which a given state variable (y_i) ultimately affects the model response (J), either directly or indirectly. For example, the term $\frac{\partial \phi}{\partial y_i}$ represents the direct effect of y_i on the model response, while the term $\frac{\partial F_i}{\partial y_j}\lambda_i$ represents how y_j affects the evolution of y_i (as governed by F_i) which in turn influences J (as given by λ_i). When looking at the terms in the adjoint model in this way it becomes evident that the additional pathways of influence in the coupled model are represented by the additional terms in its adjoint. As a result, the coupled model not only includes ABL state sensitivities ($\boldsymbol{\lambda}_a^c$), which the uncoupled model does not, but the additional pathways in the coupled surface state adjoint model lead to differences in the land surface state sensitivities ($\boldsymbol{\lambda}_s^u$ vs. $\boldsymbol{\lambda}_s^c$). Thus by integrating each adjoint model and analyzing the resulting state sensitivities, we can obtain important insight into how and why differences in sensitivity appear between coupled and uncoupled models.

The methodology for the evaluation of sensitivities for a given model response J is as follows: 1) The coupled forward model is integrated (with nominal initial condition $\mathbf{y}(t_0)$ and parameters $\boldsymbol{\alpha}$) yielding the nominal state trajectory, $\mathbf{y}(t)$. Again note that this single forward run yields the state trajectories for both the coupled ($\mathbf{y_s}(t)$ and $\mathbf{y_a}(t)$) and uncoupled ($\mathbf{y_s}(t)$) model (where it is implicit that the "forcing" of the uncoupled model is given by the nominal ABL states $\mathbf{y}_a$). 2) The nominal states are then used in the uncoupled and coupled adjoint models which are integrated backward in time to yield the corresponding adjoint variables ($\boldsymbol{\lambda}_s^u(t)$; and $\boldsymbol{\lambda}_s^c(t)$, $\boldsymbol{\lambda}_a^c(t)$) which represent the state sensitivities. The adjoint variables themselves can then be compared to see how the sensitivity of J to the model states differs between the uncoupled and coupled case. 3) The adjoint variables are then used to compute parameter sensitivity derivatives (see Chapter 2) which are given by:

$$\left(\frac{\partial J}{\partial \boldsymbol{\alpha}}\right)_u^T = \int_t \left[\frac{\partial \phi}{\partial \boldsymbol{\alpha}} - \left(\frac{\partial \mathbf{F}_s}{\partial \boldsymbol{\alpha}}\right)^T \boldsymbol{\lambda}_s^u\right] dt \tag{3.8}$$

and

$$\left(\frac{\partial J}{\partial \boldsymbol{\alpha}}\right)_c^T = \int_t \left[\frac{\partial \phi}{\partial \boldsymbol{\alpha}} - \left(\frac{\partial \mathbf{F}_s}{\partial \boldsymbol{\alpha}}\right)^T \boldsymbol{\lambda}_s^c - \left(\frac{\partial \mathbf{F}_a}{\partial \boldsymbol{\alpha}}\right)^T \boldsymbol{\lambda}_a^c\right] dt \tag{3.9}$$

These equations integrate all of the mechanisms by which a particular parameter influences the model response over the model integration: directly, via surface states, and via ABL

states. The key information in these equations are the adjoint state variables which translate how parameters ultimately influence the model response via the model state sensitivities. Note that differences in parameter sensitivities between the two models can be manifested in two ways. The first difference is that there is an extra term in the sensitivity equation for the coupled model (3.9), which corresponds to the effect a perturbation in $\boldsymbol{\alpha}$ has on the model response J via the atmospheric sensitivity pathways ($\left(\frac{\partial \mathbf{F}_a}{\partial \boldsymbol{\alpha}}\right)^T \boldsymbol{\lambda}_a^c$). The second difference is that the surface state sensitivities themselves will differ between the uncoupled and coupled models (i.e. $\boldsymbol{\lambda}_s^u \neq \boldsymbol{\lambda}_s^c$) as discussed above. Thus even if the first difference is ignored (say $\mathbf{F}_a$ does not depend on $\boldsymbol{\alpha}$) *a priori* we would expect differences in the sensitivities between the two as have been suggested in previous work using a forward sensitivity approach. The adjoint model not only allows us to quantify these differences, but yields diagnostic insight into which pathways are most important in causing the differences. Further, this information is obtained at the computational cost of one forward model run and two adjoint model runs per model response.

3.4 Surface Flux Sensitivities at the FIFE site

The simulations used in this study consist of model integrations using parameters corresponding to the First International Satellite Land Surface Climatology Project (ISLSCP) Field Experiment (FIFE) area, which is a tall grass prairie located in Kansas (Sellers et al. 1992). The forward model was tested extensively using these parameters in Chapter 2. The focus of this study is to illustrate how land-atmosphere interactions can differ between coupled and uncoupled modes and to diagnose how these differences arise (sensitivity pathways) using the adjoint framework discussed above. We are interested in investigating the sensitivities of model responses which represent the primary interactions between the land surface and ABL. Two of the primary measures of interaction between the surface and atmosphere are the surface latent and sensible heat fluxes which partition the available energy at the surface. As these fluxes are mutually dependent on both surface and atmospheric states, it should be expected *a priori* that ignoring the atmospheric feedbacks will lead to differences in the sensitivities between uncoupled and coupled models.

In specifying the model responses to be used in the adjoint framework, we chose the average daytime latent heat flux ($\overline{L_v E}$), and average daytime sensible heat flux ($\overline{H}$). These responses can be expressed analytically in the form of Equation (3.2), after which application of the adjoint framework is straightforward. For example, the average latent heat flux can be expressed as:

$$J = \overline{L_v E} = \frac{1}{\tau} \int_{t_0}^{t_f} L_v E \, dt \tag{3.10}$$

where in the notation used above, $\phi = L_v E/\tau$ (E is the sum of evaporation through the canopy and soil), and τ is the length of the model integration ($t_f - t_0$). Similarly for $\overline{H}$, ϕ in the above equation is replaced by H/τ (H includes canopy and ground sensible heat fluxes). For a nominal set of initial conditions and model parameters, the forward model is integrated a single time, and the (uncoupled and coupled) adjoint models are integrated

backwards, once for each model response, to yield the uncoupled and coupled sensitivities corresponding to that particular response.

In this study we decided to focus on the effects of primary physical parameters (which appear in most land surface parameterizations) on the model responses discussed above. We therefore limited the analysis to the following commonly specified land surface parameters: fractional vegetation cover (V_c), leaf area index (LAI), canopy and ground surface albedo ($a_{c_{\Lambda,\mu}}$ and $a_{g_{\Lambda,\mu}}$), which each have four components (over spectral band (Λ =visible,near-infrared) and direction (μ =beam,diffuse)), minimum bulk canopy resistance ($r_{c_{min}}$), aerodynamic roughness length (z_0), and the soil water retention parameters (B_s and ψ_s) of Clapp and Hornberger (1978). In addition, there are six "parameters" common to the coupled and uncoupled models which correspond to the specified surface state initial conditions ($\mathbf{y_s}(t_0)$). It should be noted that in our model canopy albedo and minimum canopy resistance are not specified time-invariant parameters (as they are in some models), but instead are diagnostic variables computed by the model. However, because they are important parameters which are often specified in land-surface models, we introduce "shadow parameters" which are coefficients (with nominal values of 1.0) that multiply $a_{c_{\Lambda,\mu}}$ and $r_{c_{min}}$ in our model. In the remainder of the chapter, any references to sensitivities to canopy albedo or minimum canopy resistance are, strictly speaking, sensitivities to these shadow parameters.

3.4.1 Forward Model Trajectory

The results presented below are for a model trajectory corresponding to a daytime integration of the forward model at the FIFE site during a typical summer day (Julian Day 200 of 1987). The daytime-only results are sufficient to illustrate the differences in turbulent flux sensitivities which appear as a result of using an uncoupled model and to explain how these differences arise at the diurnal time scale. The average daily evaporation during the day is $\overline{L_vE} = 256$ Wm^2, while the average sensible heat flux is $\overline{H} = 118$ Wm^2. The forward model integration provides the nominal state trajectory ($\mathbf{y}(t) = [\mathbf{y}_s(t), \mathbf{y}_a(t)]^T$) about which the terms in the adjoint model are evaluated. This nominal trajectory is common to all the sensitivity evaluations. For each of the model responses, the coupled and uncoupled adjoint models are integrated once to obtain all of the sensitivity information presented below.

3.4.2 Latent and Sensible Heat Flux Sensitivities

Net (Integrated) Sensitivity Differences

We first present the integrated sensitivity results for $\overline{L_vE}$ and $\overline{H}$, which are equivalent to the results commonly shown in studies using a forward finite-difference approach, namely sensitivities to initial conditions and time-invariant parameters. Since the primary focus of this study is to investigate the differences between using uncoupled vs. coupled models, the net sensitivities are not presented in terms of overall magnitude, but instead as a percent difference between the two sensitivities. The differences in the sensitivity to model state initial conditions and parameters can be expressed as $\left(\frac{\boldsymbol{\lambda}_c(t_0)-\boldsymbol{\lambda}_u(t_0)}{\boldsymbol{\lambda}_u(t_0)}\right)$ and $\left(\frac{(\partial J/\partial \boldsymbol{\alpha})_c-(\partial J/\partial \boldsymbol{\alpha})_u}{(\partial J/\partial \boldsymbol{\alpha})_c}\right)$ respectively. Once the adjoint models are integrated for each model response (yielding $\boldsymbol{\lambda}_s^u$; and $\boldsymbol{\lambda}_s^c$, $\boldsymbol{\lambda}_a^c$), the differences in sensitivity of average latent and sensible heat flux to all of the initial conditions and time-invariant model parameters are obtained from the above expressions for both the coupled and uncoupled cases. For discussion purposes below, we define an "amplified" ("dampened") sensitivity as one whose absolute value is larger (smaller) in

the coupled model than in the uncoupled model. Thus based on the expressions above, positive percent differences denote that the additional coupled model pathways amplify the uncoupled sensitivities, and vice versa for negative differences.

Figure 3-1 shows the differences in the sensitivity of average daytime latent heat flux ($\overline{L_v E}$) to each of the model initial conditions and parameters. Figure 3-1a shows the percent difference for the surface state initial conditions. The initial conditions of the three temperature states (T_c, T_g, and T_d) all have positive differences (i.e. amplified sensitivities in the coupled model) ranging from $\sim 20 - 90\%$ in magnitude. The rootzone soil moisture states (W_1 and W_2) have negative differences ($\sim 10 - 30\%$), while the deep soil moisture initial condition has a positive difference ($\sim 10\%$). Thus a positive perturbation in any of the temperature states or deep soil moisture initial condition would have an amplified effect on $\overline{L_v E}$ in the coupled model, while the sensitivity to rootzone soil moisture is dampened. How these differences arise will be discussed in detail below. Figure 3-1b shows the percent difference for the time-invariant model parameters. For the parameters there is no clear pattern in the differences; in the coupled model some parameters have amplified sensitivities while other have dampened sensitivities. The differences range in overall magnitude from as little as $\sim 5\%$ (for ψ_s) up to as much as $\sim 50\%$ (for $a_{g_{V,d}}$).

Figure 3-2 shows the same sensitivity information discussed above, but for the average sensible heat flux ($\overline{H}$). Figure 3-2a shows that the percent difference for all of the surface state initial conditions are negative. This indicates that, positive perturbations in any of the surface state initial conditions tend to have a smaller effect on the average sensible heat flux in the coupled model. The largest differences are in the canopy and ground temperatures, which both exhibit less sensitivity in the coupled model by as much as in excess of 60%. Figure 3-2b shows the percent difference for the time-invariant model parameters. Again, most of the parameters show a negative difference, indicating a dampening effect in the coupled model.

These results were compared to the previous studies mentioned above. While a quantitative comparison can be difficult due to different test sites, parameter sets, models, and other factors, the sense in which the sensitivities change between the uncoupled and coupled models were compared with the results shown in Jacobs and DeBruin (1992), Hu and Islam (1996), and Kim and Entekhabi (1998). Specifically, the results for average daily latent heat flux with respect to canopy resistance, roughness length, and albedo, match those of Jacobs and DeBruin (1992). Similarly the change in sensitivity to minimum canopy resistance for both latent and sensible heat fluxes agrees with the results of Kim and Entekhabi (1998). The comparison with Hu and Islam (1996) is not as straightforward since many of the parameters from the two models used in the studies are not precisely related. However for those parameters which are shared between the two studies, the change between coupled and uncoupled sensitivities also are of the same sense. This comparison verifies that the results from the adjoint model are consistent with results using other sensitivity techniques.

While the integrated sensitivities for $\overline{L_v E}$ and $\overline{H}$ and their differences are important, what we are most interested in is a better understanding of how these differences arise. The primary benefit to the adjoint approach is the ability to identify important sensitivity pathways through which perturbations in states and parameters propagate, and the time-varying nature of these sensitivities. For example, the sensitivities to initial conditions provide some insight, but only represent the influence of the state variable chosen at a particular and arbitrary time. A better question is: what are the differences in sensitivity to these states at any time (especially the "most important" times) and how do these differences arise? This information is given directly by the adjoint variables. Further, while

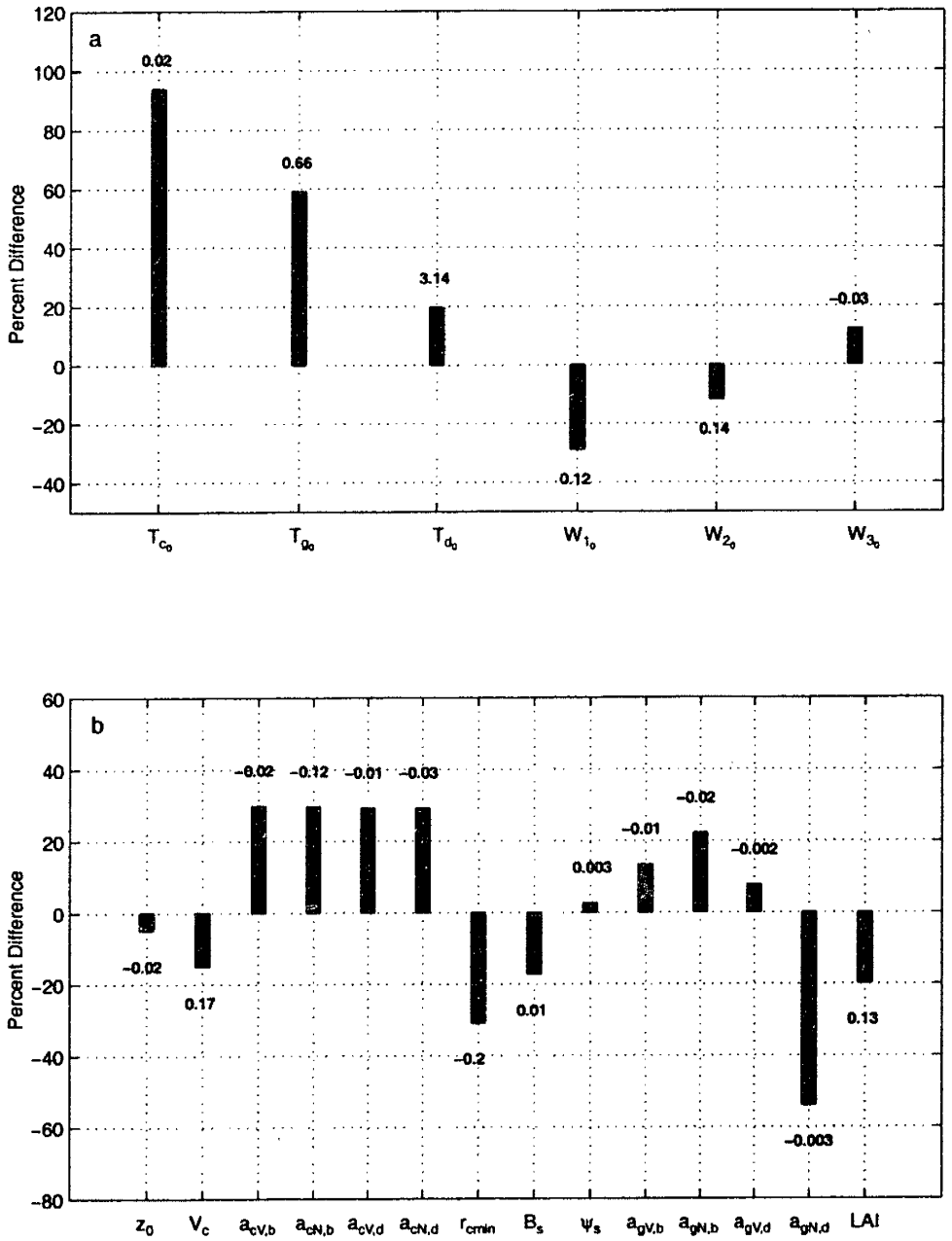

Figure 3-1: Net differences in sensitivity of average daytime latent heat flux ($\overline{L_v E}$) between the uncoupled and coupled models. a) Percent differences in initial condition sensitivities. b) Percent differences in parameter sensitivities. (The corresponding uncoupled relative sensitivity value is given for reference next to each bar in the diagram.)

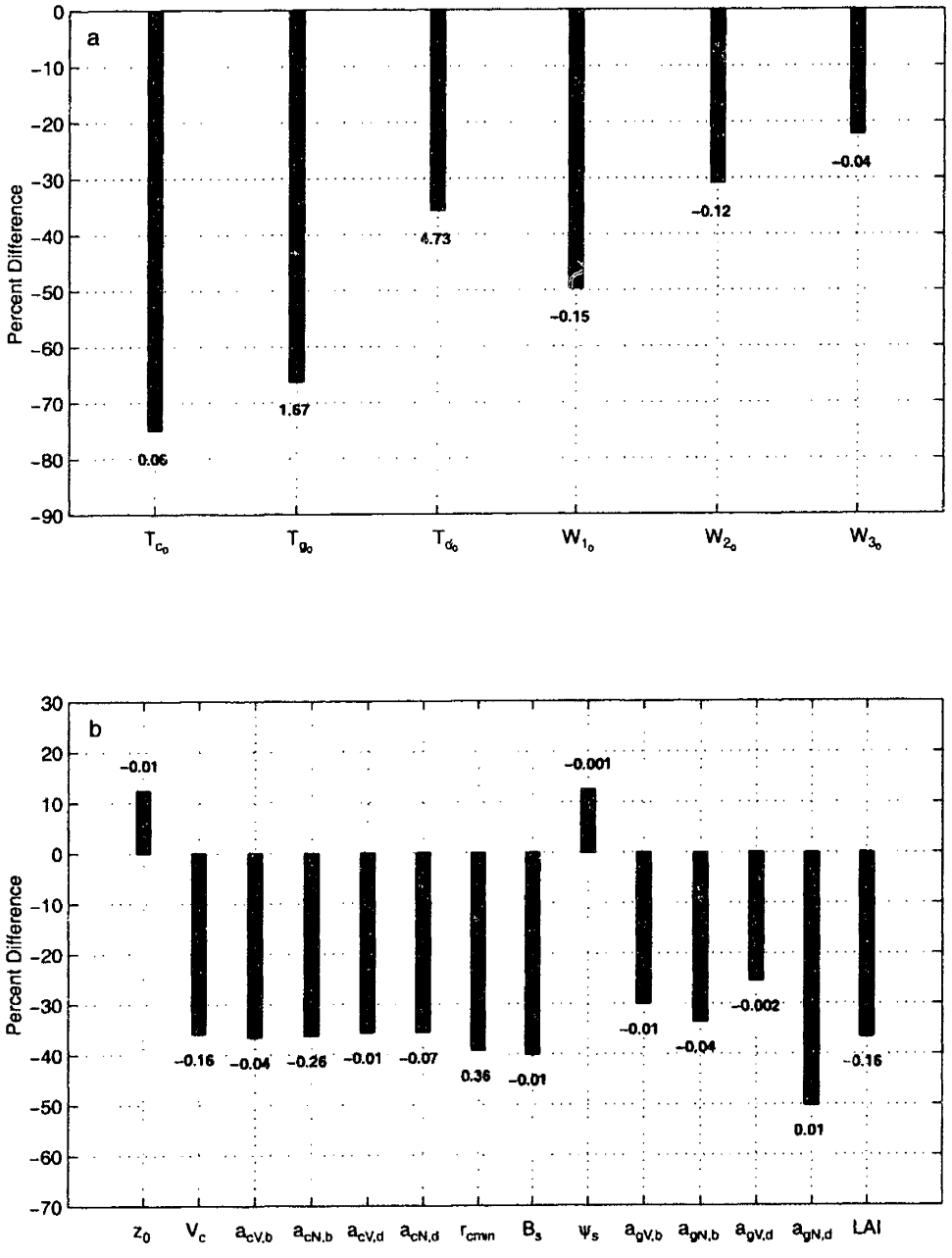

Figure 3-2: Net differences in sensitivity of average daytime sensible heat flux ($\overline{H}$) between the uncoupled and coupled models. a) Percent differences in initial condition sensitivities. b) Percent differences in parameter sensitivities. (The corresponding uncoupled relative sensitivity value is given for reference next to each bar in the diagram.)

the parameters, shown in Figures 3-1b and 3-2b are time-invariant, their influence is not. The sensitivities based on Equations (3.8) and (3.9) represent the integrated effect of the parameter over the entire model run. However the response is in fact very much dependent on how the parameters interact with the dynamic model states, and thus their influence is time-dependent. The time-varying influence of the parameters, and how they differ between the coupled and uncoupled modes can also be obtained using the adjoint variables. Thus, there are two distinct types of sensitivities in this framework: 1) state sensitivities, which represent how perturbations in the model states effect the model response, and 2) parameter sensitivities which represent how perturbations in time-invariant structural model parameters effect the model response. The differences in these sensitivities with and without boundary layer feedbacks are explored in detail below.

Differences in State Sensitivities and State Sensitivity Pathways

We first examine how the sensitivities of $\overline{L_vE}$ and $\overline{H}$ to model states differ between the uncoupled and coupled cases. It is these state sensitivities which play a key role in determining the parameter sensitivities (see Equations 3.8 and 3.9). From the definition of the adjoint model, differences in the sensitivity of the average surface turbulent fluxes to model states will show up in their adjoint variables. For the uncoupled model (where there is no ABL interaction) there only exist surface adjoint variables ($\boldsymbol{\lambda}_s^u(t)$) corresponding to each model response, while the coupled model has both surface and ABL adjoint variables ($\boldsymbol{\lambda}_s^c(t)$ and $\boldsymbol{\lambda}_a^c(t)$). Due to the additional pathways in the coupled model, the surface adjoint variables (state sensitivities) will differ between models. Based on the adjoint variables, the surface state sensitivities as a function of time for $\overline{L_vE}$ (expressed here as Wm^{-2} per percent change in y_i) are shown in Figure 3-3 for the coupled and uncoupled cases. Similarly, the surface state sensitivities for $\overline{H}$ are shown in Figure 3-4. By definition, each adjoint variable is equal to zero at the terminal time (t_f) of the model integration, i.e. perturbing the state at t_f cannot impact the time-averaged turbulent fluxes ($\overline{L_vE}$ or $\overline{H}$) over the preceding integration window. As the adjoint model is integrated backward in time it "collects" sensitivity information tracing out the sensitivity of J to each state as a function of time until the initial time (t_0) is reached, at which point the adjoint function equals the sensitivity of J to the corresponding state initial condition (which are the basis for the values given in Figures 3-1a and 3-2a). Due to the causal nature of the system, the adjoint variables are in general larger in magnitude earlier in the integration window, since perturbations earlier in the day can have a larger influence over time on $\overline{L_vE}$ or $\overline{H}$. Figure 3-3 shows that for $\overline{L_vE}$, significant differences arise between the coupled and uncoupled surface state sensitivities. Note that each pair of coupled and uncoupled adjoint functions are similar near the end of the model integration, but diverge earlier in the day. As t approaches t_f a perturbation in a given state will have an increasingly limited effect on $\overline{L_vE}$ such that even the additional pathways present in the coupled model will not allow for significant differences in response. Earlier in the day however, a perturbation can cause much more significant differences since there is enough time for the additional pathways to have a noticeable effect. For example, Figure 3-3b indicates that in the early morning hours an instantaneous 1% perturbation ($\sim 3K$) in the ground temperature (T_g) in the uncoupled model would cause a ~ 1.7 Wm^{-2} change in $\overline{L_vE}$, while in the coupled model there would be a ~ 2.8 Wm^{-2} change. Figure 3-3 indicates that the average latent heat flux has amplified sensitivity to perturbations in the temperature states (T_c, T_g, and T_d) in the coupled model throughout the day, while there is dampened sensitivity to rootzone soil moisture (W_1 and W_2). Figure 3-4 indicates

that there is a dampening of the sensitivity of $\overline{H}$ to all surface states in the coupled model. For example, an instantaneous 1% perturbation ($\sim 3K$) in T_g in the early morning would lead to a ~ 1.9 Wm^{-2} change in $\overline{H}$ in the uncoupled model, but only a ~ 0.7 Wm^{-2} change in the coupled case.

As a brief aside, in addition to the daytime results discussed so far, multi-day simulations were performed. Illustrative results of the nondimensional adjoint variables from these longer simulations are shown in Figures 3-5 and 3-6. These figures show that for the longer memory state variables (W_1, W_2, W_3, and T_d) the difference in sensitivities between the coupled and uncoupled models continue to grow larger backward in time (as in Figures 3-3 and 3-4) , while for T_c and T_g there is a pronounced diurnal cycle in the sensitivity differences (qualitatively similar to those in Figures 3-3 and 3-4; i.e higher in mid-morning, lower in evening). The implications are that the errors in uncoupled sensitivities can be even larger for long-term simulations, thus making using a coupled model even more important. The mechanisms which cause the differences in the multi-day integrations are similar to those of the daytime runs, so below we discuss only the daytime results.

Diagnosing how the differences arise (via sensitivity pathways) is done by examining the uncoupled and coupled adjoint models in more detail. The most obvious difference between the uncoupled and coupled adjoint models is the presence of ABL adjoint states ($\boldsymbol{\lambda}_a^c$), which simultaneously evolve with the surface adjoint states in the coupled adjoint model, but are absent in the uncoupled case. To illustrate the direct influence of the ABL states, the ABL state adjoint functions (expressed as Wm^{-2} per percent change in y_i) are shown in Figure 3-7 for both $\overline{L_vE}$ and $\overline{H}$. Figure 3-7a shows that for both of the turbulent fluxes the adjoint variable corresponding to potential temperature in the mixed-layer (θ) is actually greater in magnitude than any of the surface adjoint variables. For example, an instantaneous 1% perturbation in θ_0 ($\sim 3K$) would cause a ~ 17 Wm^{-2} change in $\overline{L_vE}$ and a ~ -21 Wm^{-2} change in $\overline{H}$, which, as discussed above, are both much larger than the effect a perturbation in T_g would have. This is in large part due to the relative size of the surface ground temperature reservoir, which is much smaller than the mixed-layer. Additionally, the other ABL adjoint variables are of comparable magnitude to the surface state adjoint variables, indicating the importance perturbations in ABL states can have on the turbulent surface fluxes. Also, note that the ABL adjoint states for $\overline{L_vE}$ and $\overline{H}$ generally oppose each other. This is a result of the implicit presence of the surface energy balance constraint on the system. For a perturbation in a particular state, the change in available energy (between coupled and uncoupled models) is generally much smaller than the changes in turbulent fluxes. As a result, a positive change (from uncoupled to coupled sensitivity) in one of the turbulent fluxes generally dictates a negative change in the other and vice versa. For example, Figure 3-7a shows that the change in coupled model sensitivity of $\overline{H}$ to an interactive ABL potential temperature (relative to the uncoupled model which has zero sensitivity by definition) is negative. Due to the surface energy balance constraint this dictates a positive change in the $\overline{L_vE}$ sensitivity as shown in Figure 3-7a. This important counterbalancing of changes in sensitivity will appear throughout the the analysis of sensitivity pathways shown below.

Beyond the direct influence of ABL states, it is the presence of an interactive ABL in the coupled model which provides additional sensitivity pathways, causing the land surface state sensitivities themselves to different between models. The atmospheric pathways of influence for perturbations in the surface states are represented by the $-\left(\frac{\partial \mathbf{F}_a}{\partial \mathbf{y}_s}\right)^T \boldsymbol{\lambda}_a^c$ terms in the coupled adjoint model. Note that as the adjoint models are integrated backward

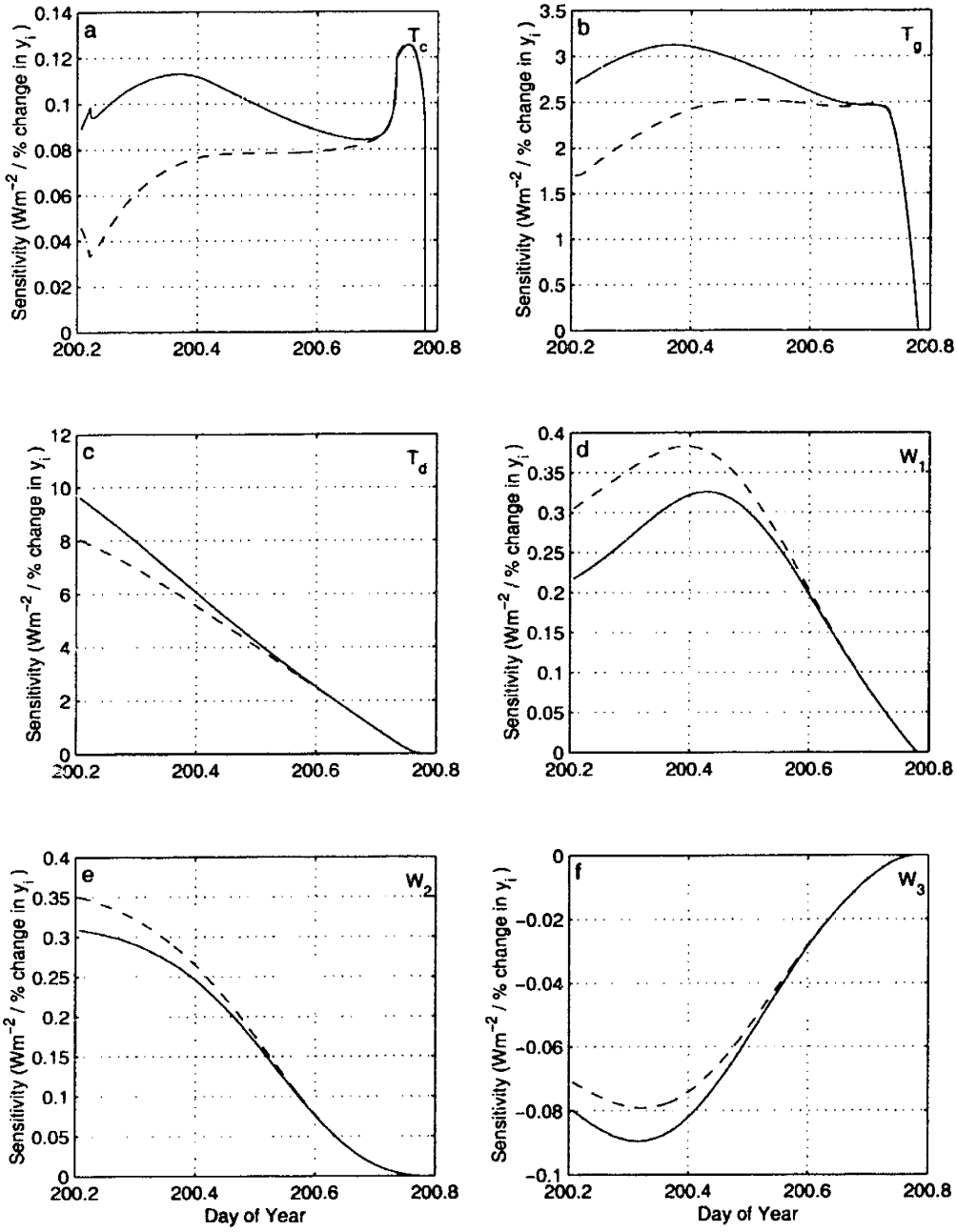

Figure 3-3: Coupled and uncoupled surface state sensitivities for average daytime latent heat flux ($\overline{L_v E}$). The solid lines correspond to the coupled model sensitivities and the dashed lines correspond to the uncoupled model sensitivities.

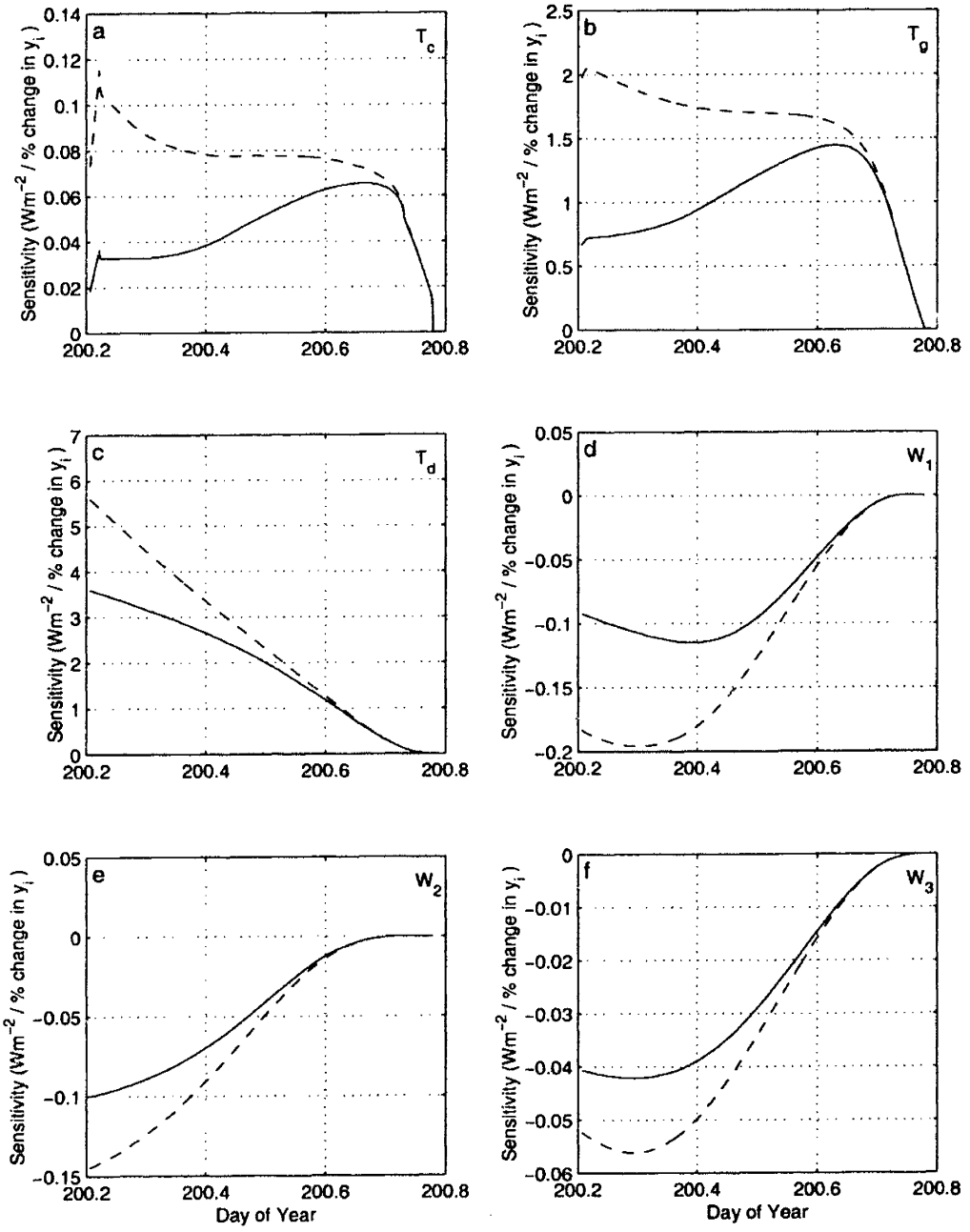

Figure 3-4: Coupled and uncoupled surface state sensitivities for average daytime sensible heat flux ($\overline{H}$). The solid lines correspond to the coupled model sensitivities and the dashed lines correspond to the uncoupled model sensitivities.

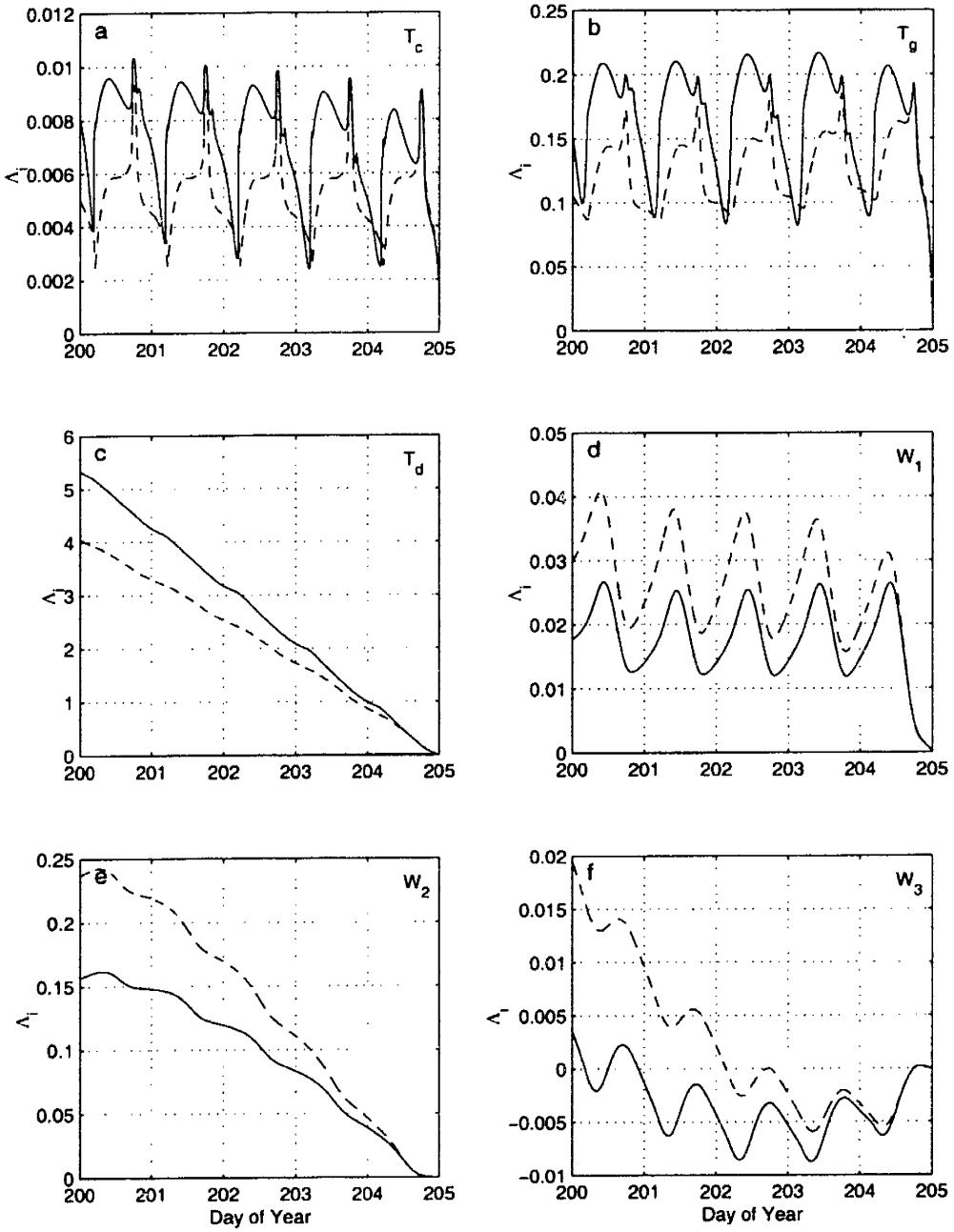

Figure 3-5: Coupled and uncoupled surface state sensitivities (given by nondimensional adjoint variables) for average latent flux (over 5 days). The solid lines correspond to the coupled model sensitivities and the dashed lines correspond to the uncoupled model sensitivities.

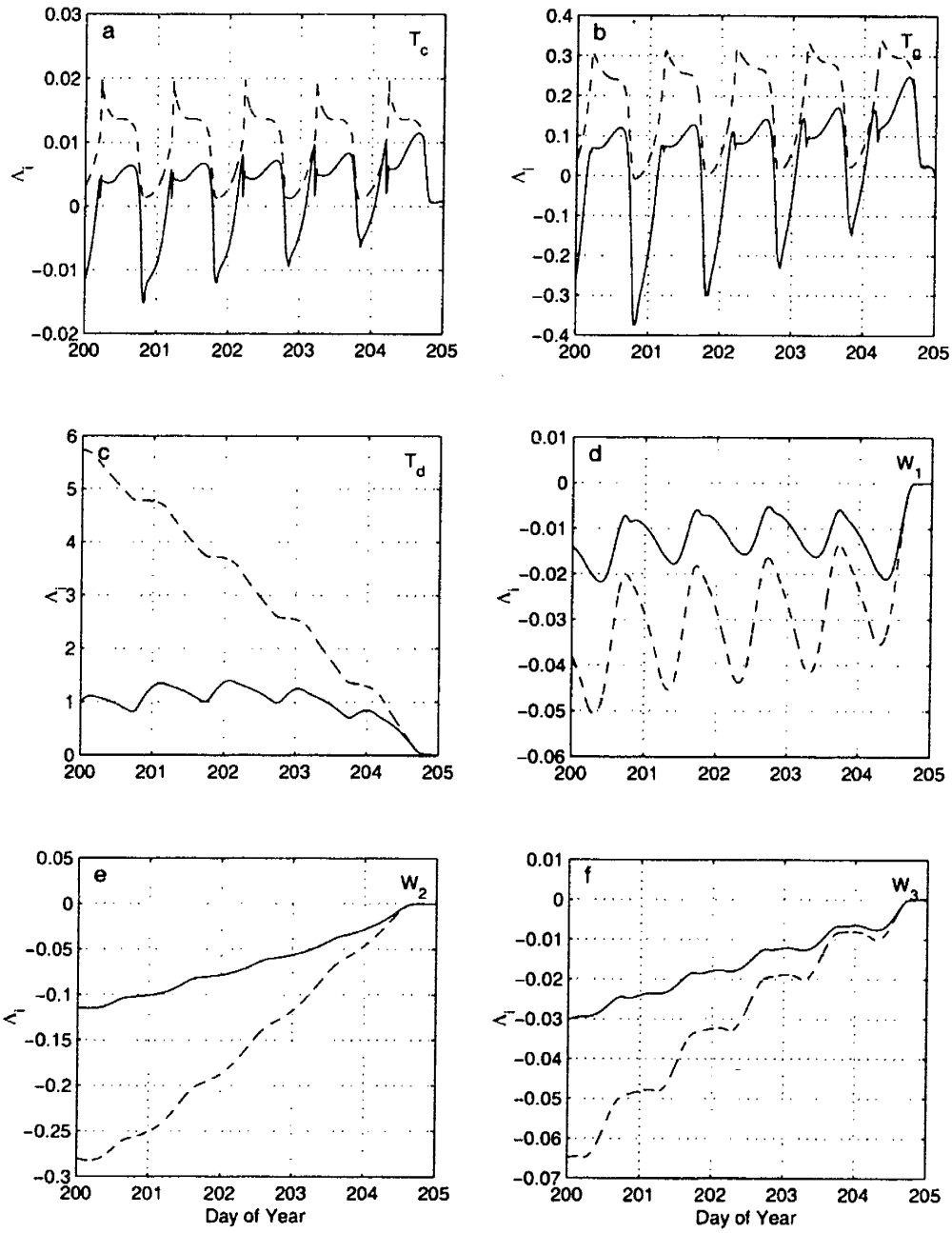

Figure 3-6: Coupled and uncoupled surface state sensitivities (given by nondimensional adjoint variables) for average sensible heat flux (over 5 days). The solid lines correspond to the coupled model sensitivities and the dashed lines correspond to the uncoupled model sensitivities.

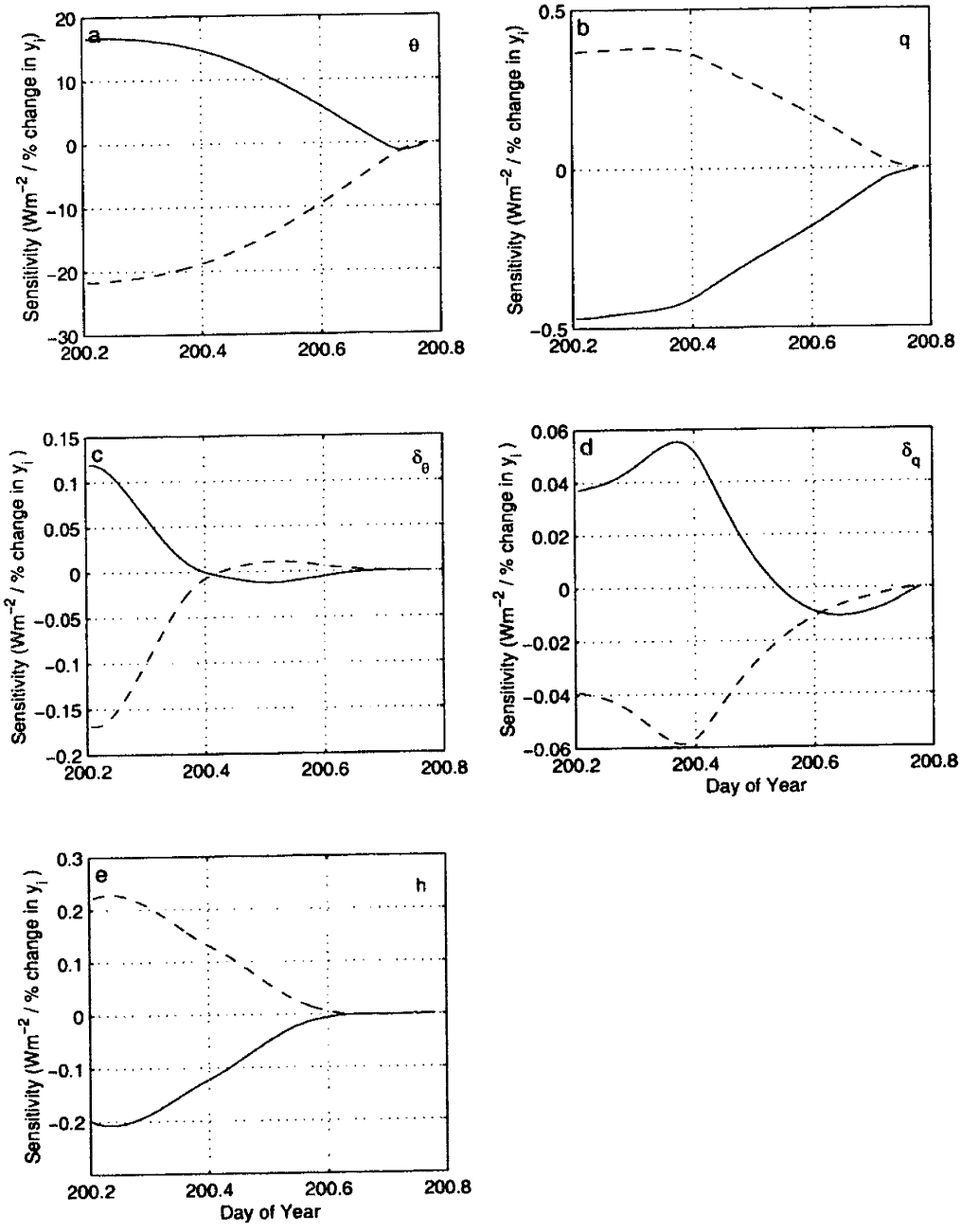

Figure 3-7: Boundary layer state sensitivities (which are only present in the coupled model) for average daytime surface turbulent fluxes. The solid lines correspond to the sensitivity of the average latent heat flux ($\overline{L_v E}$) and the dashed lines correspond to the sensitivity of the average sensible heat flux ($\overline{H}$).

in time, any differences in the surface adjoint states are initiated by these ABL pathways, since the terminal conditions of both the uncoupled and coupled surface adjoint states are equal to zero, and the forcing term $(\frac{\partial \phi}{\partial \mathbf{y}_s})$ is identical between the two models. However once these changes are initiated, further differences between the uncoupled and coupled adjoint states may arise through the $-\left(\frac{\partial \mathbf{F}_s}{\partial \mathbf{y}_s}\right)^T \boldsymbol{\lambda}_s^p$ $(p = u, c)$ terms based on the differences between $\boldsymbol{\lambda}_s^u$ and $\boldsymbol{\lambda}_s^c$. Thus in addition to the ABL pathways, the surface state pathways which exist in both models may allow additional strengthening or weakening of model sensitivities in the coupled case due to feedbacks. Focusing solely on the differences in state sensitivities, we can define a new variable $\boldsymbol{\Delta}_s = \left(\frac{\partial J}{\partial \mathbf{y}_s}\right)_c^T - \left(\frac{\partial J}{\partial \mathbf{y}_s}\right)_u^T = \boldsymbol{\lambda}_s^u - \boldsymbol{\lambda}_s^c$ to denote the difference between the uncoupled and coupled surface state sensitivities. (A similar variable could be defined for the ABL adjoint variables, but since the uncoupled ABL adjoint variables are identically zero, the variable would be equivalent to the coupled ABL adjoint states themselves.) Taking the difference of Equations (3.5) and (3.6) and integrating, the difference variable can be expressed as:

$$\boldsymbol{\Delta}_s(t) = \int_t^{t_f} \left[\left(\frac{\partial \mathbf{F}_s}{\partial \mathbf{y}_s}\right)^T \boldsymbol{\Delta}_s - \left(\frac{\partial \mathbf{F}_a}{\partial \mathbf{y}_s}\right)^T \boldsymbol{\lambda}_a^c \right] dt \tag{3.11}$$

where the common forcing term in the adjoint models drops out, and we see that the difference is governed by the ABL pathway terms and a term which represents the additional influence through the surface state pathways. To further examine how the differences arise, and in particular diagnose what pathways are most important in doing so, we can decompose the above equation term-by-term. To illustrate this, we can expand the equation for a particular element of the $\boldsymbol{\Delta}_s$ vector. For example, the equation for the difference in sensitivity to canopy temperature can be written out as:

$$\Delta_{T_c}(t) = \int_t^{t_f} \left[\frac{\partial F_{T_c}}{\partial T_c}\Delta_{T_c} + \frac{\partial F_{T_g}}{\partial T_c}\Delta_{T_g} + \frac{\partial F_{T_d}}{\partial T_c}\Delta_{T_d} + \frac{\partial F_{W_1}}{\partial T_c}\Delta_{W_1} + \frac{\partial F_{W_2}}{\partial T_c}\Delta_{W_2} + \frac{\partial F_{W_3}}{\partial T_c}\Delta_{W_3} + \right.$$

$$\left. - \frac{\partial F_\theta}{\partial T_c}\lambda_\theta^c - \frac{\partial F_q}{\partial T_c}\lambda_q^c - \frac{\partial F_{\delta_\theta}}{\partial T_c}\lambda_{\delta_\theta}^c - \frac{\partial F_{\delta_q}}{\partial T_c}\lambda_{\delta_q}^c - \frac{\partial F_h}{\partial T_c}\lambda_h^c \right] dt \tag{3.12}$$

where the first six terms represent the change in influence of each the surface state pathways and the last five terms represent the influence of the ABL pathways which exist only in the coupled model. Written out in this way it is easier to visualize how the net difference is just the sum of the differences caused via each state pathway, where each term accordingly has units of sensitivity. It should be noted that some of these terms are identically zero because certain pathways do not exist. For example in the forward model, W_3 is not directly affected by T_c, so $\frac{\partial F_{W_3}}{\partial T_c} \equiv 0$, meaning that there is no deep soil moisture pathway through which δT_c can propagate. By computing each term in the above equation, we can obtain a measure of which pathways are significant in changing the model surface state sensitivities. Further, the results will show whether each pathway has an amplifying or dampening effect.

To examine how the differences in state sensitivity are manifested over the entire model integration, Equation (3.11) is computed for $t = t_0$. This corresponds to the differences in model response (between uncoupled and coupled cases) to perturbations in the surface

state initial conditions. The decomposition of sensitivity differences by sensitivity pathways are presented in Tables 3.1 and 3.2. The results are expressed as changes in $\overline{L_v E}$ and $\overline{H}$ (Wm^{-2}) per percent change in the given surface state variable. Table 3.1 includes those results corresponding to differences in temperature sensitivities (Δ_{T_c}, Δ_{T_g}, and Δ_{T_d}) and Table 3.2 includes those for soil moisture sensitivity differences (Δ_{W_1}, Δ_{W_2}, and Δ_{W_3}). (For consistency, note that the sum of all contributions match the differences in sensitivity to initial conditions shown in Figures 3-3 and 3-4.) These results provide insight into how important individual pathways are in contributing to the sensitivity differences, and in what sense they modify the sensitivities (either amplify or dampen). If the sign of the pathway contribution is in the same sense as that of the corresponding net sensitivity, the pathway in the coupled model serves to amplify the uncoupled sensitivity, while if it is of opposite sign, the pathway dampens the sensitivity. It is most straightforward to first examine the results for ABL pathways. Since they do not exist in the uncoupled model, the results are the direct effect of "switching on" these pathways. In comparison, surface state pathways exist in both models, so the results represent the difference in surface sensitivity pathways caused by ABL feedbacks onto the surface states.

First, we summarize the sensitivity pathway results for T_c, T_g, and T_d shown in Table 3.1. For canopy temperature sensitivity differences (Δ_{T_c}), the largest effect on $\overline{H}$ is via the potential temperature (θ) pathway. For a 1% increase in T_c the θ pathway causes a -51 Wm^{-2} change in average surface sensible heat flux. Based on the surface energy balance constraint discussed above, this in turn causes a significant increase in average latent heat flux (+39 Wm^{-2}). This is a direct result of the presence of the ABL energy budget equation. A perturbation in canopy temperature warms the boundary layer, which causes a negative feedback: reducing the gradient in temperature between the surface and atmosphere, thus reducing the sensible heat flux. This significant effect, which is also seen in the ground temperature sensitivity difference (Δ_{T_g}), is absent in an uncoupled model and illustrates how sensitivity results obtained using uncoupled models can be erroneous. The evolution of the boundary layer depth, and the associated temperature and humidity inversions, also play an important role in the temperature sensitivities as evidenced by the magnitude of the h, δ_θ, and δ_q sensitivity pathways in Table 3.1. This has an important impact on the specific humidity (q) pathway, where there is a positive feedback of a canopy temperature perturbation onto $\overline{L_v E}$. A perturbation in T_c has two opposing effects on the ABL humidity budget; one is to increase q due to an increase in transpiration, and the other is to increase ABL growth which increases the entrainment of dry air into the boundary layer, thus reducing q. The specific humidity is important with respect to the daily average evaporation, as it effects the gradient in humidity between the surface and ABL. The fact that there is a net positive feedback indicates that, as a result of δT_c, the additional entrainment of dry air from the free atmosphere outweighs the additional moistening of the boundary layer from the surface, causing an increase in the gradient in humidity and thus an increase in $\overline{L_v E}$. As a result of the increase in sensitivity of $\overline{L_v E}$, there is a corresponding decrease in sensitivity to $\overline{H}$ via the q pathway. In isolation, the additional ABL pathways would cause a net change of +25 and -31 Wm^{-2} in $\overline{L_v E}$ and $\overline{H}$ respectively for a 1% change in T_c. However, the addition of the ABL pathways also cause amplifying/dampening effects on the existing surface sensitivity pathways via feedbacks on the surface states. For example, to a large extent the difference caused by the ABL pathways is counter-balanced by changes in the canopy and ground temperature pathways. For example, there are many partial feedbacks which serve to increase T_c and ultimately increase $\overline{H}$. These feedbacks include radiative feedbacks, whereby increases in θ and q cause the downward longwave radiation

to increase, which further warms the canopy, increasing canopy sensible heat flux. There is also a corresponding increase in the canopy air temperature which reduces the sensible heat flux via the ground temperature pathway. An important point illustrated by these results is that while the net sensitivity of average daytime surface turbulent fluxes to a perturbation in canopy temperature is small compared to the other temperature states (see Figures 3-3a-c and 3-4a-c), canopy temperature should not be viewed as unimportant. It is in fact a key state variable due to its direct interactions with the ABL as evidenced by the relatively large magnitude of ABL pathway sensitivities. Its importance as a conduit for sensitivity information between the surface and ABL is borne out by the relative magnitudes of the pathway sensitivities for perturbations in T_c compared to those for T_g and T_d in Table 3.1. (It is reasonable to expect that for other scenarios, e.g. surfaces with sparse vegetation, the sensitivity pathways for ground temperature perturbations would become more important.)

For ground temperature sensitivity differences (Δ_{T_g}), the ABL pathway sensitivities, are indeed of the same sense as those for canopy temperature, but of smaller magnitude. Therefore the ABL pathway mechanisms discussed above for canopy temperature have a similar, but less important effect for ground temperature sensitivities. As with the canopy temperature sensitivity differences, it is the canopy and ground temperature surface state pathways, which are the most significant. The sense of the changes are opposite however to those for canopy temperature perturbations discussed above. A perturbation in T_g causes an increase in the T_g pathway sensitivity. For the T_g pathway, the additional radiative feedbacks serve to increase T_g in the coupled model causing an increase in $\overline{H}$ (+10 Wm^{-2}) over the uncoupled model. The perturbation in T_g causes a negative feedback in $\overline{H}$ (-7 Wm^{-2}) via the canopy temperature pathway, since the air temperature is increased more in the coupled model via changes in θ. Finally, for deep ground temperature sensitivity differences (Δ_{T_d}), only the ground temperature pathway exists. Thus there are no compensating sensitivity differences via other states as there are for T_c and T_g. Note that the magnitude of the change in sensitivity via this pathway is relatively small compared to the important pathways mentioned above for T_c and T_g sensitivities.

For soil moisture perturbations (Table 3.2), the strength of pathway sensitivities are generally smaller than those for the temperature states. At the daytime scale, the largest pathway strengths are those corresponding to the differences in sensitivity to surface soil moisture (Δ_{W_1}). The most influential ABL pathway is that for specific humidity (q), which causes a negative feedback on $\overline{L_v E}$. This is a direct result of the moistening of the ABL in the coupled model by surface evaporation, which decreases the gradient in humidity between the surface and atmosphere, limiting further evaporation. Recall that for temperature perturbations, in addition to an increase in surface evaporation, there was an increase in ABL growth and thus dry-air entrainment, which served to counteract and even outweigh the direct moistening effect (causing a positive feedback). For soil moisture perturbations however there is no corresponding increase in boundary layer growth (and entrainment), and thus the net increase in q causes a negative feedback. The only other significant ABL pathway for surface soil moisture perturbations is via the specific humidity inversion (δ_q). The increase in q as a result of δW_1 causes an increase in δ_q which then enhances the entrainment of dry air into the ABL. This mechanism dries the ABL which acts as a positive feedback on $\overline{L_v E}$. However this effect is smaller than the humidity gradient effect mentioned above. As for the surface state pathways, the most significant effects are via the T_g, W_1, and T_c pathways. The T_g pathway produces a decrease in average daily evaporation (increase in sensible heat flux). This is due to the additional effect of an increase in q (due to an increase in W_1), which ultimately increases the net radiation at the surface. The increase

Table 3.1: Decomposition of uncoupled/coupled sensitivity differences of average turbulent fluxes to temperature states via each state pathway. (Values given as Wm^{-2} per percent change in state y_i).

Pathway	Temperature Sensitivities					
	Δ_{T_c}		Δ_{T_g}		Δ_{T_d}	
	$\overline{L_v E}$	$\overline{H}$	$\overline{L_v E}$	$\overline{H}$	$\overline{L_v E}$	$\overline{H}$
T_c	-28.24	34.36	6.12	-7.45	–	–
T_g	2.83	-3.56	-8.15	10.33	1.57	-1.99
T_d	0.04	-0.05	-0.09	0.12	–	–
W_1	0.00	-0.00	0.15	-0.17	–	–
W_2	0.01	-0.01	-0.00	0.00	–	–
W_3	–	–	–	–	–	–
θ	39.07	-51.49	5.81	-7.66	–	–
q	4.45	-4.04	-1.01	0.81	–	–
δ_θ	-8.48	14.40	-1.21	2.09	–	–
δ_q	1.01	-1.27	0.82	-0.94	–	–
h	-10.65	11.61	-1.45	1.57	–	–
Sum	0.04	-0.06	0.99	-1.29	1.57	-1.99
Sign of $\frac{\partial J}{\partial y_i}$	(+)	(+)	(+)	(+)	(+)	(+)
amplified/dampened (+/−)	(+)	(−)	(+)	(−)	(+)	(−)

Table 3.2: Decomposition of uncoupled/coupled sensitivity differences of average turbulent fluxes to soil moisture states via each state pathway. (Values given as Wm^{-2} per percent change in state y_i; multiplied by $\times 10^2$).

Pathway	Soil Moisture Sensitivities					
	ΔW_1		ΔW_2		ΔW_3	
	$\overline{L_v E}$	$\overline{H}$	$\overline{L_v E}$	$\overline{H}$	$\overline{L_v E}$	$\overline{H}$
T_c	3.26	-4.08	-0.09	0.12	–	–
T_g	-12.24	15.77	0.00	-0.01	-0.84	1.14
T_d	-0.11	0.16	0.00	-0.00	-0.03	0.04
W_1	6.86	-7.35	-4.08	4.42	–	–
W_2	-0.12	0.13	0.19	-0.21	-0.07	0.07
W_3	–	–	-0.08	0.12	0.07	-0.09
θ	0.44	-0.59	0.00	-0.00	–	–
q	-8.66	7.56	-0.04	0.03	–	–
δ_θ	-0.28	0.24	-0.00	0.00	–	–
δ_q	2.90	-3.68	0.01	-0.01	–	–
h	-0.84	0.91	-0.00	0.00	–	–
Sum	-8.78	9.07	-4.09	4.45	-0.87	1.16
Sign of $\frac{\partial J}{\partial y_i}$	(+)	(−)	(+)	(−)	(−)	(−)
amplified/dampened (+/−)	(−)	(−)	(−)	(−)	(+)	(−)

in net radiation causes a warming of the ground, which in combination with the suppression of evaporation (due to the decreased moisture gradient) increases $\overline{H}$. It is this effect, via the ground temperature, in combination with the specific humidity effect discussed above, which controls the net dampening effect on the sensitivity of $\overline{L_vE}$ to soil moisture.

Finally, note that there is an important difference in the tradeoff in sensitivity for the surface soil moisture compared to the temperature sensitivities discussed above. Recall that the surface energy balance constraint requires that the *difference* in sensitivities oppose each other. Thus when the $\overline{L_vE}$ and $\overline{H}$ sensitivities are of the same sign (as for temperature sensitivities; both positive) one sensitivity in the coupled model will be amplified and the other will be dampened. However if the sign in flux sensitivities are opposite, the coupled model sensitivities will either both be amplified or both dampened. For example, for soil moisture, the $\overline{L_vE}$ sensitivities are positive, while the $\overline{H}$ sensitivities are negative. Thus for Δ_{W_1} the negative change in sensitivity for $\overline{L_vE}$ causes a dampening effect (positive sensitivity + negative change), but the corresponding positive change in sensitivity for $\overline{H}$ also acts to dampen the sensitivity in the coupled model (negative sensitivity + positive change). This dampening of both turbulent flux sensitivities is seen in the W_2 sensitivity difference as well. Thus depending on the variable, the sensitivities of $\overline{L_vE}$ and $\overline{H}$ in the coupled model can both be amplified, both be dampened, or be of the opposite sense.

Differences in Parameter Sensitivity Pathways and Their Time-varying Influence

Recall that the parameter sensitivities for the uncoupled and coupled models are given by Equations (3.8) and (3.9) respectively. Thus the differences in state sensitivities described above are directly responsible for the differences in parameter sensitivities shown in Figures 3-1 and 3-2. To investigate the differences in sensitivity between the two models we can define a new variable similar to the one for differences in state sensitivities above:

$$\boldsymbol{\Delta}_\alpha = \left(\frac{\partial J}{\partial \boldsymbol{\alpha}}\right)_c^T - \left(\frac{\partial J}{\partial \boldsymbol{\alpha}}\right)_u^T = \int_{t_0}^{t_f} \left[\left(\frac{\partial \mathbf{F}_s}{\partial \boldsymbol{\alpha}}\right)^T \boldsymbol{\Delta}_s - \left(\frac{\partial \mathbf{F}_a^T}{\partial \boldsymbol{\alpha}}\right)^T \boldsymbol{\lambda}_a^c\right] dt \qquad (3.13)$$

which represents the difference in sensitivity of a given model response J (either $\overline{L_vE}$ or $\overline{H}$) to the model parameters. Since the model parameters ($\boldsymbol{\alpha}$) are time-invariant, $\boldsymbol{\Delta}_\alpha$ is a vector of single-valued numbers, which represents the integrated difference between the coupled and uncoupled sensitivities for each parameter. Equation (3.13) shows that, once the adjoint variables (state sensitivities) are known, the difference in parameter sensitivities is simply a diagnostic function which takes into account how the parameter influences the states, which then in turn have a different effect on the turbulent fluxes in the uncoupled and coupled models. While Equation (3.13) gives the net effect of a change in a given parameter, the sensitivity pathways via each state variable as well as the time-varying difference caused by each pathway is contained in the integrand of the above equation, which represents the difference in contribution of a particular parameter to the average surface turbulent fluxes (per unit time). For each parameter, the above equation can be decomposed term-by-term (as done for T_c in Equation 3.12) to diagnose the important pathways which cause the differences in sensitivity. For brevity, we only show detailed results for three of the parameters discussed above: the aerodynamic roughness length (z_0), minimum stomatal resistance ($r_{c_{min}}$), and leaf area index (LAI). The results (expressed as Wm^{-2} per percent change in α_k) are presented in Table 3.3. Just as with the state sensitivities, these results

not only give insight into the relative strength of each pathway in changing the sensitivities, but whether the coupled sensitivity is amplified or dampened via the particular pathway. Note that the net sense of change (given in the last row of Table 3.3) matches those given in Figures 3-1b and 3-2b.

For z_0, Table 3.3 indicates that the most important integrated sensitivity pathways are via the evolution of canopy and ground temperatures, and the ABL specific humidity. For the ground temperature pathway, z_0 influences T_g via the ground sensible and latent heat fluxes. A perturbation in z_0 causes both to decrease, thus increasing T_g, which causes an increase in $\overline{L_v E}$ sensitivity and a decrease in $\overline{H}$ sensitivity in the coupled model. For the canopy temperature pathway, roughness length can only influence T_c via the canopy sensible and latent heat fluxes. However for perturbations in z_0, the canopy sensible heat flux sensitivity dominates. So for an increase in z_0, the canopy sensible heat flux increases most significantly, which cools the canopy. The corresponding decrease in canopy temperature causes a larger decrease (increase) in $\overline{L_v E}$ ($\overline{H}$) in the coupled case. The next largest sensitivity pathway is that for the ABL specific humidity. The roughness length influences q via the surface latent heat fluxes and the entrainment flux at the top of the ABL. For a perturbation in z_0 the change in ground evaporation and entrainment oppose each other, while the change in canopy latent heat flux is relatively small. Throughout the day, the change in ground latent heat flux is slightly larger and controls the overall response, so that an increase in z_0 causes a decrease in ground evaporation, which then decreases q. This decrease in q (which only occurs in the coupled model) causes a positive feedback which increases $\overline{L_v E}$ in the coupled model.

While the information given for z_0 in Table 3.3 yields insight into the integrated differences via each state variable, further insight is obtained by looking at the temporal evolution of the differences in parameter sensitivities. Each parameter has a time-varying influence over the course of the day. In some cases, parameters or their corresponding state pathways may have competing influences (of opposite signs) at different times during the day such that the integrated effect appears small. This is the case for the roughness length sensitivity difference. The net temporal influence, as well as the temporal influence via the most important state pathways for $\overline{L_v E}$ are plotted in Figure 3-8 (expressed as percent differences in sensitivity per hour). For brevity the temporal results are only shown for $\overline{L_v E}$ and not $\overline{H}$. Figure 3-8a shows that the net sensitivity difference for z_0 varies significantly during the day such that in the morning hours there is a negative difference between coupled and uncoupled sensitivities, while in the afternoon there is a positive difference. Thus in the morning the coupled sensitivity is greater than the uncoupled sensitivity, with the reverse true in the afternoon. In integrating over the entire day, the opposing differences roughly cancel out yielding only a small overall difference.

In Figure 3-8a note that in addition to the state pathways discussed above, the ABL potential temperature pathway actually has the largest (most negative) influence in the early morning and one of the largest in the afternoon. In fact, the θ pathway contributes significantly to the net difference temporal pattern shown in Figure 3-8a. For a perturbation in z_0, this behavior results from an increase in warming of the boundary layer in the early morning (due to increased ground sensible heat flux and entrainment sensible heat flux), which serves to increase θ, thus increasing $\overline{L_v E}$. In the mid-morning however the sensitivity of ground sensible heat flux to z_0 switches sign, causing a cooling of the ABL, which has the opposite effect. It is only because of the strongly opposing effects that the integral over the day is small. This clearly illustrates the important insight that is obtained by looking at the temporal contributions of sensitivity differences. For the other pathways discussed

Table 3.3: Decomposition of uncoupled/coupled sensitivity differences of average turbulent fluxes to roughness length (z_0), minimum canopy resistance ($r_{c_{min}}$), and leaf area index (LAI) via each state pathway. (Values given as Wm^{-2} per percent change in parameter α_k; multiplied by $\times 10^2$).

Pathway	Δ_{z_0}		$\Delta_{r_{c_{min}}}$		Δ_{LAI}	
	$\overline{L_vE}$	$\overline{H}$	$\overline{L_vE}$	$\overline{H}$	$\overline{L_vE}$	$\overline{H}$
T_c	-1.15	1.49	11.62	-14.31	4.10	-4.88
T_g	1.77	-2.35	-0.53	0.68	-7.41	9.46
T_d	0.02	-0.02	-0.01	0.01	-0.08	0.11
W_1	-0.06	0.06	0.00	-0.00	-0.00	0.00
W_2	0.00	-0.00	-0.01	0.01	0.01	-0.01
W_3	–	–	–	–	–	–
θ	0.10	-0.06	-0.30	0.41	0.20	-0.27
q	0.95	-0.79	6.00	-5.24	-4.02	3.55
δ_θ	-0.27	0.35	0.17	-0.14	-0.16	0.13
δ_q	-0.44	0.52	-2.14	2.63	1.34	-1.71
h	-0.61	0.67	0.58	-0.63	-0.43	0.47
Sum	0.30	-0.13	15.39	-16.58	-6.45	6.86
Sign of $\frac{\partial J}{\partial \alpha_k}$	(−)	(−)	(−)	(+)	(+)	(−)
amplified/dampened (+/−)	(−)	(+)	(−)	(−)	(−)	(−)

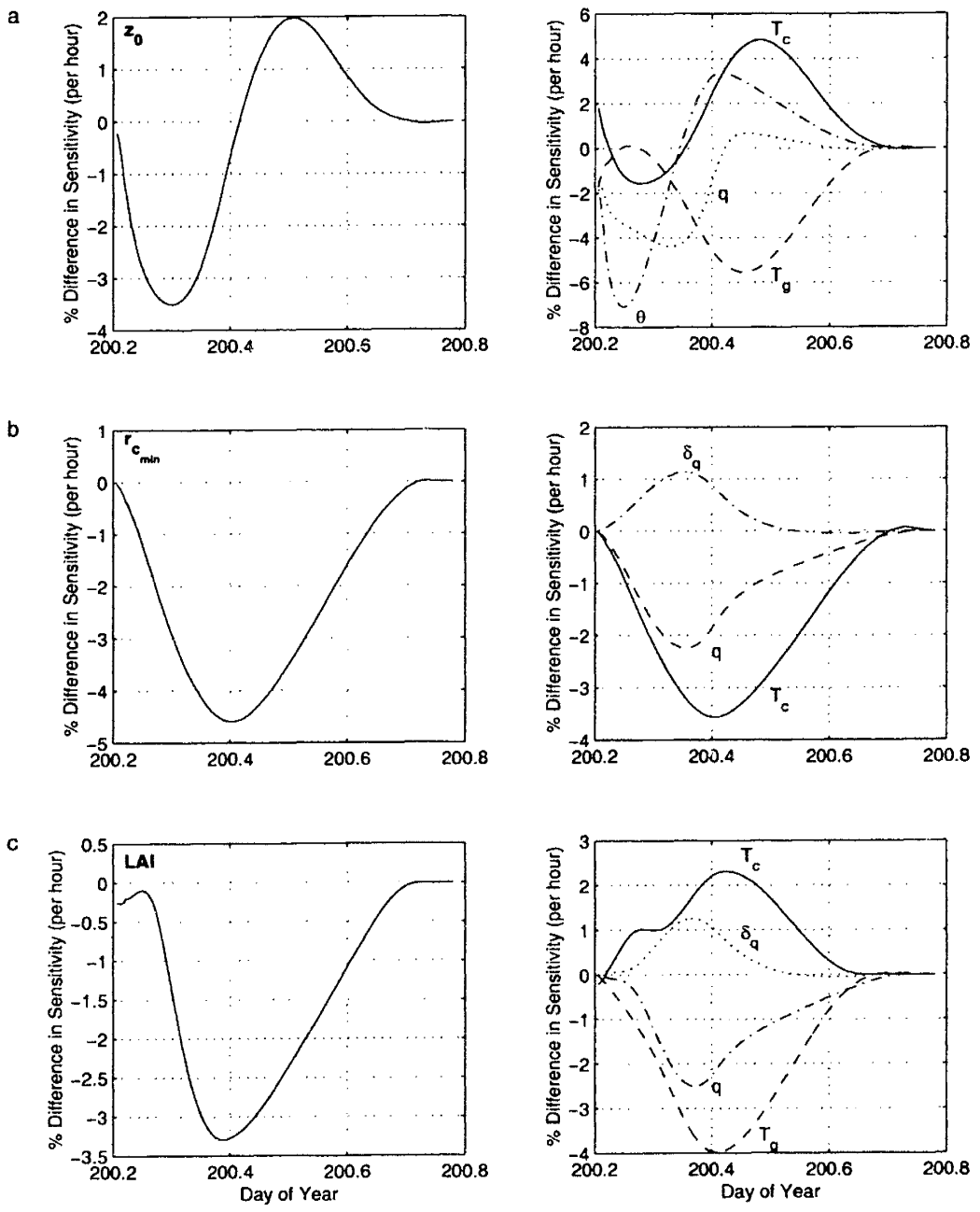

Figure 3-8: Temporal difference in sensitivity of average daytime latent heat flux ($\overline{L_v E}$) to: a)aerodynamic roughness length (z_0); b) minimum canopy resistance ($r_{c_{min}}$); and c) leaf area index (LAI). The first column of panels shows the net difference as a function of time throughout the day for each parameter, while the second column shows the contribution to the net difference via the most important sensitivity pathways.

above, the canopy and ground temperature pathways have a peak influence near midday, while the sensitivity difference via the q pathway is almost exclusively in the morning hours.

For minimum canopy resistance, Table 3.3 indicates that the most important sensitivity pathways over the model integration are through the evolution of T_c, q, and δ_q. For the canopy temperature pathway, the only sensitivity mechanism is via the canopy transpiration, which has a negative sensitivity to $r_{c_{min}}$ throughout the day. Thus a positive perturbation in $r_{c_{min}}$ decreases canopy transpiration, which increases the canopy temperature. As we saw with the state sensitivities, a perturbation in T_c actually causes an increase in $\overline{L_vE}$ in the coupled model over the uncoupled one. As a result, the sensitivity of $\overline{L_vE}$ to $r_{c_{min}}$ (which is negative) is reduced in magnitude via the canopy temperature pathway in the coupled model. For the specific humidity pathway, $r_{c_{min}}$ can affect q via both the canopy and ground evaporation fluxes, and the entrainment flux, however the sensitivity via the canopy transpiration dominates in influence. An increase in minimum canopy resistance decreases canopy transpiration, which reduces q (in the coupled model only). As a result, the increased gradient in moisture causes an increase in $\overline{L_vE}$ in the coupled model. This reduces the negative sensitivity of $\overline{L_vE}$ to $r_{c_{min}}$ in the coupled model just as the T_c pathway did. The effect via the δ_q pathway is opposite to that of q. This is due to the fact that a decrease in q (via the same mechanism described above) causes a decrease in δ_q, which reduces the dry air entrainment. This makes the ABL more moist in a relative sense, thus decreasing $\overline{L_vE}$ (amplifying the negative sensitivity). Overall, however it is the influence via the T_c and q pathways which control the net reduction in sensitivity that is seen Figure 3-1. In the same way that was done for roughness length, the temporal contributions of the differences in sensitivity of $\overline{L_vE}$ to $r_{c_{min}}$ is shown in Figure 3-8b. In contrast to the results for z_0, the difference in sensitivity to $r_{c_{min}}$ is negative throughout the day, with a clear peak in the mid-morning. As discussed above it is the control via the T_c and q pathways throughout the day which control the net difference.

Finally, for leaf area index, Table 3.3 shows the most important sensitivity pathways to be canopy and ground temperatures, and the ABL specific humidity and humidity inversion. For the T_g pathway, the dominating sensitivity mechanism for LAI is the effect on net radiation absorbed by the ground. The sensitivity of the ground net radiation to a positive perturbation in LAI is negative throughout the day, since an increase in leaf area allows less radiation to be transmitted to the ground. Thus a positive perturbation decreases the net radiation forcing of the ground, which decreases ground temperature. In the previous section it was shown that the difference in ground temperature sensitivity between the coupled and uncoupled models for $\overline{L_vE}$ was positive. Therefore the negative perturbation in T_g as a result of a perturbation in LAI serves to decrease $\overline{L_vE}$ in the coupled model. The canopy temperature evolution is effected by LAI through net radiation and canopy latent heat flux mechanisms. For a perturbation in LAI, both are increased throughout the day. However, the radiative effect is actually larger than the increase in latent heat flux, so there is a net warming of the canopy. As a result of the positive perturbation in T_c and the differences in canopy temperature sensitivity, there is an increase in $\overline{L_vE}$ in the coupled model. The specific humidity pathway is dominated by the increase in canopy transpiration, which causes an increase in q. This reduces the moisture gradient between the canopy and ABL, thus reducing $\overline{L_vE}$. The δ_q effect is again directly related to the q pathway as explained above for $r_{c_{min}}$. The temporal contributions to the sensitivity differences of $\overline{L_vE}$ to LAI are shown in Figure 3-8c. The net difference in sensitivity as a function of time is similar in form to that of $r_{c_{min}}$, in that it is negative throughout the day, with a single peak in the mid-morning. Unlike, $r_{c_{min}}$ however, which exclusively changed the $\overline{L_vE}$ sensitivity via

its effect on canopy transpiration, LAI has a radiative sensitivity pathway as well. This is seen in the importance of the T_g pathway which causes a significant negative difference in sensitivity, that is not seen in Figure 3-8b. There is also the positive contribution via T_c, that would otherwise be negative if not for the radiative effect. Overall, the surface turbulent fluxes, show significant differences in sensitivity (with a strong diurnal cycle) to all three parameters.

3.5 Summary

In this study the differences in daytime sensitivity of surface turbulent fluxes to states and parameters for a coupled land surface-atmospheric boundary layer (ABL) model in coupled and uncoupled modes were investigated using an adjoint framework. Previous studies have shown that erroneous sensitivity results may be obtained when forcing an uncoupled land surface model by specified atmospheric forcing. The adjoint framework used here not only allows for the efficient comparison of sensitivities, but allows for the diagnosis of how and why the differences arise between the coupled and uncoupled cases.

The coupled model used here consists of a detailed land surface parameterization coupled to a mixed-layer ABL model and captures the primary land-atmosphere interactions that occur on the diurnal scale (e.g. two-way coupling of surface fluxes, ABL growth, entrainment, etc.). The uncoupled model was treated as a special case of the coupled model where the atmospheric feedback pathways are "closed" and the land surface is forced by the ABL states. Based on the forward models, uncoupled and coupled adjoint models were developed, which "collect" sensitivity information backward in time over the model integration. Just as with the forward models, it is seen that the uncoupled adjoint model is a special case of the coupled adjoint, where the ABL sensitivity pathways are closed. It is because of these closed pathways that differences in sensitivity arise. Further, because the adjoint models are only functions of the nominal forward model trajectory, no explicit "uncoupled model" is needed in this study. Instead, the trajectory obtained from the coupled model was used in both adjoint models. Thus the coupled and uncoupled sensitivities were evaluated with respect to identical nominal trajectories, making the differences in response due solely to the additional feedbacks in the coupled model.

The adjoint variables obtained from each model represent the sensitivities of the average surface turbulent fluxes to each state variable throughout the model integration. By neglecting the ABL pathways, significant differences in the state sensitivities arise between models. The differences in land surface state sensitivities were decomposed and examined to determine through which pathways the differences in sensitivity arise. For the surface temperature state (canopy and ground) sensitivities it was found that the additional ABL potential temperature pathway was most important. Specifically, the interactive boundary layer is warmed by surface temperature perturbations, such that the average sensible heat flux is decreased, which corresponds to a dampening in the sensible heat flux sensitivity to canopy temperature and ground temperature in the coupled model. Based on the surface energy balance constraint, this decrease in sensible heat flux sensitivity causes an increase in average latent heat flux sensitivity to canopy and ground temperatures. While potential temperature was most important, the other ABL state pathways also played a significant role in the modification of sensitivities to surface temperatures. In addition, the "opening" of these ABL pathways caused some compensating changes in the surface state pathways themselves (most notably the canopy and ground temperatures) due to partial feedbacks

onto the surface states. However, the net effect was a decrease in the average sensible heat flux sensitivities and an increase in the average latent heat flux sensitivities to surface temperature states. Results also showed that while the magnitude of the sensitivity of average surface turbulent fluxes to canopy temperature is relatively small, its role as a conduit for sensitivity (sensitivity pathways) is quite significant due to its direct interaction with the overlying ABL. For the surface soil moisture states, the latent and sensible heat flux sensitivities were reduced in the coupled model. It was found that the ABL specific humidity was the most significant ABL pathway in terms of modifying the average latent heat flux. Soil moisture perturbations increase the ABL humidity which reduces the gradient in humidity between the surface and ABL, thus reducing the average latent heat flux. This negative change in latent heat flux sensitivity is accompanied by a positive change in the average sensible heat flux sensitivity. However since the sign of average sensible heat flux sensitivity to soil moisture is negative, this change corresponds to a dampening of the sensible heat flux sensitivity as well.

The differences in state sensitivities directly determine the differences in sensitivities of the average surface turbulent fluxes to each model parameter. While the integrated differences were given for many parameters, a more detailed evaluation of the differences for roughness length, minimum canopy resistance, and leaf area index were performed. For aerodynamic roughness length, the difference in sensitivity was relatively small and negative. However this was due partly to competing influences as a function of time-of-day. The sensitivity difference was negative in the morning, but positive in the afternoon. The differences via each pathway were characterized by some variables which had opposing effects during the day (ABL potential temperature), which in an integrated sense were small, and those that mostly contributed in a given direction (specific humidity, canopy and ground temperature), thus having a large integrated effect. For minimum canopy resistance, the influence is almost exclusively through canopy transpiration so that the most important pathways are canopy temperature and specific humidity in the ABL. The difference in sensitivity had a strong diurnal cycle, with a single distinct peak at mid-morning. The differences in sensitivity to leaf area index were similar in form to those for canopy resistance (due to its influence on canopy transpiration) however it also influences the net radiation of the canopy and ground which caused differences via those pathways.

The results from this study clearly show the importance of using a coupled model when trying to determine sensitivities of land-atmosphere interactions to surface state variables and parameters. As other have shown, these results confirm that using an uncoupled model can lead to erroneous results and therefore should be avoided except in those limited cases (i.e. short time scales) where coupling is not as important. However we go beyond this general finding in using the adjoint framework to diagnose what factors are most important in causing these differences during the course of a day. As the results presented here are confined to diurnal interactions between the land surface and atmosphere, they are not given as a final assessment of the most important factors in land-atmosphere interaction. In fact, as has been seen in previous studies, it is nearly impossible to reach a clear consensus as to the most important parameters since model sensitivities are so inherently tied to the particular trajectory being examined (e.g. desert vs. grassland vs. forest surface conditions; diurnal vs. seasonal vs. annual time scale, etc.). Moreover, our goal should not just be a ranking of parameters, but a deeper understanding of the underlying physical mechanisms that control the response of the system. So beyond the specific results presented here, we feel it is the presentation of the adjoint framework, and its potential extension to other models and scenarios, which may offer a useful tool to help better understand land-atmosphere

interactions at various spatial and temporal scales.

Chapter 4

Estimation of Land and ABL States and Fluxes Through Assimilation of Surface Temperature and Screen-Level Micrometeorology

4.1 Background

Diagnosing the surface water and energy budgets are important pursuits in many fields (e.g. hydrologic, atmospheric, and ecological science applications). Whether the goal is to use antecedent soil moisture to predict possible flooding, improve land surface forcing of numerical weather prediction or general circulation models, or estimate necessary irrigation requirements for an agricultural field, accurate estimates of the state of the land surface (moisture and temperature) and the fluxes between the surface and atmosphere are required. Unfortunately, these variables (most notably soil moisture and surface turbulent fluxes) are difficult, if not pragmatically impossible, to directly measure over large scales. Therefore we are left with the so-called "inverse problem" of trying to estimate these states and fluxes from environmental observations which are generally only indirectly related to the variable of interest.

Many recent studies have outlined methods to estimate surface states and fluxes from potentially useful data streams. Particularly, the advent of remote sensing capabilities has taken hydrology, as well as many other fields in the geosciences, from a somewhat data poor situation, reliant mostly on sparse *in-situ* measurements, to a potentially data rich environment, by increasing the types and numbers of observations which may be related to the surface parameters we would like to estimate. For example, due to the strong sensitivity of bulk soil microwave dielectric properties to volumetric soil moisture, the feasibility of surface soil moisture estimation from microwave measurements has been demonstrated (e.g. Schmugge and Jackson (1994), Entekhabi et al. (1994), Njoku and Entekhabi (1996), Jackson et al. (1999), Reichle et al. (2001a)). While there is some information content in higher frequencies (e.g. Lakshmi et al. (1997), Vinnikov et al. (1999)), the most promising results correspond to L-band (1.4 GHz) measurements, for which there currently is no

operational satellite.

As a result, other researchers have focused on using currently available remote sensing measurements, notably radiometric surface temperature, to estimate surface soil moisture and/or fluxes (e.g. Carlson et al. (1981), Wetzel et al. (1984), Wetzel and Woodward (1987), Diak and Stewart (1989), McNider et al. (1994), Gillies and Carlson (1995), Anderson et al. (1997), Kustas et al. (1999), Castelli et al. (1999), Norman et al. (2000), Lakshmi (2000), French et al. (2000), Boni et al. (2001)). These approaches generally either (i) use the physical connection between surface moisture and the thermal inertia of the surface to infer soil moisture and/or (ii) use the dependence of sensible heat flux on surface temperature to estimate the surface fluxes with surface temperature and auxiliary data. While showing promising results, these methods can sometimes fail due to heavy vegetation cover (which masks the ground surface), inaccuracies in the surface temperature measurements related to atmospheric corrections, and are susceptible to errors related to cloud effects. They often represent under-determined inverse problems and hence use empirical closure relations (e.g. ground heat flux as a fraction of net radiation).

In addition to remotely sensed variables, standard ground-based observations may contain potentially useful information about land surface states and fluxes. Recent studies have investigated the use of screen-level micrometeorological data to try to initialize surface soil moisture for mesoscale weather prediction or atmospheric boundary layer (ABL) models (e.g. Mahfouf (1991), Bouttier et al. (1993), Ruggiero et al. (1996), Callies et al. (1998), Bouyssel et al. (1999), Rhodin et al. (1999), Hess (2001), Alapaty et al. (2001)). These methods rely on the sensitivity of reference-level temperature and/or humidity to surface states primarily via the surface turbulent fluxes. While these studies have demonstrated positive results during soil-controlled evaporation regimes, the sensitivity of micrometeorology to surface conditions may be very small during periods of potential evaporation, low radiative forcing, or during strong advection events.

For the most part, the studies mentioned above, as well as many other land surface estimation schemes, have focused on using a single measurement type to try to estimate surface parameters. These studies have generally tested the limits to which the estimation can be pushed when using a single observation type. While these results are quite useful, it is also necessary to begin to design frameworks which are flexible enough to take advantage of multiple data streams that are already available or may be in the near future, and to appropriately weight each to provide an optimal estimate. Also, significant additional (synergistic) benefits may exist when combining multiple types of measurements in an estimation scheme and therefore is an area of potentially fruitful research. These benefits may take several forms: (i) the estimation scheme may be extended to provide estimates in situations where one measurement type may be unavailable or insufficiently sensitive to the parameter of interest, (ii) unresolvable states for a given measurement type may be resolved when the information contained in other observations is included, (iii) tradeoffs in sparseness (both in time and space) between measurements may allow for better interpolation, (iv) the estimation algorithms may be generally more robust. In this study, we present a variational framework to assimilate screen-level micrometeorological variables (temperature and humidity) and radiometric surface temperature in order to estimate land surface and ABL states and surface fluxes. The data assimilation approach outlined below is appealing because it allows us to combine measurements and a physical model of the system, and by appropriately weighting the sources of error in both, to ultimately produce a statistically optimal and dynamically consistent estimate of the evolving state of the system. Most importantly, included in the framework are estimates of surface fluxes and time-varying

structural model errors. The algorithm is also very flexible with respect to the inclusion of additional measurement types and therefore could easily be extended for future research applications. In Section 4.2 we briefly present the coupled model used in this study. Section 4.3 describes the variational framework. A synthetic test experiment and a case study application of this framework to the First International Satellite Land Surface Climatology Project (ISLSCP) Field Experiment (FIFE) site is described in Section 4.4, with conclusions discussed in Section 4.5.

4.2 Forward Model

The one-dimensional model we have developed for use in this study is composed of a land surface parameterization and an accompanying mixed-layer model representation of the overlying boundary layer (see Chapter 2). While many land data assimilation systems (LDAS) use an uncoupled land surface model, the choice of a coupled model is useful as it allows for: (i) a significant reduction in the auxiliary data needed to force the model (i.e. reference-level micrometeorology and downwelling longwave radiation are not needed since they are computed internally); and (ii) variables that are generally used as forcing for land surface models (i.e. reference-level temperature and humidity) are instead internal diagnostic variables which can be assimilated as observations when available. The model remains relatively simple but includes the influential processes in the land surface-ABL system. By simultaneously taking into account the coupled nature of the system, the forcing requirements for the model are reduced to incoming solar radiation, large-scale wind speed, and lapse rates in temperature and humidity above the mixed-layer. The coupled land surface-boundary layer model used here is a computationally efficient compromise between an uncoupled model and a fully coupled single-column atmospheric model, making it well-suited for use as part of a stand-alone LDAS.

The coupled model does not include a parameterization of advective flux divergence of heat and moisture into the ABL. This was primarily due to the fact that our focus was on the vertical fluxes between the surface and boundary layer. However, advection can be important as mid-latitude regimes are often characterized by intermittent frontal systems which modify the local boundary layer temperature and humidity. The advective flux divergence can also have a significant impact on the micrometeorological observations that are used in the assimilation. Instead of parameterizing the advective fluxes in the model, they are intentionally left as time-varying model error terms in the potential temperature and humidity budget equations. As will be shown below, these model error terms can be included as unknowns in the estimation algorithm.

4.3 Variational Data Assimilation Framework

Data assimilation provides a framework which allows us to merge measurements and physical models under the supposition that both provide useful information about the state of the system, while containing measurement and model errors respectively. By appropriately weighting the sources of error in both, we hope to ultimately produce a statistically optimal and dynamically consistent estimate of the evolving state of the system. In this paper we use a variational approach to assimilate radiometric surface temperature and standard reference-level temperature and humidity measurements into the coupled land surface-atmospheric boundary layer model described above, with the ultimate aim of obtaining estimates of

the evolving model states and fluxes. Variational data assimilation techniques have a well-established history in meteorology and oceanography (e.g. LeDimet and Talagrand (1986), Talagrand and Courtier (1987), Thacker and Long (1988), Li et al. (1993), Lu and Hsieh (1997), Bennett et al. (1998)). More recently these techniques have begun to be applied in land surface hydrological applications (e.g. Castelli et al. (1999), Boni et al. (2001), Reichle et al. (2001a)). The reader is referred to these references for detailed methodological developments. The key aspects of the technique are described below.

4.3.1 Model and Measurement Operators

Consider the coupled model as defined generally in dynamical form:

$$\frac{d\mathbf{y}}{dt} = \mathbf{F}(\mathbf{y}) + \boldsymbol{\omega} \qquad \mathbf{y}(t_0) = \mathbf{f}(\boldsymbol{\beta}) \tag{4.1}$$

where $\mathbf{y}(t)$ is the state vector, $\mathbf{F}$ is a nonlinear vector operator which is a function of the model states, and $\boldsymbol{\omega}(t)$ represents a time-varying and unknown model error vector. The model initial condition $\mathbf{y}(t_0)$ is a function of a time-invariant vector $\boldsymbol{\beta}$, which is used so that bounded states like soil saturation can be mapped from the variable $\boldsymbol{\beta}$ which varies over the entire real domain. The random vectors $\boldsymbol{\beta}$, and $\boldsymbol{\omega}(t)$ are characterized by their mean values ($\overline{\boldsymbol{\beta}}$ and $\overline{\boldsymbol{\omega}}(t)$) and their covariances (C_β and $\mathsf{C}_\omega(t,t')$). The mean values represent our prior knowledge of the parameters and the covariance matrices represent the postulated uncertainty about the prior values. The prior model error is generally assumed equal to zero. Posterior estimates are made by assimilating measurements.

The model states are related to the observations via the measurement equation:

$$\mathbf{Z} = \mathbf{M}(\mathbf{y}) + \boldsymbol{\nu} \tag{4.2}$$

where $\mathbf{Z}$ is the measurement vector which in this application contains vectors of surface temperature (T_s^{obs}) and reference-level temperature (T_r^{obs}) and specific humidity (q_r^{obs}) measurements throughout the assimilation window. The measurements are assumed to include unbiased measurement error with a specified covariance matrix C_ν. For simplicity measurement errors are assumed uncorrelated in this application. Estimation of biases and posterior covariance structures are possible and their feasibility needs to be shown in future studies. The measurement operator $\mathbf{M}(\mathbf{y})$ represents the diagnostic equations which map the model states onto T_s, T_r, and q_r. For completeness they are described next.

For the measurement operators used in the variational framework we need to construct the diagnostic equations that map the model states to the measurements used in this study (T_s, T_r, and q_r). The radiometric surface temperature equation is described first. Previous studies (e.g. Anderson et al. (1997)) generally relate the radiometric temperature to canopy and ground temperature via a function of the form:

$$T_s = \left[V_c T_c^n + (1 - V_c) T_g^n\right]^{\frac{1}{n}} \tag{4.3}$$

where V_c is a fractional vegetation cover (which can depend on view-angle), and the exponent n is usually equal to 4, so that T_s represents the effective temperature for the thermal radiation seen by the sensor. For ease of computation, and with generally little loss of accuracy (fourth power nearly linear shape over the limited range of temperatures encountered),

the following simplified expression is often used:

$$T_s = V_c T_c + (1 - V_c) T_g \tag{4.4}$$

which is the expression used in this study. Including (4.3) is not a problem for future studies. The radiometric surface temperature is thus simply an average of canopy and ground temperature weighted by the fractional vegetation cover. At the FIFE site the fractional vegetation cover is 80%.

The diagnostic relationships between temperature and humidity at a given reference height (z_r) and the model states is more complicated. The turbulent fluxes in the forward model are generally expressed as a gradient (in either temperature or vapor pressure) between two levels divided by a resistance term. We assume that there is no major storage of heat or moisture within the surface air layer so that the sensible and latent heat fluxes between the canopy (at height z_1) and the reference level (at height z_r) are equal to the fluxes between the reference level and the bottom of the mixed layer (at height z_m):

$$\rho c_p \frac{(T_a - T_r)}{r_{a1}} = \rho c_p \frac{(T_r - T_m)}{r_{a2}} \tag{4.5}$$

and

$$\frac{\rho c_p}{\gamma} \frac{(e_a - e_r)}{r_{a1}} = \frac{\rho c_p}{\gamma} \frac{(e_r - e_m)}{r_{a2}} \tag{4.6}$$

where r_{a1} and r_{a2} are the aerodynamic resistances between the canopy and reference-level and reference-level and mixed layer respectively (see Appendix C for list of symbols). This is exactly analogous to the procedure used to compute T_a and q_a in the model (see Appendix A). By solving these two equations for T_r and e_r the following two diagnostic relationships are obtained:

$$T_r = \frac{r_{a2}}{r_a} T_a + \frac{r_{a1}}{r_a} T_m \qquad\qquad e_r = \frac{r_{a2}}{r_a} e_a + \frac{r_{a1}}{r_a} e_m \tag{4.7}$$

where r_a is the aerodynamic resistance between the canopy air and bottom of the mixed layer (and via the series resistance rule is equal to the sum of r_{a1} and r_{a2}). Therefore the reference-level values of temperature and vapor pressure are a weighted averaged of the values within the canopy air and at the bottom of the mixed layer. Note that the reference-level specific humidity (q_r) which is the measured variable in this study is simply equal to $\frac{\epsilon}{P_s} e_r$. In the model, T_a and e_a are themselves diagnostic equations, where T_a is a weighted average of T_c, T_g, and T_m, and e_a is a weighted average of $e_*(T_c)$, $e_*(T_g)$, and e_m.

The specific expressions for the weights in the above equations can be derived as follows: The total aerodynamic resistance is given by:

$$r_a = \frac{1}{F_H(z_m)\kappa^2 U_m} \ln\left(\frac{z_m - d}{z_0}\right) \ln\left(\frac{z_m - d}{z_1 - d}\right) \tag{4.8}$$

where the stability correction factor for heat (F_H) is a function of the bulk Richardson number and is taken from Louis et al. (1982). Here z_0 is the scalar roughness length scale. The windspeed at the bottom of the mixed layer (U_m) is related to the reference-level forcing

windspeed (U_r) via:

$$U_m = U_r \left(\frac{F_M(z_r)}{F_M(z_m)} \right)^{\frac{1}{2}} \frac{\ln\left(\frac{z_m - d}{z_0}\right)}{\ln\left(\frac{z_r - d}{z_0}\right)} \tag{4.9}$$

where the stability correction factor for momentum (F_M) is also provided by Louis et al. (1982) and is of similar form to F_H. The expression for the resistance between z_1 and z_r (r_{a1}) is analogous to that of r_a and is given by:

$$r_{a1} = \frac{1}{F_H(z_r)\kappa^2 U_r} \ln\left(\frac{z_r - d}{z_0}\right) \ln\left(\frac{z_r - d}{z_1 - d}\right) \tag{4.10}$$

This can be re-written by substituting the expression relating U_m and U_r to yield:

$$r_{a1} = \frac{1}{F_H(z_r)\kappa^2 U_m} \left(\frac{F_M(z_r)}{F_M(z_m)} \right)^{\frac{1}{2}} \ln\left(\frac{z_m - d}{z_0}\right) \ln\left(\frac{z_r - d}{z_1 - d}\right) \tag{4.11}$$

Using the series resistance rule, the resistance r_{a2} is the difference between r_a and r_{a1}, which yields the expression:

$$r_{a2} = \frac{\ln\left(\frac{z_m - d}{z_0}\right)}{\kappa^2 U_m} \left[\frac{\ln\left(\frac{z_m - d}{z_1 - d}\right)}{F_H(z_m)} - \left(\frac{F_M(z_r)}{F_M(z_m)} \right)^{\frac{1}{2}} \frac{\ln\left(\frac{z_r - d}{z_1 - d}\right)}{F_H(z_r)} \right] \tag{4.12}$$

Based on these expressions the weighting terms in Equations (4.7) can be written as:

$$\frac{r_{a2}}{r_a} = 1 - \left(\frac{F_M(z_r)}{F_M(z_m)} \right)^{\frac{1}{2}} \left(\frac{F_H(z_m)}{F_H(z_r)} \right) \frac{\ln\left(\frac{z_r - d}{z_1 - d}\right)}{\ln\left(\frac{z_m - d}{z_1 - d}\right)} \tag{4.13}$$

and

$$\frac{r_{a1}}{r_a} = \left(\frac{F_M(z_r)}{F_M(z_m)} \right)^{\frac{1}{2}} \left(\frac{F_H(z_m)}{F_H(z_r)} \right) \frac{\ln\left(\frac{z_r - d}{z_1 - d}\right)}{\ln\left(\frac{z_m - d}{z_1 - d}\right)} \tag{4.14}$$

so that the diagnostic equations for T_r and e_r can simply be written as:

$$T_r = (1 - \alpha_r) T_a + \alpha_r T_m \qquad e_r = (1 - \alpha_r) e_a + \alpha_r e_m \tag{4.15}$$

where

$$\alpha_r = \left(\frac{F_M(z_r)}{F_M(z_m)} \right)^{\frac{1}{2}} \left(\frac{F_H(z_m)}{F_H(z_r)} \right) \frac{\ln\left(\frac{z_r - d}{z_1 - d}\right)}{\ln\left(\frac{z_m - d}{z_1 - d}\right)} \tag{4.16}$$

4.3.2 Objective Functional and Update Equations

To obtain an estimate that balances the uncertainties due to measurement error and model error, the following Bayesian least-squares performance index can be minimized with respect

to β and ω over the assimilation (or smoothing) window $t = [t_0, t_f]$:

$$J = [\mathbf{Z} - \mathbf{M}(\mathbf{y})]^T \, \mathsf{C}_\nu{}^{-1} \, [\mathbf{Z} - \mathbf{M}(\mathbf{y})] + [\boldsymbol{\beta} - \overline{\boldsymbol{\beta}}]^T \, \mathsf{C}_\beta{}^{-1} \, [\boldsymbol{\beta} - \overline{\boldsymbol{\beta}}] +$$

$$\int_{t_0}^{t_f} \int_{t_0}^{t_f} \boldsymbol{\omega}(t')^T \mathsf{C}_\omega{}^{-1}(t', t'') \boldsymbol{\omega}(t'') dt' dt'' + 2 \int_{t_0}^{t_f} \boldsymbol{\lambda}^T \left[\frac{d\mathbf{y}}{dt} - \mathbf{F}(\mathbf{y}) - \boldsymbol{\omega} \right] dt \quad (4.17)$$

The first term in the performance index represents the misfit between the data ($\mathbf{Z}$) and model predictions $M[\mathbf{y}]$. The next two terms penalize deviations from the prior values. All of these terms are normalized by their corresponding covariances. The final term is the adjoined system model constraint which is by definition zero, but ensures that the estimates are dynamically consistent over the assimilation window. The scalar functional is minimized by taking its first variation (see Chapter 2) which yields the forward model (as shown in Eq. 4.1) as well as the adjoint model of the system:

$$\frac{d\boldsymbol{\lambda}}{dt} = -\left(\frac{\partial \mathbf{F}}{\partial \mathbf{y}}\right)^T \boldsymbol{\lambda} - \left(\frac{\partial \mathbf{M}}{\partial \mathbf{y}}\right)^T [\delta] \mathsf{C}_\nu{}^{-1} [\mathbf{Z} - \mathbf{M}(\mathbf{y})] \qquad \boldsymbol{\lambda}(t_f) = 0 \quad (4.18)$$

and equations for the gradients in J with respect to β and ω:

$$\frac{\partial J}{\partial \boldsymbol{\beta}} = [\boldsymbol{\beta} - \overline{\boldsymbol{\beta}}]^T \, \mathsf{C}_\beta{}^{-1} - \left(\frac{\partial \mathbf{f}}{\partial \boldsymbol{\beta}}\right)^T \boldsymbol{\lambda}_0 \quad (4.19)$$

$$\frac{\partial J}{\partial \boldsymbol{\omega}(t)} = \int_{t_0}^{t_f} \boldsymbol{\omega}(t') \, \mathsf{C}_\omega{}^{-1}(t', t) \, dt' - \boldsymbol{\lambda}(t) \quad (4.20)$$

Development and testing of the accuracy of the adjoint model is described in Chapter 2. Note that the adjoint model must be integrated backward in time to obtain the adjoint variables $\boldsymbol{\lambda}(t)$. It depends on the state vector and is forced by the measurement-model misfit. The adjoint model is a powerful tool because once the adjoint variables are known, all of the gradients shown above can be computed and used in a gradient search algorithm to minimize J. This procedure is done iteratively by (i) integrating the forward model with prior parameters, (ii) integrating the adjoint model backward in time about the current state trajectory, (iii) computing the gradients and using them to update the parameters and model error, and (iv) repeating steps (i)-(iii) until sufficient convergence is achieved. While any gradient search algorithm can be used, the particularly simple method used here yields a set of update equations which are used in the above iterative procedure. The update equations are described next.

For the gradient search algorithm in this study we use a simple steepest descent method. There are certainly more efficient algorithms, but this technique was found to work for this application and yields a simple set of update equations. Future work could use a more efficient technique like the conjugate gradient method. In the steepest descent algorithm, a parameter u at iteration $k + 1$ is given by:

$$u^{k+1} = u^k - \varepsilon \left(\frac{\partial J}{\partial u}\right)^k \quad (4.21)$$

where ε is a scalar step size. For the unknown parameters in this study (β and ω) we specify the step size ε to be proportional to the corresponding uncertainty (covariance) for each variable (i.e. $\varepsilon_i = \eta_i C_i$). Substituting this along with the gradient expressions shown in Section 4.3, update equations for each parameter are given by:

$$\beta^{k+1} = \beta^k - \eta_\beta(\beta^k - \overline{\beta}) + \eta_\beta C_\beta \left(\frac{\partial \mathbf{f}}{\partial \beta}\right)^T \lambda_0^k \tag{4.22}$$

$$\omega^{k+1}(t) = (1 - \eta_\omega)\omega^k(t) + \eta_\omega \int_{t_0}^{t_f} C_\omega(t, t')\lambda^k(t')\, dt' \tag{4.23}$$

The scalar step sizes are specified to aid in convergence. Note that update equation for the model error involves a convolution integral, which is evaluated most efficiently using a Fast Fourier Transform (FFT).

4.4 Application of the Variational Framework

4.4.1 Synthetic Data Test

A synthetic test is first performed to determine which parameters are identifiable when assimilating surface temperature and reference-level micrometeorology into the coupled model. This allows us to determine whether the estimation scheme can estimate the known "truth". Given specified initial conditions and model errors, the model is used to generate (half-hourly) observations of the system that can then be used in the assimilation algorithm to attempt to recover the specified parameters. Noise is added to the observations. While not a guarantee that the estimator will work with real data, the synthetic experiment yields important insight into the information content of the assimilated observations and lends some confidence in the results from real applications.

The model states which are most closely linked with the assimilated observations are the canopy and surface ground temperature (T_c and T_g), ABL potential temperature and specific humidity (θ and q) and rootzone soil moisture (W_1 and W_2). The first four variables are explicitly related to T_s, T_r, and q_r via the measurement operators, while the soil moisture is implicit in the measurements due to its role in the partitioning of net radiation at the surface. For initial condition specification, θ_0, q_0, W_{1_0}, and W_{2_0} are most important because of the long-term memory associated with these variables, which allows errors to propagate for many days or weeks. Conversely, canopy and ground temperature have very limited memory such that errors are generally dissipated within several hours. The other ABL states (i.e. temperature and humidity inversions at the top of the ABL and ABL height) are essentially re-initialized within the model each day due to the collapse of the boundary layer in the early evening. Therefore, for multi-day assimilation windows the specification of the initial conditions of these variables is less important. Finally the deep soil moisture and ground temperature do not effect the measured variables on the time scale of this study. As a result, for this application the estimated initial conditions are limited to θ_0, q_0, W_{1_0}, and W_{2_0}.

The time-varying model error terms are conceptualized as flux errors in the prognostic equations for T_c, T_g, θ, q, W_1, and W_2. Error time series for each equation are synthetically generated using a lag-1 auto-regressive model, which by definition has an exponential

covariance structure ($C_\omega(t,t') = \sigma_\omega^2 \exp(|t-t'|/\tau_c)$). The errors are used in the reference simulation and the assimilation scheme is used to try to estimate them. The standard deviation (σ_ω) and decorrelation time scale (τ_c) of the error for each variable were specified to be 30 Wm^{-2} and 6 hours respectively. The standard deviation in the observation errors are 0.5 K for the surface and reference-level temperature and 0.5 g/kg in reference-level specific humidity.

Results from our synthetic tests show that because of the limited memory in canopy and ground temperature, errors in these prognostic equations were unidentifiable. In reality, due to the stiffness of these variables, errors which occur in these prognostic equations are most likely the result of errors in the longer memory states. Also, while surface temperature and screen-level micrometeorology were found to be sufficiently sensitive to the initial conditions in rootzone soil moisture (which set the general soil moisture trajectory), attempts to estimate time-varying errors about this trajectory were not successful. The study by Reichle et al. (2001b) has shown the potential to estimate soil moisture errors with microwave radiobrightness measurements, but reached similar conclusions for the canopy and ground temperature errors. In our synthetic experiment it was found that errors in the θ and q prognostic equations were identifiable from surface temperature and reference-level micrometeorology observations. The ability to estimate these errors are quite useful, especially considering the lack of a parameterization of advective flux divergence in our model.

Results from a five-day synthetic experiment, where initial conditions in θ, q, W_1, and W_2 and model errors in the θ and q prognostic equations (ω_θ and ω_q respectively) are estimated, are shown in Table 4.1 and Figures 4-1–4-4. Table 4.1 shows that the true initial conditions were almost perfectly recovered by the estimation algorithm and that the objective function is reduced to near the true value. Figure 4-1 shows the comparison between the prior, estimated, and actual model errors in θ and q. The model error estimates capture the primary features and low frequency variability of the actual model error (note the comparison with the 24-hour moving average of the true error). The high frequency variability generally has limited impact on the observations and therefore is not captured by the estimate. The timing of model errors is also important, in that when errors are small relative to the magnitude of other fluxes (i.e. especially near midday) they are not estimated well. However, because the relative magnitude of the errors are small at those times, their estimation is not as important. Figure 4-2 shows the significant improvement in fit between the assimilated observations and posterior predictions compared to the priors. The time series of the primary ABL and land surface state estimates are shown in comparison to the true values in Figure 4-3. The estimator performs quite well in removing large biases which were present when using the prior values. Finally, by reproducing the states, the land surface fluxes are also reproduced by the estimation algorithm (Figure 4-4).

4.4.2 Application to the FIFE site

To test the methodology presented above with real data, we applied the data assimilation framework to the dataset obtained at the FIFE site in Kansas in the summer of 1987 (see Sellers et al. (1992)). The FIFE dataset (Betts and Ball (1998)) provides the needed forcing variables for the model, surface radiometric temperature and micrometeorological measurements for the assimilation scheme, as well as flux observations for validation. In this study we present results from an application to a 20-day window in July (Julian Day 190-210). This particular period was chosen because is contains a variety of environmental conditions, some of which can confound estimation algorithms (i.e. advection, precipitation,

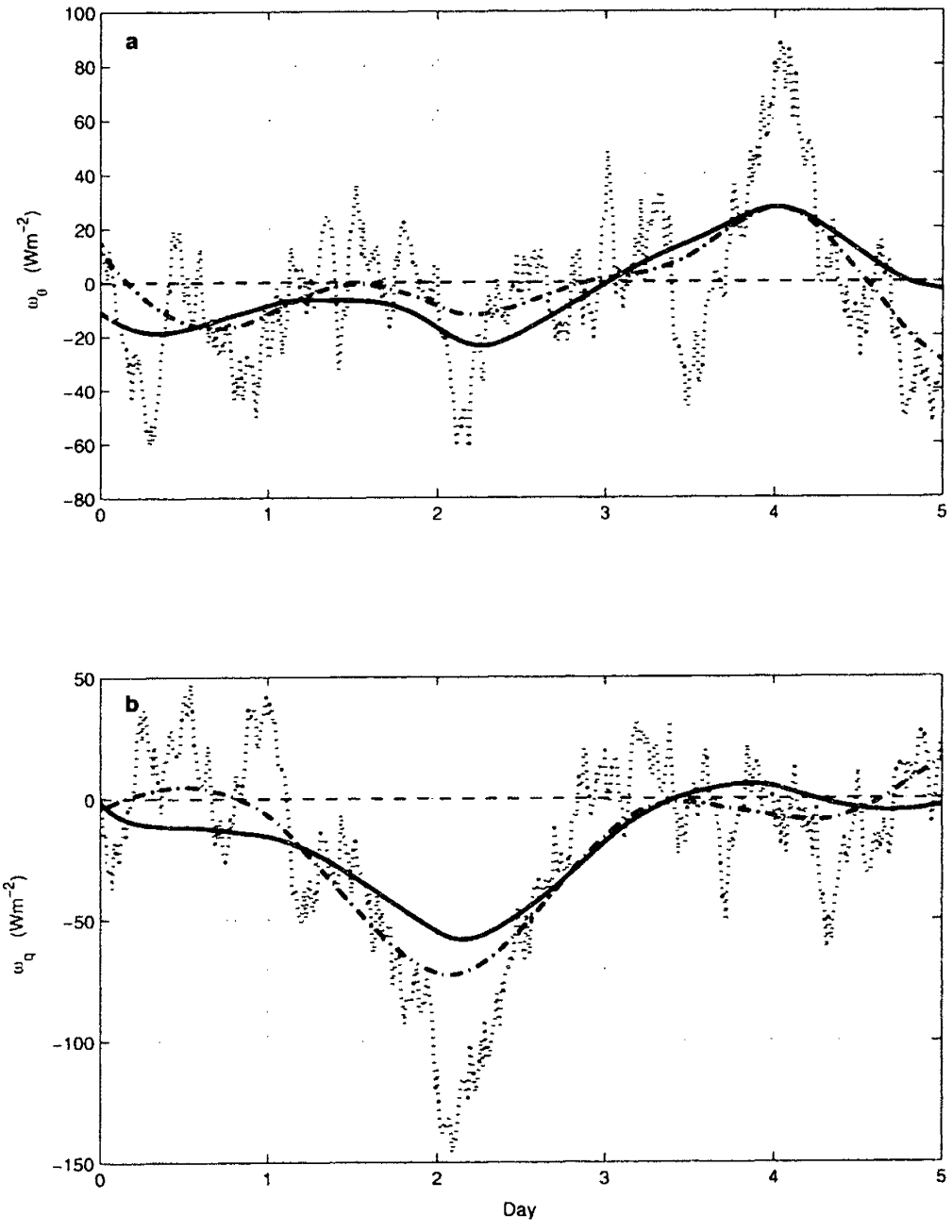

Figure 4-1: Comparison of prior (dashed line), estimated posterior (solid line), and true (dotted line) model errors in the a) mixed-layer potential temperature budget; and b) mixed-layer specific humidity budget for the synthetic experiment. Note that the prior error is by definition zero and that the estimated model errors closely resemble a moving average (dash-dot line) of the true error. (Beginning of each day on figure corresponds to midnight local time).

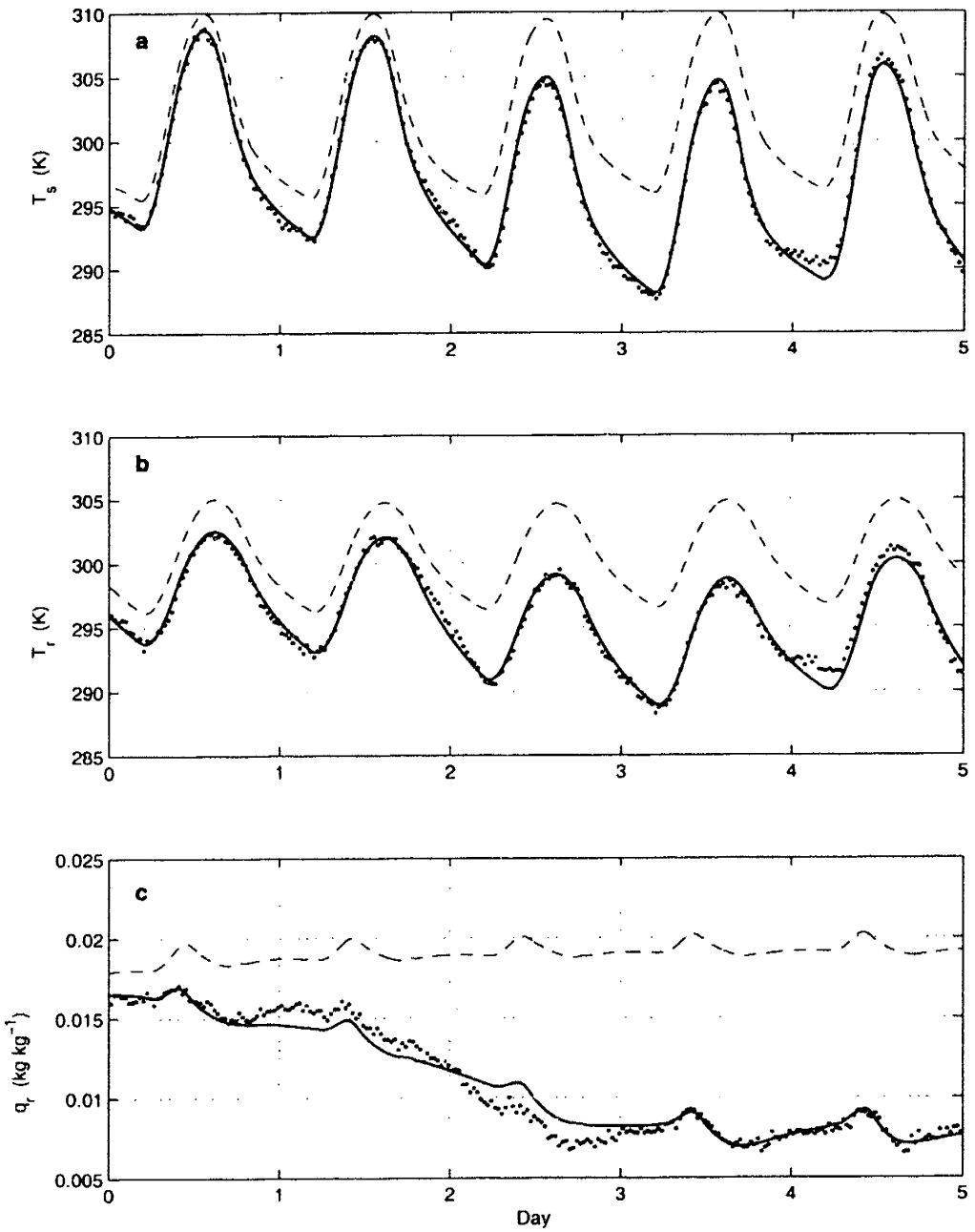

Figure 4-2: Comparison of prior (dashed line), estimated posterior (solid line), and observed (solid dots) a) surface temperature; b) screen-level temperature; and c) screen-level humidity for the synthetic experiment.

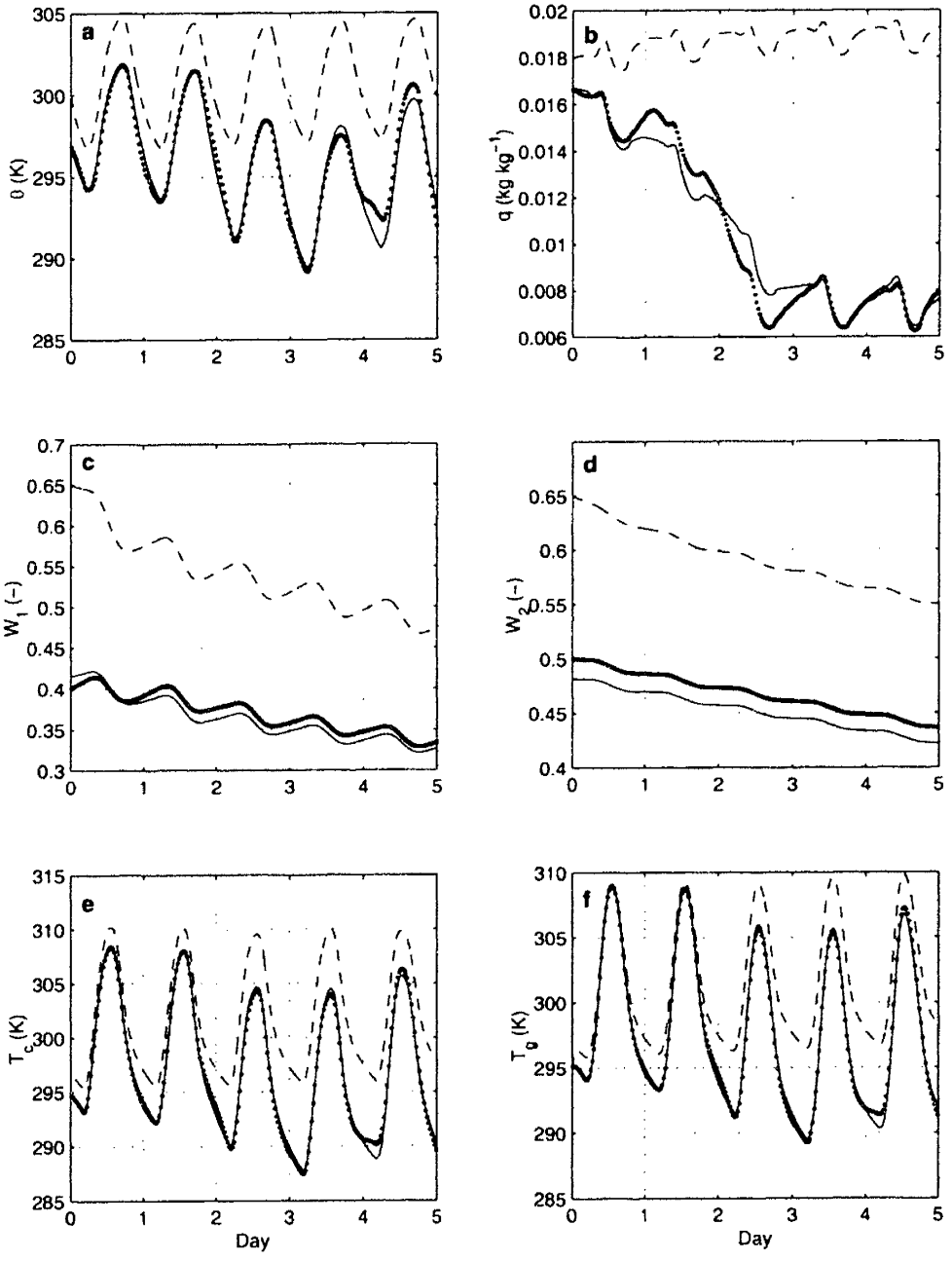

Figure 4-3: Comparison of prior (dashed line), estimated posterior (solid line), and true (solid dots) model states for the synthetic experiment.

Table 4.1: Comparison of prior and posterior (estimated) initial conditions to true values from synthetic experiment. Reduction in objective function shown in last column.

	θ_0 [K]	q_0 [kg kg^{-1}]	W_{1_0} [-]	W_{2_0} [-]	J [-]
Prior	300.0	18.0e-3	0.65	0.65	24500
Posterior	297.0	16.7e-3	0.42	0.48	1100
True	297.0	16.7e-3	0.40	0.50	950

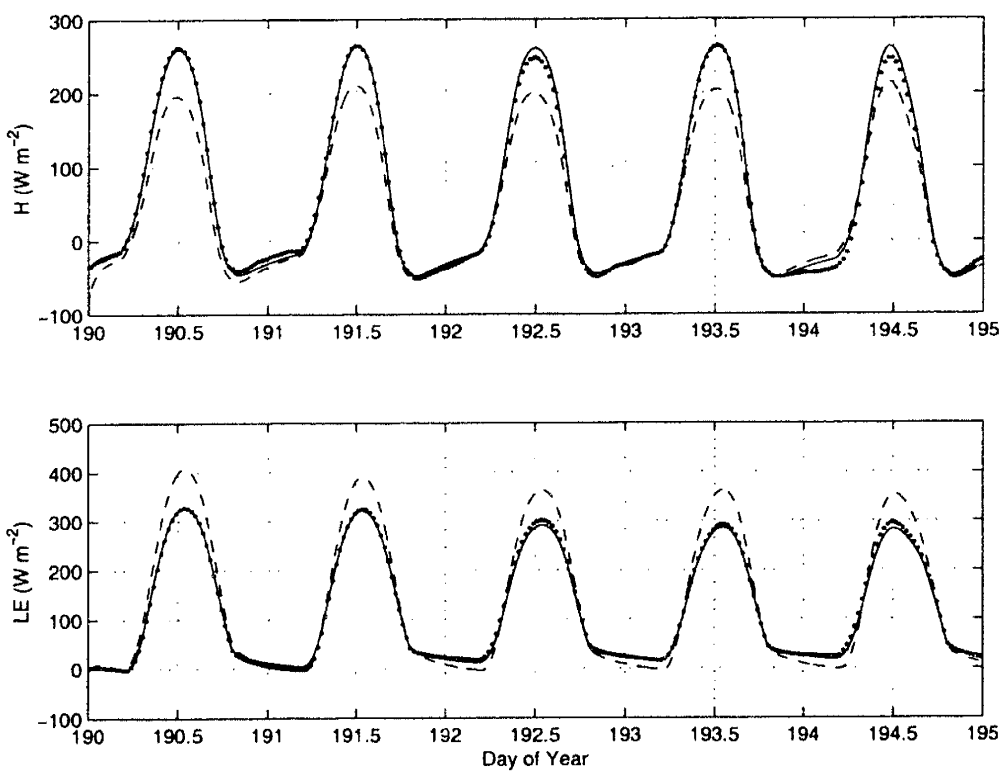

Figure 4-4: Comparison of prior (dashed line), estimated posterior (solid line), and true (solid dots) model fluxes for the synthetic experiment.

atmospherically-controlled evaporation regimes) The key surface meteorological variables at the site are shown in Figure 4-5. The estimation was performed over two consecutive assimilation windows (from Day 190-200 and Day 200-210), with model and observation error statistics equal to those described in the previous section. The first ten days are marked by several moderate storms, atmospherically-controlled evaporation, and a large advection event (on Day 193-195), which is most noticeable in the specific humidity time series. The second ten days consist of a long drydown event where the soil exerts significant control on the surface turbulent fluxes such that the screen-level micrometeorology is strongly coupled to the surface. There also appears to be a small advection event on Day 201-203. It should be mentioned that the FIFE region, as well as many mid-latitude regimes, is marked by periodic frontal systems which can advect moisture and energy of different characteristics into the region. During the course of the summer, nine identifiable events occurred (approximately one every ten days) at the FIFE site. The advection events seen in Figure 4-5 coincide with high pressure systems moving into and out of the region.

We first applied the assimilation scheme to Day 190-200. This particular scenario provides a very significant test of the scheme because there appears to be a large advection event that dominates the screen-level micrometeorology variables, concurrent with conditions where evaporation is near the potential rate (when micrometeorology is relatively insensitive to soil moisture). The model is initialized by setting the ABL potential temperature and humidity equal to the observed reference-level micrometeorology, and the rootzone soil moisture to relatively dry values which were thought to be an intentionally poor prior guess (see Table 4.2). The assimilation scheme is applied iteratively, as described above, until convergence in the initial condition and model error estimates are achieved. The posterior (estimated) initial conditions as well as the reduction in the objective function are shown in Table 4.2. The ABL temperature and humidity initial conditions do not change by a large amount, which is to be expected since the micrometeorological values should be representative of those in the ABL. However a large change is shown in the rootzone soil moisture. In fact while the prior initial rootzone soil moisture is well within the soil-controlled evaporation regime, the estimate is within the potential evaporation regime.

Table 4.2: Prior and posterior (estimated) initial conditions for each ten day assimilation window. Reduction in objective function shown in last column.

		θ_0 [K]	q_0 [kg kg^{-1}]	W_{1_0} [-]	W_{2_0} [-]	J [-]
Day 190-200	Prior	297.0	17.0e-3	0.39	0.41	87000
	Posterior	297.6	16.7e-3	0.59	0.62	7200
Day 200-210	Prior	298.0	17.5e-3	0.48	0.49	15000
	Posterior	298.6	16.6e-3	0.46	0.51	7900

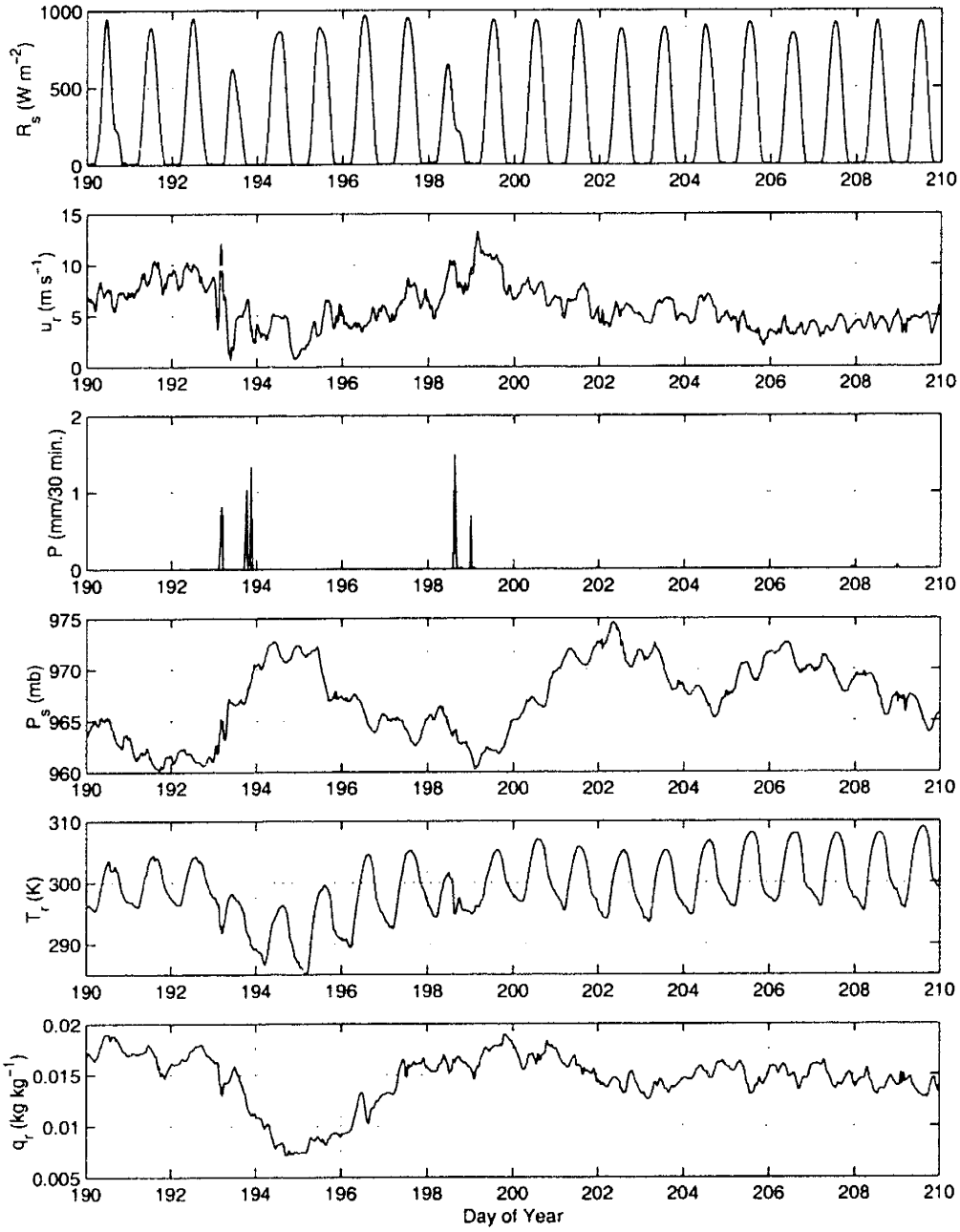

Figure 4-5: Meteorological conditions at the FIFE site during Day 190-210 in 1987. R_s is incoming solar radiation, u_r is reference-level windspeed, P is precipitation, and T_r and q_r are the reference-level air temperature and specific humidity respectively.

The estimated time-varying model errors are shown in Figure 4-6. While the error estimate represents a combination of any number of factors, it is attributed here mostly to advection processes which are not represented in the one-dimensional model. The estimate indicates significant advection of cool/dry air into the region during Day 192-195, followed by a less pronounced front of warm/moist air during Day 195-198 (note time rate of change of T_r and q_r in Figure 4-5 with the values of model error estimates in Figure 4-6). Also, the advection of moisture plays a much larger role than advection of heat with a peak flux of moisture equivalent to approximately 80 Wm^{-2}, compared to less than 20 Wm^{-2} in the ABL energy budget. In fact the drop in ABL potential temperature between Day 192-194 is mostly due to the radiative effect of a drier ABL, which captures less heat from the surface, than on cooler air entering the region. The model error estimates are quite significant, in that these results imply that it is possible to estimate processes which are not explicitly parameterized (or perhaps poorly parameterized) in the model. Another important point is that, for this particular case (with large model errors), the ability to estimate both the advection-related model error and the soil moisture initial conditions depend on using both surface temperature and micrometeorological observations in the assimilation scheme. Test cases where one or the other observation type are withheld do not converge. This is an example of the synergism that may exist when using multiple types of observations in the assimilation scheme.

The fit of the prior and estimated surface temperature and screen-level micrometeorology to the assimilated observations is shown in Figure 4-7. The improvement between the prior and posterior estimate is quite clear. The diurnal amplitude of the prior surface temperature is generally too large due to drier than actual soil moisture. Due to the dominance of the advection signal in the micrometeorological data, it is the surface temperature which is largely responsible for resolving the initial soil moisture condition. The screen-level temperature is certainly improved due to the advection, but the most pronounced difference is in the screen-level humidity. The prior is too humid during the middle part of the window and, because of the overly dry soil, is too dry by the end of the window. On the other hand, the posterior estimate captures the overall trend quite well. While, because of the very nature of the assimilation scheme, it is expected that the estimate will fit the assimilated observations well, an equally important goal is the estimation of the surface turbulent fluxes. The comparison of the prior and estimated fluxes to observations taken at the FIFE site are shown in Figure 4-8. The results clearly indicate the improved estimation of fluxes due to the assimilation of surface temperature and micrometeorological observations. The bias and root mean square error (RMSE) between the observations and estimates of surface turbulent fluxes (averaged over the daytime to remove the overly optimistic statistics obtained when comparing variables with diurnal cycles) are given in Table 4.3. The magnitude of the bias and RMSE for between the prior and posterior estimates for both the surface average daily sensible and latent heat are reduced by approximately half via the assimilation. However even after the assimilation there is a positive bias in the sensible heat flux estimates and a negative bias in the latent heat flux estimates. This may be due to biases in the FIFE observations, or model biases, or a combination of both.

Next we apply the assimilation algorithm to Day 200-210. A primary difference between the first and second assimilation windows is the issue of how to initialize the priors. The prior initial condition values for this assimilation window are taken to be the terminal conditions of the states from the first window. As a result, they are necessarily much better prior estimates than those used in the first window, since they are conditioned on the observations during Day 190-200. The other necessary input is the specification of the prior

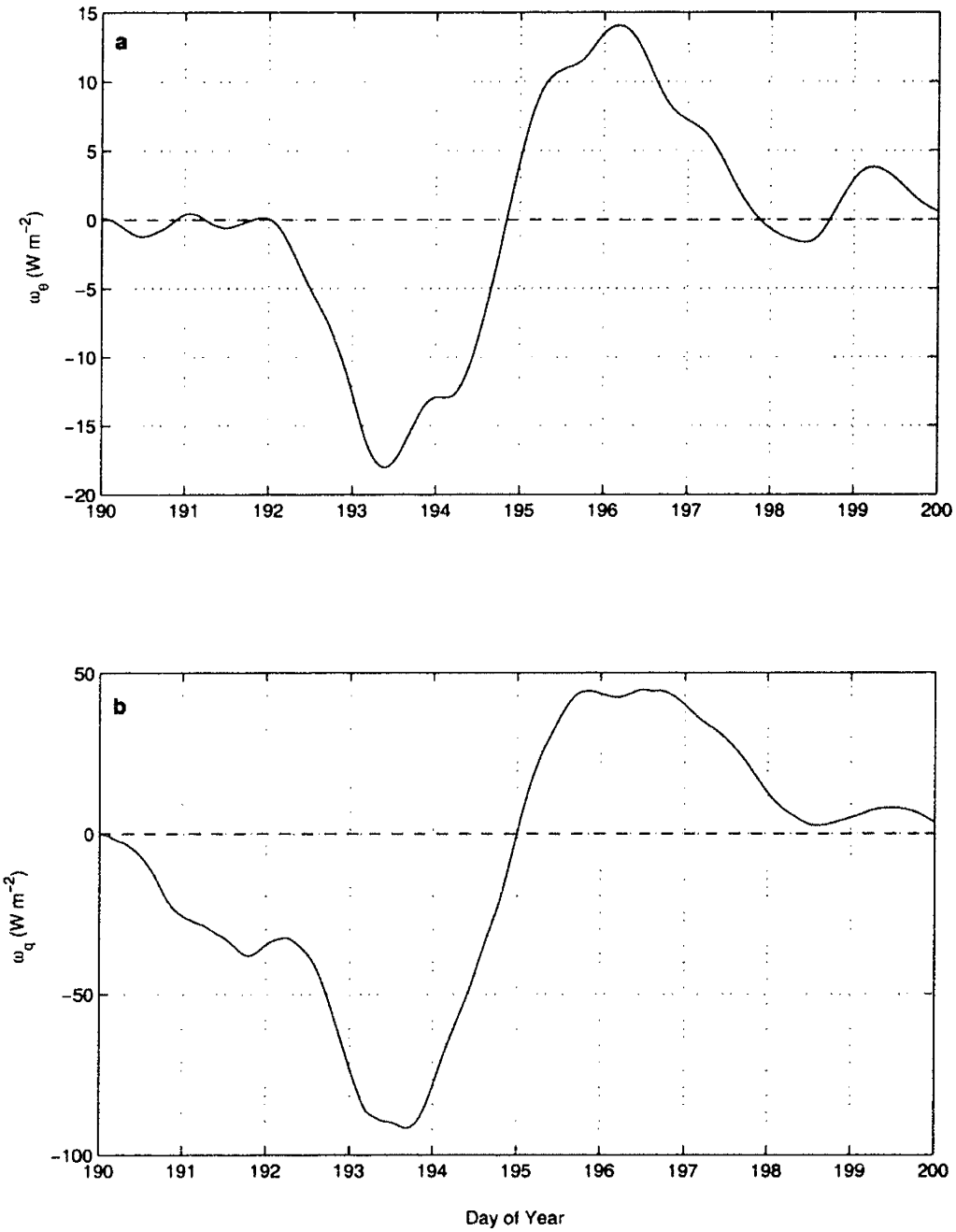

Figure 4-6: Estimated posterior model error (solid lines) in a) ABL potential temperature budget; and b) ABL specific humidity budget at FIFE during Day 190-200. Note prior model error (dashed lines) is equal to zero by convention.

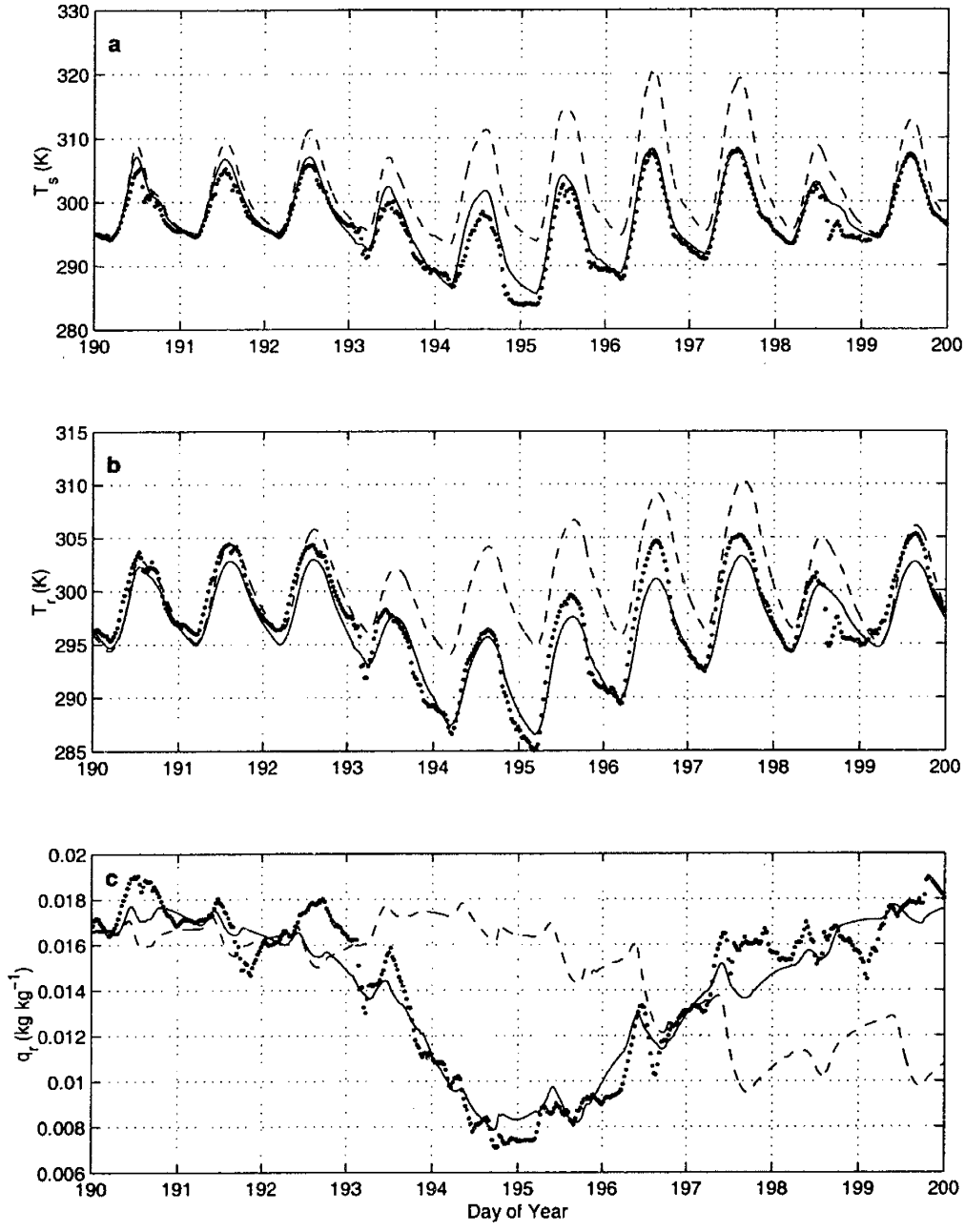

Figure 4-7: Comparison of prior (dashed line), estimated posterior (solid line), and observed (solid dots) a) surface temperature; b) screen-level temperature; and c) screen-level humidity during Day 190-200.

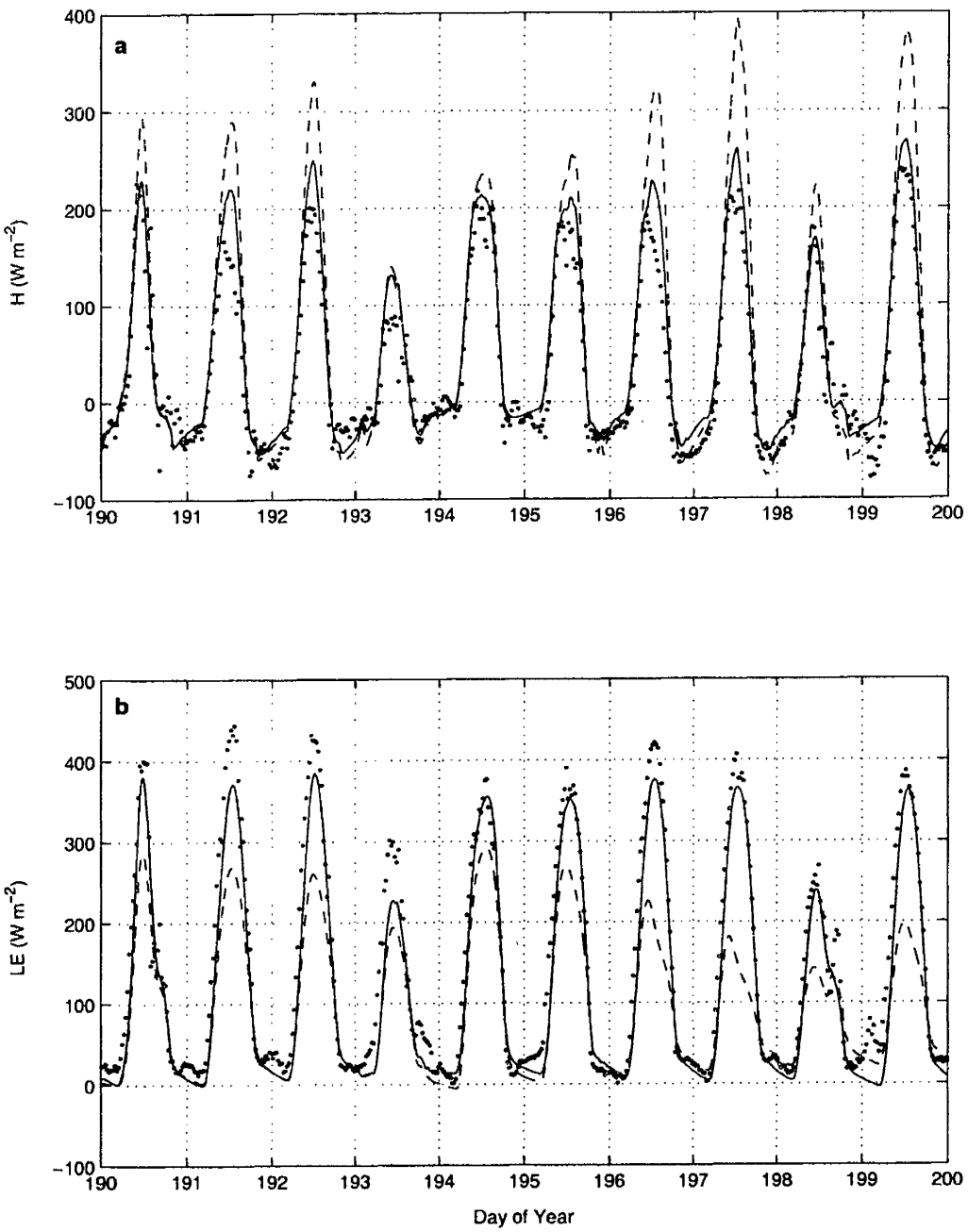

Figure 4-8: Comparison of prior (dashed line), estimated posterior (solid line), and observed (solid dots) a) surface sensible heat flux; b) surface latent heat flux during Day 190-200.

Table 4.3: Bias and RMSE between observed and estimated sensible (H) and latent (LE) heat fluxes for the two assimilation windows. The statistics based on the prior estimates are given in parentheses.

		H [W m^{-2}]	LE [W m^{-2}]
Day 190-200	Bias	27 (50)	-35 (-83)
	RMSE	30 (56)	38 (88)
Day 200-210	Bias	18 (20)	-23 (-27)
	RMSE	21 (23)	25 (28)

covariance for these initial conditions. In variational schemes (as compared to a filtering estimation scheme) there is no explicit computation of error covariances. While this leads to a significant computational reduction, it is a drawback if the methodology is applied in an operational (or semi-operational) environment with sequential assimilation windows. Instead of explicit knowledge of the evolving covariances, approximations must be used. In our application, the prior variances for the states on Day 200 were obtained using the same method employed by Rhodin et al. (1999). After the initial condition (posterior) estimates are obtained for Day 190, the posterior covariance matrix is approximated by the inverse Hessian ($[\partial^2 J/\partial y_0^2]^{-1}$), which would be exactly true if the model were linear (Tarantola (1987)). An additional error is then added to represent the uncertainty accrued over the assimilation window from Day 190 to Day 200. This error can be estimated from offline model runs.

Given these priors for the second window, the assimilation scheme is iteratively applied using the observations from Day 200-210. The initial condition estimates are shown in Table 4.2. Note that while the difference between the prior and posterior θ_0 and q_0 estimates change by similar amounts to the Day 190-200 case, the soil moisture estimates (W_{1_0} and W_{2_0}) change much less dramatically. This is primarily due to the fact that in this case prior estimates for soil moisture were already quite good as a result of the first assimilation window. If the model parameters were significantly in error, or if a large storm had just occurred, the prior estimates could conceivably be much worse than in this particular case. To test the robustness of these soil moisture estimates, another run is performed with the same (particularly dry) priors used in the Day 190-200 case. Results from that test (not shown here) show similar values for the soil moisture estimates, lending credibility to these results.

The model error estimates for the Day 200-210 window are shown in Figure 4-9. In this case the model error estimates for both the ABL energy and moisture budgets are

less than 10 Wm^{-2}. Except during night-time conditions, the magnitude of these errors are generally much smaller than those of other fluxes in the model, indicating a much less important role than the error terms for Day 190-200. The field experiment measurements shown in Figure 4-5 do not indicate significant advection events during this second time window. The comparison of the prior and posterior estimates of surface temperature and micrometeorology to the observations are shown in Figure 4-10. While the difference is not as apparent as for Day 190-200, there is still some obvious improvement which is illustrated by the reduction in the objective function by approximately one half (see Table 4.2). Finally, the statistics for daily average flux estimates are compared to the FIFE observations in Table 4.3 along with those from Day 190-200. While there is a reduction in both bias and RMSE between the prior and posterior estimates, it is much less pronounced than for the Day 190-200 case due to the smaller change in soil moisture initial conditions. Just as for Day190-200, there is a positive bias in the sensible heat flux estimates and a negative bias in the latent heat flux estimates. Note that both the bias and RMSE are significantly smaller for the Day 200-210 window. Assuming the FIFE observation error is stationary, this could be due to the fact that the model errors are smaller, indicating a stronger land-atmosphere coupling (i.e. more information in the observations), or perhaps because they are conditioned on more observations (implicitly also conditioned on those from Day 190-200). Overall however, the results indicate significant value in assimilating observations to estimate surface fluxes.

As a final test of the estimation algorithm, we are interested in the dependence of the model error estimates on the particular window chosen. This test is also related to determining whether the objective function minimization during the Days 190-200 and 200-210 has converged to disparate local minima or nearly global minimum. Accordingly, we use an overlapping assimilation window from Day 195-205 to examine how the model error estimates compare to those from the other two windows. The results are shown in Figure 4-11. Overall the posterior estimates seem to be robust, with the overlapping estimate closely matching trends in the other estimates. The largest discrepancy occurs near the end of the overlapping window. This is due to the fact that the model error is by definition equal to a convolution of the adjoint variables (see Section 4.3.2), which are equal to zero at the end of the assimilation window. The result is that the model error estimate is necessarily close to zero at the end of the assimilation window.

4.5 Summary

In this study the ability to estimate land surface and ABL states and fluxes from readily available surface radiometric temperature and climate station screen-level micrometeorology is demonstrated. The variational data assimilation framework provides an effective way to combine these measurements with a physical model of the system to provide optimal estimates which take into account both measurement and model error. A key aspect of this work is the use of a coupled model, which not only reduces the needed auxiliary forcing data required by an uncoupled model, but allows for the inclusion of observations (in this case micrometeorology) that could not otherwise be assimilated.

The results shown here illustrate the synergism that may exist when using multiple observation types. Using both surface temperature and reference-level micrometeorology measurements allow for the accurate estimation of land surface fluxes even during non-ideal conditions, where large advection-related model errors are present. Furthermore the

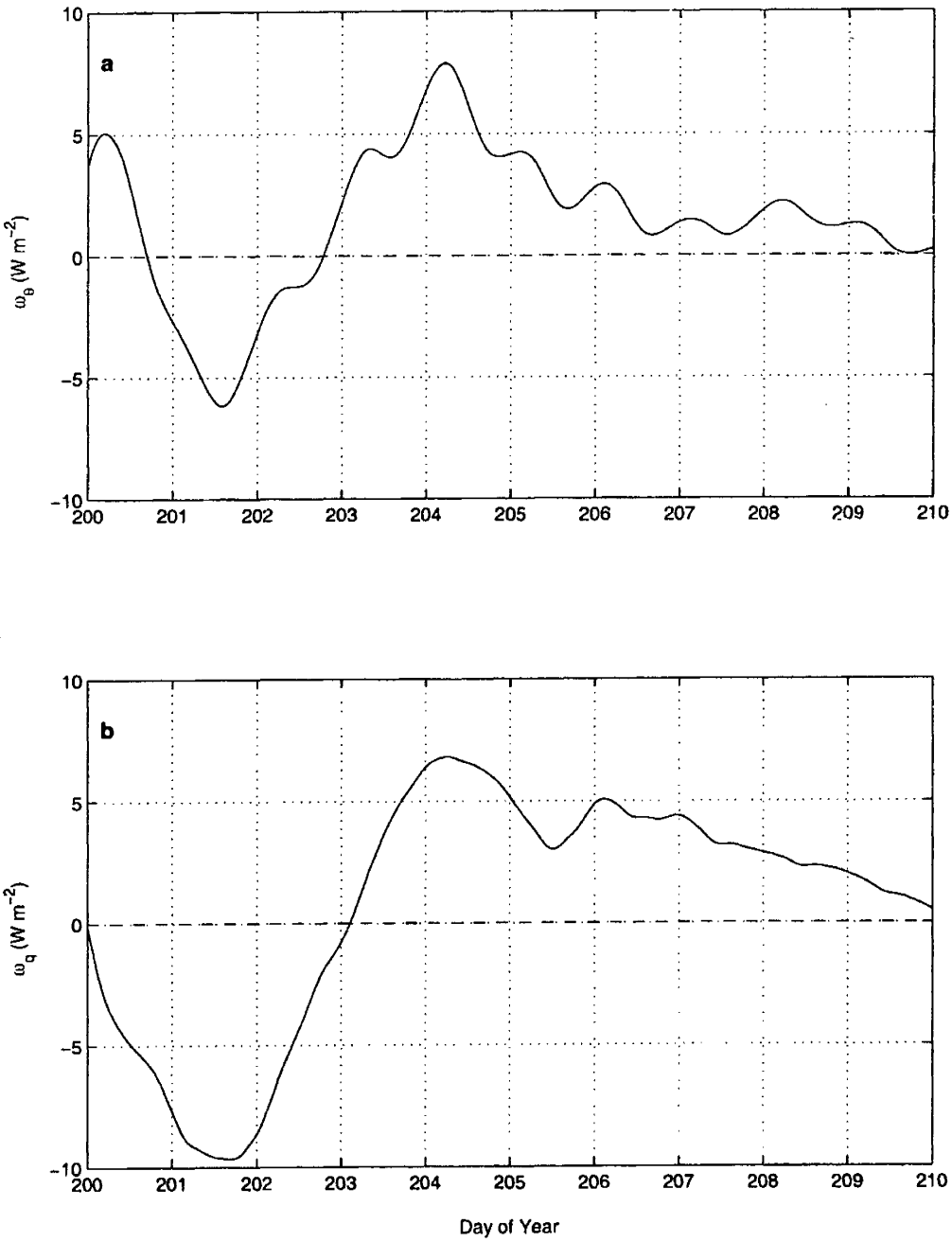

Figure 4-9: Estimated posterior model error (solid lines) in a) ABL potential temperature budget; and b) ABL specific humidity budget at FIFE during Day 200-210. Note prior model error (dashed lines) is equal to zero by convention.

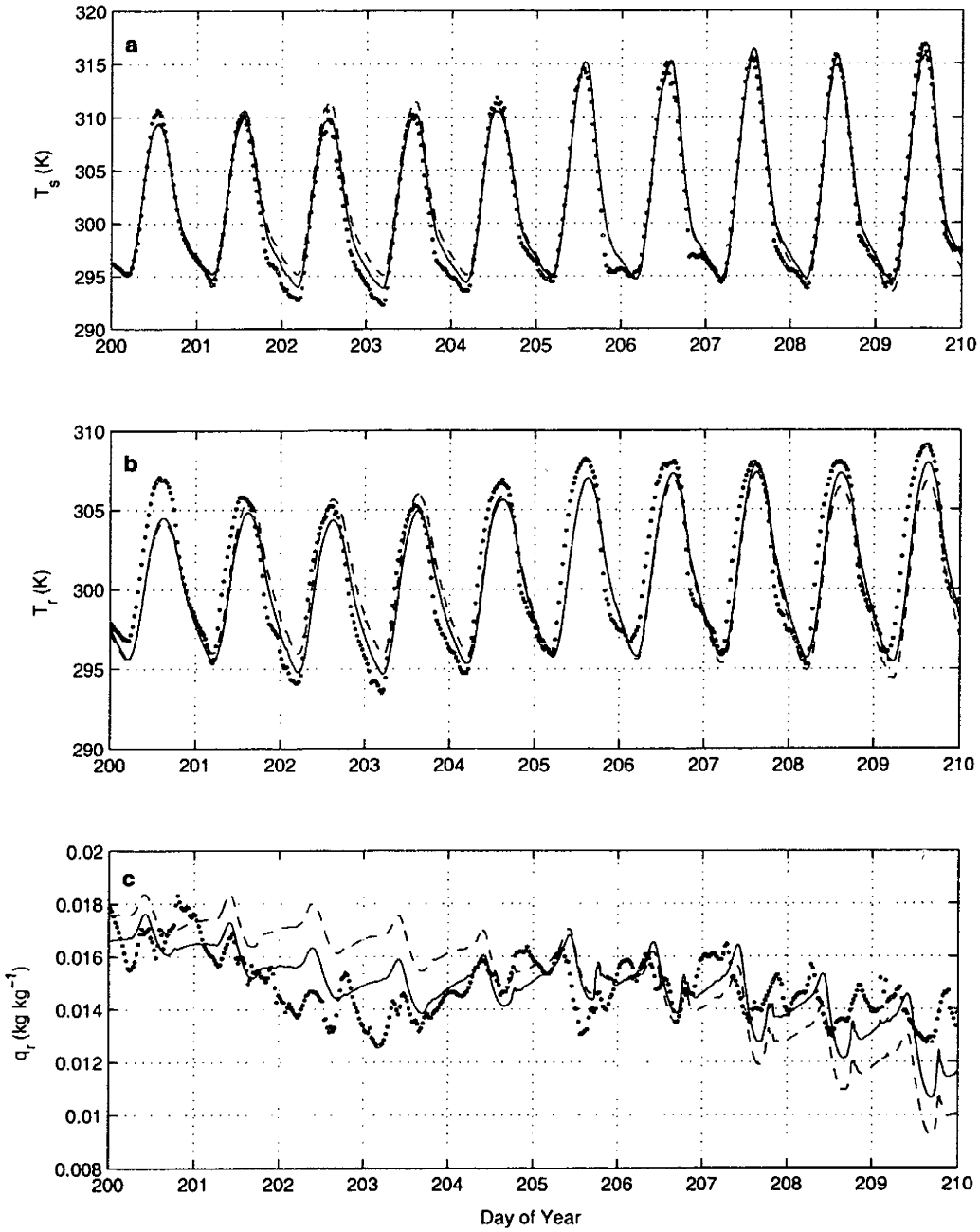

Figure 4-10: Comparison of prior (dashed line), estimated (solid line), and observed (solid dots) a) surface temperature; b) screen-level temperature; and c) screen-level humidity during Day 200-210.

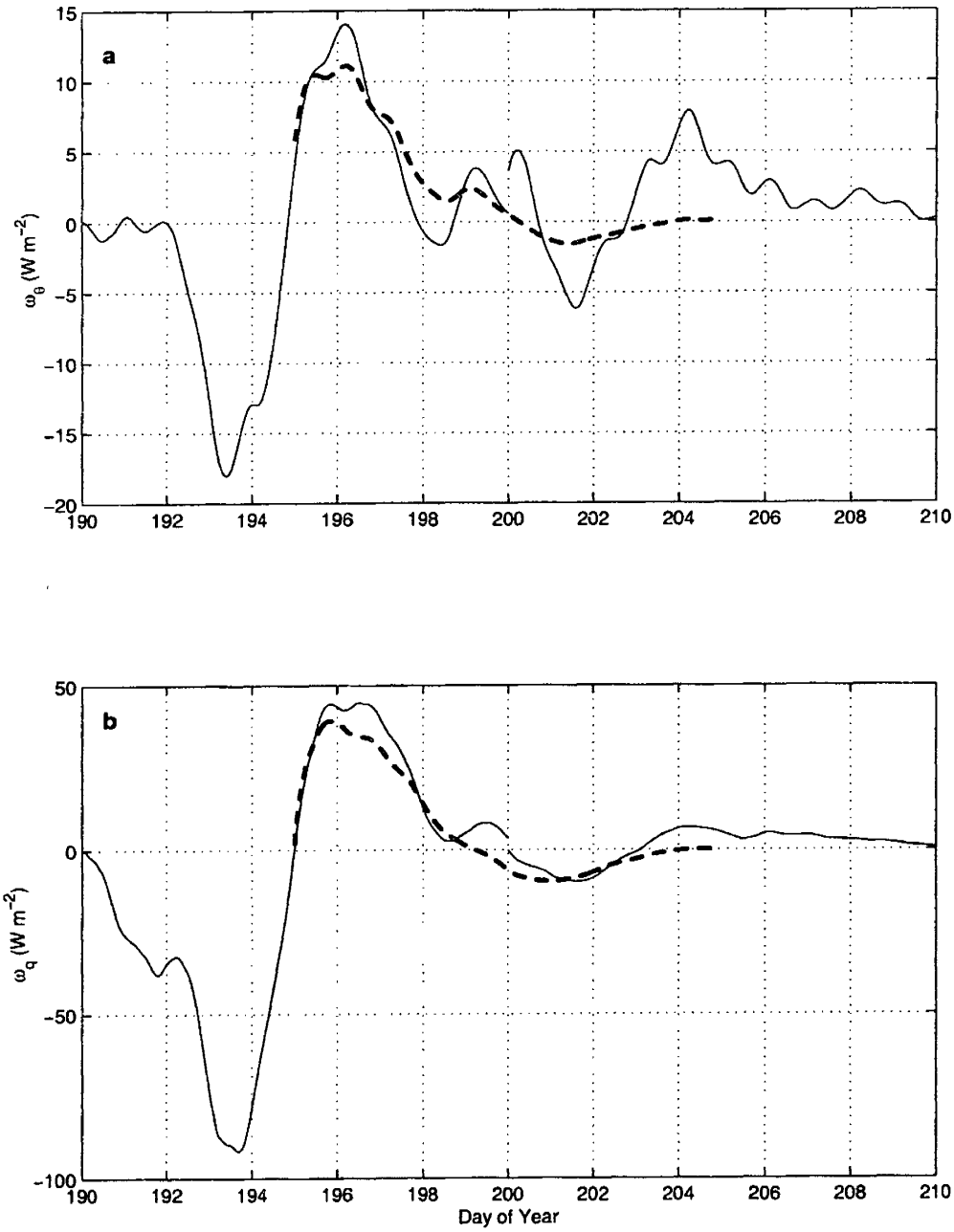

Figure 4-11: Comparison of model error posterior estimate for overlapping assimilation window over Day 195-205 (dashed lines) to those from windows over Day 190-200 and 200-210 (solid lines).

assimilation scheme is able to provide estimates of model errors. This allows diagnosis of structural model errors that may be present due to missing process representation and/or poor or biased parameterizations.

Future research directions should include an extension to a spatially-distributed domain, where heterogeneous land surface characteristics may hinder the estimation scheme, and exploration of other observation types and combinations (e.g. radiosondes, microwave radiobrightness, etc.) that may have significant information content for land data assimilation. Furthermore the possibility of mean bias estimation and adaptive prior statistics estimation needs to be explored in follow-on investigations. Finally, the insight gained in this study is not limited to the variational approach and could be used in other assimilation techniques (i.e. filtering).

Chapter 5

Boundary Layer Entrainment Estimation Through Assimilation of Radiosonde and Micrometeorology Data

5.1 Background

During the daytime, land-atmosphere interactions are primarily driven by the diurnal cycle of net radiation (largely due to solar radiation) at the land surface. The available energy is partitioned into heat and moisture fluxes (sensible and latent heat) intc the atmospheric boundary layer (ABL). Both free and forced convection in the boundary layer leads to the formation of a well mixed layer which grows throughout the day as turbulent eddies entrain generally warmer, drier air from the free atmosphere down into the ABL. In the absence of lateral advection, it is the balance between the surface turbulent fluxes and the entrainment fluxes that determine the characteristics (potential temperature and specific humidity) of the boundary layer. These ABL characteristics play an important role in cloud formation, rain production, as well as other important feedbacks in the coupled system.

There have been many studies which have tried to quantify ABL growth and entrainment. Early studies (Ball (1960); Lilly (1968); Betts (1973); Tennekes (1973); Carson (1973)) developed simple models for ABL growth where the downward entrainment of virtual heat flux was parameterized as a fraction (A_R) of the surface virtual heat flux. Based on laboratory experiments and some observational studies, results were compiled showing the ratio to be on the order of $A_R \approx 0.2$ for thermally driven convective boundary layers (Stull (1998); Stull (1988)). More complicated models were later developed that include the mechanical generation of turbulence, or forced convection, (e.g. Mahrt and Lenschow (1976); Zeman and Tennekes (1977); Smeda (1979); Driedonks (1982)). The inclusion of forced (wind-shear generated) convection generally only slightly increases the expected value of A_R because of the dominance of free (thermally generated) convection during unstable daytime conditions. More recent studies (Betts et al. (1990), Betts et al. (1992); Culf (1992); Betts and Ball (1994)) have found values of this entrainment parameter to be significantly larger ($A_R \approx 0.4$). It is unrealistic however that the forced convection mechanism can explain the large difference in A_R. Hence, the value of this parameter and its variability is still largely up for debate. For modeling land-atmosphere interactions our ability to accurately

estimate this parameter has important implications which warrants further investigation into its expected value and variability.

In this study a variational data assimilation methodology that allows for the estimation of the entrainment parameter by combining radiosonde and micrometeorological observations with a simple coupled boundary layer and land surface model is proposed. The variational (smoothing) approach is ideally suited to this particular problem where we wish to find the optimal estimate of entrainment over a daytime window given various observations. This method is also appealing because it accounts for the uncertainty in the various data streams, while enforcing the dynamics of the model (i.e. water and energy budgets in the ABL, ABL growth, etc.). By including the model, an estimate of the entrainment parameter, as well as estimates of all the system states and fluxes are obtained. The methodology is applied to the FIFE site in Kansas which allows for comparison of our estimates to the observational studies of Betts et al. (1990), Betts et al. (1992), and Betts and Ball (1994). In Section 5.2 the model used in this study is described. Section 5.3 describes the data used from the FIFE site. In Section 5.4 the variational framework is described and in Section 5.5, results from the application to the FIFE site are presented. Finally, conclusions and future applications are discussed in Section 5.6.

5.2 Coupled Boundary Layer-Land Surface Model

The model used in this study is composed of a mixed-layer model representation of the atmospheric boundary layer and a land surface parameterization. The description of the model and its testing is presented in detail in Chapter 2. The land surface component of the model is a typical soil-vegetation-atmosphere-transfer (SVAT) scheme that consists of prognostic equations for land surface temperature and soil moisture states. In this chapter the emphasis is placed on the mixed-layer model, so the reader is referred to Chapter 2 for specific details about the land surface scheme.

For the boundary layer, prognostic equations for the mixed-layer potential temperature and specific humidity state variables (which are uniform with height within the mixed-layer) represent the ABL energy and moisture budgets, and are given by:

$$\rho c_p h \frac{d\theta}{dt} = [R_{ad} + R_{cu} + R_{gu}]\epsilon_a - R_{Ad} - R_{Au} + H + H_{top} \tag{5.1}$$

$$\rho h \frac{dq}{dt} = E + E_{top} \tag{5.2}$$

where definitions of the symbols in this equation (and all others) are given in Appendix C. The evolution of the ABL potential temperature (θ) and specific humidity (q) are principally driven by the balance between the surface sensible and latent heat fluxes (H and E) and the entrainment fluxes (H_{top} and E_{top}) at the top of the mixed-layer. Note that the θ prognostic equation includes a parameterization of the radiative feedback between the surface and overlying atmosphere which accounts for the radiative flux divergence in the ABL energy budget (see Appendix A for details). The idealized model as presented here, does not include a parameterization of advective flux divergence of heat and moisture in the ABL, latent heating (condensation) in the mixed-layer, or clouds. It is therefore most applicable to clear (cloud- and rain-free) days with minimal lateral advection.

The model includes a parameterization of the daytime growth of the mixed-layer given

by:

$$\frac{dh}{dt} = \frac{2\theta G_* e^{-\xi h}}{gh\delta_\theta} + c_h \frac{H_v}{\rho c_p \delta_\theta} \tag{5.3}$$

This parameterization was derived by Smeda (1979) by considering the balance between turbulent kinetic energy (TKE) generated by wind shear (forced convection), TKE production due to thermal (free) convection, and dissipation of TKE via these two mechanisms. The proportionality constant c_h is often set to a value of 0.2. Most of the ABL growth models in the literature consist of very similar formulations or special cases of Equation (5.3). The simplest models (e.g. Betts (1973); Tennekes (1973); and Carson (1973)) consider only thermally generated turbulence (the second term), while the more general formulations (e.g. Mahrt and Lenschow (1976); Zeman and Tennekes (1977); Smeda (1979); Driedonks (1982)) also include the effects due to forced convection or wind shear (first term). During the daytime however the production of thermally generated turbulence generally dominates that of the mechanically generated turbulence, so that the evolution of the ABL height is mostly governed by the second term in Equation (5.3). As a result, the daytime growth of the boundary layer is primarily controlled by the specified parameter c_h and the surface virtual heat flux (H_v) and potential temperature inversion at the top of the ABL (δ_θ). The proper specification of the ABL growth parameter has significant implications on boundary layer energy and moisture budgets.

The inversions in potential temperature and humidity are represented as instantaneous jumps in temperature and humidity at the top of the boundary layer (see Figure 5-1). The strengths of these inversions (δ_θ and δ_q) evolve as follows:

$$\frac{d\delta_\theta}{dt} = \gamma_\theta \frac{dh}{dt} - \frac{d\theta}{dt} \tag{5.4}$$

and

$$\frac{d\delta_q}{dt} = \gamma_q \frac{dh}{dt} - \frac{dq}{dt} \tag{5.5}$$

where the parameters γ_θ and γ_q are the lapse rates in potential temperature and specific humidity immediately above the mixed layer. The potential temperature inversion δ_θ decreases (increases) as the mixed-layer warms (cools) and increases as the boundary layer grows. Similarly, δ_q increases (become more negative) as the boundary layer becomes more moist and as the boundary layer grows (γ_q is generally negative).

The entrainment fluxes mentioned above are proportional to these inversions and to the mixed-layer growth:

$$H_{top} = \rho c_p \delta_\theta \frac{dh}{dt} \qquad\qquad E_{top} = \rho \delta_q \frac{dh}{dt} \tag{5.6}$$

and represent the fluxes of generally warm and dry air into the ABL respectively. Based on the above model, an expression for the entrainment parameter A_R can be derived:

$$A_R = \frac{H_{v_{top}}}{H_v} = \frac{H_{top} + 0.07 L_v E_{top}}{H_v} = \frac{\rho \left(c_p \delta_\theta + 0.07 L_v \delta_q\right) \frac{dh}{dt}}{H_v} \tag{5.7}$$

In the case that mechanical generation of turbulence is negligible, the second term in Equa-

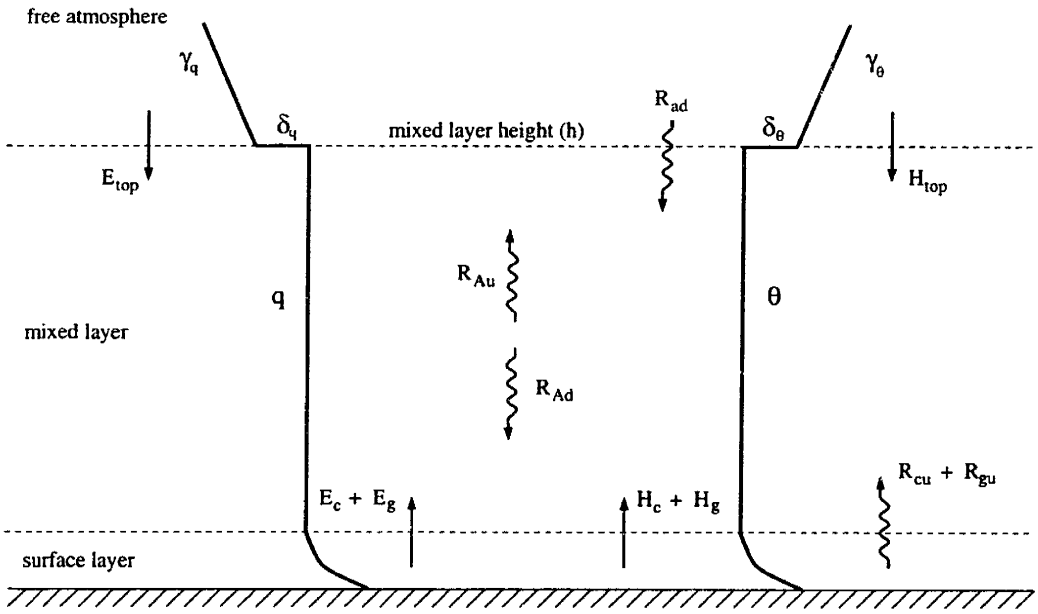

Figure 5-1: Idealized profiles of ABL states and corresponding fluxes between the mixed layer and land surface and the mixed layer and overlying atmosphere. Surface turbulent fluxes occur across the surface layer (of thickness $\sim 0.1h$) and entrainment fluxes occur across the interface between the free atmosphere and mixed layer (at height h).

tion (5.3) dominates the first, so that the expression can be simplified to yield:

$$A_R \approx \frac{\rho(c_p\delta_\theta + 0.07L_v\delta_q)c_h\frac{H_v}{\rho c_p\delta_\theta}}{H_v} = (1 + 0.07L_v\delta_q)c_h \tag{5.8}$$

Thus in models of this type, the specification of c_h largely dictates the entrainment ratio A_R. In cases where the ABL humidity inversion is small ($\delta_q \approx 0$), A_R is essentially equal to c_h. As a result of early research on the topic (discussed in Section 5.1), this parameter is often set to 0.2. However, recent suggestions that this parameter might be much larger have significant implications for boundary layer modeling studies. In this work we present a data assimilation framework which allows for the estimation of c_h using radiosonde and micrometeorology data. Once estimated, it can then be used in Equation (5.7) to determine the average daytime A_R for each day.

5.3 Data Requirements

5.3.1 Observations used for Assimilation

The primary sources of data used in this study consist of the spatially-averaged FIFE surface measurements compiled by Betts and Ball (1998), and the ABL radiosonde observations of W. Brutsaert (see Strebel et al. (1994)) during intensive field campaigns (IFCs) 1-3 during the summer of 1987 (see Sellers et al. (1992) for an overview of the FIFE experiment). The surface measurements are given at 30-minute resolution, while radiosondes were launched most days during the IFCs at roughly 90-min intervals. The FIFE database was examined to identify days during the IFCs which seemed to most closely obey the primary assumptions in our model (i.e. cloud-free with minimal lateral advection). This was done so that estimates of the entrainment parameter for a given day were not contaminated by systematic model errors, but instead represent reasonable values. All analysis was done during the growth phase of the boundary layer for each day ($\sim$ 7:30am-5:00pm local time). Three days from each IFC were chosen and are listed in Table 5.1 along with the number of successfully deployed radiosondes during the ABL growth phase, which, depending on the day, provided 3-7 observations. Examples of potential temperature profiles from a day during each IFC are shown in Figures 5-2–5-4. Note the evolution of the well mixed-layer (uniform θ with height) in these figures. Specific humidity profiles exhibit similar characteristics. Also, note that the profile above the mixed-layer is relatively constant throughout the day. From the radiosonde data, estimates of mixed-layer height (h), potential temperature (θ), and specific humidity (q) were obtained.

The mixed-layer height observations have a direct connection to the c_h parameter (Equation 5.3), while the potential temperature and humidity observations are linked to c_h via the entrainment fluxes in the budget Equations (5.1) and (5.2). Additionally, we chose to include the (30-min) screen-level temperature (T_r) and specific humidity (q_r) from the Betts and Ball (1998) dataset (typically 18-19 observations per day) in the assimilation scheme presented in Section 5.4. The micrometeorological data is more indirectly connected to c_h, but can contain useful information via their dependence on θ and q (see Chapter 4). The particular number of micrometeorological observations for each day are given in Table 5.1.

Table 5.1: Number of radiosonde and micrometeorology observations during growth phase of ABL for each analysis day.

IFC	Date (Julian Day)	# of ABL (Sonde) Obs.	# Micromet. Obs.
1	Jun 04 (155)	6	19
	Jun 05 (156)	6	19
	Jun 06 (157)	3	19
2	Jun 26 (177)	4	19
	Jul 06 (187)	7	19
	Jul 11 (192)	5	18
3	Aug 15 (227)	6	18
	Aug 16 (228)	7	19
	Aug 17 (229)	5	19

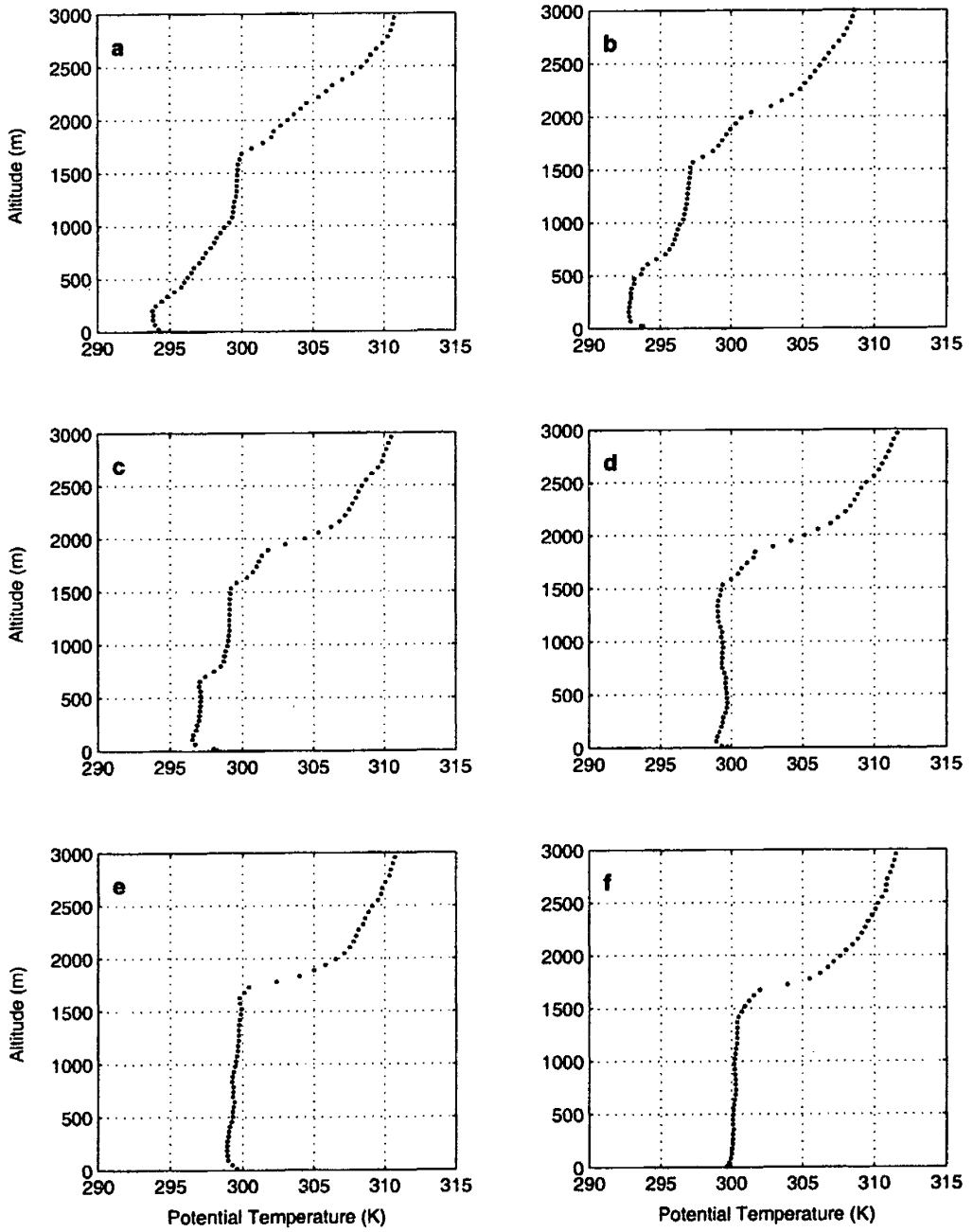

Figure 5-2: Potential temperature profiles for June 5 (Julian Day 156). The panels correspond to (local) launch times of: a) 7:45am; b) 9:15am; c) 10:30am; d) 12pm; e) 3pm; and e) 4:45pm.

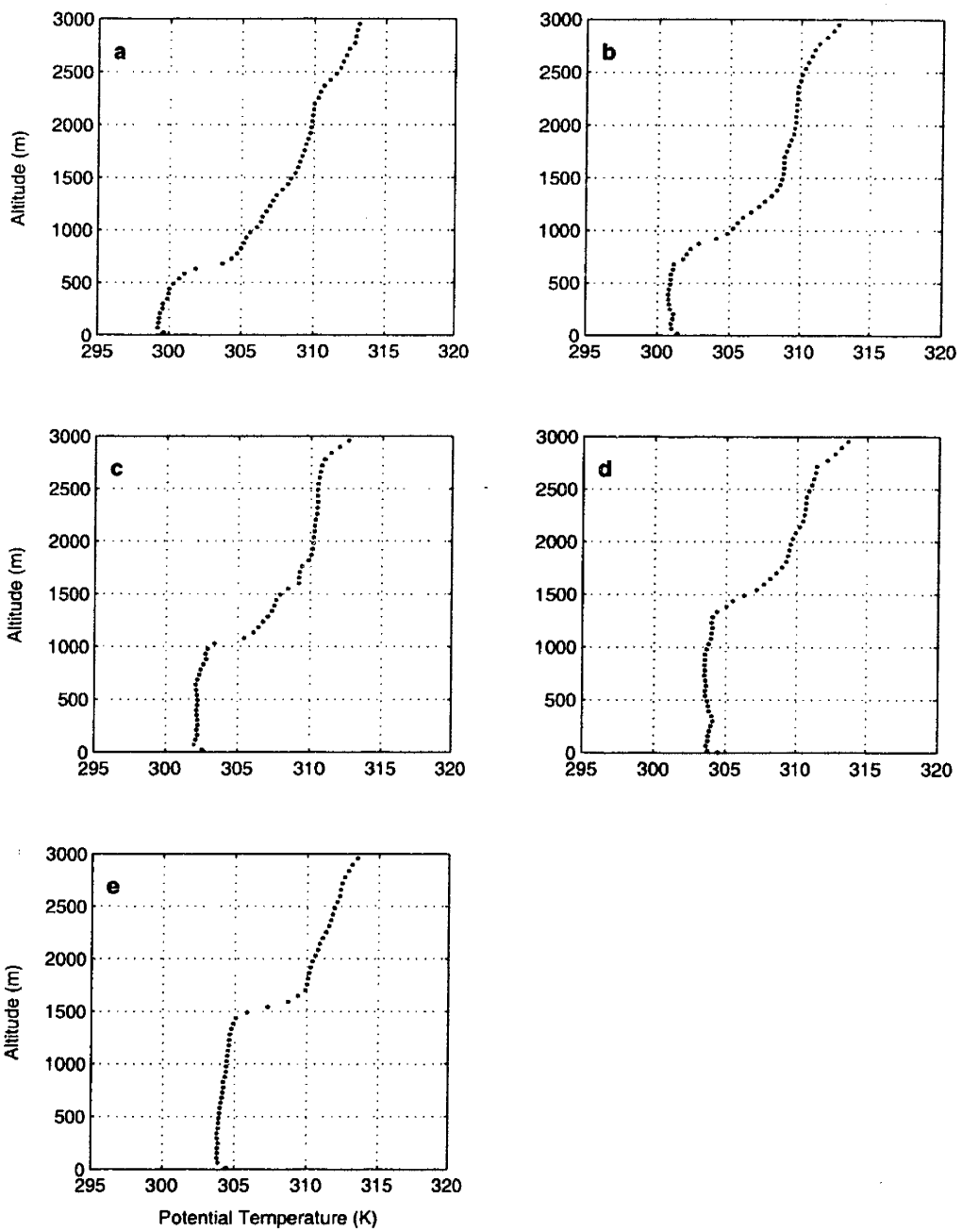

Figure 5-3: Potential temperature profiles for July 11 (Julian Day 192). The panels correspond to (local) launch times of: a) 7:45am; b) 9:15am; c) 10:30am; d) 12:30pm; and e) 1:45pm.

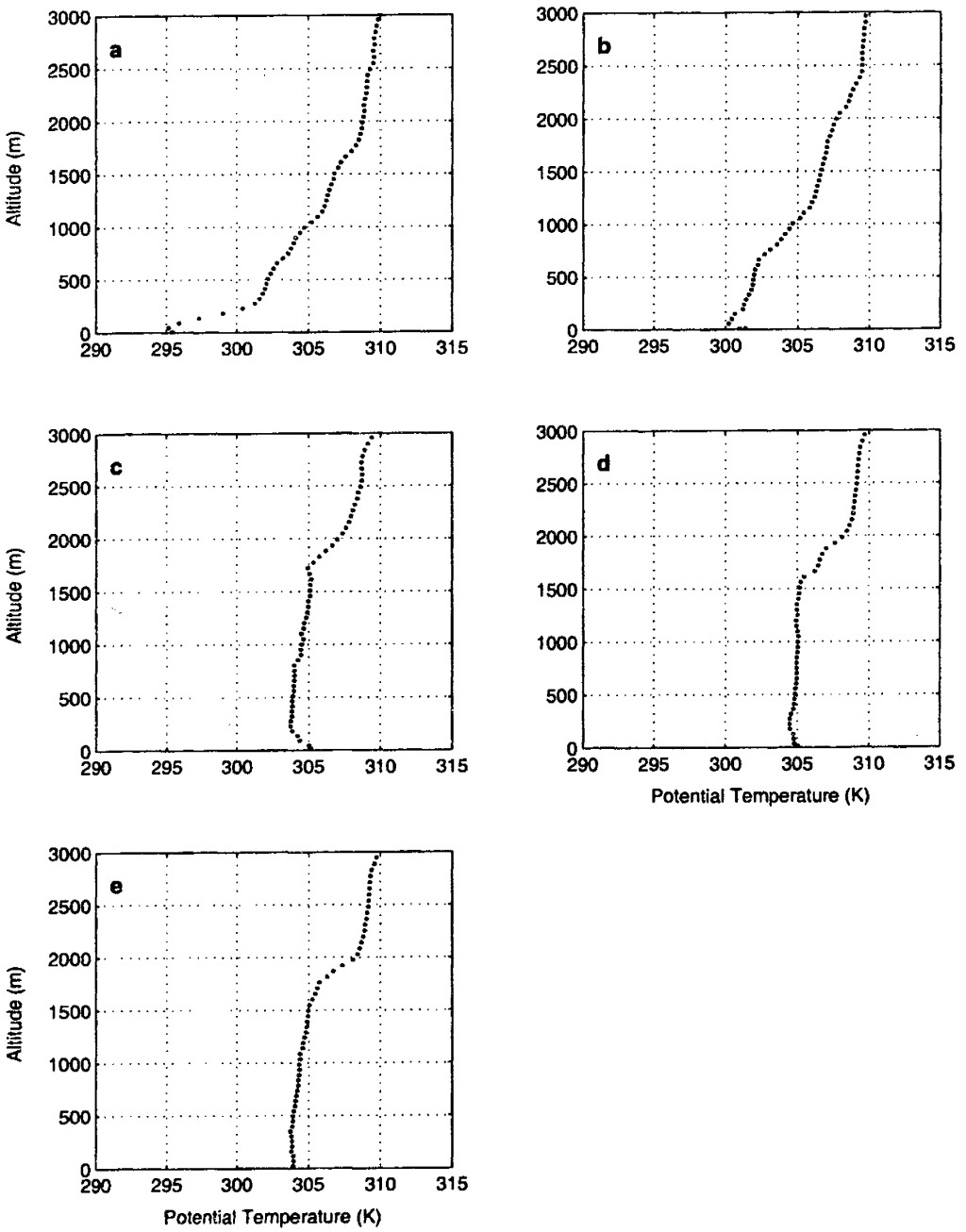

Figure 5-4: Potential temperature profiles for August 17 (Julian Day 229). The panels correspond to (local) launch times of: a) 7:45am; b) 9:15am; c) 1:30pm; d) 3:15pm; and e) 4:30pm.

5.3.2 Forcing data

The model described above requires incoming solar radiation and reference-level wind speed as forcing variables. Time series of these variables are provided by the surface dataset. Cloud-free days were purposely chosen so that radiative forcing of the surface was large (i.e. peak solar radiation > 900 Wm^{-2}; peak net radiation > 600 Wm^{-2}). The wind speed varied from day to day with a range of 1-10 ms^{-1}. The mean wind speed for each day is given in Table 5.2. Because our model includes forced convection in the mixed-layer growth equation, we would expect (with all else equal) days with higher windspeeds to have larger values of the entrainment parameter A_R.

The model also requires the lapse rates in potential temperature and specific humidity above the mixed-layer. For each day, an early morning radiosonde ($\sim$ 7:30am local time) was used to estimate these lapse rates. Quadratic functions were fit to the profiles in potential temperature and specific humidity above the early morning mixed-layer and generally provided an adequate fit to the observations. Examples of these fits for the three days discussed above are given in Figure 5-5. With respect to boundary layer growth, the most important fit is in potential temperature (due to its influence on δ_θ) at intermediate heights, which correspond to the maximum growth rates at mid-day. Note that the profiles in potential temperature generally provide a better fit than the specific humidity profiles. A higher order function could be used to fit the radiosonde profiles, however the lapse rates are meant to represent the general characteristics of the free atmosphere and the quadratic fits seem more than adequate for our purposes. The temperature profile is most important with respect to the estimation of boundary layer growth, and is represented very well. The lapse rates γ_θ and γ_q are, by definition, equal to the the derivative of these profiles with respect to z (evaluated at h). Thus γ_θ and γ_q are specified as linear functions of h for each day. The equations for these parameters are given in Table 5.2 for each day.

5.3.3 Initial conditions

Initial conditions of the states at the beginning of each day are required for the model. The surface state initial conditions can be inferred with reasonable accuracy from the FIFE surface dataset. The ABL initial conditions are estimated from the radiosonde data. Because ABL growth and entrainment is quite sensitive to the initial ABL states, an ensemble of ABL initial conditions (around the estimated values) are used in our framework to obtain a more robust estimate of the entrainment parameter. This ensemble approach is incorporated in the estimation algorithm and is discussed in more detail below.

5.4 Data Assimilation Framework

5.4.1 Estimation algorithm

Data assimilation provides a framework which allows us to merge measurements and physical models under the supposition that both provide useful information about the state of the system. The model presented above can be written in the following concise form:

$$\frac{d\mathbf{y}}{dt} = \mathbf{F}(\mathbf{y};\boldsymbol{\alpha}) \qquad \mathbf{y}(t_0) = \mathbf{y}_0 \tag{5.9}$$

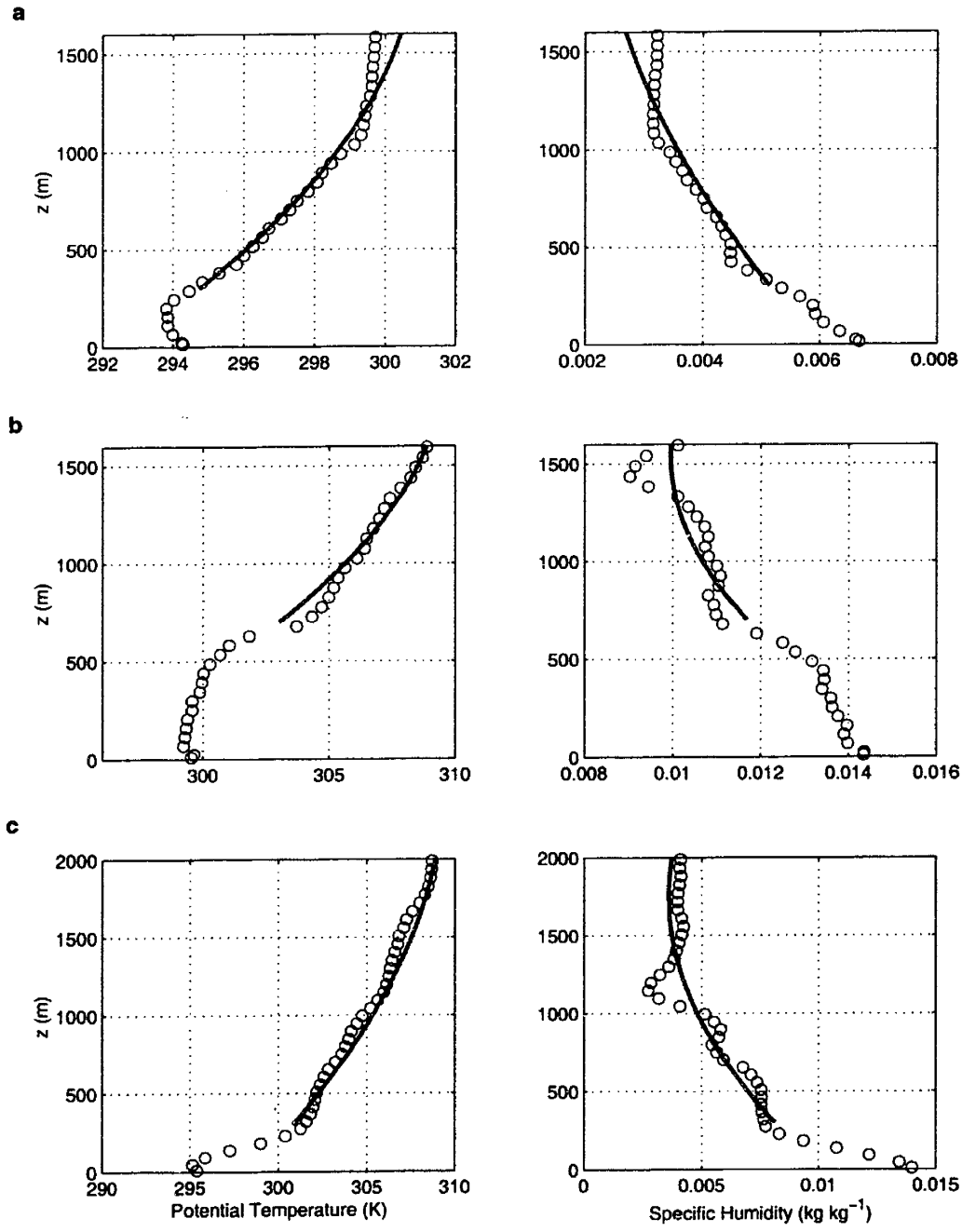

Figure 5-5: Examples of quadratic fits of θ and q profiles above the mixed-layer for a) June 5, b) July11, and c) August 17. These profiles are used to determine the lapse rates γ_θ and γ_q as a function of mixed layer height h (shown in Table 5.2).

Table 5.2: The mean reference-level (2m) windspeed forcing and lapse rate parameters (as a function of mixed-layer height) for each analysis day. The lapse rates are derived by taking the derivative of a fitted quadratic function to an early morning radiosonde for each day.

Julian Day	Mean Windspeed (ms^{-1})	γ_θ (K km^{-1})	γ_q ($kgkg^{-1}$ km^{-1})
155	1.4	$4.8 - 1.8 \times 10^{-3}h$	$-0.9 \times 10^{-3} + 0.2 \times 10^{-6}h$
156	5.1	$8.1 - 3.9 \times 10^{-3}h$	$-3.02 \times 10^{-3} + 1.2 \times 10^{-6}h$
157	6.9	$6.1 + 0.5 \times 10^{-3}h$	$-0.7 \times 10^{-3} + 3.2 \times 10^{-6}h$
177	2.1	$0.6 + 1.0 \times 10^{-3}h$	$-0.4 \times 10^{-3} - 0.2 \times 10^{-6}h$
187	5.6	$17.6 - 9.0 \times 10^{-3}h$	$-14.6 \times 10^{-3} + 4.6 \times 10^{-6}h$
192	9.7	$14.9 - 7.3 \times 10^{-3}h$	$-7.6 \times 10^{-3} + 4.9 \times 10^{-6}h$
227	7.2	$24.0 - 15.6 \times 10^{-3}h$	$-13.1 \times 10^{-3} + 7.3 \times 10^{-6}h$
228	4.7	$12.6 - 3.7 \times 10^{-3}h$	$-11.8 \times 10^{-3} + 3.4 \times 10^{-6}h$
229	3.1	$8.6 - 3.3 \times 10^{-3}h$	$-7.6 \times 10^{-3} + 4.3 \times 10^{-6}h$

where $\mathbf{y}(t)$ is the state vector, $\mathbf{F}$ is a nonlinear vector operator which is a function of the model states and the time-invariant model parameters ($\boldsymbol{\alpha}$). The model initial conditions $\mathbf{y}_0$ can be estimated from observations as described above. While the vector $\boldsymbol{\alpha}$ can contain any number of model parameters, in this study we focus solely on the uncertain parameter c_h. The random parameter c_h is characterized by its prior expected value $\overline{c_h}$ and its prior covariance C_{c_h} (or in this single-valued case its variance $\sigma^2_{c_h}$). In this application we specify $\overline{c_h}$=0.2 and $\sigma_{c_h} = 0.1$.

The model states are related to the observations via the so-called measurement equation:

$$\mathbf{Z} = \mathbf{M}(\mathbf{y}) + \boldsymbol{\nu} \tag{5.10}$$

where $\mathbf{Z}$ is the measurement vector, which in this application contains vectors of ABL observations: mixed-layer height (h^{obs}), potential temperature (θ^{obs}), and specific humidity (q^{obs}) and reference-level micrometeorology observations: temperature (T_r^{obs}) and specific humidity (q_r^{obs}) throughout the daytime assimilation window. The measurement operator $\mathbf{M}(\mathbf{y})$ represents the diagnostic equations which map the model states onto the observed variables. For the ABL observations, there is simply a one-to-one correspondence between the measurements and model states, while for the screen-level observations, a more complicated relationship exists (see Chapter 4). The measurements are assumed to include unbiased measurement error with a specified covariance matrix C_ν. For simplicity, measurement errors are assumed uncorrelated in this application. The measurement error standard deviations for θ, q, h, T_r, and q_r observations are: 1K, 2×10^{-3} kg/kg, 150m, 1K, and 1×10^{-3} kg/kg respectively.

To obtain a posterior estimate of the unknown entrainment parameter (conditioned on the data), the following Bayesian least-squares performance index can be minimized with respect to c_h over the assimilation window $t = [t_0, t_f]$:

$$J = [\mathbf{Z} - \mathbf{M}(\mathbf{y})]^T \, \mathsf{C}_\nu{}^{-1} \, [\mathbf{Z} - \mathbf{M}(\mathbf{y})] + [c_h - \overline{c_h}] \, (\sigma^2_{c_h})^{-1} \, [c_h - \overline{c_h}] + 2\int_{t_0}^{t_f} \boldsymbol{\lambda}^T \left[\frac{d\mathbf{y}}{dt} - \mathbf{F}(\mathbf{y}, c_h)\right] dt \tag{5.11}$$

The first term in the performance index represents the misfit between the data ($\mathbf{Z}$) and model predictions ($\mathbf{M}(\mathbf{y})$). The second term penalizes deviations from the prior value of c_h. These two terms are normalized by their corresponding (co)variances. The final term is the adjoined model constraint which is by definition zero, but ensures that the estimated states are dynamically consistent over the assimilation window. The scalar functional J is minimized by taking its first variation (see Chapter 2) which yields the forward model (as shown in Eq. 5.9) as well as the adjoint model of the system:

$$\frac{d\boldsymbol{\lambda}}{dt} = -\left(\frac{\partial \mathbf{F}}{\partial \mathbf{y}}\right)^T \boldsymbol{\lambda} - \left(\frac{\partial \mathbf{M}}{\partial \mathbf{y}}\right)^T [\delta] \mathsf{C}_\nu{}^{-1} [\mathbf{Z} - \mathbf{M}(\mathbf{y})] \qquad \boldsymbol{\lambda}(t_f) = 0 \tag{5.12}$$

and an equation for the gradient in J with respect to c_h:

$$\frac{\partial J}{\partial c_h} = [c_h - \overline{c_h}] \, (\sigma^2_{c_h})^{-1} - \int_{t_0}^{t_f} \left(\frac{\partial \mathbf{F}}{\partial c_h}\right)^T \boldsymbol{\lambda} \, dt \tag{5.13}$$

Note that while only the h evolution equation (Equation 5.3) is a direct function of c_h, all of the ABL Equations (5.1)–(5.5) are functions of the mixed-layer growth and thus included in the integral in Equation (5.13).

Note that the adjoint model must be integrated backward in time to obtain the adjoint variables $\boldsymbol{\lambda}(t)$. The adjoint model is a coupled set of differential equations that depends on the state vector via the forward model Jacobian ($\partial\mathbf{F}/\partial\mathbf{y}$) and is forced by the measurement-model misfit. Once the adjoint variables are known, the above gradient can be computed and used in a gradient search algorithm to minimize J. Here we use a simple steepest descent method. In the steepest descent algorithm, a parameter (u) at iteration $k+1$ is given by:

$$u^{k+1} = u^k - \varepsilon \left(\frac{\partial J}{\partial u} \right)^k \tag{5.14}$$

where ε is a scalar step size. For the unknown parameter in this study (c_h), we specify the step size ε to be proportional to the corresponding uncertainty (variance) in the parameter (i.e. $\varepsilon = \eta\sigma^2_{c_h}$). Substituting this along with the gradient expression shown above, the update equation for c_h is given by:

$$c_h^{k+1} = c_h^k - \eta(c_h^k - \overline{c_h}) + \eta\sigma^2_{c_h} \int_{t_0}^{t_f} \left(\frac{\partial \mathbf{F}}{\partial c_h} \right)^T \boldsymbol{\lambda}\, dt \tag{5.15}$$

The estimation procedure is done iteratively by (i) integrating the forward model with the most recent parameter estimate, (ii) integrating the adjoint model backward in time about the current state trajectory, (iii) updating the parameter using Equation (5.15), and (iv) repeating steps (i)-(iii) until sufficient convergence is achieved. For this problem, convergence can usually be achieved in 5-10 iterations.

5.4.2 Ensemble Approach

The above approach yields a single estimate of the parameter c_h for a given set of initial conditions and forcing. However it does not give error bounds on this estimate. Further, the estimate is a function of specified inputs for which it may contain errors. For this reason we chose to extend the traditional variational framework above to include an ensemble approach. Based on the uncertainty of radiosonde observations, and the sensitivity of ABL growth to mixed-layer initial conditions (especially in δ_θ) and free-atmosphere lapse rates (especially γ_θ), we chose to randomize the ABL initial conditions (θ_0, q_0, $\delta_{\theta 0}$, δ_{q0}, and h_0) and lapse rate (γ_θ and γ_q) inputs to the above algorithm. This was done in the following way: From the radiosonde data we formed best estimates of these variables as described in Section 5.3. Using these estimates as the mean conditions we generated an ensemble of realizations from a normal distribution with the given mean and a specified standard deviation. The estimation algorithm was then run for each replicate to obtain an ensemble of c_h estimates. With this ensemble we can not only provide a mean estimate of c_h, but error bounds as well. The standard deviations used for θ_0, q_0, $\delta_{\theta 0}$, δ_{q0}, and h_0 are: 1K, 2×10^{-3} kg/kg, 0.5 K, 0.5×10^{-3} kg/kg, and 100 m respectively. As mentioned above, the mean lapse rates were determined by fitting functions to an early morning radiosonde, and are of the form:

$$\gamma_\theta = a_{\theta 1} + a_{\theta 2} h \qquad\qquad \gamma_q = a_{q1} + a_{q2} h \tag{5.16}$$

The ensemble for these parameters was obtained by generating coefficients in each equation from a normal distribution with a mean given by the estimate and a coefficient of variation of 10%. Through testing of the above ensemble/variational algorithm it was found that ensembles of 50 replicates provided stationary estimates of the mean and standard deviation of c_h for a particular day. Therefore the results in the following section were obtained by applying this technique (with 50 replicates) for each of the nine FIFE IFC days.

5.5 Results

To estimate the entrainment parameter we applied the methodology described above to each of the nine FIFE days using all of the observations described in Section 5.3.1. Due to the strong connection between the ABL observations and entrainment we would expect a good estimate of the parameter c_h and thus A_R. These results are presented in Section 5.5.1. Following this set of experiments we re-ran the estimation algorithm (only assimilating micrometeorology) to determine if there is any skill in the estimation (relative to the first set of estimates) when using only more readily available micrometerology data. These results are presented in Section 5.5.2.

5.5.1 Estimates Using both ABL and Micrometeorology Observations

In applying the above procedure, an ensemble of posterior c_h estimates were obtained for each of the FIFE days examined. For a given day, the posterior c_h ensemble provides an ensemble of estimates of all model states and fluxes throughout the day. To get a sense of how the posterior estimate is obtained, Figures 5-6–5-8 show the estimated (averaged across ensemble) prior and posterior ABL states and reference-level temperature and humidity compared to the assimilated observations for June 5, July 11, and August 17. These correspond to the same three days whose potential temperature profiles were shown in Figures 5-2–5-4 and are representative of the other FIFE days examined. The posterior c_h estimate minimizes the total model-measurement misfit throughout the day. This is evident in Figures 5-6–5-8 where in general the posterior estimates are closer to the observations than are the prior estimates. The largest changes are generally associated with the mixed-layer height (h), ABL specific humidity (q), and reference-level humidity (q_r). The change in h is positive in all cases indicating the prior value of c_h is too small. The significant changes in q and q_r are due to the large additional entrainment of dry air (E_{top}) associated with increased boundary layer growth. For θ and T_r the posterior is closer to the observations, but the change is surprisingly small considering the expected increased entrainment of warm air into the boundary layer. This is explained by the fact that while the increased sensible heat flux (H_{top}) has a warming effect, a deeper boundary layer has a cooling effect. In other words, the net flux ($H + H_{top}$) per unit depth, which is responsible for the temperature evolution, is of similar magnitude in both the prior and posterior cases. This effect is not seen in the humidity variables since the entrainment flux is negative (i.e. increased entrainment and deeper mixed-layer both have a drying effect). These results would imply that assimilating ABL potential temperature and/or screen-level temperature alone would not necessarily provide a robust estimate of c_h due to the weaker signal. However when used in conjunction with the mixed-layer height and humidity observations, a robust estimate is indeed obtained (discussed below).

Table 5.3 shows the prior and posterior values of the objective function for each analysis day. Given good assumptions about the parameter and observation error statistics, the

objective function value should be a chi-squared random variable with an expected (mean) value equal to the number of measurements, and a variance of two times the number of measurements (Bennett (1999)). These statistics are easily computed based on the number of observations given in Table 5.1. Note that there are two micrometeorology measurements and three ABL measurements at each observation time. For example, the total number of measurements for Day 155 is $3 \times 6 + 2 \times 19$ for a total of 56 measurements. Therefore the expected value of the objective function is 56, with a standard deviation of $\sqrt{2 \times 56} = 11$. Table 5.3 shows the expected value and corresponding standard deviation for each day in relation to the prior and posterior objective function values. In general, the prior values are significantly different that the expected value, while the posterior values are within 1–2 standard deviations of the expected value. These results give statistical confidence about our entrainment parameter estimates.

Table 5.3: Comparison of prior and posterior objective functional values to expected value for case where ABL and micrometerology observations are assimilated.

IFC	Julian Day	J (prior)	E[J] (Std. Dev.)	J (posterior)
1	155	219	56 (11)	59
	156	292	56 (11)	64
	157	83	47 (10)	34
2	177	86	50 (10)	52
	187	354	59 (11)	42
	192	286	51 (10)	57
3	227	155	54 (10)	57
	228	314	59 (11)	66
	229	236	53 (10)	42

Figures 5-9–5-11 show the estimated surface and entrainment fluxes for June 5, July 11, and August 17. A key point in these figures is that the model predicted surface fluxes match the observed FIFE data reasonably well (Figures 5-9a,b; 5-10a,b; and 5-11a,b). While this is mostly due to the correct specification of land surface initial conditions, it is important because the virtual heat flux H_v is largely responsible for driving mixed-layer growth throughout the day (see Equation (5.3)). These results give further credibility to the entrainment estimates that are discussed in detail below. The estimated entrainment fluxes (Figures 5-9c,d; 5-10c,d; and 5-11c,d) generally peak shortly after noon when the

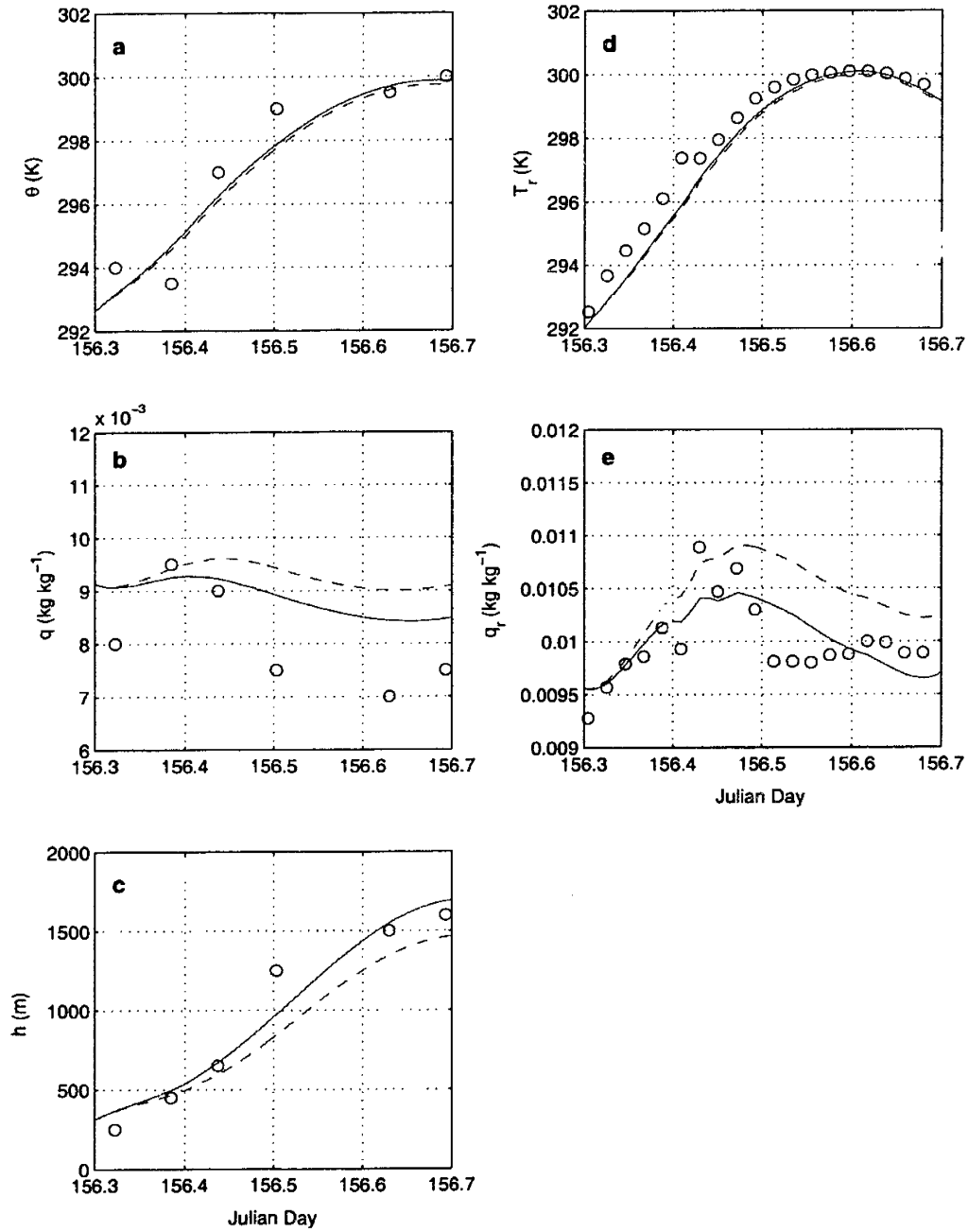

Figure 5-6: Comparison of mean prior (dashed lines) and posterior (solid lines) estimates to assimilated observations (open circles) for June 5. Mean estimates are obtained by averaging over the ensemble.

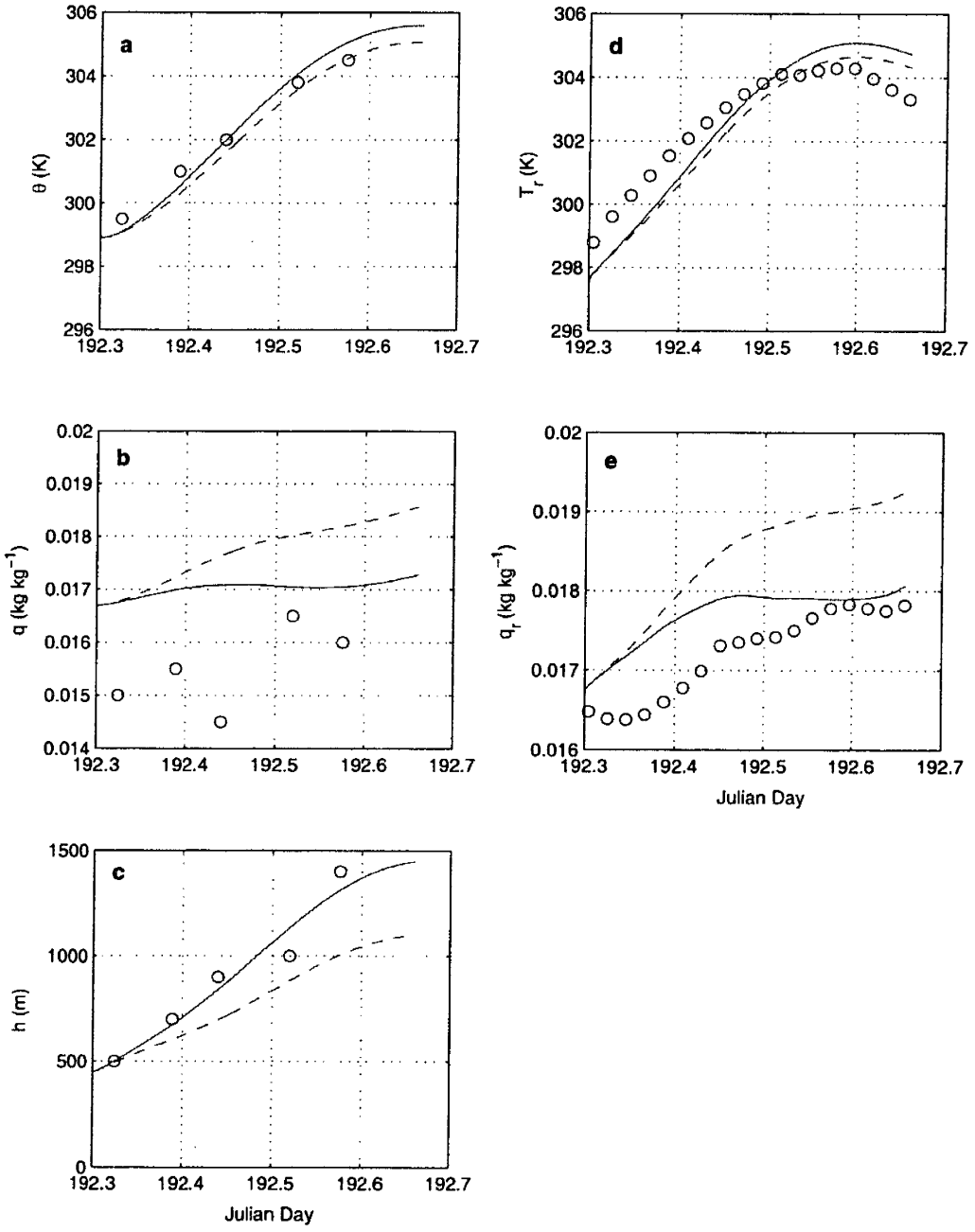

Figure 5-7: Comparison of mean prior (dashed lines) and posterior (solid lines) estimates to assimilated observations (open circles) for July 11. Mean estimates are obtained by averaging over the ensemble.

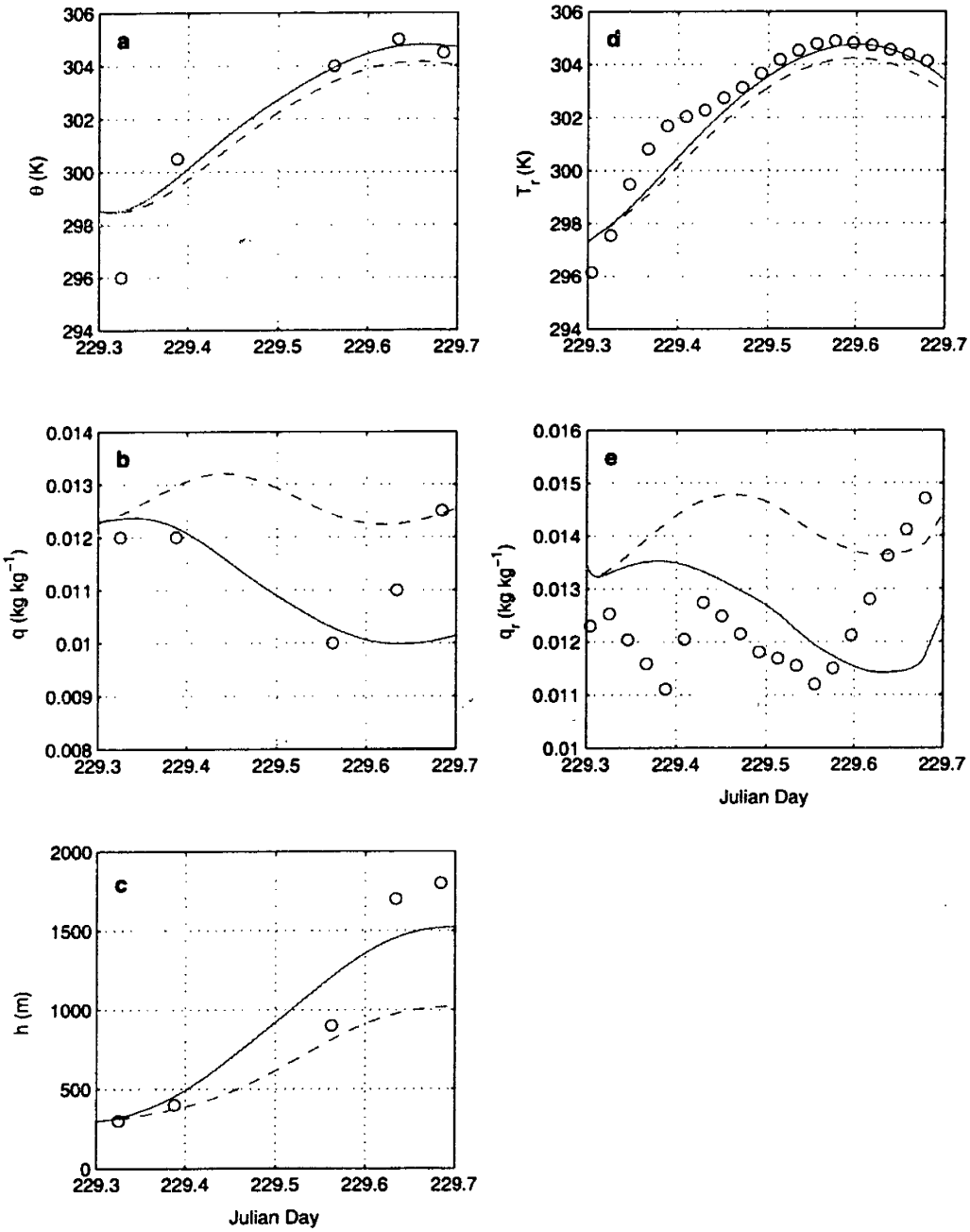

Figure 5-8: Comparison of mean prior (dashed lines) and posterior (solid lines) estimates to assimilated observations (open circles) for August 17. Mean estimates are obtained by averaging over the ensemble.

boundary layer growth rate is at its maximum. The magnitude of these fluxes depend on both dh/dt (and thus the estimate of c_h), as well as the inversions and lapse rates in potential temperature and humidity at the top of the mixed layer. For these three cases the magnitude of the peak entrainment fluxes vary from 75-125 Wm^{-2} for sensible heat and 400-700 Wm^{-2} for latent heat (note negative sign). The large (negative) latent heat flux serves to balance the surface evaporation, which keeps the ABL humidity relatively constant throughout the day.

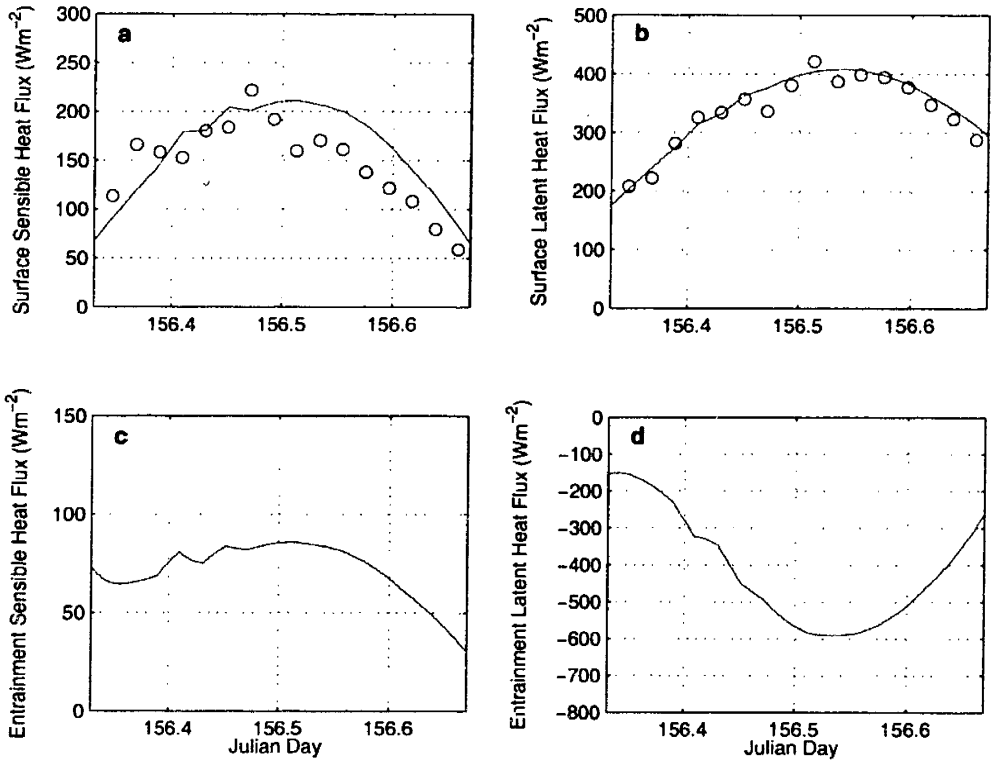

Figure 5-9: Surface and entrainment fluxes for June 5 (Julian Day 156). The panels correspond to a) surface sensible heat; b) surface latent heat; c) mixed-layer top sensible heat entrainment; and c) mixed-layer top latent heat entrainment flux. The observed surface fluxes are given by 'o' symbols.

A summary of the results for all of the days is provided in Table 5.4. The mean posterior estimates of c_h, daytime average surface (H and L_vE) and entrainment (H_{top} and L_vE_{top}) fluxes, and the resulting values of A_R (computed with Equation (5.7)) are given along with error bounds computed from the ensemble. Note that in all cases the estimate of c_h is larger than the prior estimate of 0.2. There is also quite a bit of variability in the estimates, which range from a low of 0.34 on June 4 to a high of 0.88 on August 16. The mean value of c_h across all days is 0.55 $\pm$ 0.11. As a result of day to day variability in c_h estimates, surface fluxes, and lapse rates above the mixed-layer, there is significant variability in the entrainment fluxes. This is especially true of the average latent heat entrainment flux which varies from a low of -271 ($\pm$ 25) Wm^{-2} on June 5 to a high of -514 ($\pm$ 51) Wm^{-2} on August 16. This difference is due to the combination of relatively small boundary layer growth and

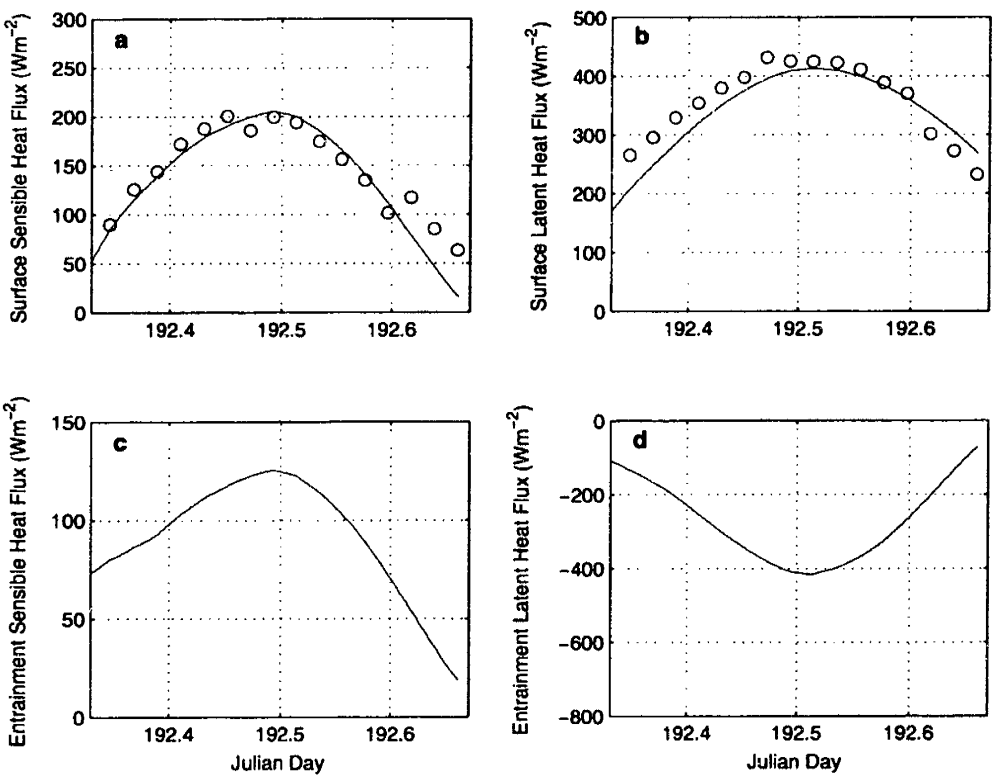

Figure 5-10: Surface and entrainment fluxes for July 11 (Julian Day 192). The panels correspond to a) surface sensible heat; b) surface latent heat; c) mixed-layer top sensible heat entrainment; and c) mixed-layer top latent heat entrainment flux. The observed surface fluxes are given by 'o' symbols.

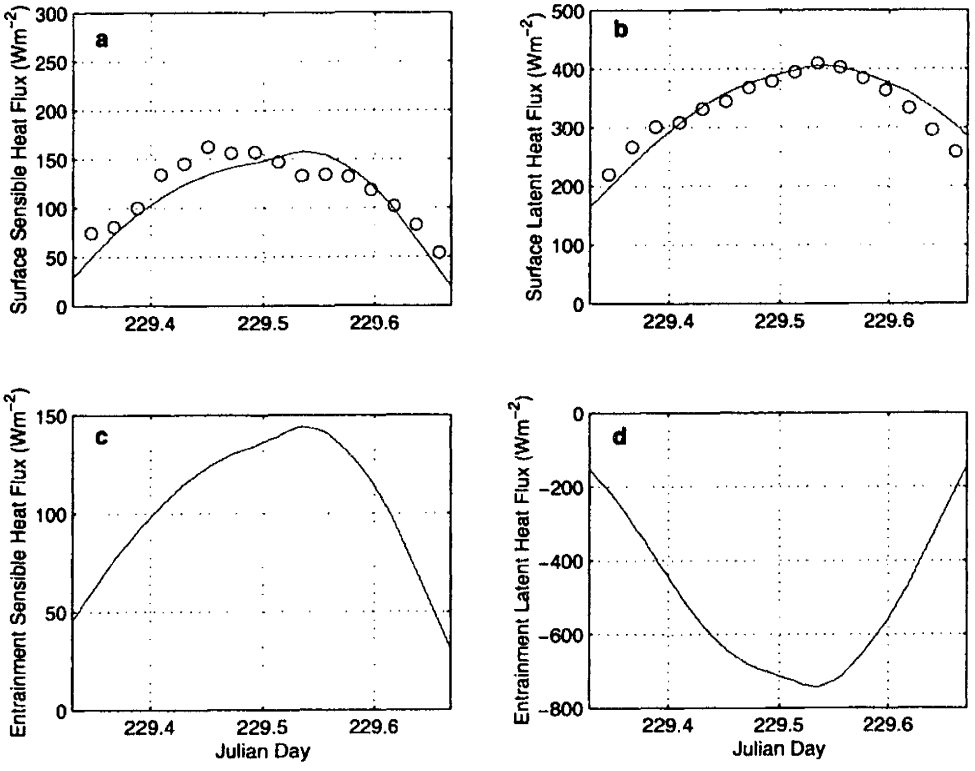

Figure 5-11: Surface and entrainment fluxes for August 17 (Julian Day 229). The panels correspond to a) surface sensible heat; b) surface latent heat; c) mixed-layer top sensible heat entrainment; and c) mixed-layer top latent heat entrainment flux. The observed surface fluxes are given by 'o' symbols.

smaller lapse rate γ_q on June 5 compared to large boundary layer growth and large lapse rate γ_q (very dry) on August 16.

The entrainment ratio A_R also exhibits large variability over the nine days examined. The range in A_R is from 0.22 ($\pm$ 0.10) to 0.54 ($\pm$ 0.12), with an average of 0.40 $\pm$ 0.11. Despite significantly different methodologies, our average is in very good agreement with the results of Betts and Ball (1994) who estimated A_R to be 0.44 $\pm$ 0.21 for FIFE using budget analyses of radiosonde data. In other studies, observations taken during independent ABL flights led to A_R estimates of 0.43 $\pm$ 0.12 (Betts et al. 1990) and 0.38 $\pm$ 0.16 (Betts et al. 1992) at FIFE. All of these independent estimates are significantly larger than the early quotes of $A_R \approx 0.2$.

Interestingly, our A_R estimates appear to exhibit some seasonality (see Figure 5-12) with generally larger values later in the summer. While Betts and Ball (1994) did not analyze data from IFC 1, their results also suggest a potentially higher value in IFC 3 ($A_R \approx 0.57$) compared to IFC 2 ($A_R \approx 0.43$). In our study there are no obvious systematic biases in the forcing data that would explain this result. For example, the surface virtual heat flux (roughly proportional to ABL growth) is actually largest on average during IFC 1. Also, IFC 2 and 3 have generally larger potential temperature lapse rates (more stable), which would suggest a suppression of ABL growth. Finally, the contribution of mechanically generated turbulence to ABL growth would be expected to be largest during IFC 2 which has the largest average wind speed. Given the limited number of days and error bounds on the results, the seasonality of A_R is inconclusive, however these results may suggest some underlying combination of available energy, vegetation phenology, moisture availability, etc. that explains this trend. This is certainly an area for further investigation. The methodology presented above can easily be applied to other field experiments to determine A_R and see if similar values and trends are present.

5.5.2 Estimates Using only Micrometeorology Observations

The results presented above provide a good baseline estimation of entrainment and should be applied to field experiment sites where both radiosonde and micrometeorology data are available (for reference these results are called the "base case"). Often a single morning radiosonde or pair of morning/afternoon radiosondes are available for a given region, but the diurnal cycle of boundary layer characteristics are not directly observed. In order to attempt to extend our methodology to these cases, we investigated the estimation of entrainment from micrometeorology observations only. As seen above, entrainment is sensitive to the lapse rates in temperature and humidity above the mixed layer. Thus we assume that a representative characterization of the lapse rates are available, either via single early morning radiosonde or by some other means. The summary of the results from these experiments ("micromet" case) are shown in Table 5.5.

In general, the micromet. estimates for c_h are lower than those in the base case (except for Day 177). However, for most days the difference is within about one standard deviation of the baseline results in Table 5.4. The mean estimate is 0.48 $\pm$0.20 compared to 0.55 $\pm$ 0.11. Note that the ensemble spread is much larger in the micromet. case. This make sense because the reference-level observations are more indirectly connected to mixed-layer growth (and thus c_h) than are the ABL observations.

The difference in surface fluxes between the two cases are quite small due mostly to the same surface state initial conditions. For the micromet. case the ensemble spread in the surface fluxes is generally smaller than in the base case. Conversely, the uncertainty

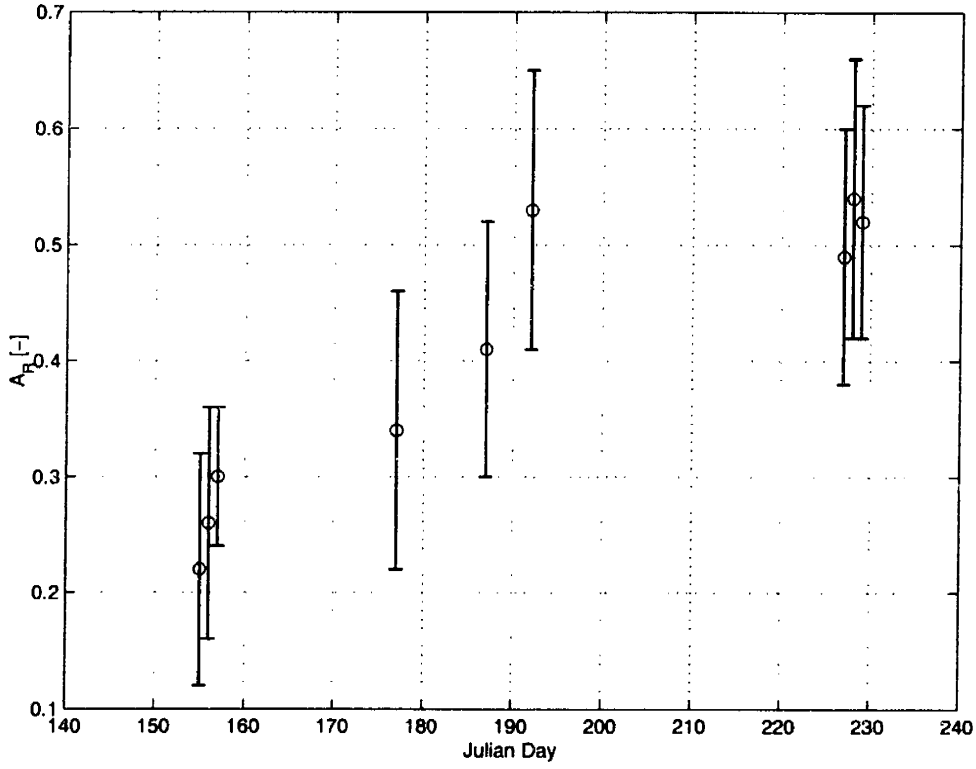

Figure 5-12: Estimates of A_R at the FIFE site as a function of Julian Day.

in the entrainment fluxes is much larger (often by a factor of 2). This is explained by the fact that the reference-level observations are most closely related to the surface fluxes, while ABL observations are related to both surface and entrainment fluxes. By minimizing only the misfit in the micrometeorology data, the uncertainty in surface fluxes is reduced. However, when the misfit to all observations is minimized (base case), there is some middle ground with smaller overall uncertainty (slightly larger surface flux uncertainty, but smaller entrainment flux uncertainty).

The mean daily A_R estimates in the micromet. case are generally smaller than those in the base case. Also, the larger uncertainty in the entrainment fluxes is propagated to a larger uncertainty in the individual A_R estimates. While the uncertainty in these estimates may prevent one from making any conclusions about the variability of A_R, the mean value is within one standard deviation of the base case (0.34 compared to 0.40). These results imply that reasonable estimates of average entrainment may be possible using only reference-level micrometeorology data in the estimation algorithm.

5.6 Summary

In this study a new methodology for the estimation of boundary layer entrainment is presented. The ensemble/variational data assimilation framework used is very flexible and can easily accommodate different observations types, sampling frequency, etc. and takes into account the corresponding uncertainty in each data source to yield an optimal estimate

of the ABL growth parameter c_h and entrainment ratio A_R. These parameters are very important in determining the characteristics of the boundary layer which play an important role in cloud formation, rain production, as well as other important feedbacks in the coupled system. The variational approach enforces the model (ABL budgets, boundary layer growth dynamics, etc.) as a strong constraint, so that the algorithm ultimately yields optimal and dynamically consistent estimates of all model states and fluxes.

In this particular study the technique to assimilate radiosonde estimates of mixed-layer height, potential temperature, and specific humidity, along with screen-level micrometeorology (temperature and humidity) from nine IFC days during FIFE 1987 is shown. The mean estimate of $A_R = 0.40 \pm 0.11$ over the nine days showed good agreement with independent estimates from recent studies. The results corroborate the contention that, at least for the FIFE site, A_R is much larger than the originally held value of 0.2. In addition to the mean estimate, our results suggest that there may be some seasonality to the A_R parameter, with higher values later in the summer. This is an issue that needs to be explored in more detail in the future.

The algorithm is also applied to the case where only micrometeorological observations are assimilated. This was done to test the applicability of the algorithm to sites where extensive radiosonde observations may not be available. Results from these tests showed that lack of ABL observations generally caused an underestimation of the A_R parameter, while increasing the uncertainty about the mean estimate. The mean estimates however were generally within one standard deviation of those from the base case (ABL and micrometeorology observations), indicating that the mean estimates provided under this reduced observation scenario may contain potentially useful information.

Overall, results from this study are encouraging and indicate that the variational assimilation method presented here yields robust and reasonable estimates of boundary layer entrainment. Reliable estimates are extremely important, since, as our results suggest, entrainment fluxes can play a significant role in the evolution of boundary layer states. The framework is sufficiently general that it can be extended to include other observation types and should be applicable to other sites where estimates of entrainment are desired.

Table 5.4: Estimates of the entrainment parameter c_h and average (during ABL growth phase) surface and entrainment fluxes for each day when assimilating all observations. The entrainment parameter A_R is computed from Equation 5.7. The error bounds given in the table correspond to ± one standard deviation.

IFC	Julian Day	c_h	H ($\mathrm{Wm^{-2}}$)	L_vE ($\mathrm{Wm^{-2}}$)	H_{top} ($\mathrm{Wm^{-2}}$)	L_vE_{top} ($\mathrm{Wm^{-2}}$)	A_R
1	155	0.34 ± 0.11	146 ± 10	313 ± 8	64 ± 17	-392 ± 23	0.22 ± 0.10
	156	0.37 ± 0.11	145 ± 11	321 ± 9	70 ± 16	-380 ± 23	0.26 ± 0.10
	157	0.39 ± 0.07	150 ± 10	343 ± 7	71 ± 10	-271 ± 25	0.30 ± 0.06
2	177	0.48 ± 0.15	112 ± 9	295 ± 6	71 ± 16	-370 ± 29	0.34 ± 0.12
	187	0.59 ± 0.13	100 ± 12	332 ± 11	74 ± 13	-341 ± 28	0.41 ± 0.11
	192	0.61 ± 0.12	129 ± 14	324 ± 12	100 ± 16	-277 ± 24	0.53 ± 0.12
3	227	0.56 ± 0.10	96 ± 8	342 ± 6	79 ± 13	-282 ± 22	0.49 ± 0.11
	228	0.88 ± 0.10	97 ± 6	309 ± 5	100 ± 13	-514 ± 51	0.54 ± 0.12
	229	0.77 ± 0.09	95 ± 5	315 ± 3	93 ± 11	-452 ± 24	0.52 ± 0.10
	Mean:	0.55 ± 0.11					0.40 ± 0.11

Table 5.5: Estimates of the entrainment parameter c_h and average (during ABL growth phase) surface and entrainment fluxes for each day when assimilating only screen-level micrometeorology observations. The entrainment parameter A_R is computed from Equation 5.7. The error bounds given in the table correspond to ± one standard deviation.

IFC	Julian Day	c_h	H ($\mathrm{Wm^{-2}}$)	L_vE ($\mathrm{Wm^{-2}}$)	H_{top} ($\mathrm{Wm^{-2}}$)	L_vE_{top} ($\mathrm{Wm^{-2}}$)	A_R
1	155	0.34 ± 0.25	146 ± 8	313 ± 6	64 ± 37	-396 ± 64	0.22 ± 0.22
	156	0.36 ± 0.20	145 ± 10	321 ± 7	69 ± 31	-379 ± 60	0.25 ± 0.19
	157	0.33 ± 0.18	151 ± 8	342 ± 5	61 ± 32	-261 ± 22	0.24 ± 0.18
2	177	0.51 ± 0.26	111 ± 7	295 ± 5	75 ± 33	-370 ± 25	0.37 ± 0.25
	187	0.44 ± 0.14	104 ± 11	327 ± 9	58 ± 17	-296 ± 49	0.29 ± 0.14
	192	0.53 ± 0.16	129 ± 10	323 ± 7	90 ± 25	-259 ± 38	0.47 ± 0.17
3	227	0.33 ± 0.16	100 ± 7	339 ± 5	55 ± 19	-222 ± 42	0.32 ± 0.16
	228	0.84 ± 0.24	97 ± 5	309 ± 4	95 ± 22	-499 ± 69	0.51 ± 0.19
	229	0.64 ± 0.21	96 ± 5	314 ± 2	78 ± 22	-420 ± 45	0.41 ± 0.19
	Mean:	0.48 ± 0.20					0.34 ± 0.19

Chapter 6

Summary and Conclusions

6.1 Original Contributions and Key Findings

This thesis develops a coupled land surface-boundary layer model and its corresponding adjoint. Together they form a very general framework which has be applied to exploratory sensitivity analysis and data assimilation studies of the coupled system.

In Chapter 2 the model and adjoint are presented and tested using data from the FIFE site. The framework is applied to an illustrative sensitivity experiment and data assimilation example. The importance of the coupled system is seen in the sensitivity experiment, where average daily ground temperature is heavily influenced (more than other surface states) by ABL potential temperature (via radiative fluxes and surface sensible heat flux) and specific humidity (via radiative and latent heat flux). The adjoint variables show how the influence of each state variable evolves in time and the time distribution of parameter influence (via interaction with dynamic model states) are found. In the synthetic data assimilation example, the model initialization problem is solved using only a minimal set of basic land temperature measurements and auxiliary forcing variables (solar radiation, large-scale wind speed, and free atmosphere profiles of temperature and humidity). As a result, great improvement was obtained in simulation of model states and surface fluxes.

In Chapter 3 the variational framework is applied to the specific problem of land-atmosphere coupling and feedback. At the heart of the analysis is the simple assertion that an offline land surface model is a special case of a coupled model, where the atmospheric pathways that allow propagation of perturbations are "closed". Thus even if the nominal model trajectories of the two models are the same, we would expect the responses of each model to perturbations in states or parameters to be different because of the additional feedbacks in the coupled model. Previous studies have tried to address this issue through the parallel integration of a coupled and uncoupled model. However in many cases, the specification of atmospheric forcing yields a different nominal trajectory for each model. Thus differences in sensitivity can be a combination of differences in the nominal trajectories as well as due to the additional interaction pathways. Using an adjoint sensitivity approach, the nominal trajectories are not only identical, but it is shown that the uncoupled adjoint model is a special case of the coupled adjoint model, where the terms relating to atmospheric feedback are explicitly included in the coupled adjoint, and missing in the uncoupled adjoint.

The framework is applied to the FIFE site where the model response functionals were the daytime average surface turbulent fluxes. Integrating the adjoint models about the

consistent and common trajectory provided by the (coupled) forward model yields the sensitivities of the surface fluxes to all of the model states and parameters, which are shown to be significantly different because of boundary layer feedbacks. Specifically, it was shown that the ABL potential temperature has a strong positive (negative) feedback on average daytime latent (sensible) heat flux, for perturbations in the surface (canopy and ground) temperature states. In other words, perturbations in the surface temperature state, warms the boundary layer, which shuts off further sensible heat flux (reduced temperature gradient) and therefore requires an increase in latent heat flux to meet the surface energy balance. Boundary layer growth and entrainment was also shown to be an important sensitivity pathway, as perturbations in surface temperature caused increased boundary layer growth and entrainment, which has a drying effect on the ABL, that then drives more evaporation (positive feedback). For soil moisture perturbations, the primary feedback loop was via the ABL specific humidity, which due to moistening from increased evaporation led to a negative feedback on latent heat flux (reduced moisture gradient). The sensitivity is further reduced because perturbations in soil moisture lead to less sensible heat flux and therefore less boundary layer growth and dry air entrainment into the ABL, which has a moistening effect that further reduces the moisture gradient. Differences in parameter sensitivities were also examined and generally showed a strong diurnally varying behavior, indicating, as expected, that coupling is generally strongest at mid-day. However while some differences were in a given direction (either damped or amplified) throughout the day, others had opposing influences at different times of the day, which would not be easily diagnosed using a traditional forward sensitivity approach. We expect that there would also be seasonal sensitivity differences if the methodology were extended to longer simulations.

In Chapter 4 a variational data assimilation approach is used to estimate land and ABL states and fluxes via the assimilation of standard reference-level temperature and humidity and radiometric surface temperature. While upcoming remote sensing missions (particularly L-band measurements) will be extremely useful, our focus was on the estimation of uncertain fluxes with currently available observations. In particular the advantages of the coupled model are used to explore the assimilation of micrometeorological variables which are generally used as forcing for offline models. Results from an application to the FIFE site showed that using both surface temperature and micrometeorology allows for the accurate estimation of land surface fluxes even during non-ideal conditions, where large advection-related model errors are present and evaporation is atmospherically controlled. This is a very good test of the robustness of the land data assimilation system, as results generally improve during strong surface-controlled evaporation regimes, where the sensitivity of the observations to surface states is increased. The results illustrate the possible synergism that can exist between different measurements, which when used in isolation might cause divergence in the estimation scheme. Furthermore the assimilation scheme shows promise in diagnosing model errors that may be present due to missing process representation and/or biased parameterizations.

In Chapter 5 boundary layer growth and entrainment are estimated using the variational data assimilation framework. Entrainment is an important process in the system since it is the primary connection between the strongly coupled land-ABL system with the generally warmer and drier free atmosphere. In the study micrometeorology and radiosonde observations from the intensive field campaigns at FIFE are assimilated. The traditional variational framework was modified slightly to include an ensemble approach, which not only yields a (mean) estimate of entrainment, but a measure of its uncertainty as well. The results here indicate a much larger ratio of entrainment to surface fluxes (0.40 ± 0.11)

compared to early proposed values (0.2). These results are consistent however with recent estimates at the FIFE site using independent estimation methods. The estimates given here are more robust however because they explicitly account for appropriate error in each data source (as opposed to direct use of the measurements in observational studies), and contain meaningful error bars derived from the estimation algorithm rather than empirical error estimates. The fact that the entrainment parameter is larger than first hypothesized only serves to bolster the argument about the importance of land-atmosphere coupling. Interestingly, the results appear to show a seasonal cycle in the entrainment ratio, which is not easily explained from the input forcing data. Also, there is some skill in entrainment estimation when only micrometeorology is used in the assimilation, suggesting the potential for more widespread applications.

6.2 Future Work

The results and experience from this thesis point to numerous potential areas of future research. Below these efforts are separated into those that are more or less direct ("short-range") extensions of the current study, which use the modeling framework as currently developed, and those that build upon the ideas discussed here, but may require new more significant ("long-range") extensions.

6.2.1 Short-range Extensions

Coupled Sensitivity Studies:

- Land surface states. While average fluxes were examined in Chapter 3, the differences in sensitivity of long-term averaged surface states (temperature and moisture) to other model states and parameters would yield insight into how the equilibrium state sensitivities may be significantly different for coupled vs. uncoupled models.

- Longer time scales. Integrating the model over storm/interstorm cycles as well as over seasonal time scales may yield interesting insight into the time-varying strength of coupling between the land and ABL.

- Other land surface regimes. We would also expect differences in coupling for different land surface types (i.e. tropical forest vs. arid regime, etc.). This type of extension may lead to insight about regions of the globe where coupling is important and others where it is not.

State and Flux Estimation:

- Incorporation of other observations. For data assimilation studies, the variational framework is very flexible in terms of including additional observations. The idea of synergism between measurements is an area that should be explored in much more detail. Adding other remotely-sensed variables (e.g. microwave brightness temperatures from various wavelengths and especially L-band) and in-situ measurements (e.g. ground temperature) may further extend our ability to estimate surface states and fluxes. A simple example of possible synergism would be the ability for high frequency observations like micrometeorology or radiometric surface temperature (multiple observations

per day), to aid in the interpolation between high-information lower frequency measurements like polar-orbiting microwave radiometers (observations every 2-3 days).

- Model error/biases. The area of model error and bias estimation needs further examination since imperfect models are an inevitable part of any assimilation algorithm. The identification of structural model errors and model biases can be particularly difficult to diagnose. Again, the inclusion of many observation types may allow for the further identification of model errors.

- Parameter estimation. Instead of identifying model biases due to poor parameter specification, the variational framework could instead be used to estimate particular parameters. The adjoint sensitivity approach could be used as a screening tool to identify the level of sensitivity of a particular observation type to model parameters. This may be especially relevant to time-invariant parameters, that once estimated could simply be used in the state estimation framework.

Boundary Layer Entrainment:

- Seasonal variability. Trying to gain an understanding of the seasonal variability in the entrainment parameter should be the aim of further investigation. The approach outlined in this thesis could easily be extended to other sites with longer observation records.

- Geographic variability. In addition to the possibility of seasonal variability in the entrainment parameter, we might expect a geographic (land surface regime) dependence. The estimation of entrainment could be applied to field sites with disparate land surface conditions to determine whether the large entrainment results are specific to the grassland FIFE site or are more widely valid.

- Model error. In our estimation of entrainment there was no inclusion of model error. Including model errors related to advection of boundary layer characteristics, cloud cover, and other processes may allow for extension of the technique and may elucidate reasons for the variability in boundary layer growth and entrainment.

6.2.2 Long-range Extensions

Coupling/Feedback in Hydrologic Systems:

- Large scale/spatially-distributed models. The studies contained in this thesis are exploratory in nature due to the simplified 1D model. Future studies should explore issues related to large-scale dynamics and heterogeneity in the land surface component of the system. These could span from basin-scale studies, where heterogeneous landscapes interact directly with the overlying boundary layer, to regional or continental scale studies, where inclusion of a more complete atmospheric model would be required. Development of the adjoint for more complicated models may be a limiting factor in using a variational approach. Automatic adjoint compilers may be useful tools for more complicated models.

- Coupling between other processes and/or subsystems. Coupling of the land surface and boundary layer to other subsystems, for example inclusion of groundwater/surface

water interactions, and ABL/large-scale free atmosphere interactions should be considered, especially when dealing with longer time scales and larger spatial scales. Other important processes such as clouds, moist convection/precipitation could be added to the simple model. Two-way interaction involving these processes along with the processes considered in our model are sure to lead to other important feedbacks in the system. The adjoint of more complicated models that include these other processes could be used in the same way as shown in Chapter 3, where the effects of "closing" certain feedback pathways could be explored.

- "Local" vs. "remote" feedbacks. In our study, the focus was on "local" feedbacks, where there is two-way interaction between the land surface and overlying atmosphere. The use of more complicated models allows for further exploration of "remote" feedbacks, where perturbations in a particular state or parameter at a given location may influence conditions at another remote part of the domain. Examples of this type of feedback would be soil moisture-rainfall feedback due to precipitation recycling.

- ABL entrainment. Research into boundary layer growth and entrainment may warrant using more complex models (e.g. large-eddy simulations or models which represent the actual vertical profiles in temperature, humidity and wind) than the slab ABL used here. These models may yield insight into how to better parameterize entrainment in simple slab models.

Data Assimilation:

- Observation information content. The simple land data assimilation system used here provides a very useful tool to investigate the information content of different observation types, both in isolation and in various combinations. It can be used in observing system simulation experiments (OSSEs) to determine useful observations that could be ultimately be used in more operational (large-scale) settings.

- Methodological developments. The simple model also provides a useful test-bed for methodological developments. While in this study we focused on a variational approach, the extension to other methods, i.e. Ensemble Kalman Filtering, as well as the further exploration of combination Variational/Ensemble techniques is an area which should be explored in more detail.

- Extension to large-scale coupled models. Most operational land data assimilation systems which have been developed up to now have focused on the use of offline land surface models. Further investigation is necessary to determine whether the additional computational burden of coupled models will lead to improved estimates, through additional observations and better representation of the system. As mentioned above, using variational approaches with complex atmospheric models may be limited by the development of corresponding adjoint models. Therefore, especially in operational (real-time) environments, ensemble filtering techniques may be most appropriate since they do not require a tangent-linear or adjoint model.

Appendix A

Detailed Model Formulation and Numerical Solution

This appendix fully describes the one-dimensional forward model used in this study. The model described below will be referred to as the "complete model" as it contains full parameterizations of the important processes in the coupled land-atmosphere system. In the complete model there are parameterizations with discontinuities and "on-off" switches that might not be amenable to the development of the adjoint model. This complete model will therefore form the basis for a "simplified model" upon which the adjoint will be developed. The simplified model will attempt to best represent the processes and output of the complete model while eliminating or modifying the discontinuities and any other components which may prove troublesome in the application of the adjoint. The complete model is developed first so that the consequences of any potential model simplifications can be compared directly to the complete model and validated accordingly.

The model consists of a SVAT-type land surface representation which models the surface energy and water balances and includes an explicit representation of a vegetation canopy overlying the soil. The land surface model is coupled to a mixed layer model of the atmospheric boundary layer. The coupled model allows for two-way interaction between the vegetation/soil system and the atmosphere which results in feedback mechanisms that affect the response of the overall system.

The organization of the appendix is as follows. Section A.1 describes the prognostic equations which make up the core of the model. In Section A.2 the radiative transfer models of the atmospheric boundary layer and vegetation canopy, which determine the radiative fluxes in the system, are developed. Section A.3 describes the turbulent sensible and latent heat fluxes from the canopy and ground surface. In section A.4 the aerodynamic model used to determine the wind profile in the canopy is developed, which is needed to determine the aerodynamic resistances used in the turbulent flux calculations. Section A.5 describes the model for moisture transport within the soil column. Finally, in Section A.6 the numerical solution scheme used to integrate the model forward in time is described.

A.1 Forward Model Prognostic Equations

A.1.1 Land Surface Model Prognostic Equations

The model presented below represents the water and energy balances at the land surface which consists of a homogeneous vegetation canopy overlying soil. The prognostic equations are given below. A schematic representation of the model is shown in Figure A-1.

Canopy energy balance:

The canopy energy balance is given by:

$$C_c \frac{dT_c}{dt} = R_{nc} - H_c - L_v E_c \tag{A.1}$$

where C_c is the canopy heat capacity ($0.0002 L_T C_w$), T_c is the canopy temperature, R_{nc} is the net radiative flux incident on the canopy, and H_c and $L_v E_c$ are the turbulent sensible and latent heat fluxes from the canopy.

Surface soil energy balance:

The energy balance at the soil surface is represented by the force-restore model (Deardorff 1978):

$$C_g \frac{dT_g}{dt} = (R_{ng} - H_g - L_v E_g) - \frac{2\pi C_d}{\tau_d}(T_g - T_d) \tag{A.2}$$

$$C_g = 0.5 \left(\frac{H_s C_{soil} \tau_d}{\pi} \right)^{1/2}$$

$$H_s = 0.4186 \left[\frac{1.5(1-\theta_s) + 1.3\theta_s W_1}{0.75 + 0.65\theta_s - 0.4\theta_s W_1} \right]$$

$$C_{soil} = [C_{min}(1-\theta_s) + C_w \theta_s W_1]$$

where C_g is the surface soil heat capacity (C_{soil} is the weighted volumetric heat capacities of the soil minerals and water), T_g is the surface soil temperature, R_{ng} is the net radiative flux incident on the ground surface, H_g and $L_v E_g$ are the turbulent fluxes from the ground, C_d is the deep soil heat capacity, and τ_d is the diurnal period of the heat wave. The first term on the right hand side in parentheses represents the ground heat flux which serves as a periodic forcing of the system, while the second term represents a restoring term which, in the absence of forcing, returns the surface ground temperature (T_g) to the column-averaged temperature (T_d) exponentially in time. This efficient model allows one to avoid a more complicated heat diffusion model for ground heat flow and has been shown to be relatively accurate in past studies (e.g. Bhumralkar (1975), Deardorff (1978), Lin (1980)).

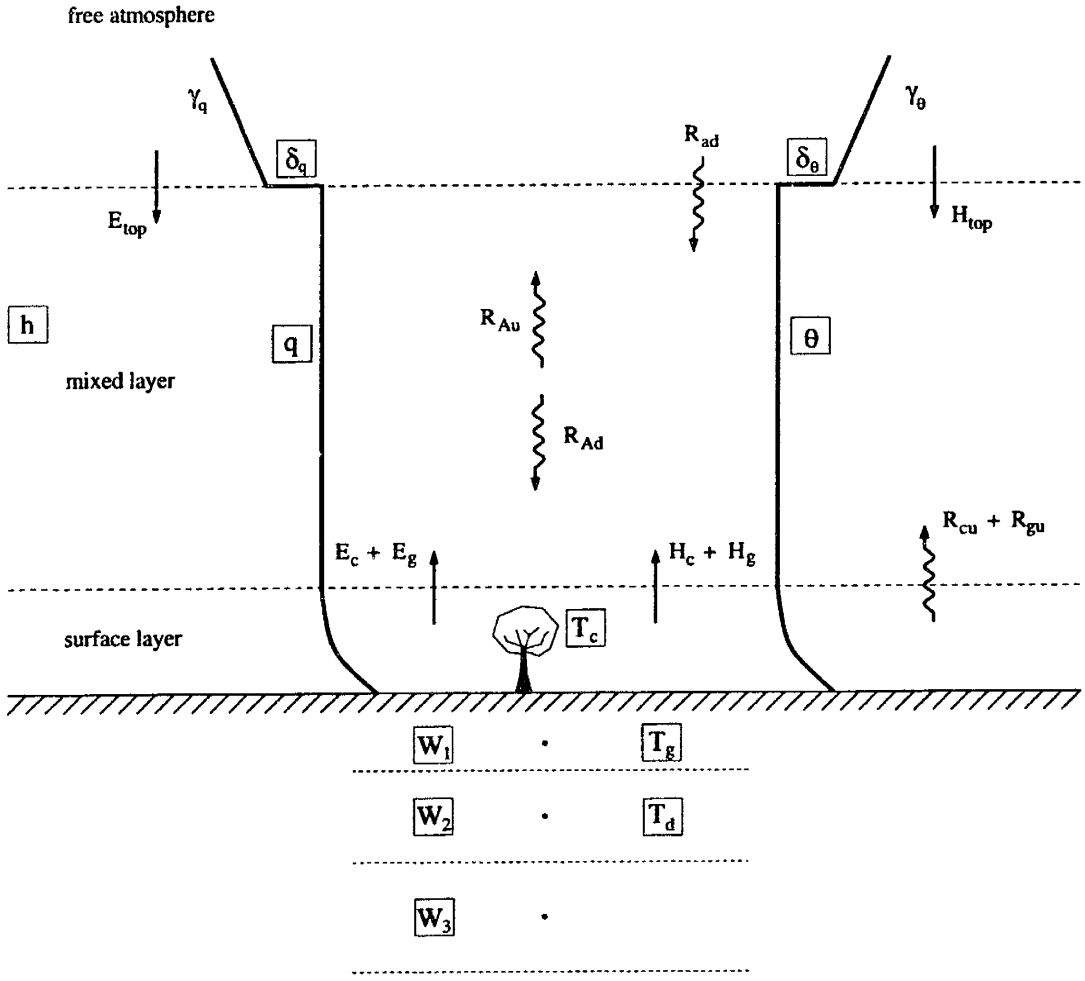

Figure A-1: Schematic diagram of coupled land surface-atmospheric boundary layer model. The system state variables are bounded by boxes. All symbols are defined in Appendix C.

Deep soil energy balance:

The above formulation requires the modeling of the deep (column-averaged) soil temperature (T_d). It is assumed to evolve sinusoidally over the year due to the ground heat flux forcing:

$$C_d \frac{dT_d}{dt} = \frac{1}{2(365\pi)^{1/2}}(R_{ng} - H_g - L_v E_g) \tag{A.3}$$

In general, T_d evolves rather slowly over the course of the year and thus for applications involving short time scales may be specified as constant in time.

Canopy interception:

The canopy is assumed to have an interception store that evolves according to:

$$\frac{dM_{cw}}{dt} = P - D_d - D_c - \frac{1}{\rho_w} E_{ci} \tag{A.4}$$

where P is the precipitation incident on the canopy, D_d is the canopy throughfall, D_c is the canopy drainage, and E_{ci} is the interception loss.

Surface and subsurface moisture balance:

For our model we discretize the soil column into three layers: a surface layer, rootzone layer, and recharge zone. This discretization is arbitrary and can easily be modified to include a finer discretization. The soil moisture in each layer (W_1, W_2, W_3 respectively) evolves according to the following equations:

$$\frac{dW_1}{dt} = \frac{1}{\theta_s d_1}[P_{W1} - Q_{1,2} - \frac{1}{\rho_w} E_g - \frac{1}{\rho_w} E_{c1}] \tag{A.5}$$

$$\frac{dW_2}{dt} = \frac{1}{\theta_s d_2}[Q_{1,2} - Q_{2,3} - \frac{1}{\rho_w} E_{c2}] \tag{A.6}$$

$$\frac{dW_3}{dt} = \frac{1}{\theta_s d_3}[Q_{2,3} - Q_3] \tag{A.7}$$

where θ_s is the soil porosity, d_i is the depth if each soil layer, P_{W1} is the infiltration into the surface soil layer, E_g, and E_c are the ground evaporation and canopy transpiration respectively, and $Q_{1,2}$, $Q_{2,3}$, and Q_3 are the moisture fluxes between layers and out of the bottom layer. Note that transpiration is assumed to occur from the top two layers only (i.e. the depth of the rootzone corresponds to the bottom of layer 2).

A.1.2 Mixed layer ABL Model Prognostic Equations

The model consists of a slab-type representation of the boundary layer with uniform potential temperature and specific humidity profiles throughout the mixed layer, which is overlain with inversions in the potential temperature and specific humidity (see Figure A-1). In the

model there is no entrainment zone; instead it is represented by an instantaneous jump in temperature and humidity at the top of the mixed layer.

ABL budget equations:

The ABL budget equations consist of the energy and moisture balances in the mixed layer:

$$\rho c_p h \frac{d\theta}{dt} = [R_{ad} + R_{cu} + R_{gu}]\epsilon_a - R_{Ad} - R_{Au} + H_c + H_g + H_{top} \tag{A.8}$$

$$\rho h \frac{dq}{dt} = E_c + E_g + E_{top} \tag{A.9}$$

where h is the height of the ABL, θ is the potential temperature of the ABL, q is the specific humidity of the ABL, R_{ad} is the downwelling longwave radiation from the atmosphere above the ABL, R_{cu} is the upward longwave radiation from the canopy, R_{gu} is the longwave radiative flux from the ground into the mixed layer, ϵ_a is the ABL column emissivity, R_{Ad} is the downwelling longwave radiation from the ABL, R_{Au} is the upwelling radiative flux from the ABL, and H_{top} and E_{top} are the respective sensible and latent heat fluxes at the top of the ABL due to entrainment of the overlying warm-dry air. The entrainment fluxes are functions of boundary layer growth and therefore will be discussed below. Note that these budget equations do not consider advection of heat or moisture into the area by large scale atmospheric phenomena as we wish to focus on interactions due to boundary layer processes alone.

Mixed layer height evolution:

The above equations assume that potential temperature and specific humidity profiles are constant with height (up to a height h) due to the turbulent mixing in the boundary layer. However as mentioned above, the height of the boundary layer is a dynamic quantity which evolves throughout the day due to both free and forced convection. The virtual heat flux at the surface (H_v) which is responsible for the mixing due to free convection, is primarily responsible for ABL growth during the day. When the virtual heat flux vanishes at the end of the day, the turbulence dissipates quickly, and the ABL collapses to a residual level which is maintained through forced convection. Smeda (1979) derived a model for the diurnal evolution of the ABL height by considering the balance of turbulent energy due to convection, turbulent energy generated by the wind, and dissipation of turbulent energy. Following his derivation we have an expression for the growth of the ABL height in terms of kinetic energy generation, dissipation, and surface heat flux:

$$\frac{dh}{dt} = \frac{2(G_* - D_*)\theta}{gh\delta_\theta} + \frac{H_v}{\rho c_p \delta_\theta} \tag{A.10}$$

where G_* is the mechanically generated turbulent kinetic energy, D_* is the dissipation of kinetic energy, and the second term is the thermally generated turbulent energy. While in general this formulation could also include the effect large scale subsidence on boundary layer growth, it is not considered here.

Most of the mechanical generation of turbulent energy occurs in the surface layer. The

rate of such generation is given by:

$$G = \tau \frac{\partial U}{\partial z}$$

so that the total mechanical generation of turbulent kinetic energy within the whole depth of the ABL is then given by:

$$G_* = \int_0^h G dz \approx \tau_0 U_m$$

where τ_0 is the surface shear (constant with height) and U_m is the mean wind speed in the mixed layer. The dissipation of turbulent kinetic energy is given by:

$$D_* = D_1 + \delta D_2$$

where D_1 is the dissipation of wind-generated energy, D_2 is the dissipation of the turbulence that was created by the surface heat flux, and $\delta = 0$ in stable conditions and $\delta = 1$ in unstable conditions. Assuming that the dissipation of mechanically generated turbulent energy is proportional to G_* and that it decreases exponentially with height, D_1 is given by:

$$D_1 = G_*(1 - e^{-\xi h})$$

where Kim and Entekhabi (1998) used a value of 0.01 for ξ and Smeda (1979) tested the model using values of 0, 0.001, and 0.01. The dissipation of convectively generated turbulent energy is also assumed to be proportional to the surface virtual heat flux and is given by:

$$D_2 = c_D w_*^3 = 0.4 \left(\frac{gh}{\theta} \frac{H_v}{\rho c_p} \right)$$

The form of this expression is suggested by scaling arguments, where the proportionality factor 0.4 used by Smeda (1979) was taken from Mahrt and Lenschow (1976). They based the parameter value on observations of Lenschow (1974), who used a value 0.43, and laboratory measurements by Willis and Deardorff (1974) which showed c_D varying with height in the boundary layer from 0 to 0.6 (with an average of ≈ 0.36). For now we proceed using the bulk boundary layer value of 0.4 suggested above, however the potential effects of the uncertainty in this parameter on model behavior can be examined in the adjoint sensitivity analysis. Finally, the surface virtual heat flux is given by:

$$H_v = H + 0.61 \theta c_p E \approx H + 0.07 L_v E$$

Based on these parameterizations, we can rewrite Equation (A.10) separating the generation/dissipation of turbulent energy into that by forced convection and free convection as:

$$\frac{dh}{dt} = \frac{2\theta G_* e^{-\xi h}}{gh\delta_\theta} + (1 - 2c_D\delta) \frac{H_v}{\rho c_p \delta_\theta}$$

where the first term is only a function of wind shear and the second only of surface heating. During the daytime, the second term in this equation usually dominates the first. Therefore

boundary layer growth during the day is essentially proportional to the surface virtual heat flux and inversely proportional to the potential temperature inversion at the top of the mixed layer. This expression also suggests an upper limit on the value of c_D during the daytime ($\delta = 1$) of 0.5 in which case there would be no growth due to thermally driven convection. For $c_D = 0.4$ the coefficient of the second term is 0.2. In general, lower values of c_D will promote more boundary layer growth. When the surface virtual heat flux switches sign near sunset, there is a transition from unstable to stable conditions which causes the collapse of the ABL as the turbulence dissipates. By assuming $H_{top} = 0$ (i.e. $dh/dt = 0$) when the surface virtual heat flux switches sign, Smeda (1979) solved for h during the transition, which is given by:

$$h = -\frac{2(G_* - D_1)\rho c_p \theta}{H_v g} = -\frac{2G_* \rho c_p \theta}{H_v g} e^{-\xi h} \tag{A.11}$$

where Equation (A.11) is to be applied just after the collapse for a period of time until the following condition is met:

$$\left| \frac{dh}{dt} - \frac{H_v}{\rho c_p \delta_\theta} \right| < 0.05 \left| \frac{H_v}{\rho c_p \delta_\theta} \right| \tag{A.12}$$

which is when the magnitude of the mechanically generated turbulence becomes less than five percent of the magnitude of the turbulence due to virtual heat flux. Note that Equation (A.11) is an implicit nonlinear equation in h. Also, the condition marking the end of the transition period is somewhat empirical and is designed solely to bring h down to a small value before it starts growing again. This kind of transition in the model structure does not strictly fit into the classical adjoint formulation and therefore will need special attention in the development of the adjoint (described below).

Entrainment Fluxes:

Due to the boundary layer growth, warm dry air from above will be entrained into the mixed layer. Therefore there are fluxes of sensible and latent heat across the interface between the free atmosphere and mixed layer as it ascends. The amount of moisture entrained (A_E) is equal to the product of the average moisture inversion strength ($\bar{\delta}_q$) and the change in boundary layer height (δh) and is shown in Figure A-2a. Therefore the entrainment rate for moisture is given by:

$$E_{top} = \rho \frac{dA_E}{dt} = \rho \delta_q \frac{dh}{dt} \tag{A.13}$$

Similarly, the amount of heat entrained (A_H) is equal to the product of the average potential temperature inversion strength ($\bar{\delta}_\theta$) and the change in boundary layer height(δh) (see Figure A-2b). Therefore the entrainment rate for sensible heat is:

$$H_{top} = \rho c_p \frac{dA_H}{dt} = \rho c_p \delta_\theta \frac{dh}{dt} \tag{A.14}$$

However the entrainment fluxes occur only during the growth phase of the ABL. Entrainment is not a reversible process (i.e. there are no fluxes in the opposite direction as the boundary layer shrinks later in the day). Entrainment only occurs when the surface virtual heat flux is positive. This in fact corresponds to that part of the day when large thermals

created by surface heating do in fact entrain air from above the boundary layer. Therefore once H_v becomes negative both H_{top} and E_{top} are set to zero. This phenomenon constitutes one of the on/off switches that will need to be dealt with carefully in the adjoint model.

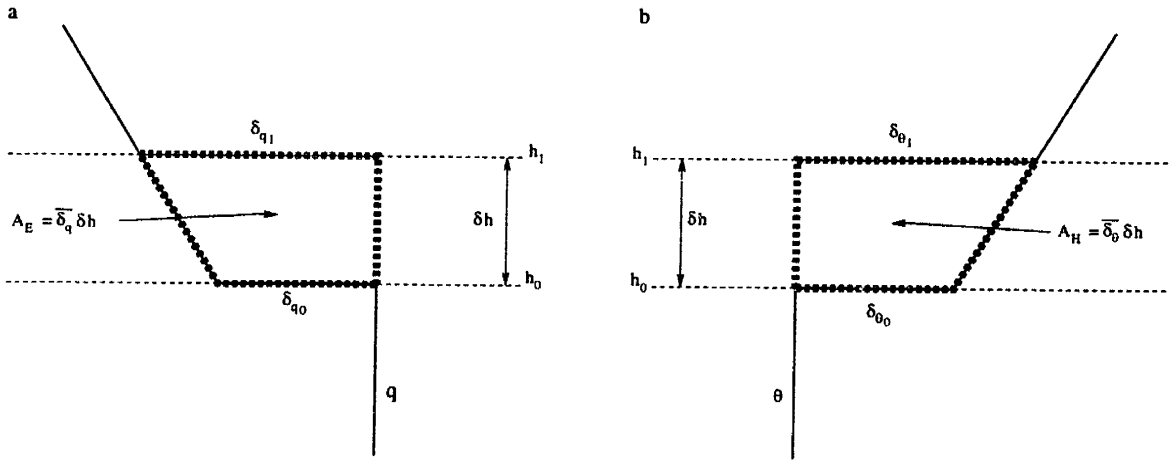

Figure A-2: Schematic of amount of moisture and heat entrained as mixed layer height increases a distance δh.

Inversion strength equations:

As the state of the system evolves, the strength of the inversions in potential temperature (δ_θ) and specific humidity (δ_q) at the top of the ABL also evolve. For the potential temperature inversion there are two factors which cause it to change. As the boundary layer warms, the inversion strength decreases. Also, as the boundary layer grows the inversion strength will increase. Therefore the prognostic equation for potential temperature inversion strength can be written as:

$$\frac{d\delta_\theta}{dt} = \gamma_\theta \frac{dh}{dt} - \frac{d\theta}{dt} \tag{A.15}$$

Along similar lines, the specific humidity inversion strength will increase (become more negative) as the boundary layer becomes more moist, and will also increase as the boundary layer grows. The result is the following prognostic equation for the specific humidity inversion:

$$\frac{d\delta_q}{dt} = \gamma_q \frac{dh}{dt} - \frac{dq}{dt} \tag{A.16}$$

Note that the first term in each of the above equations corresponds to entrainment and are therefore equal to zero when H_v is negative. The lapse rates in potential temperature (γ_θ) and specific humidity (γ_q) above the ABL can be considered to be forcing parameters. When they are not known, the lapse rates can be estimated (see Brutsaert (1975)) by assuming a "Standard Atmosphere" (i.e. exponential profiles for pressure (P), thermodynamic

temperature (T), and vapor pressure (e) above the mixed layer):

$$P(z) = P_h \exp\left(-\frac{g}{R_d\theta}[z-h]\right)$$

$$T(z) = T_{h+} \exp\left(-\frac{\gamma_T}{\theta}[z-h]\right)$$

$$e(z) = e_{h+} \exp\left(-\left[5.8\times10^3\frac{\gamma_T}{\theta^2} + 5.5\times10^{-5}\right][z-h]\right)$$

where

$$P_h = P_s\left[1-\frac{gh}{\theta c_p}\right]^{\frac{c_p}{R_d}}$$

$$T_{h+} = (\theta+\delta_\theta)\left(\frac{P_h}{P_s}\right)^{\frac{R_d}{c_p}}$$

where γ_T is the lapse rate in thermodynamic temperature (positive when temperature decreases with height), P_h is the pressure at the top of the ABL, and T_{h+} and e_{h+} are the thermodynamic temperature and vapor pressure just above the inversion at the top of the ABL.

During and after the collapse in h, special care must also be taken in determining inversions at the top of the mixed layer. There are very few studies which try to model the mixed layer over the entire diurnal cycle and thus finding information about the behavior of these variables at night is difficult. Smeda (1979) specifies δ_θ during stable conditions as the difference between the potential temperature in the mixed layer and the surface temperature. During the transition phase, Kim and Entekhabi (1998) specify δ_θ as Smeda (1979) does, however immediately after the transition the temperature inversion is modeled as:

$$\frac{d\delta_\theta}{dt} = -\frac{1}{2}\frac{d\theta}{dt}$$

which is the same as Equation (A.15) with no entrainment and with the added coefficient of 1/2. Initially, one may be inclined to simply use the above equation without the 1/2 factor, however in preliminary tests this led to large inversion strengths in the morning (due to the decrease in θ overnight) which unrealistically retarded boundary layer growth the following day. One potential explanation for this is that the behavior of the system is fundamentally different at night when the mixed layer is overlain by a residual layer rather than the free atmosphere. While the free atmosphere temperature may vary much more slowly than the boundary layer temperature (due to surface forcing), the residual layer above the nighttime mixed layer is most likely cooling significantly during the night along with the mixed layer. As a consequence, one would expect that this would lead to a smaller temperature inversion at the top of the mixed layer than would be predicted by Equation (A.15) without entrainment. The factor of 1/2 used above seems to be effectively taking this into account.

For generality we could model the inversion strength during stable conditions as:

$$\frac{d\delta_\theta}{dt} = -c_\delta \frac{d\theta}{dt}$$

where c_δ is a model parameter which can be given the nominal value of $1/2$.

To further justify the form of this equation a slightly more rigorous argument for the behavior of the night-time inversion can be made. Immediately following the collapse of the ABL it can be argued that the the potential temperature in the residual layer (θ_{res}) is equal to θ in the mixed layer. While the mixed layer is overlain by the residual layer the inversion can be thought of as $\delta_\theta = \theta_{res} - \theta$, which would suggest $\delta_\theta = 0$ immediately after the collapse. Further, when the turbulence decays, the turbulent fluxes become small so that radiative cooling tends to dominate the behavior of the ABL temperature. Given this, we can write the prognostic equations for θ and θ_{res} schematically as:

$$\rho c_p h \frac{d\theta}{dt} = \mathcal{R}_\theta$$

and

$$\rho c_p (h_{res} - h) \frac{d\theta_{res}}{dt} = \mathcal{R}_{\theta_r}$$

where $\mathcal{R}_\theta$ and $\mathcal{R}_{\theta_r}$ represent the net radiative fluxes in each layer. Based on these equations we can write an equation for the evolution of night-time δ_θ:

$$\frac{d\delta_\theta}{dt} = \frac{d(\theta_{res} - \theta)}{dt} = \frac{\mathcal{R}_{\theta_r}}{\rho c_p (h_{res} - h)} - \frac{\mathcal{R}_\theta}{\rho c_p h}$$

Now if we assume that the net radiative fluxes are of the same order for each layer, i.e. $\mathcal{R}_\theta \approx \mathcal{R}_{\theta_r}$, we can write:

$$\frac{d\delta_\theta}{dt} = \frac{\mathcal{R}_\theta}{\rho c_p}\left[\frac{1}{(h_{res} - h)} - \frac{1}{h}\right] = \frac{\mathcal{R}_\theta}{\rho c_p h}\left[\frac{2h - h_{res}}{h_{res} - h}\right] = \left[\frac{2h - h_{res}}{h_{res} - h}\right]\frac{d\theta}{dt}$$

which is in the same form as the equation shown above except that the coefficient is a function of the state variable h instead of a constant. The coefficient represents the relative thickness of each layer, so that when each layer is the same thickness (i.e. $h = h_{res} - h$), they will cool at the same rate. Generally the residual layer is much thicker than the night-time mixed layer so that it cools more slowly, which would lead to a night-time temperature inversion. A typical maximum boundary layer height is on the order of $1000 - 2000$m, making $h_{res} \sim 750 - 1500$m (using the Kim and Entekhabi (1998) formulation), while after the collapse h remains relatively small overnight with a typical value of 250-300m. Using $h_{res} = 750$m and $h = 250$m the coefficient is equal to $-1/2$. So for now we will proceed using the above equation for the night-time evolution of δ_θ, and for simplicity set the coefficient to a constant equal to $-1/2$.

In addition to the potential temperature inversion, we must also specify the night-time inversion in specific humidity at the top of the mixed layer. Kim and Entekhabi (1998) first set the residual specific humidity equal to the value of $q + \delta_q$ just before collapse. They then extrapolate the exponential specific humidity profile down to the new ABL height so

that the inversion is:

$$\delta_q = q_{res} \exp\left(\left[5.8 \times 10^3 \frac{\gamma_T}{\theta^2} + 5.5 \times 10^{-5} - \frac{g}{R_d \theta}\right][h_{res} - h]\right) - q$$

After the transition they model δ_q using Equation (A.16) without entrainment. An alternative approach is to think of the night-time specific humidity inversion in terms of the relationship between the mixed layer and residual layer at night. Immediately after the collapse we would expect that the specific humidity in the residual layer is similar to that in the mixed layer (i.e. $q_{res} = q$ just before the collapse instead of $q + \delta_q$), and that consequently $\delta_q \approx 0$. As the night proceeds there are no sources or sinks of moisture for the residual layer, so we would expect it to remain constant. For the mixed layer we would expect only small changes in q, with the source of moisture being surface evaporation after the collapse and perhaps early in the morning. Therefore, based on this, the inversion in specific humidity during the night would be directly related to changes in q as predicted in Equation (A.16) without entrainment:

$$\frac{d\delta_q}{dt} = -\frac{dq}{dt}$$

A.1.3 Model in Vector Notation:

The prognostic equations for our dynamical model are now completely specified. It should be reiterated that the model is discontinuous in time, with the discontinuity due to the transition phase (collapse) of the boundary layer. For compactness we write the model as:

$$\frac{d\mathbf{y}}{dt} = \mathbf{F}(\mathbf{y}, \mathbf{u}(t)) \tag{A.17}$$

where $\mathbf{y}$ is the state vector, $\mathbf{F}(\mathbf{y})$ is a vector function of the states (as represented by the fluxes shown in the above prognostic equations), and $\mathbf{u}(t)$ is the external forcing of the model (which includes incoming solar radiation, precipitation, and wind speed). The definitions of the model fluxes and forcing in the above equations are described in detail in the following sections. This discontinuous model presents no significant problems in terms of its numerical implementation, yet in terms of developing the adjoint model will most likely prove troublesome. Therefore the treatment of the discontinuity in the simplified model, upon which the adjoint will be derived, will be examined thoroughly.

A.2 Radiative Fluxes

A.2.1 Atmospheric Radiative Transfer

Shortwave radiation:

For shortwave radiation we do not consider absorption by the ABL since absorption occurs mainly in the higher atmosphere, however we do consider attenuation of the solar radiation as it passes through the atmosphere. We also partition the shortwave radiation into visible (VIS) and near-infrared (NIR) wavelength bands as well as direct beam (b) and diffuse (d) fluxes. This is done since these are the fluxes needed as input to the vegetation radiative transfer model (as described below). We model the effective solar constant(S_e) as

(Hartmann 1994):

$$S_e = S\left(\frac{\bar{d}}{d}\right)^2 cos(\theta_z)$$

where S is the solar constant, $(\bar{d}/d)^2$ represents a correction for the eccentricity of the earth's orbit around the sun, and θ_z is the solar zenith angle. We represent the incident direct beam solar radiation at the (canopy) surface for wavelength band Λ as:

$$F_{\Lambda,b(0)} = S_e f_\Lambda \tau_s f_b$$

and similarly for diffuse radiation as:

$$F_{\Lambda,d(0)} = S_e f_\Lambda \tau_s (1 - f_b)$$

where f_Λ is the fraction of solar radiation in band Λ (typically $f_{VIS} = 0.5$ and $f_{NIR} = 0.5$), τ_s is the solar transmission of the atmosphere (typically 0.75 for cloudless sky), and f_b is the fraction of solar radiation which is still direct beam once it reaches the surface (typically 0.8 for cloudless sky). Note that in cases where surface incident solar radiation ($S^{\downarrow}$) is available as forcing, $S_e\tau_s$ in the above expressions is replaced by $S^{\downarrow}$.

Longwave radiation:

The longwave radiation from the free atmosphere overlying the ABL depends on the pressure, temperature, and humidity profiles above the ABL. For clear skies using the profiles shown in the previous section, Brutsaert (1975) derived the expression:

$$R_{ad} = \sigma \epsilon_{ad} T_{h+}^4 \tag{A.18}$$

where ϵ_{ad} is the effective emissivity above the ABL and is given by:

$$\epsilon_{ad} = 1.24\left(\frac{R_v P_h q_{h+}}{100 R_d T_{h+}}\right)^m$$

where m is an empirical constant with a value of 1/7. Note that ϵ_{ad} is dependent on the state variables θ, q, δ_θ, δ_q, and h.

The incoming and outgoing longwave radiation are attenuated by absorption in the mixed layer. The expression for the column emissivity was derived by Brubaker and Entekhabi (1995):

$$\epsilon_a = A\left(\frac{2}{3}\frac{qP_s}{g}\left[1 - \left(\frac{P_h}{P_s}\right)^{\frac{3}{2}}\right]\right)^m$$

where A is an empirical constant with a value of $0.54(kg/m^2)^{-1/7}$. The term within the brackets represents the scaled amount of (mainly water vapor) mass in the air column.

The expressions for the upward and downward longwave radiative fluxes emanating from within the mixed layer may be given in terms of the potential temperature:

$$R_{Ad} = \sigma \epsilon_d \theta^4 \tag{A.19}$$

$$R_{Au} = \sigma \epsilon_u \theta^4 \tag{A.20}$$

Following Brubaker and Entekhabi (1995) the expressions for the effective directional emissivities of the mixed layer are:

$$\epsilon_d = A \left(\frac{2}{3} \frac{qP_s}{g} \right)^m m \int_{y_h}^{1} y^{\frac{8R_d}{3c_p}} (1-y)^{m-1} dy$$

$$\epsilon_u = A \left(\frac{2}{3} \frac{qP_s}{g} \right)^m m \int_{y_h}^{1} y^{\frac{8R_d}{3c_p}} (y-y_h)^{m-1} dy$$

where $y = \left(\frac{P}{P_s}\right)^{3/2}$. From the above expressions, it holds that $\epsilon_d > \epsilon_u$. Note that ϵ_a, ϵ_d, and ϵ_u depend on the states θ, q, and h. Each of the emissivities discussed above are plotted in Figure A-3 to show how they depend on the θ and q for nominal values of h, δ_θ, and δ_q. Note that the emissivities are most heavily dependent on humidity with only a slight variation with temperature. Since the emissivities are not very sensitive to potential temperature their dependence on q and h are shown in Figure A-4. From this figure is it shown that ϵ_{ad} is not very sensitive to h, while for the other emissivities, the sensitivity to h is, under some conditions, comparable to the sensitivity with respect to q.

A.2.2 Vegetation Radiative Transfer

The vegetation radiative transfer model is derived from the two-stream approximation used by Sellers (1985) which describes the interception, reflection, transmission, and absorption of radiation by the vegetation and underlying soil. Here we present a brief summary of the model. For a complete description of the two-stream model, the reader is referred to Sellers (1985).

The incoming radiation at the top of the canopy consists of both shortwave and longwave radiation. The model further requires that the incoming radiation be separated into three wavelength bands: visible (VIS), near-infrared (NIR), and thermal (T), as well as into direct beam (b) radiation and diffuse (d) radiation. It is assumed that all incoming thermal radiation is diffuse while incoming shortwave has both direct beam and diffuse components. The visible radiation band corresponds to incoming radiation of wavelength less that $0.7\mu m$ while the near-infrared band corresponds to solar wavelengths greater than $0.7\mu m$. By solving the two-stream radiative transfer equations, Sellers (1985) obtained expressions for the diffuse radiation within the canopy due to a given incident flux. The diffuse radiation within the canopy (normalized by the incident flux) due to direct beam radiation is given by:

$$I^{\uparrow}(L) = \frac{h_1}{s} \exp(-K_{vrt}L) + h_2 \exp(-h_{vrt}L) + h_3 \exp(h_{vrt}L)$$

$$I^{\downarrow}(L) = \frac{h_4}{s} \exp(-K_{vrt}L) + h_5 \exp(-h_{vrt}L) + h_6 \exp(h_{vrt}L)$$

Similarly, the normalized diffuse radiative flux within the canopy due to diffuse incident

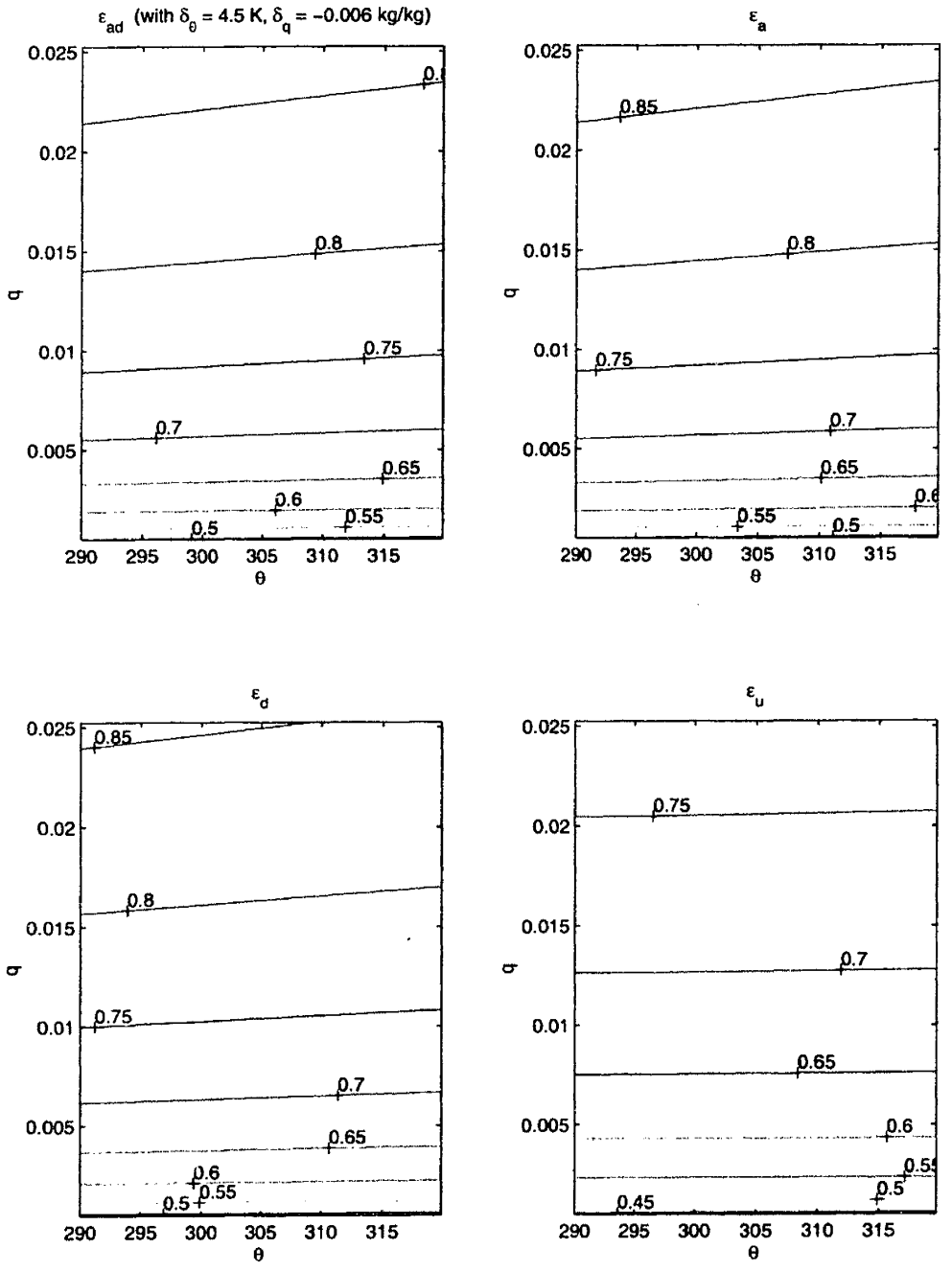

Figure A-3: Dependence of ABL emissivities on potential temperature (θ) and specific humidity (q) for a mixed layer depth of 1000m.

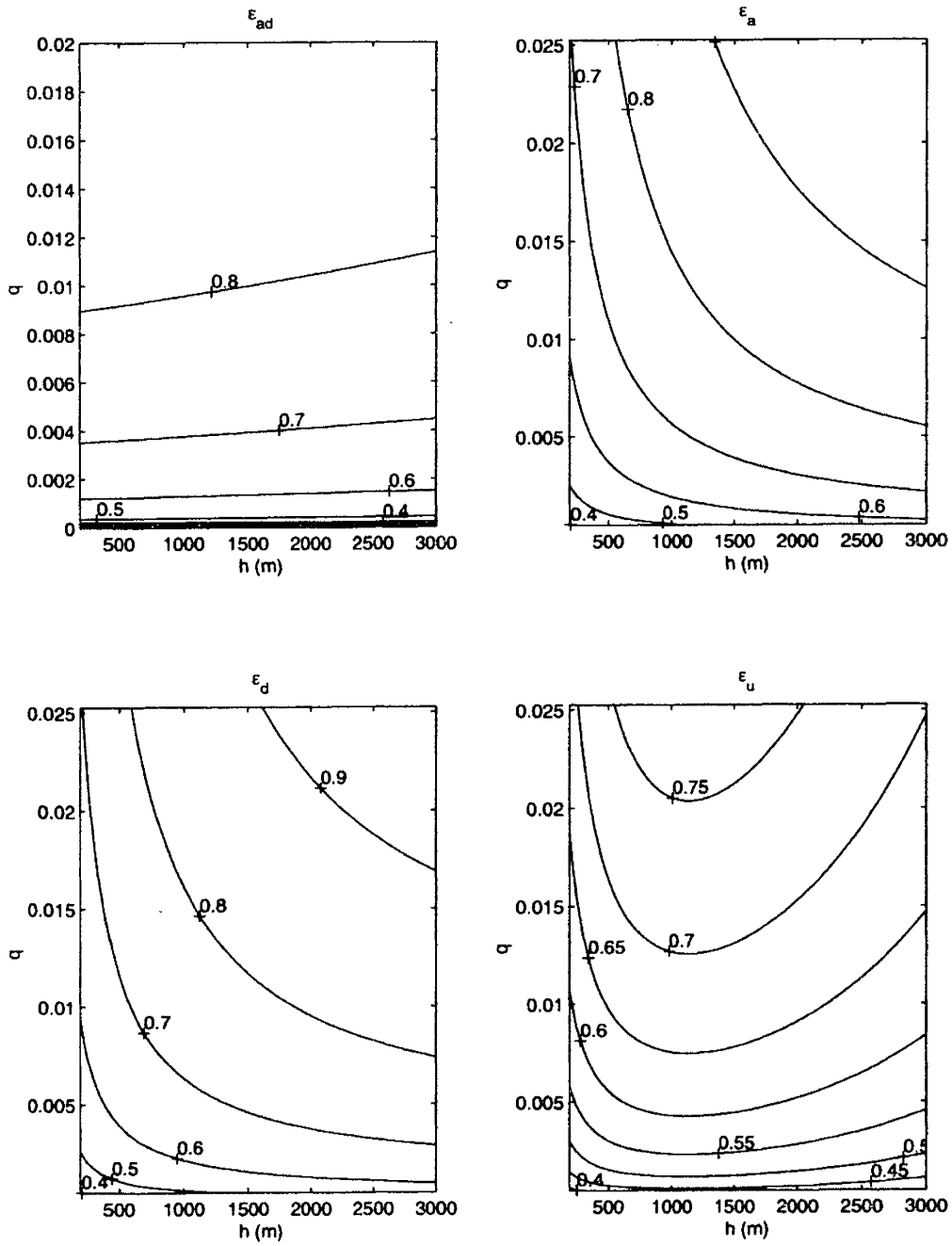

Figure A-4: Dependence of ABL emissivities on specific humidity (q) and ABL height (h) for at a potential temperature of 300 K.

radiation is given by:

$$I^{\uparrow}(L) = h_7 \exp(-h_{vrt}L) + h_8 \exp(h_{vrt}L)$$

$$I^{\downarrow}(L) = h_9 \exp(-h_{vrt}L) + h_{10} \exp(h_{vrt}L)$$

where $I^{\uparrow}$ and $I^{\downarrow}$ are the (upward and downward) diffuse fluxes normalized by the incident flux; the coefficients (h_{vrt}, h_i, and K_{vrt}) are algebraic expressions of model parameters given in Sellers (1985), and L is the cumulative leaf area index (LAI) at a given depth into the canopy. With these equations the radiation absorbed by the canopy and ground can be determined.

Solar radiation absorbed by the canopy and ground:

The solar radiation absorbed by the canopy in wavelength band Λ (VIS or NIR) and direction μ (b or d) is given by:

$$F_{\Lambda,\mu(c)} = F_{\Lambda,\mu(0)} \left[(1 - a_{c_{\Lambda,\mu}}) - I_g^{\downarrow}(1 - a_{g_{\Lambda,d}}) - \exp(-\frac{K_{vrt}L_T}{V_c})(1 - a_{g_{\Lambda,b}}) \right] V_c$$

while the solar radiation absorbed by the ground is given by:

$$F_{\Lambda,\mu(g)} = F_{\Lambda,\mu(0)} \left[(1 - V_c)(1 - a_{g_{\Lambda,d}}) + V_c \left(I_g^{\downarrow}(1 - a_{g_{\Lambda,d}}) + \exp(-\frac{K_{vrt}L_T}{V_c})(1 - a_{g_{\Lambda,b}}) \right) \right]$$

where $F_{\Lambda,\mu(0)}$ is the incident solar radiative flux at the canopy top. Note that $\exp(-\frac{K_{vrt}L_T}{V_c}) = 0$ for diffuse flux calculation. The canopy albedo ($a_{c_{\Lambda,\mu}}$) for beam and diffuse radiation respectively is given by:

$$a_{c_{\Lambda,b}} = I^{\uparrow}(L = 0) = \frac{h_1}{s} + h_2 + h_3$$

and:

$$a_{c_{\Lambda,d}} = I^{\uparrow}(L = 0) = h_7 + h_8$$

$I_g^{\downarrow}$ is the downward diffuse flux leaving the bottom of the canopy which for beam radiation is:

$$I_g^{\downarrow} = I^{\downarrow}(L = L_T) = \frac{h_4}{s} \exp(-K_{vrt}L_T) + h_5 \exp(-h_{vrt}L_T) + h_6 \exp(h_{vrt}L_T)$$

and for diffuse radiation is:

$$I_g^{\downarrow} = I^{\downarrow}(L = L_T) = h_9 \exp(-h_{vrt}L_T) + h_{10} \exp(h_{vrt}L_T)$$

Finally, $a_{g_{\Lambda,\mu}}$ is the ground albedo for each wavelength and direction and L_T is the total LAI, both of which are specified model parameters.

Thermal radiation absorbed by the canopy and ground:

The thermal radiation absorbed by the canopy is given by:

$$F_{T,d(c)} = F_{T,d(0)} V_c \delta_T - 2\sigma T_c^4 V_c \delta_T + \epsilon_g \sigma T_g^4 V_c \delta_T$$

while the thermal radiation absorbed by the ground is:

$$F_{T,d(g)} = F_{T,d(0)}(1 - V_c \delta_T) + \sigma T_c^4 V_c \delta_T - \epsilon_g \sigma T_g^4$$

where $F_{T,d(0)}$ is the incident thermal radiative flux $(R_{ad}(1-\epsilon_a)+R_{Ad})$, and δ_T is the fraction of incident thermal radiation absorbed by the canopy:

$$\delta_T = 1 - \exp\left(\frac{-L_T}{\overline{\mu}}\right)$$

Net radiation absorbed by the canopy and ground:

The above expressions give five components of absorbed radiation: $F_{VIS,b}$, $F_{NIR,b}$, $F_{VIS,d}$, $F_{NIR,d}$, and $F_{T,d}$ for both the canopy and ground. The net radiation absorbed by the canopy and ground is therefore just the sum of these components:

$$R_{n_c} = \sum_{\Lambda} \sum_{\mu} F_{\Lambda,\mu(c)} \tag{A.21}$$

$$R_{n_g} = \sum_{\Lambda} \sum_{\mu} F_{\Lambda,\mu(g)} \tag{A.22}$$

A.3 Turbulent Fluxes

The turbulent fluxes in the model consist of the sensible and latent heat fluxes from the canopy and ground. A resistance formulation is used to describe the fluxes of heat and water from the surface. A schematic of the resistance network is shown in Figure A-5. The fluxes from the canopy into the canopy air are given by:

$$H_c = \frac{\rho c_p (T_c - T_a)}{r_b} \tag{A.23}$$

$$L_v E_c = L_v (E_{ct} + E_{ci}) \tag{A.24}$$

where

$$L_v E_{ct} = \frac{\rho c_p}{\gamma} \frac{(e_*(T_c) - e_a)}{\overline{r_c} + 2r_b}(1 - W_c) \tag{A.25}$$

$$L_v E_{ci} = \frac{\rho c_p}{\gamma} \frac{(e_*(T_c) - e_a)}{2r_b} W_c \tag{A.26}$$

where $W_c = M_{cw}/S_c$ is the canopy wetness fraction. Similarly, the ground sensible and latent heat fluxes into the canopy air are given by:

$$H_g = \frac{\rho c_p (T_g - T_a)}{r_d} \tag{A.27}$$

$$L_v E_g = \frac{\rho c_p}{\gamma} \frac{(h_{soil} e_*(T_g) - e_a)}{r_{soil} + r_d} \tag{A.28}$$

where h_{soil} is the soil relative humidity, given by:

$$h_{soil} = \begin{cases} \exp\left(\frac{\psi_1 g}{RT_g}\right) & e_*(T_g) \geq e_a \\ 1 & e_*(T_g) < e_a \end{cases}$$

where r_b is the bulk canopy boundary layer resistance, and r_d is the aerodynamic resistance between the ground and canopy air space. All three of these resistances are functions of the wind speed above, within, and below the canopy and thus require an aerodynamic model of the system. The description of the aerodynamic resistances are included in the next section. The other resistances, $\overline{r_c}$ (the bulk stomatal resistance of the canopy) and r_{soil} are not functions of the aerodynamics and are described below.

Note that the sensible and latent heat fluxes depend on the canopy air temperature (T_a) and vapor pressure (e_a) which are not state variables. They can be determined diagnostically however by assuming that the heat and moisture storage capacity of the canopy air is negligible. First, the sensible and latent heat fluxes from the canopy air into the mixed layer can be expressed as:

$$H_m = \frac{\rho c_p (T_a - T_m)}{r_a}$$

$$L_v E_m = \frac{\rho c_p}{\gamma} \frac{(e_a - e_m)}{r_a}$$

where T_m is the air temperature at a height z_m (the height of the bottom of the mixed layer),

$$T_m = \theta \left(\frac{P_m}{P_s}\right)^{\frac{R_d}{c_p}}$$

e_m is the vapor pressure at height z_m ($P_m q/\epsilon$), and r_a is the aerodynamic resistance between the canopy height and z_m. Under this assumption the conservation of heat and moisture from the surface to the mixed layer can be expressed as:

$$H_c + H_g = H_m$$

and

$$L_v E_c + L_v E_g = L_v E_m$$

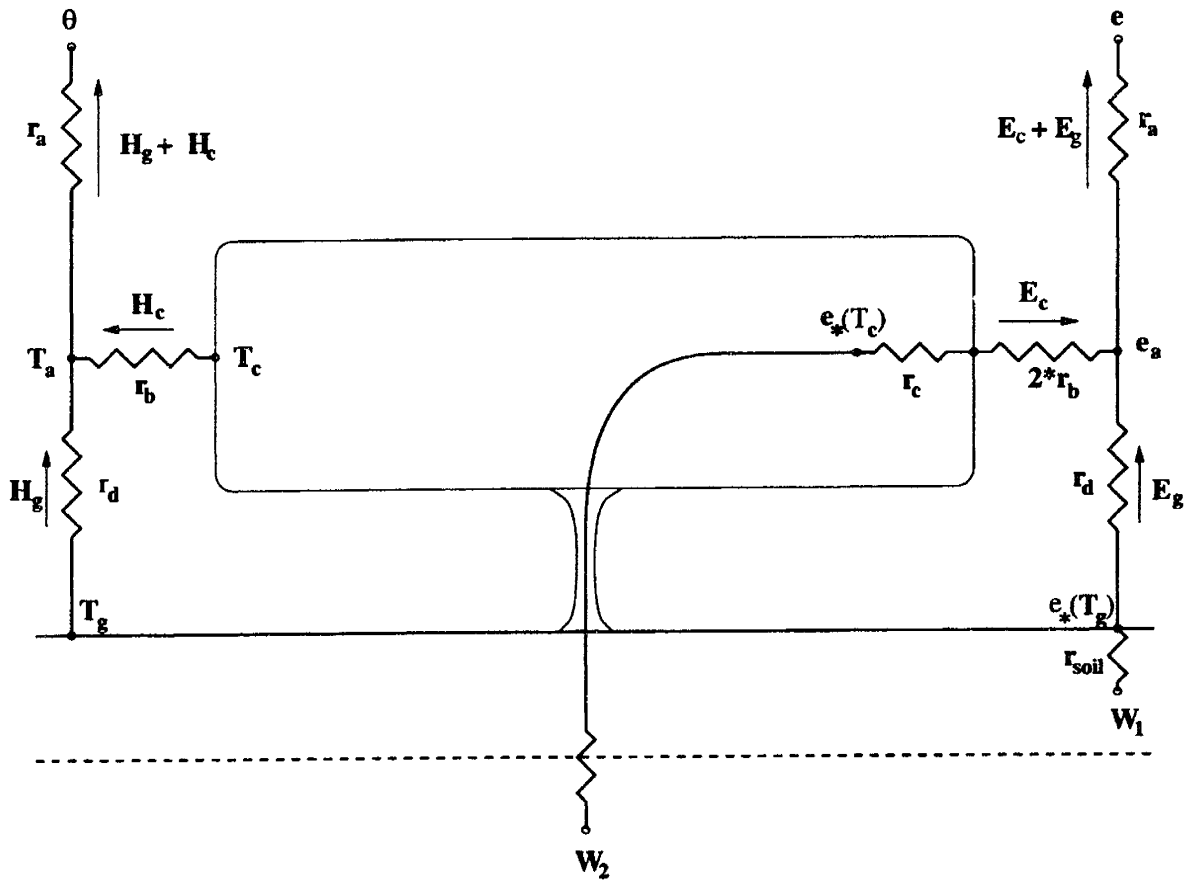

Figure A-5: Resistance network used in determination of sensible and latent heat fluxes from the ground and canopy.

which can be solved for T_a and e_a respectively:

$$T_a = \frac{\frac{1}{r_b}T_c + \frac{1}{r_d}T_g + \frac{1}{r_a}T_m}{\frac{1}{r_b} + \frac{1}{r_d} + \frac{1}{r_a}}$$

$$e_a = \frac{\left(\frac{W_c}{2r_b} + \frac{(1-W_c)}{r_c+2r_b}\right)e_*(T_c) + \frac{h_{soil}}{r_{soil}+r_d}e_*(T_g) + \frac{1}{r_a}e_m}{\frac{W_c}{2r_b} + \frac{(1-W_c)}{r_c+2r_b} + \frac{h_{soil}}{r_{soil}+r_d} + \frac{1}{r_a}}$$

which indicates that the canopy air temperature is a weighted average of the canopy, ground, and potential temperatures. The canopy air vapor pressure is a similar weighted average of the canopy and ground saturated vapor pressures, and mixed layer vapor pressure values. Note however that these equations are implicit (and nonlinear) in T_a and e_a respectively, since the resistances themselves are functions of T_a and e_a. Thus these equations are solved iteratively.

Canopy stomatal resistance:

The stomatal resistance of a single leaf is the means by which a plant controls the gas exchange between the leaf interior and free atmosphere (Sellers 1985). The leaf response is due to a variety of environmental factors. Jarvis (1976) proposed an expression for stomatal resistance as a function of environmental variables in the following form:

$$r_s = \left[\frac{a_2}{b_2 + F\downarrow} + c_2\right][f(\psi_l)f(T_c)f(\delta e)]^{-1}$$

where a_2, b_2,and c_2 are species dependent constants (see Dorman and Sellers (1989)), $F\downarrow$ is the downward photosynthetically active radiation (PAR) flux, and $f(\psi_l)$, $f(T_c)$, and $f(\delta e)$ are adjustment factors accounting for the influence of leaf water potential, leaf temperature, and vapor pressure deficit respectively.

The above expression gives the resistance of a single leaf, but for our model we require a bulk resistance for the entire canopy. If we assume that leaves at all levels in the canopy react in a similar way to incident PAR the bulk canopy resistance may be written as (Sellers (1985)):

$$\frac{1}{\overline{r_c}} = V_c N_c f(\Sigma)\int_0^{L_T}\int_0^{\pi/2}\int_0^{2\pi}\frac{O(\xi,\theta)}{r_s(F,\xi,\theta)}sin\theta\ d\xi\ d\theta\ dL$$

where V_c is the fractional canopy cover (currently set to 1.0), N_c is the green leaf fraction, and $f(\Sigma)$ is the product of the three stress terms in the stomatal resistance equation.

A solution based on the Ross-Goudriaan χ_L function (which is already used in the vegetation radiative transfer model) is:

$$\frac{1}{\overline{r_c}} = V_c N_c f(\Sigma)\frac{1}{kc_2}\left[\frac{b_2}{dF_0}\ln\left(\frac{\mu d\exp(kL_T) + G(\mu)}{\mu d + G(\mu)}\right) - \ln\left(\frac{\mu d + G(\mu)\exp(-kL_T)}{\mu d + G(\mu)}\right)\right]$$

$$d = \frac{a_2 + b_2c_2}{c_2F_0}$$

which can be rewritten as:

$$\frac{1}{\overline{r_c}} = f(\Sigma)\frac{1}{r_{cmin}}$$

where r_{cmin} is the minimum canopy resistance for a given PAR flux (direct beam only). Since this only applies to direct radiation, Koster and Suarez (1996) use a slightly different formulation which takes into account diffuse PAR flux as well:

$$\frac{1}{\overline{r_c}} = V_c N_c f(\Sigma)\frac{1}{k' c_2}\left[k' L_T + \left(\frac{b}{F_0 d} - 1\right)\ln\left(\frac{d\exp(k' L_T) + \Psi}{d + \Psi}\right)\right] \qquad \text{(A.29)}$$

where the new constants are defined in Koster and Suarez (1996).

The forms of the stress factor expressions which account for the effects of leaf water potential, leaf temperature, and vapor pressure deficit each vary between 0 and 1 and are taken from Sellers et al. (1986) and are shown in Figure A-6. The canopy temperature stress function is given by:

$$f(T_c) = \begin{cases} 0 & T_c < T_l \\ h_{rc3}(T_c - T_l)(T_u - T_c)^{h_{rc4}} & T_l < T_c < T_u \\ 0 & T_c > T_u \end{cases}$$

$$h_{rc3} = \frac{1}{(T_0 - T_l)(T_u - T_0)^{h_{rc4}}}$$

$$h_{rc4} = \frac{(T_u - T_0)}{(T_0 - T_l)}$$

where T_0 is the optimum temperature $[f(T_0) = 1]$ (typically the mean temperature found in the surrounding environment), T_l is the lower temperature limit $[f(T_l) = 0]$ (typically 273K), and T_u is the upper temperature limit $[f(T_u) = 0]$ (typically 318K). The stress factor for the vapor pressure deficit within the canopy air is given by:

$$f(\delta e) = \begin{cases} 1 & \delta e < 0 \\ 1 - h_{rc5}[e_*(T_a) - e_a] & 0 < \delta e < 1/h_{rc5} \\ 0 & \delta e > 1/h_{rc5} \end{cases}$$

where h_{rc5} is a species dependent constant (see Dorman and Sellers (1989)). Finally, the effects of soil moisture on transpiration are felt through the leaf water potential stress

function:

$$f(\psi_l) = \begin{cases} 0 & \psi_l < \psi_{c2} \\ \frac{\psi_l - \psi_{c2}}{\psi_{c1} - \psi_{c2}} & \psi_{c2} < \psi_l < \psi_{c1} \\ 1 & \psi_l > \psi_{c1} \end{cases}$$

where ψ_{c1} is the leaf water potential at which the stomata start to close, and ψ_{c2} is the leaf water potential at which the stomata are completely closed (see Dorman and Sellers (1989)). The leaf water potential can be calculated using a catenary model of the water transfer pathway from rootzone to leaf following van der Honert (1948):

$$\psi_l = \psi_r - z_T - \frac{E_{ct}}{\rho_w}(r_{plant} + r_{root})$$

where ψ_r is the soil moisture potential in the rootzone, z_T is the height of the transpiration source (taken as z_1), r_{plant} is the area-averaged resistance imposed by the plant vascular system, and r_{root} is the area-averaged resistance of the soil and root system. Note that the canopy resistance is a function of transpiration (which itself is a function of canopy resistance). This constitutes a nonlinearity in the model which is solved iteratively. The soil moisture potential in the rootzone is expressed as the weighted depth averaged soil moisture potential:

$$\psi_r = \frac{1}{z_d}\sum_{0}^{z_d} \psi_i d_i$$

where z_d is the rooting depth, ψ_i is the soil moisture potential in each layer (described in Section 6),and d_i is the depth of the ith soil layer.

The area-averaged resistance of the soil and root system is given by the following relationship proposed by Federer (1979):

$$r_{root} = \frac{R_r/D_r + \alpha_f/K_r}{z_d}$$

where

$$\alpha_f = \frac{1}{8\pi D_r}\left[V_r - 3 - 2\ln\left(\frac{V_r}{1 - V_r}\right)\right]$$

where R_r is the resistance per unit root length (s/m), D_r is the root density (m/m^3), V_r is the volume of root per unit volume of soil (m^3/m^3), and K_r is the mean soil hydraulic conductivity in the rootzone.

Following the calculation of E_{ct}, the rate of extraction of transpired water from the ith soil layer is then:

$$E_{ct_i} = \frac{d_i}{z_d}\left(\frac{\psi_i - \psi_l - z_T}{r_{plant} + r_{root}}\right)\rho_w$$

a)

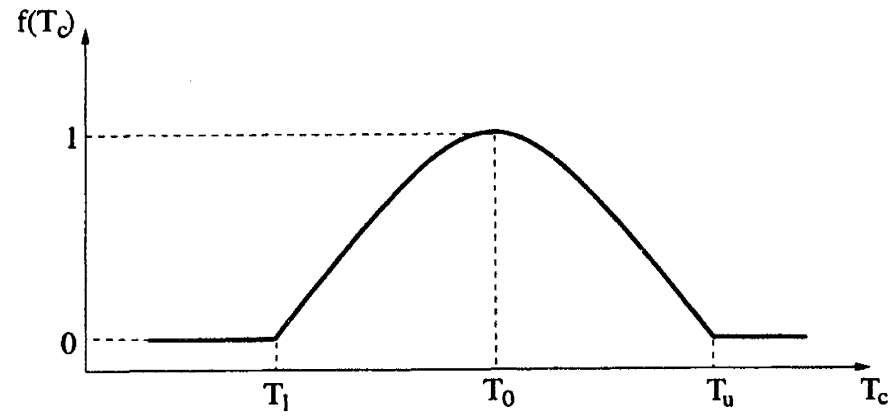

b)

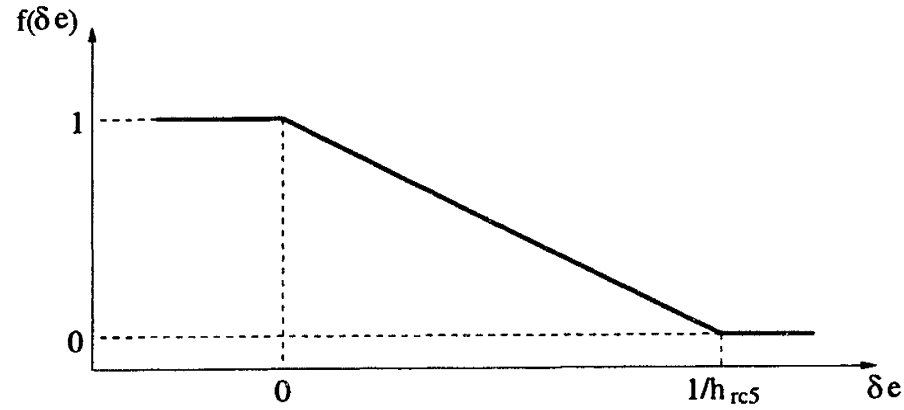

c)

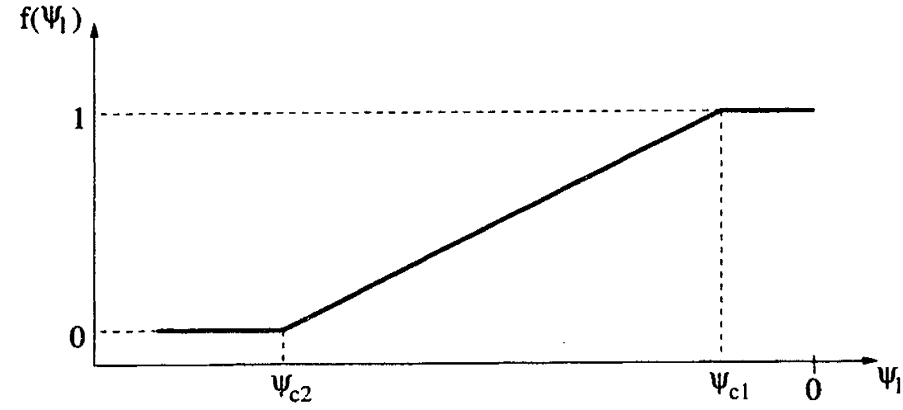

Figure A-6: Schematic diagrams of canopy resistance stress factors $f(T_c)$, $f(\delta e)$, and $f(\psi_l)$

Soil resistance:

The soil resistance model is the same one used in SiB2 (Sellers et al. 1996) and is only a function of the soil moisture in the uppermost soil layer:

$$r_{soil} = \exp(8.206 - 4.255W_1)$$

A.4 Aerodynamics

Wind Interactions with Canopy:

The model used to determine the aerodynamic resistances and wind profile due to the presence of a vegetation canopy is borrowed heavily from the LSX model (Bonan et al. 1993) which is slightly more crude, but more computationally efficient than the model used in SiB or SiB2. Figure A-7 shows a schematic of the vertical profile of wind speed near the land surface in our model. In our model there exists three distinct regions. Region I is the free-air region above the canopy ($z_1 \leq z$), Region II is the canopy region ($z_2 \leq z \leq z_1$), and Region III is the air region between the bottom of the canopy and the ground ($0 \leq z \leq z_2$). Note that for generality we differentiate between the reference height (z_r) which corresponds to the height at which surface layer wind forcing is specified and the height of the mixed layer (z_m).

Region I

For Region I, a constant-flux layer is assumed with a mixing-length logarithmic profile of $u(z)$ modified by stratification:

$$U(z) = \sqrt{\frac{\tau_0}{\rho}} \frac{1}{k} \ln\left(\frac{z-d}{z_0}\right) F_M^{-1/2}$$

where $U(z)$ is the mean horizontal wind speed ($\sqrt{u^2+v^2}$), τ is the horizontal wind stress (independent of height within Region I), ρ is the density of air, and k is the von Karman constant. The zero-plane displacement height (d) is prescribed as 0.7 times the canopy height (h_{can}), and the canopy roughness length is computed to satisfy the boundary conditions (see below). Note that τ_0 is the same shear stress used in the boundary layer growth formulation. The stability correction factors for momentum and heat respectively are taken from Louis et al. (1982):

$$F_M = \begin{cases} 1 - \dfrac{2bRi_B}{1+2ba^2c_m\left(\frac{(z-d)}{z_0}|Ri_B|\right)^{1/2}} & Ri_B \leq 0 \ (unstable) \\ \dfrac{1}{(1+2b\frac{Ri_B}{\sqrt{1+d_aRi_B}})} & 0 \leq Ri_B \ (stable) \end{cases}$$

and

$$F_H = \begin{cases} 1 - \dfrac{3bRi_B}{1+3ba^2c_h\left(\frac{(z-d)}{z_0}|Ri_B|\right)^{1/2}} & Ri_B \leq 0 \ (unstable) \\ \dfrac{1}{(1+3bRi_B\sqrt{1+d_aRi_B})} & 0 \leq Ri_B \ (stable) \end{cases}$$

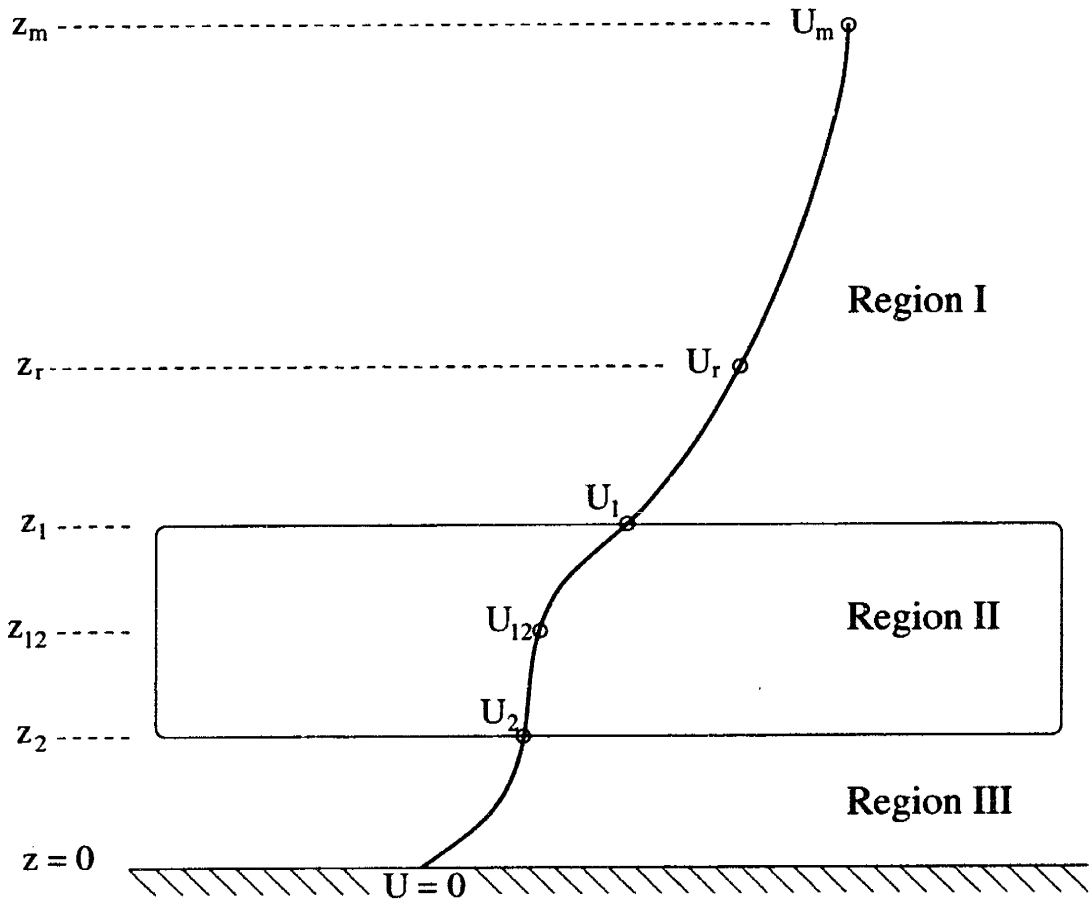

Figure A-7: Schematic representation of wind profile above (Region I), within (Region II), and below (Region III) the vegetation canopy. Note that $U = \sqrt{u^2 + v^2}$.

where $b = 5$, $c_m = 7.5$, $c_h = 5$, $d_a = 5$, and

$$a^2 = \frac{k^2}{\left[\ln\left(\frac{z-d}{z_0}\right)\right]^2}$$

While F_M and F_H are conditionally dependent on Ri_B, Louis et al. (1982) chose the parameters so that the functions are continuous and differentiable at the origin. The bulk Richardson number (Ri_B) is defined by:

$$Ri_B = \frac{g(z_m - z_1)(\theta - T_a)}{0.5(\theta + T_a)U_m^2}$$

While some studies define the Richardson number between the surface and the micrometeorological reference height (z_r) we define it this way so that it is representative of the stability of the air between the canopy top and the mixed layer. Note that to be consistent when calculating the stability correction factors, the value of z should be set to z_m.

Region II

Within the canopy, the wind stress is not constant due to the force imparted by the vegetation. A diffusive model is used for Region II (Cowan (1968), Goudriaan (1977)):

$$\frac{d}{dz}\left(\frac{\tau_1}{\rho}\right) = CU^2$$

$$\frac{\tau_1}{\rho} = (DU)\frac{dU}{dz}$$

The first equation is a basic drag law for the vegetation, with the drag proportional to the square of the wind speed. The second equation is a first-order closure for the vertical momentum flux, with the diffusion coefficient equal to DU. The general solution to the above equations is:

$$U(z) = \sqrt{A\exp(\lambda z) + B\exp(-\lambda z)}$$

$$\tau_1(z) = \frac{\rho\lambda D}{2}[A\exp(\lambda z) - B\exp(-\lambda z)]$$

where $\lambda = \sqrt{2C/D}$, $C = 0.4/h_{can}$, $D = 0.1h_{can}$, and A and B are arbitrary constants used to satisfy boundary conditions (see below).

Region III

Below the canopy the wind profile is again assumed to have a logarithmic profile:

$$U(z) = \sqrt{\frac{\tau_2}{\rho}}\frac{1}{k}\ln\left(\frac{z}{z_{0g}}\right)$$

where $z_{0g} = 0.002$ m is the prescribed ground roughness length.

Boundary Conditions and Solution of Wind and Shear Stress Profiles

The distinct solutions for each region shown above are coupled by continuity in wind speed and shear stress at their boundaries. There are five boundary conditions in five unknowns:

$$U(z_m) = \sqrt{\frac{\tau_0}{\rho}}\frac{1}{k}\ln\left(\frac{z_m - d}{z_0}\right)F_M^{-1/2} = U_m$$

$$U(z_1) = \sqrt{\frac{\tau_0}{\rho}}\frac{1}{k}\ln\left(\frac{z_1 - d}{z_0}\right)F_M^{-1/2} = U(z_1) = \sqrt{A\exp(\lambda z_1) + B\exp(-\lambda z_1)}$$

$$\tau_0 = \tau_1 = \frac{\rho\lambda D}{2}[A\exp(\lambda z_1) - B\exp(-\lambda z_1)]$$

$$U(z_2) = \sqrt{A\exp(\lambda z_2) + B\exp(-\lambda z_2)} = U(z_2) = \sqrt{\frac{\tau_2}{\rho}}\frac{1}{k}\ln\left(\frac{z_2}{z_{0g}}\right)$$

$$\tau_1 = \frac{\rho\lambda D}{2}[A\exp(\lambda z_2) - B\exp(-\lambda z_2)] = \tau_2$$

where the unknowns are τ_0 (above the canopy), z_0, A, B, and τ_2 (below the canopy). The five unknowns can be determined through algebraic manipulation of the five equations above to yield a complete solution for the profiles in windspeed and shear stress from the ground to the ABL measurement height (z_m).

Aerodynamic Resistances:

With the complete profile of wind speed in the surface layer known, the aerodynamic resistances can be determined. The aerodynamic resistance between the canopy air space and the ABL measurement height is given by:

$$r_a = r_{a1} + r_{a2}$$

where r_{a1} is the aerodynamic resistance from the canopy top to the measurement height which can be derived as follows:

$$r_{a1} = \int_{z_1}^{z_m}\frac{1}{K_{a1}}dz$$

which is given by Bonan et al. (1993) as:

$$r_{a1} = \frac{1}{F_H k^2 U_m}\ln\left(\frac{z_m - d}{z_0}\right)\left(\frac{z_m - d}{z_1 - d}\right)$$

The resistance between the canopy top and the canopy airspace at the canopy source height (taken to be z_{12}) is expressed as:

$$r_{a2} = \int_{z_{12}}^{z_1}\frac{1}{K_{a2}}dz = \int_{z_{12}}^{z_1}\frac{1}{DU(z)}dz$$

where D is constant with height and can thus be taken outside the integral. Two approaches can be used to determine the resistance. The vertical domain between z_{12} and z_1 can be discretized and then the integral can be evaluated numerically:

$$r_{a2} = \frac{\Delta z}{2D} \sum_i \left(\frac{1}{U_i} + \frac{1}{U_{i+1}} \right)$$

or, as done by Bonan et al. (1993), the wind speed can be assumed to be roughly constant between z_{12} and z_1 (taken to be the average) which yields:

$$r_{a2} = \frac{z_1 - z_{12}}{0.5D(U_1 + U_{12})}$$

If the numerical integration is performed with only one discretization of the domain, the results are not strictly the same between the two methods, but practically speaking yield similar numerical values.

Similarly, the aerodynamic resistance between the ground and the canopy air space can be derived in a similar way:

$$r_d = r_{d1} + r_{d2}$$

where

$$r_{d1} = \frac{1}{k^2 U_2} \ln\left(\frac{z_2}{z_{0g}}\right) \ln\left(\frac{z_2}{z_{0g}}\right)$$

for the resistance between the ground and the canopy bottom. The resistance between the canopy bottom and canopy source height (using a coarse discretization) is:

$$r_{d2} \approx \frac{z_{12} - z_2}{2D} \left(\frac{1}{U_2} + \frac{1}{U_{12}} \right) \approx \frac{z_{12} - z_2}{0.5D(U_{12} + U_2)}$$

Finally, the bulk boundary layer resistance in the canopy air is given by:

$$r_b = \frac{C_{rb}}{\sqrt{U_{12}}}$$

where C_{rb} is a specified constant.

With regards to the two alternatives in windspeed profile determination, we currently proceed with Approach #2. However for the reasons stated above it might be desirable to change to Approach #1 in the future.

A.5 Moisture Transport

Precipitation and Infiltration:

The precipitation input to the model is given by P and at this point in the model development is assumed to consist of no snow. To determine the direct throughfall (D_d) an analogous model to the transmission of radiation is used:

$$D_d = \delta_p P \tag{A.30}$$

where

$$\delta_p = \exp(-K_p L_T)$$

where K_p is the extinction coefficient for rainfall (which is the same as for a vertical beam of radiation). The amount of intercepted rainfall is thus:

$$I = (1 - \delta_p)P$$

The canopy storage limit in meters is given by:

$$S_c = 0.0001 L_T$$

Therefore the canopy drainage (or overflow) is:

$$D_c = (1 - \delta_p)P - (S_c - M_{cw}) \tag{A.31}$$

At the ground surface, the potential infiltration rate ($P_{W_1}(max)$) is simply given as:

$$P_{W_1}(max) = K_s$$

The infiltration excess runoff (R) is then:

$$R = \begin{cases} D_c + D_d - K & D_c + D_d \geq K \\ 0 & D_c + D_d \leq K \end{cases}$$

Finally, the infiltration into the top soil layer is given by:

$$P_{W_1} = D_c + D_d - R \tag{A.32}$$

Diffusion of water in the soil:

The equation used to describe vertical exchanges between soil layers is:

$$Q = K\left[\frac{\partial \psi}{\partial z} + 1\right]$$

where the soil hydraulic properties are modeled following Clapp and Hornberger (1978):

$$K_i = K_s W_i^{(2B+3)}$$

$$\psi_i = \psi_s W_i^{-B}$$

Therefore the fluxes between layers 1 and 2 and layers 2 and 3 are given by:

$$Q_{1,2} = K_{1,2}\left[\left(\frac{\partial \psi}{\partial z}\right)_{1,2} + 1\right] \tag{A.33}$$

$$Q_{2,3} = K_{2,3}\left[\left(\frac{\partial\psi}{\partial z}\right)_{2,3} + 1\right] \tag{A.34}$$

For the discretized model the hydraulic conductivity between layers is the same formulation used in Sellers et al. (1996):

$$K_{i,i+1} = \left[\frac{K_i\psi_i - K_{i+1}\psi_{i+1}}{\psi_{i+1} - \psi_i}\right]\left[\frac{B}{B+3}\right]$$

and the discretized pressure gradient is:

$$\left(\frac{\partial\psi}{\partial z}\right)_{i,i+1} = \frac{\psi_{i+1} - \psi_i}{0.5(d_i + d_{i+1})}$$

For the lower boundary condition (if a water table depth boundary condition is not used) we assume $(\partial\psi/\partial z) \ll 1$ and thus the drainage out of the lowest layer is:

$$Q_3 = K(W_3) = K_s W_3^{(2B+3)} \tag{A.35}$$

A.6 Numerical Solution Scheme

To numerically implement the model it is necessary to first decide on an appropriate solution strategy. Deciding on this strategy involves weighing the competing factors of numerical efficiency, stability, and accuracy. While some of the details related to these issues will only be resolved once the code is written, the framework of the model is presented here.

As stated earlier, the model can be written compactly as:

$$\frac{d\mathbf{y}}{dt} = \mathbf{F}(\mathbf{y}, \mathbf{u}(t))$$

where $\mathbf{F}$ is the nonlinear vector function representing the right-hand-sides of the prognostic equations given in Section 2 (which are coupled through the state variables) and $\mathbf{u}(t)$ is the external model forcing (which under the current formulation is limited to incoming solar radiation, precipitation and wind speed at a specified reference level). Again, keep in mind that this model has a discontinuity at the time at which the boundary layer collapses.

A standard finite difference scheme can be applied to integrate the model forward in time. In general, explicit schemes are very computationally efficient, but are only conditionally stable, while implicit schemes are generally more computationally expensive, but are unconditionally stable. In order to balance the competing factors of computational expense and stability, we adopt a solution strategy which has been used in other land-atmosphere models (e.g. Sellers et al. (1996); Dickinson et al. (1986)). We split the state vector into two components, the "fast" response variables ($\mathbf{y_f}$) and the "slow" response variables ($\mathbf{y_s}$):

$$\mathbf{y_f} = [T_c, T_g, \theta, q, \delta_\theta, \delta_q, h]^T$$

$$\mathbf{y_s} = [T_d, M_{cw}, W_1, W_2, W_3]^T$$

This distinction is drawn based on the physical argument that the fast response variables evolve more quickly over a small time step than the other variables. By making this dis-

tinction, a mixed-type solution scheme can be implemented where, over a given time step, the fast response variables are first integrated using an implicit scheme, after which, using the updated $\mathbf{y_f}$ values, the slow response variables are solved for using an explicit scheme. In using this solution strategy, two things are gained: 1) Those variables which are more prone to numerical instabilities (due to their fast response) are solved for implicitly; 2) Reducing the size of the state vector which is solved using an implicit scheme yields considerable computational savings. A more detailed description of the solution algorithm is discussed below. The prognostic equations can be decomposed into fast and slow response and written as:

$$\frac{d\mathbf{y_f}}{dt} = \mathbf{F_f}(\mathbf{y_f}, \mathbf{y_s}, \mathbf{u_f}(t))$$

$$\frac{d\mathbf{y_s}}{dt} = \mathbf{F_s}(\mathbf{y_s}, \mathbf{y_f}, \mathbf{u_s}(t))$$

Discretizing the fast response equation using an implicit finite difference scheme:

$$\frac{\mathbf{y_f}^{n+1} - \mathbf{y_f}^{n}}{\Delta t} = \mathbf{F_f}(\mathbf{y_f}^{n+1}, \mathbf{y_s}^{n}, \mathbf{u_f}^{n})$$

where n is the time level, yields the following system of nonlinear equations (where it is understood that $\mathbf{F_f}$ is also evaluated about $\mathbf{y_s}^n$ and $\mathbf{u_f}^n$):

$$\mathbf{y_f}^{n+1} - \Delta t(\mathbf{F_f}(\mathbf{y_f}^{n+1})) - \mathbf{y_f}^{n} = 0$$

Linearizing $\mathbf{F_f}$ around $\mathbf{y_f}^*$ yields:

$$\mathbf{y_f}^{n+1} - \Delta t \left[\mathbf{F_f}(\mathbf{y_f}^*) + \left.\frac{\partial \mathbf{F_f}}{\partial \mathbf{y_f}}\right|_{\mathbf{y_f^*}} (\mathbf{y_f}^{n+1} - \mathbf{y_f}^*) \right] - \mathbf{y_f}^{n} = 0$$

which can be expressed in the canonical form for a system of linear equations:

$$\mathbf{A}\mathbf{y_f}^{n+1} = \mathbf{b}$$

where

$$\mathbf{A} = \left[\mathbf{I} - \Delta t \left.\frac{\partial \mathbf{F_f}}{\partial \mathbf{y_f}}\right|_{\mathbf{y_f^*}} \right]$$

and

$$\mathbf{b} = \left[\Delta t \left(\mathbf{F_f}(\mathbf{y_f}^*) - \left.\frac{\partial \mathbf{F_f}}{\partial \mathbf{y_f}}\right|_{\mathbf{y_f^*}} \mathbf{y_f}^* + \right) + \mathbf{y_f}^{n} \right]$$

To get the finalized solution for $\mathbf{y_f}^{n+1}$ use an iterative scheme (where m is the iteration index):

1. Initialization: $\mathbf{y_f}^* = \mathbf{y_f}^n$ $(m = 1)$

2. Linearize $\mathbf{F_f}$ about $\mathbf{y_f}^*$

3. Solve $\quad \mathbf{A}_m \mathbf{y_f}_m^{n+1} = \mathbf{b}_m$

4. Set $\mathbf{y_f}^* = \mathbf{y_f}_m^{n+1}$

5. Re-linearize $\mathbf{F_f}$ about $\mathbf{y_f}^*$

6. Solve $\quad \mathbf{A}_m \mathbf{y_f}_m^{n+1} = \mathbf{b}_m$

7. Check convergence: Is $\quad \left| \mathbf{y_f}_m^{n+1} - \mathbf{y_f}_{m-1}^{n+1} \right| \leq \epsilon_{tol}$?

   YES $\rightarrow \mathbf{y_f}^{n+1} = \mathbf{y_f}_m^{n+1}$

   NO $\rightarrow$ Repeat steps 4-7

Once the solution of the fast response equations are obtained, the slow response variables are updated explicitly. The discretized slow response prognostic equation is written as:

$$\frac{\mathbf{y_s}^{n+1} - \mathbf{y_s}^n}{\Delta t} = \mathbf{F_s}(\mathbf{y_s}^n, \mathbf{y_f}^{n+1}, \mathbf{u_s}^n)$$

which yields the explicit update equations:

$$\mathbf{y_s}^{n+1} = \mathbf{y_s}^n + \Delta t[\mathbf{F_s}(\mathbf{y_s}^n, \mathbf{y_f}^{n+1}) + \mathbf{u_s}^n]$$

Now the complete set of state variables at time $t = n + 1$ is known. This procedure is then simply repeated at each time step from the initial time to the final time (with special care at the discontinuity) to get the integrated state variables over the desired time interval.

Appendix B

Forward Model Modifications for Use in Adjoint Model

In Chapter 2 the adjoint technique was described for a general model and model response functional. The forward model to be used in this study was described in detail in Appendix A. This model was described as the "complete model" in that it was developed with the primary objective being that it accurately represent the coupled land-atmosphere system. In doing so, some of the parameterizations and model formulations contained various components that are not necessarily amenable to the development of the adjoint model. The complete model forms the basis for a "simplified model" upon which the adjoint is to be developed. The simplified model will attempt to best represent the processes and output of the complete model while eliminating or modifying those aspects which would otherwise prevent the application of the adjoint technique. To help illustrate the necessary conditions and model modifications needed for application of the adjoint method, we again present the key equations derived in Chapter 2:

$$\frac{d\mathbf{y}}{dt} = \mathbf{F}(\mathbf{y}, \boldsymbol{\alpha}) \qquad \textbf{Forward Model}$$

$$J = \int_t \phi(\mathbf{y}, \boldsymbol{\alpha}) dt \qquad \textbf{Model Response Functional}$$

$$\frac{d\boldsymbol{\lambda}}{dt} = -\frac{\partial \mathbf{F}}{\partial \mathbf{y}}^T \boldsymbol{\lambda} + \frac{\partial \phi}{\partial \mathbf{y}}^T \qquad \textbf{Adjoint Model}$$

$$\delta J = \int_t \left(\frac{\partial \phi}{\partial \boldsymbol{\alpha}}^T - \frac{\partial \mathbf{F}}{\partial \boldsymbol{\alpha}}^T \boldsymbol{\lambda} \right)^T dt \, \delta\boldsymbol{\alpha} - \boldsymbol{\lambda}_0^T \delta \mathbf{y}_0 \qquad \textbf{Model Response Variation}$$

In order to apply the adjoint technique we must modify those aspects of the model which do not fit within the framework above. Specifically, we must be wary of:

1. On/off and conditional switches in model formulation—the adjoint method assumes a model which is continuous in time.

2. Implicit functional dependencies in model—$\mathbf{F}$ and ϕ should be expressed as explicit

functions of y and α.

3. Non-differentiable functions—differentiability of $\mathbf{F}$ and ϕ with respect to model states and parameters is required in both the adjoint model and the model response variational.

B.1 On/off switches in time

The above formalism assumes that the physical model can be expressed in the continuous form shown above where there are no source terms which switch on or off in time. The complete model however contains certain on/off switches that do not allow this formulation to be strictly applicable. In particular, the switches have to do with: 1) entrainment of air from above the ABL, and 2) the collapse of the ABL. In cases where the model is applied only during daytime (ABL growth) conditions, the on/off switches are not an issue. However to make the adjoint applicable over full diurnal cycles, we address the switches below.

B.1.1 Entrainment

A particular on/off switch is the entrainment of heat and moisture from above the boundary layer as it grows. The prognostic equations for potential temperature and specific humidity contain the terms H_{top} and E_{top} respectively, which represent the entrainment fluxes of heat and moisture at the ABL–free atmosphere interface as the boundary layer grows. These fluxes however are only nonzero when $H_v > 0$. Thus they switch on in the morning once the surface warms to a higher temperature than the ABL and switch off in the late afternoon when the opposite occurs. Similarly there are on/off switches in the prognostic equations for the inversions in temperature and humidity. The first term in each equation corresponds to changes in δ_θ or δ_q due to entrainment, so these terms are also only nonzero when $H_v > 0$.

B.1.2 ABL growth and collapse

The other on/off switch has to do with the collapse of the ABL during the afternoon (when the virtual heat flux switches sign). During the transition period (usually $\sim$ 1 hour) the boundary layer height goes from being a prognostic variable before the transition:

$$\frac{dh}{dt} = \frac{2\theta G_* e^{-\xi h}}{gh\delta_\theta} + (1 - 2c_D\delta)\frac{H_v}{\rho c_p \delta_\theta} \tag{B.1}$$

to a diagnostic variable throughout the transition:

$$h = -\frac{2G_*\rho c_p \theta}{H_v g} e^{-\xi h} \tag{B.2}$$

Also, at the beginning time of the collapse the inversions in temperature (δ_θ) and humidity (δ_q) are set to small values representing the fact that the mixed layer is then overlain by a residual layer with properties similar to those just before collapse. Further, the beginning and ending times of the transition are set by a conditional relationship which is itself a function of the state variables. All of these factors complicate the development of the adjoint model. The problem has to do with three switch times during the diurnal cycle:

1) The time at which entrainment begins; 2) The time at which the mixed layer begins to collapse and entrainment ceases; 3) The time at which the transition period ends. The development of the adjoint model is greatly simplified if these switch times are known and fixed, in which case the general formulation can simply be applied in a piecewise fashion throughout the day. In forward runs of the complete model we have seen that the timing of these switches are in fact not very sensitive to parameter perturbations. Therefore, for the simplified model, from which the adjoint will be developed, we will assume that these times can indeed be specified. The procedure will involve running the complete model and marking the three switch times over each diurnal cycle. These switch times will then be inputs to the simplified model (and adjoint model) allowing a piecewise integration. As will be shown below, the adjoint can then be developed in a straightforward manner. The other primary complication with respect to the development of the adjoint is the specification of h, δ_θ, and δ_q during the transition in the complete model. The transition equation for h specified originally by Smeda (1979) is a nonlinear implicit diagnostic equation. Due to the fact that its specification is already highly empirical and it only serves to complicate the adjoint results, we change the specification to:

$$\frac{dh}{dt} = -\zeta(h - h_{res})$$

where h_{res} is a residual height that can be obtained from the complete model run and ζ is simply a decay constant which is set to a value that causes the mixed layer to collapse to the appropriate level over the transition time. Similarly we model the inversions during the transition by:

$$\frac{d\delta_\theta}{dt} = -\zeta(\delta_\theta - \delta_{\theta_{res}})$$

$$\frac{d\delta_q}{dt} = -\zeta(\delta_q - \delta_{q_{res}})$$

where $\delta_{\theta_{res}}$ and $\delta_{q_{res}}$ are also taken from the complete model output. These simplifications are admittedly empirical, however the formulations for h, δ_θ, δ_q during the transition in the complete model are highly empirical themselves since the behavior of the boundary layer during its collapse is not well understood. These simplifications however are only applied over a very short interval during a diurnal cycle and do not appear to have a significant effect on the model response we are interested. With these simplifications the forward model over a diurnal cycle can be represented piecewise by:

$$\frac{\partial \mathbf{y}}{\partial t} = \mathbf{F}_1(\mathbf{y}, \boldsymbol{\alpha}) \qquad t_0 < t < t_1$$

$$\frac{\partial \mathbf{y}}{\partial t} = \mathbf{F}_2(\mathbf{y}, \boldsymbol{\alpha}) \qquad t_1 < t < t_2$$

$$\frac{\partial \mathbf{y}}{\partial t} = \mathbf{F}_3(\mathbf{y}, \boldsymbol{\alpha}) \qquad t_2 < t < t_3$$

$$\frac{\partial \mathbf{y}}{\partial t} = \mathbf{F}_1(\mathbf{y}, \boldsymbol{\alpha}) \qquad t_3 < t < t_f$$

where t_1, t_2, and t_3 represent the three transition times discussed above, and $\mathbf{F}_1$, $\mathbf{F}_2$, and $\mathbf{F}_3$ represent the appropriate prognostic equations during those times. The corresponding adjoint model is:

$$\frac{\partial \boldsymbol{\lambda}}{\partial t} = -\left(\frac{\partial \mathbf{F}_1}{\partial \mathbf{y}}\right)^T \boldsymbol{\lambda} + \frac{\partial \phi}{\partial \mathbf{y}} \qquad t_0 < t < t_1$$

$$\frac{\partial \boldsymbol{\lambda}}{\partial t} = -\left(\frac{\partial \mathbf{F}_2}{\partial \mathbf{y}}\right)^T \boldsymbol{\lambda} + \frac{\partial \phi}{\partial \mathbf{y}} \qquad t_1 < t < t_2$$

$$\frac{\partial \boldsymbol{\lambda}}{\partial t} = -\left(\frac{\partial \mathbf{F}_3}{\partial \mathbf{y}}\right)^T \boldsymbol{\lambda} + \frac{\partial \phi}{\partial \mathbf{y}} \qquad t_2 < t < t_3$$

$$\frac{\partial \boldsymbol{\lambda}}{\partial t} = -\left(\frac{\partial \mathbf{F}_1}{\partial \mathbf{y}}\right)^T \boldsymbol{\lambda} + \frac{\partial \phi}{\partial \mathbf{y}} \qquad t_3 < t < t_f$$

with

$$\boldsymbol{\lambda}(t_f) = 0$$

Once the adjoint model for a single diurnal cycle is developed, multiple-day integrations are a straightforward extension.

B.2 Implicit functional dependencies

In the forward model there are several instances where certain variables are expressed as nonlinear implicit functions, which in practice can be solved numerically, however are not amenable to the adjoint formulation. Particularly, the aerodynamic resistance and canopy resistance contain such implicit formulations. The suggested changes are shown below.

B.2.1 Aerodynamic resistance

In the complete model the canopy air temperature is a function of the three model temperature states, which are weighted by the aerodynamic resistances r_a, r_b, and r_d, where each resistance is a function of the wind speed above or within the canopy. The wind speed profile is in turn a function of the stability correction factor (F_M) which is a function of the bulk Richardson number. Therefore we have:

$$T_a = T_a(r_a(T_a), r_b(T_a), r_d(T_a))$$

Note that T_a is a function of the aerodynamic resistances, which are themselves functions of T_a. The above relationships are obviously nonlinear and involve several implicit relationships between variables. These kinds of relationships can be solved iteratively for each variable in a numerical model as they are done in the complete model. However, we would like to simplify the model in such a way as to eliminate the implicit relationships while maintaining realistic behavior of the model.

First, we slightly change the expression for the bulk Richardson number:

$$Ri_B = \frac{g(z_m - z_1)(\theta - T_s)}{0.5(\theta + T_s)U_m^2} \tag{B.3}$$

where we have replaced T_a with "T_s", a surface temperature, which approximates the air temperature at the surface. We can approximate it using either T_c or a weighted surface temperature, $T_c V_c + T_g(1 - V_c)$. By changing the formulation of Ri_B it is now only a function of forcing inputs and state variables.

Next, since r_{a1} is generally much larger than r_{a2} we express r_a as:

$$r_a = \frac{1}{F_H k^2 U_m} \ln\left(\frac{z_m - d}{z_0}\right)\left(\frac{z_m - d}{z_1 - d}\right) \tag{B.4}$$

where we specify z_0 as a model parameter. The implication of this simplification is that we underestimate r_a and consequently weight θ too heavily in the computation of T_a. This is something we must look for in the validation of the simplified model. Following Sellers and Dorman (1987) we simplify the other aerodynamic resistances as well:

$$r_d = \frac{C_{rd}}{U_1} \tag{B.5}$$

and

$$r_b = \frac{C_{rb}}{\sqrt{U_1}} \tag{B.6}$$

where

$$U_1 = U_r \frac{\ln(\frac{z_1 - d}{z_0})}{\frac{z_r - d}{z_0})}$$

where the parameters C_{rd} and C_{rb} can be taken from Sellers and Dorman (1987) or determined from the more complicated formulations used in the complete model. By simplifying the aerodynamic resistances and other variables in this way we have removed the implicit relationships that exist in aerodynamic part of the complete model.

From the complete model we were able to determine the average values for the parameters which are introduced above: $z_0 = 0.07m \approx 0.12h_{can}$, $C_{rd} = 62sm^{-1}$, and $C_{rb} = 13sm^{-1}$. As hoped, there is almost no change to the model output when these simplifications are used. The only state variables which even show a noticeable change are T_c and T_g which are slightly underestimated ($< 1K$) at midday causing a small decrease in upward longwave at the surface and a slight increase in sensible heat flux. Other than this, there is no discernible change in the model output, therefore we are comfortable with these simplifications to the complete model formulation.

B.2.2 Canopy resistance

The other implicit relationships in the model exist due to the way in which the canopy resistance is formulated. Similarly to the canopy air temperature, the canopy air vapor pressure is a function of three other vapor pressures which are weighted by resistances, where the canopy resistance is itself a function of e_a through the vapor pressure deficit and

leaf potential stress factors. The vapor pressure deficit function is given by:

$$f(\delta e) = \begin{cases} 1 & \delta e < 0 \\ 1 - h_{rc5}[e_*(T_a) - e_a] & 0 < \delta e < 1/h_{rc5} \\ 0 & \delta e > 1/h_{rc5} \end{cases} \tag{B.7}$$

The simplest solution is to replace e_a with e_m (which is a function of q) to represent the vapor pressure deficit between the surface and ABL. However, in general, e_m is smaller than e_a and thus we would expect that the parameter h_{rc5} may need to be adjusted accordingly to account for the bias introduced. By imposing the constraint that we want the modified stress factor values to match those from the original formulation we can write that the modified parameter h'_{rc5} should equal:

$$h'_{rc5} = h_{rc5} \frac{(e_*(T_a) - e_a)}{(e_*(T_a) - e_m)} \tag{B.8}$$

where we would expect this quantity to vary slightly over the diurnal cycle. To make h'_{rc5} a constant parameter we simply average the complete model output over the day, which gives a value of $1.95 \times 10^{-4} Pa^{-1}$ as compared to the original value of $2.38 \times 10^{-4} Pa^{-1}$. In performing simulations with the modified parameter we see no significant additional errors in the output from the simplified model.

The other implicit nonlinear relationship is due to the dependence of $\overline{r_c}$ on transpiration itself through the leaf potential stress function:

$$f(\psi_l) = \begin{cases} 0 & \psi_l < \psi_{c2} \\ \frac{\psi_l - \psi_{c2}}{\psi_{c1} - \psi_{c2}} & \psi_{c2} < \psi_l < \psi_{c1} \\ 1 & \psi_l > \psi_{c1} \end{cases} \tag{B.9}$$

where

$$\psi_l = \psi_r - z_T - \frac{E_{ct}}{\rho_w}(r_{plant} + r_{root}) \tag{B.10}$$

Deciding the best alternative for solving this particular problem is difficult. The stress function $f(\psi_l)$ is very important because it represents the control of soil moisture on transpiration. One alternative is to use a simpler more empirical formulation for the soil moisture control on transpiration. First however we will try to use an approximation to the formulation given in the complete model. The transpiration in the complete model is given by:

$$L_v E_{ct} = \frac{\rho c_p}{\gamma} \frac{(e_*(T_c) - e_a)}{\overline{r_c} + 2r_b}(1 - W_c) \tag{B.11}$$

Now to remove the implicit relationships we define a modified transpiration E_{ct}^* as:

$$L_v E_{ct}^* = \frac{\rho c_p}{\gamma} C_* \frac{(e_*(T_c) - e_m)}{\overline{r_c}} (1 - W_c) \tag{B.12}$$

where we have again replaced e_a by e_m and removed the the resistance $2r_b$ from the denominator. The first change is to remove the dependence on e_a, the second will allow us to remove the implicit dependence of transpiration on itself through the leaf potential stress function. How this is done will become clearer as we proceed. Finally, note that both modifications would in general cause E_{ct}^* to be larger than E_{ct}. As a result we add the free parameter C_* (which we would expect to be less than 1.0) to allow us to match the two values. By imposing the constraint that $E_{ct} = E_{ct}^*$ and solving for C_* we obtain:

$$C_* = \frac{\overline{r_c}}{\overline{r_c} + 2r_b} \frac{(e_*(T_c) - e_a)}{(e_*(T_c) - e_m)} \tag{B.13}$$

This quantity is determined from the complete model. We now rewrite E_{ct}^* as:

$$L_v E_{ct}^* = \frac{\alpha}{\overline{r_c}} = \frac{\alpha f(\Sigma)}{r_{cmin}} = \frac{\alpha f(T_c) f(\delta e) f(\psi_l)}{r_{cmin}} = \beta f(\psi_l)$$

where

$$\alpha = \frac{\rho c_p}{\gamma} C_* (e_*(T_c) - e_m)(1 - W_c)$$

and

$$\beta = \frac{\alpha f(T_c) f(\delta e)}{r_{cmin}}$$

Now rearranging the above expression we have:

$$L_v E_{ct}^* - \beta f(\psi_l) = 0$$

Under no-stress conditions ($f(\psi_l) = 1$) we see that $L_v E_{ct}^* = \beta$, while under complete stress ($f(\psi_l) = 0$), $L_v E_{ct}^* = 0$. Under intermediate conditions:

$$L_v E_{ct}^* - \beta \left(\frac{\psi_l - \psi_{c2}}{\psi_{c1} - \psi_{c2}} \right) = 0$$

Note that ψ_l is a linear function of E_{ct} (which we replace by E_{ct}^*) , and that the above equation is linear in ψ_l, so we have a linear equation for E_{ct}^*. Upon solving for E_{ct}^* we have:

$$E_{ct}^{*} = \frac{\eta(\psi_r - z_T - \psi_{c2})}{L_v + \eta r_{veg}} \tag{B.14}$$

where

$$\eta = \frac{\beta}{\psi_{c1} - \psi_{c2}}$$

and

$$r_{veg} = \frac{r_{plant} + r_{root}}{\rho_w}$$

Now, as stated above, E_{ct}^{*} can replace E_{ct} in the determination of ψ_l:

$$\psi_l = \psi_r - z_T - \frac{E_{ct}^{*}}{\rho_w}(r_{plant} + r_{root}) \tag{B.15}$$

B.3 Non-differentiable functions

The final part of the complete model which must be modified, are those components which are not strictly differentiable. In general non-differentiable functions can be of different types, those which are discontinuous with respect to dependent variables, those which contain conditional dependencies, and those with a combination of the two. For these types of functions in our model, the problem of non-differentiability usually arises only at the discrete points where the discontinuity is located or where the conditional dependence switches. To ensure differentiability there are several options: First, it may be that throughout the model integration the state variables stay within a certain range of the domain which does not include a "switch". If this is the case, then the function would be differentiable. The benefit is that the original function is used, while the drawback is that the model results must be checked beforehand in each case to see whether a switch is activated in that particular forward model run. Another option is to try to replace each function with a "smoothed" version. The benefit of this solution is that the function then becomes differentiable over the entire domain. Thus the model does not need to be checked beforehand to determine in which range the state variables lie. The primary drawback of this approach is that it is not always trivial to define a suitable replacement function which is both differentiable and also a good representation of the original function. Ultimately we need differentiability, but we also want the simplified model to behave similarly to the complete model. Additionally, the conditional function is often dependent on physical parameters, so formulating the replacement functions while maintaining some physical connection to these parameters is very important. The third option is a combination of the two mentioned above. It may be that in a forward model run the states lie within a region that contains a switch. Therefore we cannot use the original function. We could however replace the original function with a smoothed one designed to fit the function accurately only over the range in which the states lie. For example a given function may have two switches. In trying to fit a function that contains both switches, accuracy may be lost in the region we know the model states

lie in. Therefore it may be desirable to fit the function very accurately over the particular region we are interested. This again requires that the model results be checked beforehand and therefore limits the application of a general adjoint model for any set of model states and parameters. Ultimately, the most appropriate solution is highly dependent on the individual function under consideration and its context within the larger model. The specific occurrences of these functions and potential solutions are presented below.

B.3.1 Ground Evaporation

Soil relative humidity:

The evaporation from the ground is given by:

$$L_v E_g = \frac{\rho c_p}{\gamma} \frac{(h_{soil} e_*(T_g) - e_a)}{r_{soil} + r_d} \tag{B.16}$$

where the soil relative humidity is a conditional function defined in the following way:

$$h_{soil} = \begin{cases} \exp\left(\frac{\psi_1 g}{RT_g}\right) & e_*(T_g) \geq e_a \\ 1 & e_*(T_g) < e_a \end{cases} \tag{B.17}$$

This function is both discontinuous and conditional. It is complicated by the fact that the conditional arguments do not appear directly in the function itself (which makes smoothing difficult). Physically, $e_*(T_g)$ is generally much larger than e_a during the day and is often still larger at night (even under wet conditions when e_a is relatively large). In fact, unless the canopy air is extremely moist, the second condition will only be met at night when T_g becomes relatively small. Since the first condition is much more likely, we should examine the implications of eliminating the second condition and using the following unconditional specification of soil relative humidity:

$$h_{soil} = \exp\left(\frac{\psi_1 g}{RT_g}\right) \tag{B.18}$$

This function is most heavily dependent on ψ_1 which is a function of the soil moisture in the first layer (W_1). This function is plotted for soil types ranging from sand to clay in Figure 3a. To determine the accuracy of this representation over all conditions we need to examine two things: the difference between h_{soil} when using Equation (B.17) vs. (B.18) while $e_*(T_g) < e_a$, and how this inaccuracy ultimately affects the ground evaporation. If $e_*(T_g) < e_a$, the soil relative humidity should be equal to 1.0. As can be seen in Figure 1a, for different soil types there exist different threshold soil moisture values above which there is no appreciable difference between using Equation (B.17) vs. (B.18) for when $e_*(T_g) < e_a$. For example, for sand h_{soil} is essentially equal to 1.0 for any relative saturation greater than 0.2. Similarly for loam or clay this is true for W_1 greater than 0.4 and 0.6 respectively. Therefore under these soil moisture conditions there is absolutely no accuracy lost in using Equation (B.18) over (B.17). So it would seem that except for surface soil moisture lower than these respective values, the approximation is very good. In terms of using it universally (below

these threshold values) we can argue that even when h_{soil} is not accurately represented the effect on ground evaporation is minimal. The two most important factors which determine the ground evaporation in Equation (B.16) are the resistance (in the denominator) and the gradient in vapor pressure (in the numerator). In Figure B-1b, the soil resistance is plotted vs. soil moisture. The resistance corresponding to the threshold soil moisture values given above are $1500s/m$ (sand), $800s/m$ (loam), and $200s/m$ (clay). For these resistances (which are even higher for drier soil), the evaporation from the ground will approach zero regardless of the formulation for h_{soil}, and therefore (B.18) may be an allowable alternative. Finally in terms of the vapor pressure gradient, in the instances where $e_*(T_g) < e_a$ (generally at night) the difference $h_{soil}e_*(T_g) - e_a$ is small, making the evaporation small, so that an error in h_{soil} should not affect E_g very much. These arguments can be tested in the numerical model, but all point to the fact that Equation (B.18) seems to be a reasonable representation for h_{soil} that is both accurate and everywhere differentiable.

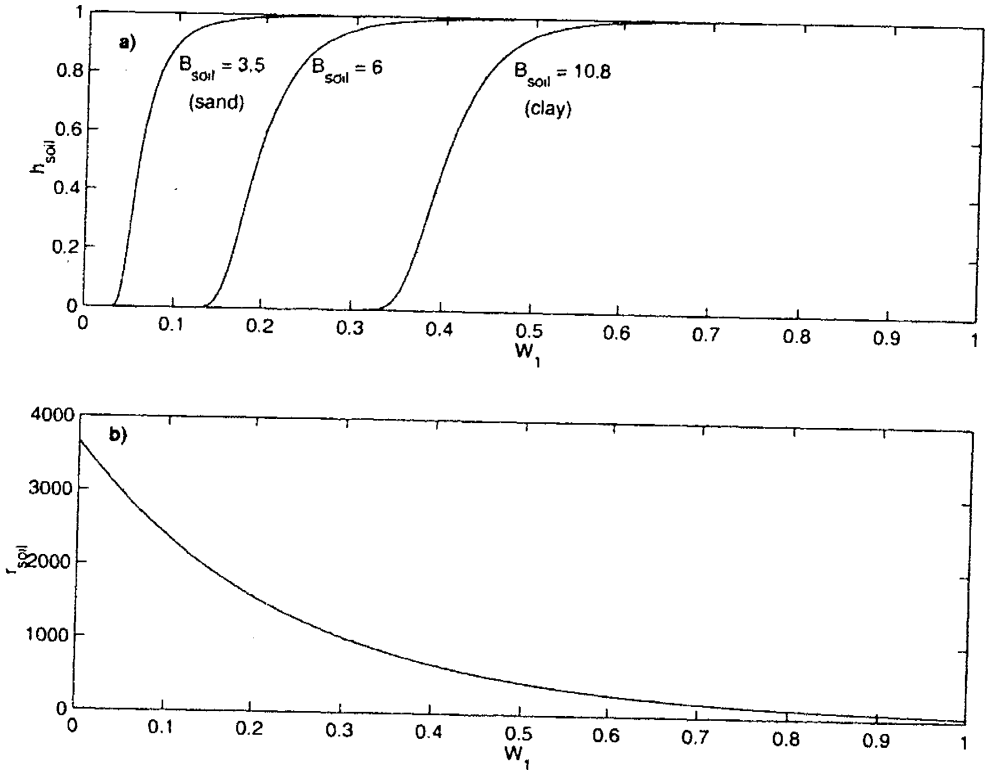

Figure B-1: a) Soil relative humidity vs. soil moisture in layer 1 over the range of soil types from sand to clay (for a nominal value of $T_g = 300K$). b) Soil resistance vs. soil moisture in layer 1.

B.3.2 Canopy Transpiration Stress Functions

The bulk canopy resistance is defined in Equation (A.29). Each of the stress functions $f(T_c)$, $f(\delta e)$, $f(\psi_l)$ in the canopy resistance formulation are not strictly differentiable due to conditional dependencies.

Temperature stress function:

The canopy temperature stress function is given by:

$$f(T_c) = \begin{cases} 0 & T_c < T_l \\ h_{rc3}(T_c - T_l)(T_u - T_c)^{h_{rc4}} & T_l < T_c < T_u \\ 0 & T_c > T_u \end{cases} \tag{B.19}$$

where the parameters h_{rc3} and h_{rc4} are themselves functions of the lower and upper temperature cutoffs (T_l and T_u respectively) and the optimal temperature T_0. Below T_l and above T_u the stress function is equal to zero, which effectively shuts off any transpiration. At the intermediate optimal temperature, the stress function is equal to one (no stress) and everywhere else is between 0 and 1. While this function is strictly non-differentiable at canopy temperatures equal to T_l or T_u it is one of the few cases where we may be able to keep the original function without doing any smoothing. This is because while $f(T_c)$ does exert stress it rarely shuts off canopy transpiration. For example for the case of grassland (as at the FIFE site) T_l and T_u have respective values of 283 K and 318 K (Koster and Suarez 1996). Over the entire 1987 FIFE record ($\sim$ 90 days), the minimum and maximum surface temperature never reach these extremes. However the FIFE data is from the summer months, so while it is safe to assume T_u will not be reached during the other months of the year, T_l most likely will be during the winter. Since snow processes are not included in the model, it is not anticipated that model runs will be performed for winter months, however in using Equation (B.19) care must be taken during Spring or Fall months that T_c does not go below T_l, otherwise a new formulation for $f(T_c)$ will need to be devised. If this turns out to be the case then a suitable approximation for $f(T_c)$ may be a function similar in form to a normal or log-normal distribution. However for now we will proceed using the function as it is currently formulated.

Vapor pressure deficit stress function:

The vapor pressure deficit stress was modified earlier and is given by:

$$f(\delta e) = \begin{cases} 1 & \delta e < 0 \\ 1 - h'_{rc5}[e_*(T_a) - e_m] & 0 < \delta e < 1/h'_{rc5} \\ 0 & \delta e > 1/h'_{rc5} \end{cases} \tag{B.20}$$

This stress function decreases linearly from 1 to 0 as δe varies between 0 and $1/h'_{rc5}$. While δe is most often in the differentiable range, it is much more likely than in the case of $f(T_c)$ that $f(\delta e)$ will be non-differentiable at some point during a typical model run. Therefore is it necessary to replace it with a smooth function. The replacement that we have chosen is a function of the form:

$$f(\delta e) = \frac{1}{2} + \frac{1}{2}\tanh\left[\beta_{\delta e}\left(e_*(T_a) - e_m - \frac{1}{2h'_{rc5}}\right)\right] \tag{B.21}$$

which asymptotes to 0 and 1 and is centered about the point $\delta e = 1/2h'_{rc5}$. The free parameter $\beta_{\delta e}$ can be used to fit the function. We have chosen to simply use least-squares to best fit the function over the entire range by choosing the optimal β_{de}. When using least-squares it was determined that $\beta_{\delta e} = -2.65h_{rc5}$. The optimal fit for the case when $h_{rc5} = 2.38 \times 10^{-4} Pa$ is shown in Figure B-2a. Note that the smoothed equation fits rather well throughout most of the range of δe. However, as a result of the smoothing, the locations of the points at which there is either no stress ($f(\delta e) = 1$) or complete stress ($f(\delta e) = 0$) have been moved outward such that the "no-stress" condition now occurs at $\sim -1000Pa$ (instead of $0Pa$) and the "complete-stress" condition now occurs at $\sim 5500Pa$ instead of $4200Pa$. While we would ideally like to retain the original locations for the two switch points we found that if the function is fit to the two switch points, the behavior within the intermediate range is represented rather poorly. In addition, the maximum difference between the fitted function and the original is 0.06 (which only occurs at the switch points) and is therefore not a major concern, especially since there is a significant level of uncertainty in the form of the stress functions and the associated parameter values.

Leaf potential stress function:

The form of the leaf potential stress function is very similar to that of the vapor pressure deficit stress. Therefore we can use a similar strategy in fitting a smooth function to it:

$$f(\psi_l) = \frac{1}{2} + \frac{1}{2}\tanh\left[\beta_\psi\left(\psi_l - \overline{\psi_c}\right)\right] \tag{B.22}$$

where $\overline{\psi_c} = \frac{1}{2}(\psi_{c1} + \psi_{c2})$ and the free parameter β_ψ is again used to fit the function using least-squares. For this function, the optimal value for the fitting parameter is $\beta_\psi = 2.65/(\psi_{c1} - \psi_{c2})$. The comparison between the smoothed function and the original formulation is shown in Figure B-2b. As in the case of $f(\delta e)$, this smoothed version of $f(\psi_l)$ fits well over the entire range of ψ_l.

B.4 Validation of Simplified Model

To verify the simplified model (with all of its modifications) we compare it to the complete model in order to gauge the effects of the simplifications on the model states and surface fluxes. Since the complete model has already been verified, we validate the simplified model by comparing it directly to output from the complete model. We have chosen to do so for a "wet" and "dry" case using the FIFE August 15, 1987 forcing. The only difference between the two cases is the initial soil moisture states, where in the wet case there is no soil moisture stress, and in the dry case there is soil moisture control on transpiration. We first examine the wet case. The comparison of model states and surface fluxes are shown in Figures B-3 andB-4 respectively. From Figure B-3 we see that, overall, the simplified model states match the complete model quite well. There is no discernible difference between the variables θ, δ_θ, δ_q, while there is a slight difference in the ABL height (h) and the soil moisture states.

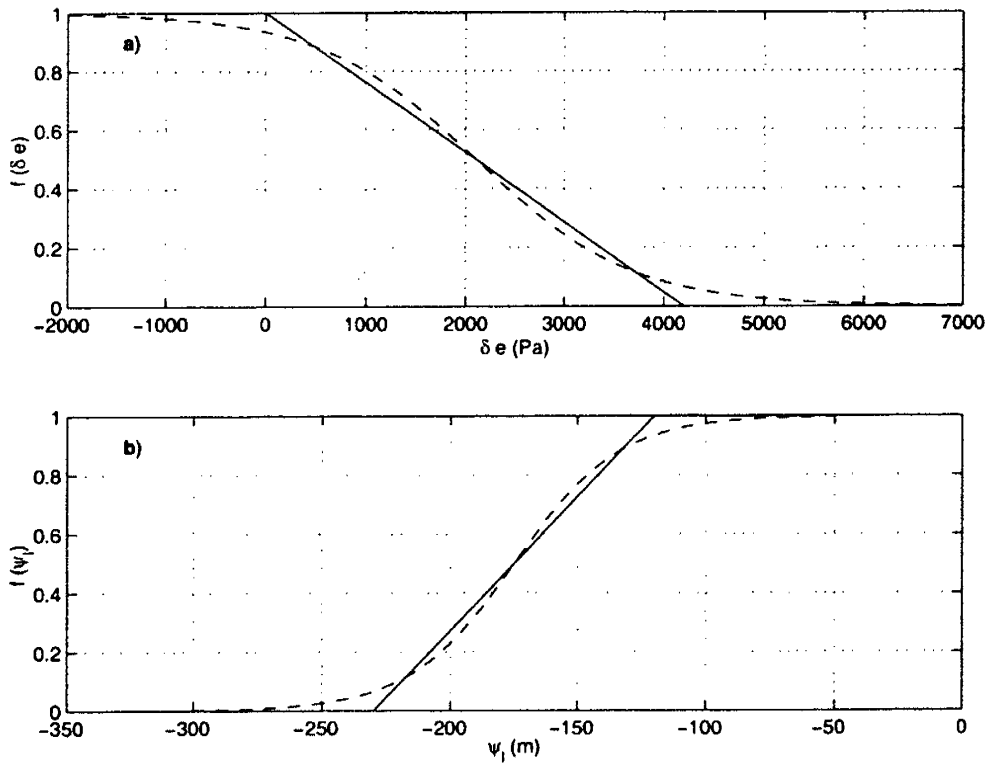

Figure B-2: a)Smooth approximation to $f(\delta e)$ for $h_{rc5} = 2.38 \times 10^{-4}$Pa. b) Smooth approximation for $f(\psi_l)$ for $\psi_{c1} = -120$m and $\psi_{c2} = -230$m.

The most significant differences occur in canopy and ground temperature at midday, but in both cases the difference is less than 1 degree Kelvin. There is also a slight error in specific humidity at midday, but again it is small. In terms of the fluxes, we see in Figure B-4 that the discrepancies in surface temperature cause an error in the upward longwave flux and in the sensible heat flux. Overall, though the simplified model matches quite well as there is no difference in net radiation and only minimal differences in evapotranspiration and downward longwave. For the dry case, the state and flux comparison are shown in Figures B-5 and B-6 respectively. In the dry case we see similar behavior in terms of the underestimation of canopy and ground temperature at midday. In this case there is slightly more discrepancy in q, h, and W_2 than for the wet case. The primary effect on surface fluxes is again an overestimation of sensible heat flux and an underestimation of upward longwave. In this case the difference in H is enough to cause a more significant change in the growth of the ABL causing more entrainment of dry air (thus the underestimation of q). Overall, however, we see that in both cases the effects of the simplifications on the behavior of the model are well within acceptable limits and by implementing them we are now able to proceed to the development of the adjoint model of the system.

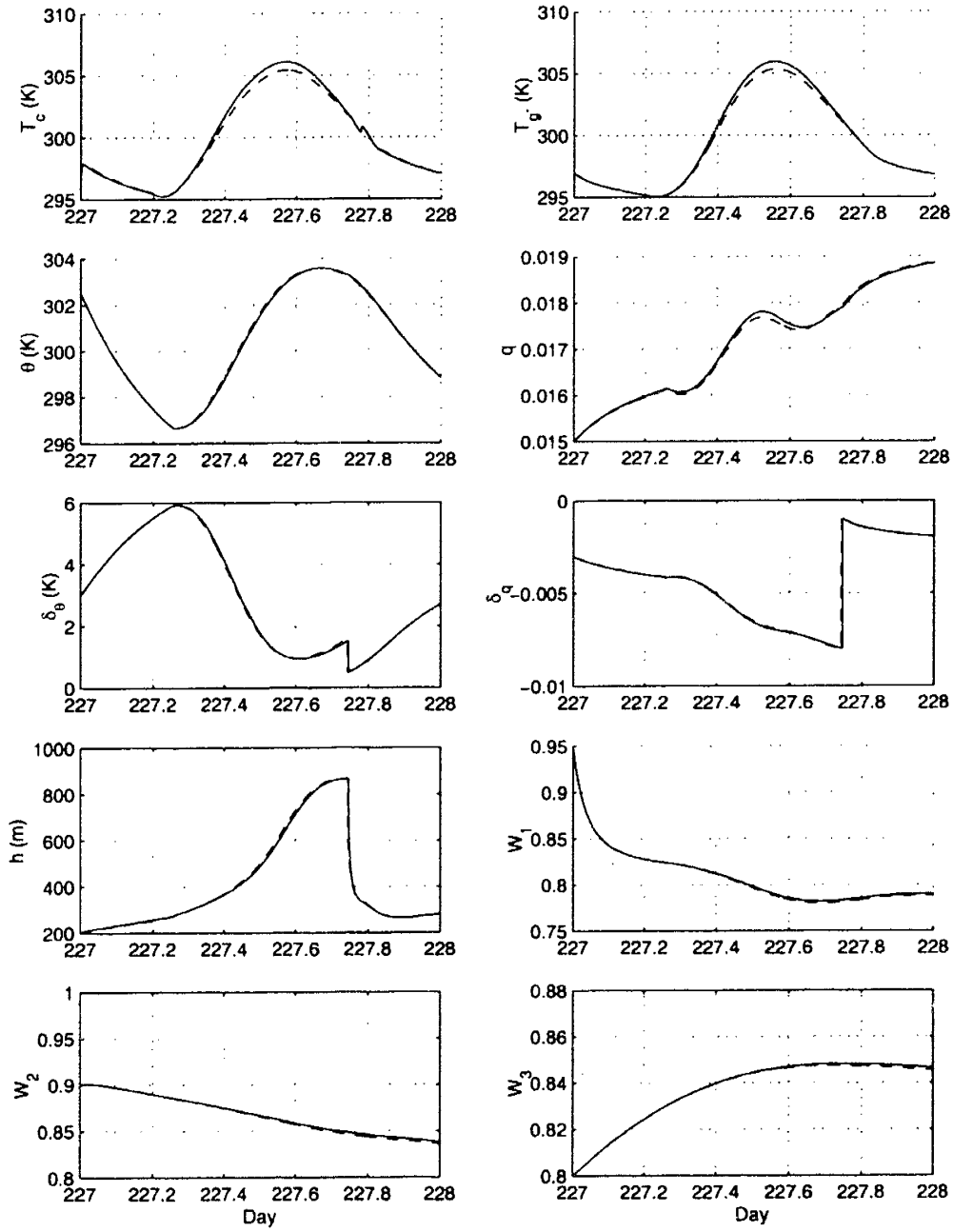

Figure B-3: Comparison of the model states between the complete model (solid lines) and the simplified model (dashed lines) for the "wet" case.

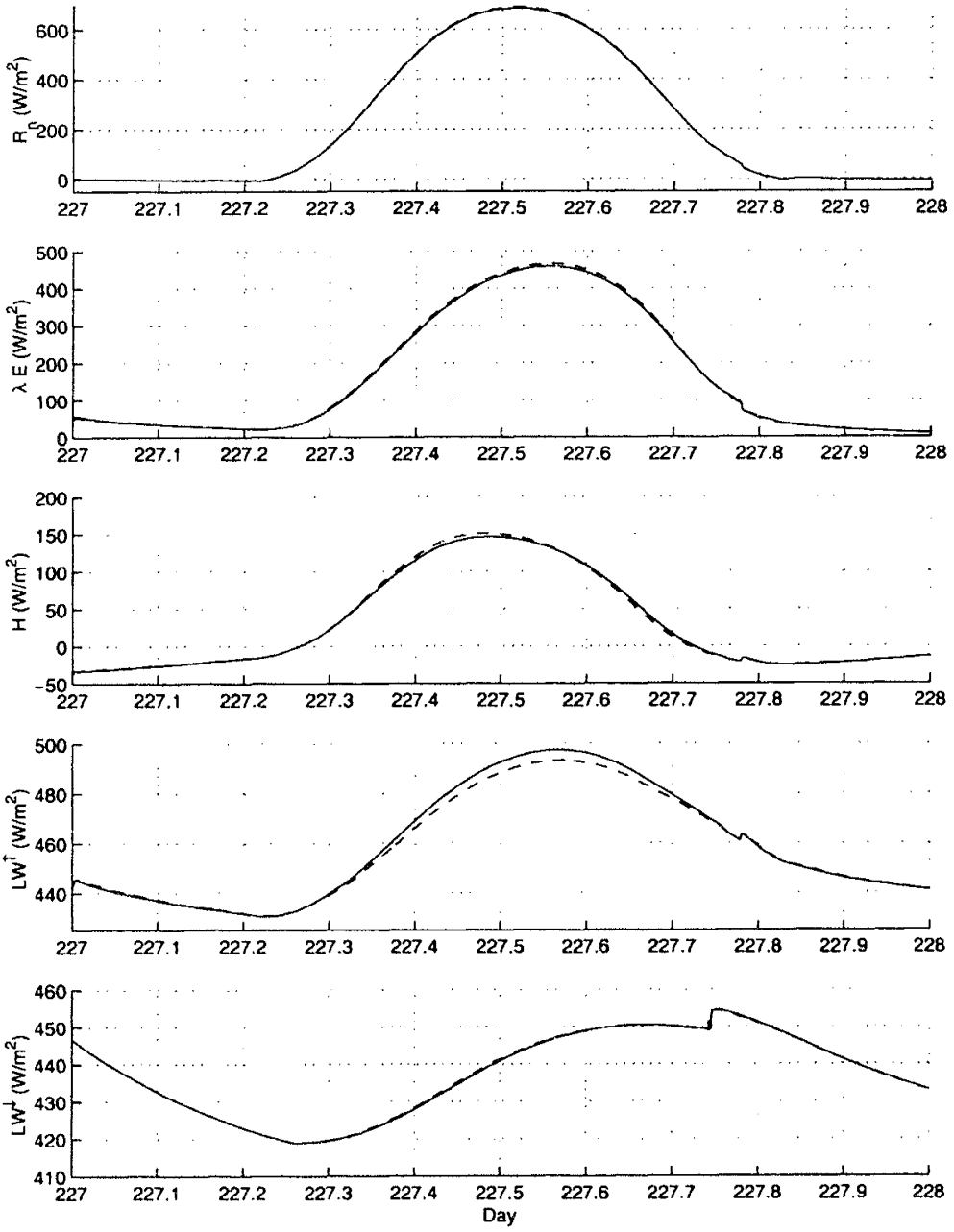

Figure B-4: Comparison of the surface fluxes between the complete model (solid lines) and the simplified model (dashed lines) for the "wet" case.

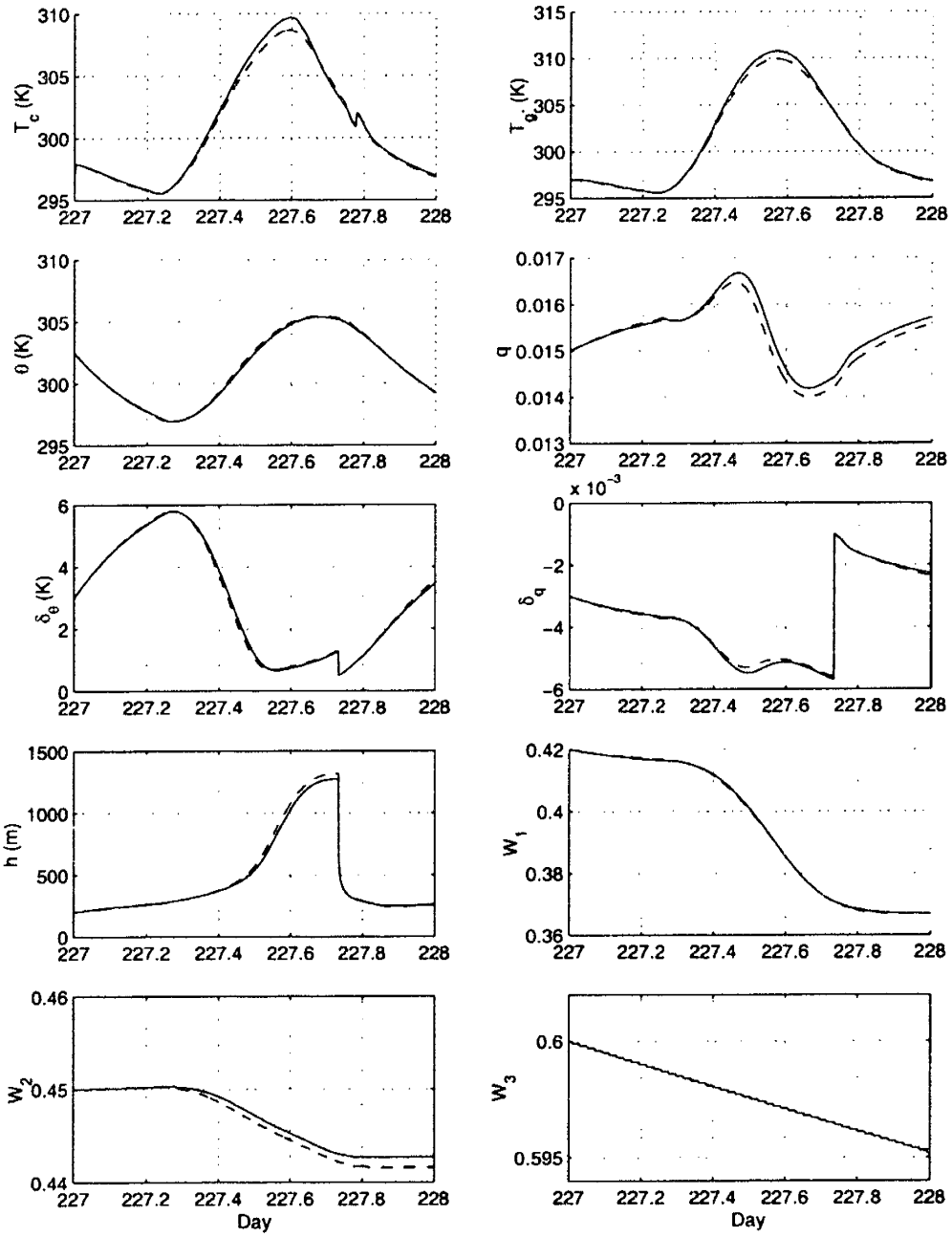

Figure B-5: Comparison of the model states between the complete model (solid lines) and the simplified model (dashed lines) for the "dry" case.

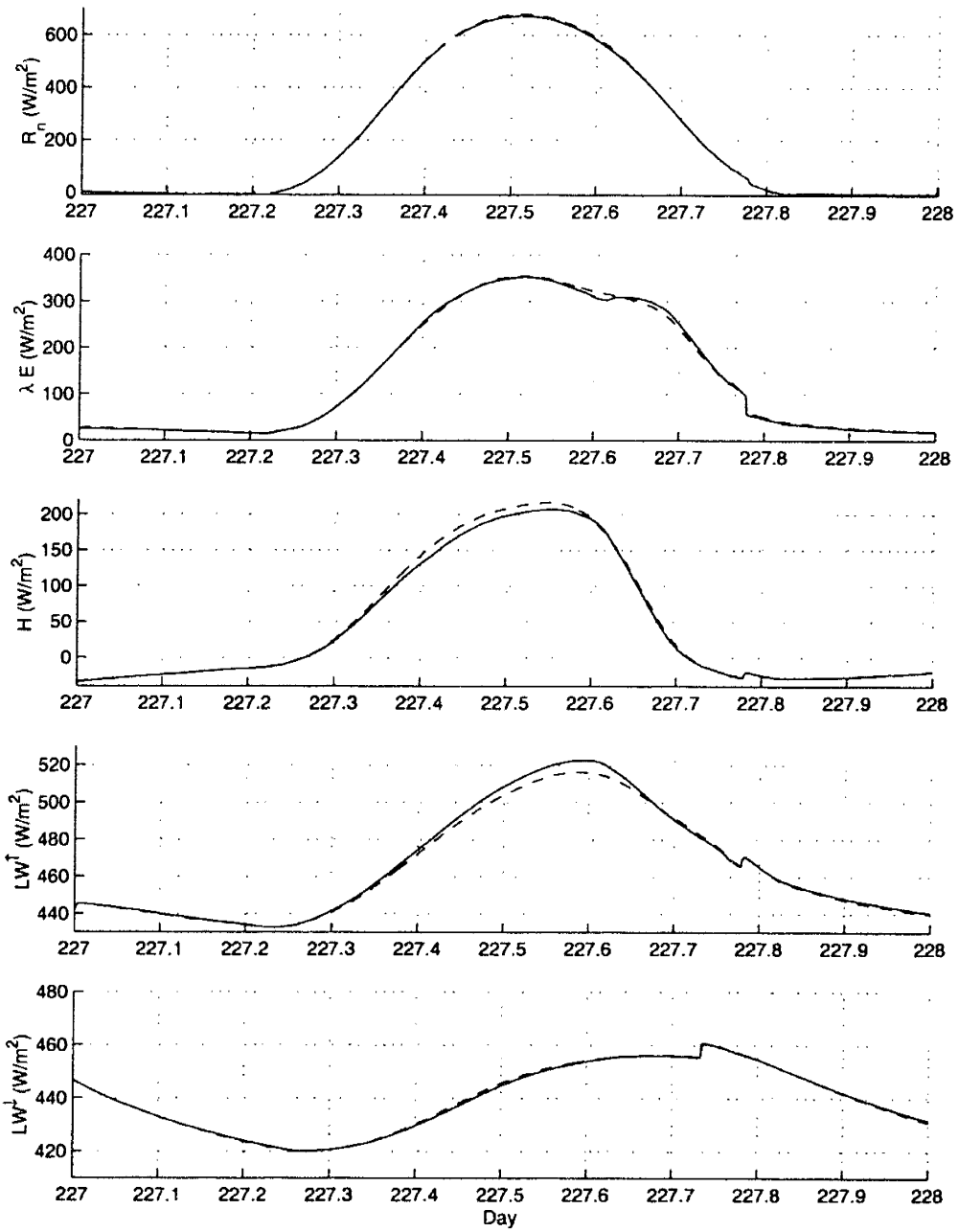

Figure B-6: Comparison of the surface fluxes between the complete model (solid lines) and the simplified model (dashed lines) for the "dry" case.

Appendix C

List of Symbols

A_R	ratio of entrainment virtual heat flux to surface virtual heat flux	[-]
$a_{c_{\Lambda,\mu}}$	canopy albedo of wavelength band Λ and direction μ	[-]
$a_{g_{\Lambda,\mu}}$	ground albedo of wavelength band Λ and direction μ	[-]
a_{q_1}	coefficient in humidity lapse rate equation	kg kg^{-1} m^{-1}
a_{q_2}	coefficient in humidity lapse rate equation	kg kg^{-1} m^{-2}
a_{θ_1}	coefficient in potential temperature lapse rate equation	K m^{-1}
a_{θ_2}	coefficient in potential temperature lapse rate equation	K m^{-2}
B_s	Clapp-Hornberger parameter	[-]
C_c	canopy heat capacity	J m^2 K^{-1}
C_g	surface soil heat capacity	J m^2 K^{-1}
C_d	deep soil heat capacity	J m^2 K^{-1}
C_{r_b}	coefficient in canopy aerodynamic resistance	(m s^{-1})$^{-3/2}$
C_{r_d}	coefficient in ground aerodynamic resistance	[-]
C_{y_0}	prior initial condition error covariance	
C_β	prior initial condition parameter error covariance	
C_ν	measurement error covariance	
$\mathsf{C}_\omega(t,t')$	prior model error covariance	
c_h	ABL growth proportionality constant	[-]
$\overline{c_h}$	prior value of ABL growth proportionality constant	[-]
c_p	dry air specific heat	J kg^{-1} K^{-1}
D_*	net dissipation of turbulent kinetic energy	m^3 s^{-3}
D_1	dissipation of mechanically generated turbulent kinetic energy	m^3 s^{-3}
D_2	dissipation of thermally generated turbulent kinetic energy	m^3 s^{-3}
D_c	canopy drainage	m s^{-1}
D_d	canopy throughfall	m s^{-1}
D_r	root density	m m^{-3}
d	zero-plane displacement height	m
d_1	thickness of soil layer 1	m
d_2	thickness of soil layer 2	m
d_3	thickness of soil layer 3	m
E_g	evaporation from ground	kg m^{-2} s^{-1}
E_c	transpiration from canopy	kg m^{-2} s^{-1}
E_{c1}	transpiration taken from soil layer 1	kg m^{-2} s^{-1}
E_{c2}	transpiration taken from soil layer 2	kg m^{-2} s^{-1}
E_{top}	dry air entrainment	kg m^{-2} s^{-1}

$e_*(T)$	saturated vapor pressure at temperature T	Pa
e_a	canopy air vapor pressure	Pa
e_m	mixed-layer vapor pressure	Pa
e_r	reference-level air vapor pressure	Pa
$\mathbf{F}$	nonlinear vector operator in dynamical model	
$\mathbf{F}_a$	nonlinear vector operator for ABL states in dynamical model	
F_H	stability correction for heat	[-]
F_M	stability correction for momentum	[-]
$\mathbf{F}_s$	nonlinear vector operator for surface states in dynamical model	
F_{T_c}	canopy temperature prognostic equation	K s^{-1}
F_{T_d}	deep ground temperature prognostic equation	K s^{-1}
F_{T_g}	ground surface temperature prognostic equation	K s^{-1}
F_h	mixed-layer height prognostic equation	m s^{-1}
F_q	mixed-layer specific humidity prognostic equation	kg kg^{-1} s^{-1}
F_{W_1}	layer 1 soil saturation prognostic equation	s^{-1}
F_{W_2}	layer 2 soil saturation prognostic equation	s^{-1}
F_{W_3}	layer 3 soil saturation prognostic equation	s^{-1}
F_{δ_q}	specific humidity inversion prognostic equation	kg kg^{-1} s^{-1}
F_{δ_θ}	potential temperature inversion prognostic equation	K s^{-1}
$F_{\Lambda,\mu(c)}$	radiation incident on canopy in band Λ and direction μ	W m^{-2}
$F_{\Lambda,\mu(g)}$	radiation incident on ground in band Λ and direction μ	W m^{-2}
F_θ	mixed-layer potential temperature prognostic equation	K s^{-1}
f_b	fraction of direct beam solar radiation to reach the surface	[-]
f_Λ	fraction of solar radiation to reach the surface in band Λ	[-]
G_*	production of mechanical turbulent energy	m^3 s^{-3}
g	gravitational acceleration	m s^{-2}
H	total sensible heat flux	W m^{-2}
$\overline{H}$	average daytime sensible heat flux	W m^{-2}
H_c	sensible heat flux from canopy	W m^{-2}
H_g	sensible heat flux from ground	W m^{-2}
H_{top}	sensible heat flux entrainment	W m^{-2}
H_v	virtual heat flux	W m^{-2}
$H_{v_{top}}$	virtual entrainment heat flux	W m^{-2}
h	mixed layer height	m
h^{obs}	observed mixed layer height	m
h_{soil}	soil relative humidity	[-]
J	model response or objective functional	
L_v	latent heat of vaporization	J kg^{-1}
L_vE	total latent heat flux	W m^{-2}
$\overline{L_vE}$	average daytime latent heat flux	W m^{-2}
LAI	leaf area index	m^2 m^{-2}
L_T	leaf area index	m^2 m^{-2}
$LW^\uparrow$	total upward longwave radiation	W m^{-2}
$LW^\downarrow$	total downward longwave radiation	W m^{-2}
$\mathbf{M}(\mathbf{y})$	measurement operator	
N_p	number of parameters	
N_s	number of state variables	
P_h	pressure at height h	Pa

P_s	surface pressure	Pa
P_{W_1}	infiltration into soil layer 1	m s^{-1}
$Q_{1,2}$	flow between soil layer 1 and 2	m s^{-1}
$Q_{2,3}$	flow between soil layer 2 and 3	m s^{-1}
Q_3	gravitational drainage from layer 3	m s^{-1}
q_0	initial condition of mixed-layer specific humidity	kg kg^{-1}
q	mixed-layer specific humidity	kg kg^{-1}
q^{obs}	observed mixed-layer specific humidity	kg kg^{-1}
q_{h+}	specific humidity immediately above h	kg kg^{-1}
q_r	reference-level specific humidity	kg kg^{-1}
q_r^{obs}	reference-level specific humidity observations	kg kg^{-1}
R	runoff	m s^{-1}
R_{Ad}	downwelling longwave radiation from within the mixed layer	W m^{-2}
R_{Au}	upwelling longwave radiation from within the mixed layer	W m^{-2}
R_{ad}	downwelling longwave radiation from above the mixed layer	W m^{-2}
R_{cu}	upwelling longwave radiation from canopy into the mixed layer	W m^{-2}
R_d	gas constant for dry air	J kg^{-1} K^{-1}
R_{gu}	upwelling longwave radiation from ground into the mixed layer	W m^{-2}
R_{nc}	net radiation absorbed by canopy	W m^{-2}
R_{ng}	net radiation absorbed by ground	W m^{-2}
R_v	gas constant for water vapor	J kg^{-1} K^{-1}
r_a	aerodynamic resistance between canopy air and reference level	s m^{-1}
r_{a_1}	aerodynamic resistance between canopy air and reference-level	s m^{-1}
r_{a_2}	aerodynamic resistance between reference-level and mixed-layer bottom	s m^{-1}
r_b	aerodynamic resistance between canopy and canopy air	s m^{-1}
$\overline{r_c}$	bulk canopy resistance	s m^{-1}
$\overline{r}_{c_{max}}$	maximum bulk canopy resistance	s m^{-1}
$\overline{r}_{c_{min}}$	minimum bulk canopy resistance	s m^{-1}
r_d	aerodynamic resistance between ground and canopy air	s m^{-1}
r_k	relative sensitivity of J to parameter α_k	[-]
r_k^c	coupled relative sensitivity of J to parameter α_k	[-]
r_k^u	uncoupled relative sensitivity of J to parameter α_k	[-]
r_{plant}	area-averaged plant vascular resistance	s
r_{root}	area-averaged resistance of soil-root system	s
r_s	single-leaf stomatal resistance	s m^{-1}
r_{soil}	soil resistance	s m^{-1}
S	solar constant	W m^{-2}
S_e	effective solar constant	W m^{-2}
$S^{\downarrow}$	surface incident shortwave radiation	W m^{-2}
t	time	s
t_0	initial time	s
t_f	terminal time	s
T_a	canopy air temperature	K
T_{c_0}	initial of canopy temperature	K
T_c	canopy temperature	K
T_{d_0}	initial condition of deep soil temperature	K
T_d	deep soil temperature	K

T_{h+}	temperature immediately above h	K
T_{g_0}	initial condition of surface ground temperature	K
T_g	surface ground temperature	K
T_g^{obs}	observed surface ground temperature	K
$\overline{T_g}$	average surface ground temperature	K
T_l	lower temperature limit in canopy temperature stress function	K
T_m	temperature at bottom of mixed-layer	K
T_o	optimum temperature in canopy temperature stress function	K
T_r	reference-level temperature	K
T_r^{obs}	reference-level temperature observations	K
T_s	radiometric surface temperature	K
T_s^{obs}	surface temperature observations	K
T_u	upper temperature limit in canopy temperature stress function	K
U_m	windspeed at bottom of mixed-layer	m s^{-1}
U_r	windspeed at reference-level	m s^{-1}
$\mathbf{u}$	model forcing vector	
V_c	fractional vegetation cover	[–]
V_r	volume of roots per unit volume of soil	m^3 m^{-3}
W_1	layer 1 soil saturation	[–]
W_{1_0}	initial condition of layer 1 soil saturation	[–]
W_2	layer 2 soil saturation	[–]
W_{2_0}	initial condition of layer 2 soil saturation	[–]
W_3	layer 3 soil saturation	[–]
w_*	convective velocity	m s^{-1}
$\mathbf{y}_0$	initial condition of model state vector	
$\overline{\mathbf{y}}_0$	prior initial condition of model state vector	
$\mathbf{y}_f$	final condition of model state vector	
$\mathbf{y}$	model state vector	
$\mathbf{y}_s$	surface model state vector	
$\mathbf{y}_a$	ABL model state vector	
z_0	aerodynamic roughness length	m
z_1	canopy height	m
z_d	depth of root zone	m
z_m	height to bottom of mixed-layer	m
z_r	reference-level height	m
$\mathbf{Z}$	measurement vector	
$\boldsymbol{\alpha}$	vector of structural model parameters	
$\boldsymbol{\beta}$	vector of initial condition model parameters	
$\overline{\boldsymbol{\beta}}$	prior vector of initial condition model parameters	
$\boldsymbol{\Delta}_s$	difference in surface state sensitivities between coupled and uncoupled models	
$\boldsymbol{\Delta}_\alpha$	difference in parameter sensitivities between coupled and uncoupled models	
$[\delta]$	diagonal matrix of Dirac delta functions with respect to observation times	[–]
δ_{q0}	initial condition in humidity inversion strength	kg kg^{-1}
δ_q	specific humidity inversion strength	kg kg^{-1}

$\delta_{\theta 0}$	initial condition in potential temperature inversion strength	K
δ_θ	potential temperature inversion strength of	K
δ_T	fraction of incident thermal radiation absorbed by canopy	[-]
ϵ	ratio of gas constant of dry air to gas constant of water vapor	[-]
ϵ_a	mixed layer bulk emissivity	[-]
ϵ_{ad}	effective emissivity above mixed layer	[-]
ϵ_d	effective mixed layer downward emissivity	[-]
ϵ_g	ground surface emissivity	[-]
ϵ_u	effective mixed layer upward emissivity	[-]
ϕ	nonlinear function in model response functional J	
η_i	gradient search step size for parameter i	[-]
γ	psychrometric constant	Pa K^{-1}
γ_q	lapse rate of q above h	kg kg^{-1} m^{-1}
γ_θ	lapse rate of θ above h	K m^{-1}
κ	von Karman constant	[-]
$\boldsymbol{\lambda}_0$	initial condition of adjoint state vector	
$\boldsymbol{\lambda}_f$	final condition of adjoint state vector	
$\boldsymbol{\lambda}$	adjoint state vector	
$\boldsymbol{\lambda}_s^c$	coupled surface adjoint state vector	
$\boldsymbol{\lambda}_s^u$	uncoupled surface adjoint state vector	
$\boldsymbol{\lambda}_a^c$	coupled ABL adjoint state vector	
Λ_{i_0}	initial condition of relative sensitivity for state y_i	
Λ_i	relative sensitivity for state y_i	
$\boldsymbol{\nu}$	measurement error vector	
ω_θ	time-varying error in mixed-layer potential temperature budget	W m^{-2}
ω_q	time-varying error in mixed-layer specific humidity budget	W m^{-2}
$\boldsymbol{\omega}$	vector of time-varying model error	
$\overline{\boldsymbol{\omega}}$	prior vector of time-varying model error	
ψ_{c1}	upper limit (no stress) in leaf potential stress function	m
ψ_{c2}	lower limit (complete stress) in leaf potential stress function	m
ψ_l	leaf potential	m
ψ_r	depth-averaged soil moisture potential	m
ψ_s	Clapp-Hornberger matric head parameter	m
ρ	air density	kg m^{-3}
ρ_w	density of water	kg m^{-3}
σ	Stefan-Boltzmann constant	W m^{-2} K^{-4}
$\sigma^2_{c_h}$	ABL growth parameter prior error variance	
$\boldsymbol{\sigma}^2_\omega$	vector of model error variances	
τ	length of model integration	s
τ_a	annual period	days
τ_c	decorrelation time scale	s
τ_d	diurnal period	s
θ	mixed layer potential temperature	K
θ^{obs}	observed mixed layer potential temperature	K
θ_0	initial condition of mixed-layer potential temperature	K
θ_s	soil porosity	[-]
ξ	mechanical turbulence dissipation parameter	m^{-1}

Bibliography

Alapaty, K., N.L. Seaman, D.S. Niyogi and A.F. Hanna , 2001: Assimilating surface data to improve the accuracy of atmospheric boundary layer simulations, *J. Appl. Meteorol.*, **40**, 2068–2082.

Alapaty, K., S. Raman and D.S. Niyogi , 1997: Uncertainty in the specification of surface characteristics: A study of prediction errors in the boundary layer, *Boundary-Layer Meteorol.*, **82**, 473–500.

Anderson, M.C., J.M. Norman, G.R. Diak, W.P. Kustas and J.R. Mecikalski , 1997: A two-source time-integrated model for estimating surface fluxes using thermal infrared remote sensing, *Remote Sens. Environ.*, **60**, 195–216.

Asrar, G.R. , 1998: Earth science strategic enterprise plan 1998-2002, *Technical report*, NASA, Washington D.C. pp. 54.

Ball, F.K. , 1960: Control of inversion height by surface heating, *Q. J. R. Meteorol. Soc.*, **86**, 483–394.

Bao, J.-W. and T.T. Warner , 1993: Treatment of on/off switches in the adjoint method: FDDA experiments with a simple model, *Tellus*, **45A**, 525–538.

Bastidas, L.A., H.V. Gupta, S. Sorooshian, W.J. Shuttleworth and Z.L. Yang , 1996: The land surface-atmosphere interaction: A review based on observational and global modeling perspectives, *J. Geophys. Res.*, **101**, 7209–7225.

Bennett, A.F. , 1999: Inverse methods and data assimilation, lecture notes of the 1999 summer school at the college of oceanic and atmospheric sciences at oregon state university, *Technical report*, Corvallis, Oregon. pp. 235.

Bennett, A.F., B.S. Chua, D.E. Harrison and M.J. McPhadden , 1998: Generalized inversion of tropical atmosphere-ocean data and a coupled model of the tropical pacific, *J. Climate*, **11(7)**, 1768–1792.

Betts, A.K. , 1973: Non-precipitating cumulus convection and its parameterization, *Q. J. R. Meteorol. Soc.*, **99**, 178–196.

Betts, A.K. and J.H. Ball , 1994: Budget analysis of FIFE 1987 sonde data, *J. Geophys. Res.*, **99**, 3655–3666.

Betts, A.K. and J.H. Ball , 1998: FIFE surface climate and site-averaged dataset 1987-89, *J. Atmos. Sci.*, **55 (7)**, 1091–1108.

Betts, A.K., R.L. Desjardins and J.I. MacPherson , 1992: Budget analysis of the boundary layer grid flights during FIFE 1987, *J. Geophys. Res.*, **97**, 18,533–18,546.

Betts, A.K., R.L. Desjardins, J.I. MacPherson and R.D. Kelly , 1990: Boundary layer heat and moisture budgets from FIFE, *Boundary-Layer Meteorol.*, **50**, 109–137.

Bhumralkar, C.M. , 1975: Numerical experiments on the computation of ground surface temperature in an atmospheric general circulation model, *J. Appl. Meteorol.*, **14**, 1246–1258.

Bonan, G.B., D. Pollard and S.L. Thompson , 1993: Influence of subgrid-scale heterogeneity in leaf area index, stomatal resistance, and soil moisture on grid-scale land-atmosphere interactions, *J. Climate*, **6**, 1882–1897.

Boni, G., F. Castelli and D. Entekhabi , 2001: Sampling strategies and assimilation of ground temperature for the estimation of surface energy balance components, *IEEE Trans. Geosci. Rem. Sens.*, **39**, 165–172.

Bouttier, F., J.-F. Mahfouf and J. Noilhan , 1993: Sequential assimilation of soil moisture from atmospheric low-level parameters. part II: Implementation in a mesoscale model, *J. Appl. Meteorol.*, **32**, 1352–1364.

Bouyssel, F., V. Cassé and J. Pailleux , 1999: Variational surface analysis from screen level atmospheric parameters, *Tellus*, **51A**, 453–468.

Brubaker, K.L. and D. Entekhabi , 1995: An analytic approach to modeling the land-atmosphere interaction 1. Construct and equilibrium behavior, *Water Resour. Res.*, **31(3)**, 619–632.

Brutsaert, W. , 1975: On a derivable formula for long-wave radiation from clear skies, *Water Resour. Res.*, **11**, 742–744.

Callies, U., A. Rhodin and D.P. Eppel , 1998: A case study on variational soil moisture analysis from atmospheric observations, *J. Hydrol*, **212-213**, 95–108.

Carlson, T., J.K. Dodd, S.G. Benjamin and J.N. Cooper , 1981: Satellite estimation of the surface energy balance, moisture availability and thermal inertia, *J. Appl. Meteorol.*, **20**, 67–87.

Carson, D.J. , 1973: The development of a dry inversion-capped convectively unstable boundary layer, *Q. J. R. Meteorol. Soc.*, **99**, 450–467.

Castelli, F., D. Entekhabi and E. Caporali , 1999: Estimation of surface heat flux and an index of soil moisture using adjoint-state surface energy balance, *Water Resour. Res.*, **10**, 3115–3125.

Clapp, R.B. and G.M. Hornberger , 1978: Empirical equations for some soil hydraulic properties, *Water Resour. Res.*, **14**, 601–604.

Colello, G.D., C. Grivet, P.J. Sellers and J.A. Berry , 1998: Modeling of energy, water, and CO_2 flux in a temperate grassland ecosystem with SiB2: May-October 1987, *J. Atmos. Sci.*, **55 (7)**, 1141–1169.

Collins, D.C. and R. Avissar , 1994: An evaluation with the Fourier amplitude sensitivity test (FAST) of which land-surface parameters are of greatest importance in atmospheric modeling, *J. Climate*, **7**, 681–703.

Cowan, I.R. , 1968: Mass, heat, and momentum exchange between stands of plants and their atmospheric environment, *Quart. J. Roy. Meteorol. Soc.*, **94**, 523–544.

Cuenca, R. H., M. Ek and L. Mahrt , 1996: Impact of soil water property parameterization on atmospheric boundary layer simulation, *J. Geophys. Res.*, **101**, 7269–7277.

Culf, A.D. , 1992: An application of simple models to Sahelian convective boundary-layer growth, *Boundary-Layer Meteorol.*, **58**, 1–18.

Deardorff, J.W. , 1978: Efficient prediction of ground surface temperature and moisture, with inclusion of a layer of vegetation, *J. Geophys. Res.*, **83(C4)**, 1889–1903.

Diak, G.R. and T.R. Stewart , 1989: Assessment of surface turbulent fluxes using geostationary satellite surface skin temperatures and a mixed layer planetary boundary layer model scheme, *J. Geophys. Res.*, **94**, 6357–6373.

Dickinson, R.E., P.J. Kennedy, A. Henderson-Sellers and M. Wilson , 1986: Biosphere-Atmosphere Transfer Scheme (BATS) version 1E as coupled to the NCAR Community Climate Model, *Technical Report TN-275+STR*, NCAR, Boulder, Colorado. pp. 72.

Dorman, J.L. and P.J. Sellers , 1989: A global climatology of albedo, roughness length and stomatal resistance for atmospheric general circulation models as represented by the Simple Biosphere model (SiB), *J. Appl. Meteorol.*, **28**, 833–855.

Driedonks, A.G.M , 1982: Models and observations of the growth of the atmospheric boundary layer, *Bound.-Layer Meteorol.*, **23**, 283–306.

Ek, M. and R.H. Cuenca , 1994: Variation in soil parameters: Implications for modeling surface fluxes and atmospheric boundary-layer development, *Boundary-Layer Meteorol.*, **70**, 369–383.

Entekhabi, D. , 1995: Recent advances in land-atmosphere interaction research, *Rev. Geophys.*, pp. 995–1003.

Entekhabi, D., H. Nakamura and E.G. Njoku , 1994: Solving the inverse problem for soil moisture and temperature profiles by sequential assimilation of multifrequency remotely sensed observations, *IEEE Trans. Geosci. Rem. Sens.*, **32**, 438–448.

Entekhabi, E., G. Asrar, A.K. Betts, K.J. Beven, R.L. Bras, C.J. Duffy, T. Dunne, R.D. Koster, D.P. Lettenmaier, D.B. McLaughlin, W.J. Shuttleworth, M.T. van Genuchten, M-Y. Wei and E.F. Wood , 1999: An agenda for land surface hydrology research and a call for the second international hydrological decade, *Bull. Amer. Meteorol. Soc.*, **80**, 2043–2058.

Errico, R.M. and T. Vukicevic , 1992: Sensitivity analysis using an adjoint of the PSU-NCAR mesoscale model, *Mon Wea. Rev.*, **120**, 1644–1660.

Errico, Ronald M. , 1997: What is an adjoint model?, *Bull. Amer. Meteorol. Soc.*, **78**, 2577–2591.

Federer, C.A. , 1979: A soil-plant-atmosphere model for transpiration and availability of soil water, *Water Resour. Res.*, **15(3)**, 555–562.

French, A.N., T.J. Schmugge and W.P. Kustas , 2000: Estimating surface fluxes over the SGP site with remotely sensed data, *Phys. Chem. Earth (B)*, **25**, 167–172.

Gao, X., S. Sorooshian and H.V. Gupta , 1996: Sensitivity analysis of the biosphere-atmosphere transfer scheme, *J. Geophys. Res.*, **101**, 7279–7289.

Gill, Philip E., Walter Murray and Margaret H. Wright , 1981: *Practical Optimization*, Academic Press, Inc.

Gillies, R.R. and T.N. Carlson , 1995: Thermal remote sensing of surface soil water content with partial vegetation cover for incorporation into climate models, *J. Appl. Meteorol.*, **34**, 745–756.

Goudriaan, J. , 1977: *Crop Micrometeorology: A Simulation Study*, Center for Agricultural Publishing and Documentation. Wageningen, the Netherlands.

Hall, Matthew C.G. , 1986: Application of adjoint sensitivity theory to an atmospheric general circulation model, *J. Atmos. Sci.*, **43**, 2644–2651.

Hall, Matthew C.G. and Dan G. Cacuci , 1983: Physical interpretation of the adjoint functions for sensitivity analysis of atmospheric models, *J. Atmos. Sci.*, **40**, 2537–2546.

Hall, M.C.G., D.G. Cacuci and M.E. Schlesinger , 1982: Sensitivity analysis of a radiative-convective model by the adjoint method, *J. Atmos. Sci.*, **39**, 2038–2050.

Hartmann, D.L. , 1994: *Global physical climatology*, Academic Press.

Henderson-Sellers, A. , 1993: A factorial assessment of the sensitivity of the BATS land-surface parameterization scheme, *J. Climate*, **6**, 227–247.

Henderson-Sellers, Ann, Z.-L. Yang and R.E. Dickinson , 1993: The project for inter-comparison of land-surface parameterization schemes, *Bull. of the Amer. Met. Soc.*, **74**, 1335–1349.

Hess, R. , 2001: Assimilation of screen-level observations by variational soil moisture, *Meteorol. Atmos. Phys.*, **77**, 145–154.

Hu, Z. and S. Islam , 1995: Prediction of ground surface temperature and soil moisture content by the force-restore method, *Water Resour. Res.*, **31**, 2531–2539.

Hu, Z. and S. Islam , 1996: A method to evaluate the importance of interactions between land surface and atmosphere, *Water Resour. Res.*, **32(8)**, 2497–2505.

Jackson, T.J., D.M. LeVine, A.Y. Hsu, A. Oldak, P.J. Starks, C.T. Swift, J.D. Isham and M. Haken , 1999: Soil moisture mapping at regional scales using microwave radiometry: The Southern Great Plains hydrology experiment, *IEEE Trans. Geosci. Rem. Sens.*, **37**, 2136–2151.

Jacobs, C.M.J. and H.A.R. DeBruin , 1992: The sensitivity of regional transpiration to land-surface characteristics: significance of feedback, *J. Climate*, **5**, 683–698.

Jarvis, P.G. , 1976: The interpretation of the variations in leaf water potential and stomatal conductance found in canopies in the field, *Phil. Trans. R. Soc. B*, **273**, 593–610.

Kim, C.P. and D. Entekhabi , 1998: Feedbacks in the land-surface and mixed-layer energy budgets, *Boundary-Layer Meteorol.*, **88**, 1–21.

Koster, R.D. and M.J. Suarez , 1996: Energy and water balance calculations in the Mosaic LSM, *Technical Report Technical Memorandum 104606, Vol. 9*, NASA.

Kustas, W.P., J.H. Preuger, K.S. Humes and P.J. Starks , 1999: Estimation of surface heat fluxes at field scale using surface layer versus mixed-layer atmospheric variables with radiometric temperature observations, *J. Appl. Meteorol.*, **38**, 224–238.

Lakshmi, V. , 2000: A simple surface temperature assimilation scheme for use in land surface models, *Water Resour. Res.*, **36**, 3687–3700.

Lakshmi, V., E.F. Wood and B.J. Choudhury , 1997: Evaluation of special sensor microwave/imager satellite data for regional soil moisture estimation over the red river basin, *J. Appl. Meteorol.*, **36**, 1309–1328.

LeDimet, F.-X. and O. Talagrand , 1986: Variational algorithms for analysis and assimilation of meteorological observation: Theoretical aspects, *Tellus*, **38A**, 97–110.

Lenschow, D.H. , 1974: Model of the height variation of the turbulence kinetic energy budget in the unstable planetary boundary layer, *J. Atmos. Sci.*, **31**, 465–470.

Li, Y., I.M. Navon, P. Courtier and P. Gauthier , 1993: Variational data assimilation with a semi-implicit global shallow water equation model and its adjoint, *Mon. Wea. Rev.*, **121**, 1759–1769.

Li, Z. and I.M. Navon , 1998: Adjoint sensitivity of the earth's radiation budget in the NCEP medium-range forecasting model, *J. Geophys. Res.*, **103(D4)**, 3801–3814.

Lilly, D.K. , 1968: Models of cloud-topped mixed layers under a strong inversion, *Q. J. R. Meteorol. Soc.*, **94**, 292–309.

Lin, J.D. , 1980: On the force-restore method for prediction of ground surface temperature, *J. Geophys. Res.*, **85(C6)**, 3251–3254.

Louis, J.F., M. Tiedtke and J.F. Geleyn , 1982: A short history of the operational PBL parameterization at ECMWF, *Technical report*, ECMWF, Reading, England. Workshop on PBL parameterization.

Lu, J. and W.W. Hsieh , 1997: Adjoint data assimilation in coupled atmosphere-ocean models: Determining model parameters in a simple equatorial model, *Q. J. R. Meteorol. Soc.*, **123**, 2115–2139.

Mahfouf, J.F. , 1991: Analysis of soil moisture from near-surface parameters: A feasibility study, *J. Appl. Meteorol.*, **30**, 1534–1547.

Mahrt, L. and D.H. Lenschow , 1976: Growth dynamics of the convectively mixed layer, *J. Atmos. Sci.*, **33**, 41–51.

Manabe, S. , 1969: Climate and ocean circulation 1. The atmospheric circulation and the hydrology of the Earth's surface, *Mon. Wea. Rev.*, **97**, 739–773.

McLaughlin, D. , 1995: Recent developments in hydrologic data assimilation, *Rev. Geophys., Suppl.*, pp. 977–984.

McLaughlin, D. and L.R. Townley , 1996: A reassessment of the groundwater inverse problem, *Water Resour. Res.*, **32**, 1131–1161.

McNaughton, K.G. and T.W. Spriggs , 1986: A mixed-layer model for regional evaporation, *Bound.-Layer Meteorol.*, **34**, 243–262.

McNider, R.T., A.J. Song, D.M. Casey, P.J. Wetzel, W.L. Crosson and R.M. Rabin , 1994: Toward a dynamic-thermodynamic assimilation of satellite surface temperature in numerical atmospheric models, *Mon. Wea. Rev.*, **122**, 2784–2803.

Mihailovic, D.T., H.A.R. de Bruin, M. Jeftic and A. van Duken , 1992: A study of the sensitivity of land surface parameterizations to the inclusion of different fractional covers and soil textures, *J. Appl. Meteorol.*, **31**, 1477–1487.

Mintz, M. , 1984: The sensitivity of numerically simulated climates to land-surface boundary conditions, *in* J. Houghton (ed.), *The Global Climate*, Cambridge University Press, pp. 79–105.

Niyogi, D.S., S. Raman and K. Alapaty , 1999: Uncertainty in the specification of surface characteristics, Part 2: Hierarchy of interaction explicit statistical analysis, *Boundary-Layer Meteorol.*, **91**, 341–366.

Njoku, E.G. and D. Entekhabi , 1996: Passive microwave remote sensing of soil moisture, *J. Hydrol*, **184(1)**, 101–130.

Norman, J.M., W.P. Kustas, J.H. Prueger and G.R. Diak , 2000: Surface flux estimation using radiometric temperature: A dual-temperature-difference method to minimize measurement errors, *Water Resour. Res.*, **36**, 2263–2273.

Pitman, A.J. , 1994: Assessing the sensitivity of a land-surface scheme to the parameter values using a single column model, *J. Climate*, **7**, 1856–1869.

Quinn, P., K. Beven and A. Culf , 1995: The introduction of macroscale hydrological complexity into land surface-atmosphere tranfer models and the effect on planetary boundary layer development, *J. Hydrol.*, **166**, 421–444.

Rabier, F., P. Courtier and O. Talagrand , 1992: An application of adjoint models to sensitivity analysis, *Beitr. Phys. Atmosph.*, **65**, 177–192.

Reichle, R., D. Entekhabi and D.B. McLaughlin , 2001a: Downscaling of radiobrightness measurements for soil moisture estimation: A four-dimensional variational data assimilation approach, *Water Resour. Res.*, **37(9)**, 2353–2364.

Reichle, R., D. McLaughlin and D. Entekhabi , 2001b: Variational data assimilation of microwave radiobrightness observations for land surface hydrology applications, *IEEE Trans. Geosci. Rem. Sens.*, **39**, 1708–1718.

Rhodin, A., F. Kucharski, U. Callies, D.P. Eppel and W. Wergen , 1999: Variational analysis of effective soil moisture from screen-level atmospheric parameters: Applications to a short-range weather forecast model, *Q. J. R. Meteorol. Soc.*, **125**, 2427–2448.

Ruggiero, F.H., K.D. Sashegyi, R.V. Madala and S. Raman , 1996: The use of surface observations in four-dimensional data assimilation using a mesoscale model, *Mon Wea. Rev.*, **124**, 1018–1033.

Schmugge, T. and T.J. Jackson , 1994: Mapping of surface soil moisture with microwave radiometers, *Meteorol. Atmos. Phys.*, **54**, 213–223.

Sellers, P.J. , 1985: Canopy reflectance, photosynthesis, and transpiration, *Int. J. Remote Sensing*, **6(8)**, 1335–1372.

Sellers, P.J., D.A. Randall, G.J. Collatz, J.A. Berry, C.B. Field, D.A. Dazlich, C. Zhang, G.D. Collelo and L. Bounoua , 1996: A revised land surface parameterization (SiB2) for atmospheric GCMs. Part I: Model formulation, *J. Climate*, **9**, 676–705.

Sellers, P.J., F.G. Hall, G. Asrar, D.E. Strebel and R.E. Murphy , 1992: An overview of the first international satellite land surface climatology project (ISLSCP) field experiment (FIFE), *J. Geophys. Res.*, **97(D17)**, 18345–18371.

Sellers, P.J. and J.L. Dorman , 1987: Testing of the simple biosphere model (SiB) using point micrometeorological and biophysical data, *J. Clim. Appl. Meteorol.*, **26**, 622–651.

Sellers, P.J., Y. Mintz, Y.C. Sud and A. Dalcher , 1986: A simple biosphere model (SiB) for use within general circulation models, *J. Atmos. Sci.*, **43**, 505–531.

Shukla, J. and Y. Mintz , 1982: Influence of land-surface evapotranspiration on the earth's climate, *Science*, **215**, 1498–1500.

Skaggs, Todd H. and D.A. Barry , 1996: Sensitivity methods for time-continuous, spatially discrete groundwater contaminant transport models, *Water Resour. Res.*, **32**, 2409–2420.

Smeda, M.S. , 1979: A bulk model for the atmospheric planetary boundary layer, *Bound.-Layer Meteorol.*, **17**, 411–427.

Strebel, D.E., D.R. Landis, K.F. Huemmrich and B.W. Meeson , 1994: *Surface Observations and Non-image Data Sets (vol. 1)*, CD-ROM, NASA, GSFC, Greenbelt, Maryland, USA.

Stull, R.B. , 1988: *An Introduction to Boundary Layer Meteorology*, Kluwer Academic Publishers.

Stull, R.B. , 1998: Mixed layer depth model based on turbulent energetics, *J. Atmos. Sci.*, **33**, 1268–1278.

Sun, N.-Z. and W. W.-G. Yeh , 1990: Coupled inverse problems in groundwater modeling 1. Sensitivity analysis and parameter identification, *Water Resour. Res.*, **26**, 2507–2525.

Sun, W.-Y. and M.G. Bosilovich , 1996: Planetary boundary layer and surface layer sensitivity to land surface parameters, *Boundary-Layer Meteorol.*, **77**, 353–378.

Talagrand, O. and P. Courtier , 1987: Variational assimilation of meteorological observations with the adjoint vorticity equation. I: Theory, *Quart. J. Roy. Meteor. Soc.*, **113**, 1311–1328.

Tarantola, A. , 1987: *Inverse Problem Theory: Methods for data fitting and model parameter estimation*, Elsevier. Amsterdam.

Tennekes, H. , 1973: A model for the dynamics of the inversion above a convective boundary layer, *J. Atmos. Sci.*, **30 (5)**, 558–567.

Thacker, W.C. and R.B. Long , 1988: Fitting dynamics to data, *J. Geophys. Res.*, **93(C2)**, 1227–1240.

van der Honert, T.H. , 1948: Water transport as a catenary process, *Discuss. Faraday Soc.*, **3**, 146–153.

Vinnikov, K.Y., A. Robock, S. Qiu, J.K. Entin, M. Owe, B.J. Chodhury, S.E. Hollinger and E.G. Njoku , 1999: Satellite remote sensing of soil moisture in illinois, united states, *J. Geophys. Res.*, **104**, 4145–4168.

Walker, J. and P.R. Rowntree , 1977: The effect of soil moisture on circulation and rainfall in a tropical model, *Quart. J. Roy. Meteorol. Soc.*, **103**, 29–46.

Wetzel, P.J., D. Atlas and R.H. Woodward , 1984: Determining soil moisture from geosynchronous satellite infrared data: A feasibility study, *J. Clim. Appl. Meteorol.*, **23**, 375–391.

Wetzel, P.J. and R.H. Woodward , 1987: Soil moisture estimation using GOES-VISSR infrared data: A case study with a simple statistical method, *J. Clim. Appl. Meteorol.*, **26**, 107–117.

Willis, G.E. and J.W. Deardorff , 1974: A laboratory model of the unstable planetary boundary layer, *J. Atmos. Sci.*, **31**, 1297–1307.

Wilson, M.F., A. Henderson-Sellers, R.E. Dickinson and P.J. Kennedy , 1987: Sensitivity of the bioshpere-atmosphere transfer scheme (BATS) to the inclusion of variable soil characteristics, *J. Clim. Appl. Meteorol.*, **26**, 341–362.

Xu, Qin , 1996a: Generalized adjoint for physical processes with parameterized disconinuities. Part I: Basic issues and heuristic examples, *J. Atmos. Sci.*, **53 (8)**, 1123–1142.

Xu, Qin , 1996b: Generalized adjoint for physical processes with parameterized disconinuities. Part II: Vector formulations and matching conditions, *J. Atmos. Sci.*, **53 (8)**, 1143–1155.

Yeh, W. W.-G. , 1986: Review of parameter identification procedures in groundwater hydrology: The inverse problem, *Water Resour. Res.*, **22**, 95–108.

Yeh, W. W.-G. and N.-Z. Sun , 1990: Variational sensitivity analysis, data requirements, and parameter identification in a leaky aquifer system, *Water Resour. Res.*, **26**, 1927–1938.

Zeman, O. and H. Tennekes , 1977: Parameterization of the turbulent energy budget at the top of the daytime atmospheric boundary layer, *J. Atmos. Sci.*, **34**, 111–123.

Zivković, M., J.-F. Louis and J.-L. Moncet , 1995: Sensitivity analysis of a radiation parameterization, *J. Geophys. Res.*, **100**, 12,827–13,840.

Zou, X. , 1997: Tangent linear and adjoint of "on-off" processes and their feasibility for use in 4-dimensional variational data assimilation, *Tellus*, **49A**, 3–31.

THESIS PROCESSING SLIP

FIXED FIELD: ill. _____ name _____

index _____ biblio _____

► **COPIES:** (Archives) Aero Dewey (Barker) Hum

Lindgren Music Rotch Science Sche-Plough

TITLE VARIES: ► ☐ _____

_____

_____

NAME VARIES: ► ☑ Adam _____

_____

IMPRINT: **(COPYRIGHT)** _____

_____

► **COLLATION:** _____

_____

► **ADD: DEGREE:** _____ ► **DEPT.:** _____

► **ADD: DEGREE:** _____ ► **DEPT.:** _____

SUPERVISORS: _____

_____

NOTES:

cat'r: date:

page:

► J96

► **DEPT:** C.E

► **YEAR:** 2000 ► **DEGREE:** Ph.D

► **NAME:** MARGULIS, Steven A.

_____